Xin Zhao

Terrestrial Laser Scanning Data Analysis for Deformation Monitoring

München 2019

Terrestrial Laser Scanning Data Analysis for Deformation Monitoring

Von der Fakultät für Bauingenieurwesen und Geodäsie

der Gottfried Wilhelm Leibniz Universität Hannover

zur Erlangung des Grades

Doktor-Ingenieur (Dr.-Ing.)

genehmigte Dissertation

Vorgelegt von

M.Sc. Xin Zhao

Geboren am 26.07.1986 in Shanxi, P.R. China

München 2019

Adresse der DGK:

Ausschuss Geodäsie der Bayerischen Akademie der Wissenschaften (DGK)

Alfons-Goppel-Straße 11 ● D – 80 539 München
Telefon +49 – 331 – 288 1685 ● Telefax +49 – 331 – 288 1759
E-Mail post@dgk.badw.de ● http://www.dgk.badw.de

Declaration

Hereby I declare that

- I know the Regulations for doctoral candidates at the Faculty of Civil Engineering and Geodetic Science (Promotionsordnung).

- I have completed the thesis independently; used materials by others are listed in the references.

- I didn't pay any monetary benefits for regards to content.

- the dissertation has not been used as a M.Sc. or similar thesis before, and that the thesis or parts of it have not been published before.

- I didn't previously apply for any exam as a doctoral candidate.

Xin Zhao   20. June. 2019

Abstract

Deformation monitoring of structures is one of the main tasks of engineering geodesy. In the projects related with deformation monitoring, terrestrial laser scanning (TLS) has become a powerful tool among all the data acquisition approaches due to its high precision and spatial resolution in capturing 3D point clouds. Therefore, it allows to entirely monitor the behavior of objects. The challenge lies in the definition and computation of the difference between the 3D point clouds in order to model the deformations. Various methods exist, from which the geometry-based method is one of the most popular ones. The key procedure in this strategy is to approximate the point cloud of an epoch by mathematic models, mostly in a linear Gauss-Markov model. The geometry changes of the object are detected by comparing the approximated models of various epochs. The traditional manual deformation monitoring is increasingly automatized in order to be easily implemented and cost-efficient. The automatic selection of an adequate mathematic model in the data approximation, which includes stochastic and functional parts, is the basis of the automization of the deformation monitoring procedure and will have influence on the reliability of the results.

The thesis carries out some investigations in the above-mentioned background. In the initial study, the risk of a commonly misspecified variance-covariance matrix (VCM), i.e. neglecting the mathematical correlations and assuming homoscedasticity, on the results of a congruency test, is highlighted. The significant influence of a misspecified stochastic model on the deformation judgment motivates further investigations on a refined, heteroscedastic VCM based on a more detailed uncertainty budget of TLS measurements. The specified VCM can in generally be evaluated by means of two hypothesis testing procedures, i.e. a nested model misspecification test and a non-nested model selection test. In addition, the functional model also has strong influence on the deformation decision. Under this consideration, the more flexible B-spline models are applied in the approximation and their performances are compared statistically with that of polynomial models in two case studies, where the superiority and limitation of them are exemplarily revealed. Besides the widely-used model selection procedures based on information criteria, we adopted two of the hypotheses test-based approaches, i.e. simulation-based Cox's test and Vuong's non-nested test, to generally discriminate statistically between parametric models. The introduced automatic selection processes for the stochastic and functional models significantly improve the quality of the deformation monitoring process. It is therefore the basis for an interdisciplinary monitoring process.

Keywords: terrestrial laser scanning, deformation monitoring, congruency test, variance-covariance matrix, functional model, B-spline, hypothesis test

Zusammenfassung

Die Überwachung von künstlichen und natürlichen Objekten ist eine Hauptaufgabe der Ingenieurgeodäsie. Aufgrund seiner hohen Präzision und räumlichen Auflösung ist das terrestrische Laserscanning (TLS) unter allen Vorgehensweisen für die Datenerfassung ein weit anerkanntes Verfahren in der Deformationsüberwachung geworden. Es ermöglicht somit die quasi vollständige Überwachung von Objekten. Die größte Herausforderung liegt in der Vergleichbarkeit der 3D-Punktwolken. Hierfür existierten eine Reihe von Methoden, unter denen die geometrie-basierte Methode die bekannteste ist. Das zentrale Vorgehen basiert auf der Approximation der 3D-Punktwolke einer Epoche mit einem parametrischen Modell, zumeist mit Hilfe eines linearen Gauss-Markov Modells. Die geometrischen Veränderungen des Objektes werden dann durch den Vergleich der approximierten Modelle aus verschiedenen Epochen ermittelt. Die herkömmliche manuelle Deformationsanalyse wird zunehmend automatisiert, um einfach und kostengünstig implementiert zu werden. Die automatische Anwendung eines adäquaten mathematischen Modells in der Datenapproximation, das stochastische und funktionale Teile umfasst, ist die Grundlage für die Automatisierung des Deformationsprocesses. Dies hat einen signifikanten Einfluss auf die Zuverlässigkeit der Ergebnisse.

Aus diesem Grund beschäftigt sich die Dissertation mit den oben genannten Themen. In der ersten Studie wird die Gefahr einer fehlerhaften Spezifikation der Varianz-Kovarianz-Matrix (VKM), insbesondere durch Nichtbeachtung der mathematischen Korrelationen und der Annahme der Homoskedastizität, auf die Ergebnisse des Kongruenztestes, diskutiert. Der signifikante Einfluss eines fehlerhaft spezifizierten stochastischen Modells auf den Kongruenztest begründet die weitere Forschung über eine verfeinerte, heteroskedastische VKM, die auf einem detaillierteren Unsicherheitsbudget von TLS-Messungen basiert. Die spezifizierte VKM wird durch zwei Hypothesentests bewertet: den „nested model misspecification test"und den „non-nested model selection test", welche generell auch für die Validierung weiterer Versuche benutzt werden können. Darüber hinaus hat das funktionale Modell auch einen starken Einfluss auf die Qualität der Ergebnisse. Daher werden flexible B-Spline Modelle in der Approximation angewendet und mit polynomialen Modellen in zwei Fallstudien statistisch verglichen, sodass die Überlegenheit und Einschränkungen der beiden Verfahren beispielhaft gezeigt werden kann. Neben den weit verbreiteten auf Informationskriterien basierenden Modellauswahlverfahren wurden im Rahmen der Dissertation zwei hypothesentest-basierte Herangehensweisen verwendet. Mit Hilfe des „simulation-based Cox's test"und des „Vuong's non-nested test"wird statistisch zwischen parametrischen Modellen unterscheiden. Die eingeführten Beurteilungsverfahren für die stochastischen und funktionalen Modelle tragen zu einer signifikanten Qualitätssteigerung des Überwachungsprozesses bei. Die Vorgehensweise ist damit die Basis für das interdisziplinäre Monitoring.

Stichworte: Terrestrisches Laserscanning, Deformationsüberwachung, Kongruenztests, Varianz-Kovarianz-Matrix, B-Spline, funktionales Modell, Hypothesentests

List of Figures

List of Tables

Abbreviation

AIC   Akaike information criterion

BIC   Bayesian information criterion

DEM   digital elevation model

EDM   electronic distance meters

EIV   errors-in-variables

FOV   field of view

GHM   Gauss-Helmert model

GMM   Gauss-Markov model

GNSS   global navigation satellite systems

GUM   Guide to the Expression of Uncertainty in Measurement

ICP   iterative closest point

IMU   inertial measurement unit

KLIC   Kullback-Leibler information criterion

LOP   law of propagation of uncertainty

NURBS   Non-uniform rational B-Splines

RANSAC   random sample consensus

TLS   terrestrial laser scanning (scanner)

TOF   time-of-fight

UMPI   uniformly most powerful invariant

VCM   variance-covariance matrix

Contents

Contents

1 Introduction

1.1 Motivation of the study

For the sake of personal safety and a proper security, the society has the need in minimizing the risk that can occur due to unexpected collapses of natural and artificial objects. Structural safety monitoring (e.g. for bridges, tunnels, dams, and tall buildings, etc.) allows us to see what is happening to the objects over time. Structures might appear static to the casual observer, but the forces of wind, temperature, traffic load and geologic hazard may affect their shape, size and location. Such changes are collectively referred to as deformations. Deformation of a structure can produce long-term damage and may ultimately lead to structural failure, that's why deformation monitoring has become one of the main tasks as well as the most common application of engineering geodesy. With the development of software and hardware elements, the traditional manual deformation monitoring is increasingly automatized. The highly automatic deformation monitoring system optimizes the manual fieldwork by setting up automatic measurement schedules to collect data at regular intervals. Based on the measurements, the geometry changes of objects can be detected and quantified, which are used for the further comprehensive deformation analysis.

Compared with traditional point-wise deformation monitoring, terrestrial laser scanning (TLS) has become a powerful tool in this field due to its high precision and spatial resolution in capturing 3D point clouds which facilitate to entirely monitor the behaviour of objects. Deformation monitoring through point clouds can be based on different comparison methods, one of the most popular is the geometry-based approach, i.e. to compare the approximated mathematical models which describe the geometrical features of the object in various epochs. The key point in deformation monitoring is to decide whether a significant geometry change actually occurs between two or more measured epochs. In other words, the congruency problem for the repeated measured epochs has to be solved. The focus of the thesis lies on the statistical congruence judgments and the influence factors, i.e. the misspecified stochastic model and inadequate functional model, that may affect the decisions. Furthermore, to guarantee the reliability of judgments on the possible geometry changes, efforts are devoted to developing model selection approaches based on the hypotheses testing framework for both stochastic and functional models. It is noticeable that the automatic model selection approaches serve as the basis of the automization of geometry-based deformation monitoring procedure. Therefore, we use the term "monitoring" in the title.

The congruency tests proposed by Pelzer (1971) are usually employed to solve this kind of problem, which have proved to be the uniformly most powerful invariant (UMPI) test in the Gauss-Markov models (GMM) with normal random deviations and specified variance-covariance matrix (VCM) (cf. Kargoll, 2012, Chapter 3). In geometry-based deformation monitoring, the correctness of the approximated mathematical model serves as the prerequisite of the UMPI property for the congruency test. The parameters of the mathematical model are in most cases estimated in a least-squares adjustment where the reliable adjusted results depends both on the selected functional model, i.e. the relationship between the parameters to be estimated and the observations, as well as on the stochastic model, i.e. the VCMs. Consequently, on the one hand, it is crucial to approximate the scattered points by a proper functional model to describe the geometrical changes; on the other hand, searching for a realistic stochastic model and developing the statistical approach to evaluate its adequacy is also relevant.

1.2 Proposal and content

Since the optimality of the congruency test only applies on the prerequisite of adequate estimations, the misspecified functional or stochastic model may weaken the power of the test. As the initial research, in the context of adequate functional models, the risk of commonly misspecified VCMs, i.e. neglecting heteroscedasticity or mathematical correlation, on the power of congruency test, is highlighted.

The significance of a realistic VCM for the congruency test motivates the further research on a refined, heteroscedastic VCM based on a more detailed uncertainty budget of TLS measurements. The correctness of a specified VCM in the context of the given dataset is further statistically evaluated by means of a nested model misspecification test and a non-nested model selection test. The aims of this study is not only to provide the results of an initial attempt of specifying VCM for TLS measurements, but also to present testing procedures which will in the future be used to validate further attempts at improving the stochastic model for TLS measurements.

As the other pillar of the least-squares adjustment, the functional model also has strong influence on the congruency test. Commonly, the most parsimonious, yet sufficiently accurate functional model for the object is selected through information-theoretic approaches, i.e. Akaike information criterion (AIC) and the Bayesian information criterion (BIC). As an alternative solution, our focus lies on the hypotheses test-based approaches. They offer the advantage that the significant probabilistic differences between models can be detected. These information has not been provided by the methods mentioned previously. In the following numerical examples, two of the commonly used parametric models, i.e. polynomials and B-splines, are approximated with similar parameters and discriminated statistically under the given dataset. Besides providing alternative model selection approaches, in the numerical examples, we also try to reveal the performance of competing models in reflecting detailed geometries and their robustness when data gap exists.

The investigation, on the one hand, reveals the great significance of the specified VCMs and adequate functional model in geometry-based deformation monitoring. On the other hand, the thesis develops and applies the statistical evaluation approaches, which serve as alternative ways beyond the global test and information-theoretic approaches, in selecting the proper stochastic and functional models. The thesis is structured as follows. Chapter 2 introduces the basics of TLS, i.e. classification, scanning principal, error budgets and calibration approaches, as well as the procedures of TLS-based deformation monitoring (field work, data pre-processing and methodology). Chapter 3 provides the commonly-used deformation models. In particular, the congruency model is introduced and the significant influence of the misspecified stochastic models on the congruency based deformation analysis is highlighted. Motivated by the results of Chapter 3, the subsequent research, which is shown in Chapter 4, attempts to establish a refined stochastic model, which is evaluated statistically through testing procedures. The focuses of Chapter 5 lies on the selection of proper parametric models to approximate the point clouds by means of hypotheses test-based approaches. In addition, the performances of the commonly-used parametric models, i.e. B-splines and polynomials, are compared and discussed in two case studies. Chapter 6 concludes the thesis and gives an outlook on open questions.

2 On the application of TLS in deformation monitoring

The traditional methods of point-wise deformation monitoring technology with global navigation satellite systems (GNSS), tacheometers and levels have in many cases been surpassed by the use of TLS, which allows a better discretization in time and in the space of an object. Therefore TLS facilitates a more realistic modeling of the deformation. In this chapter, the basics of TLS, i.e. the classification according to the ranging approaches and scanning principal, are outlined in the subsection 2.1. Since errors are inevitable in data acquisition procedures, the error budget of TLS measurements caused by various influence factors are roughly summarized in the subsection 2.2. The main focus of this chapter lies on the subsection 2.3, where the procedure of deformation monitoring with TLS measurements is explained.

2.1 Fundamentals of TLS

The TLS systems are characterized by the non-contact measurement techniques and sequentially generate 3D coordinates of a surface in a given field of view with an intensity value as a fourth dimension. The raw measurements of TLS are polar coordinates of each point, i.e. range, horizontal and vertical angles[1], which are further automatically converted to 3D Cartesian coordinates. Accordingly, the core components of TLS are the ranging and beam deflection systems.

2.1.1 Range measurement system

The non-contact ranging approach is the key component of airborne and terrestrial laser scanner. As summarized by Vosselman and Maas (2010, subsection 1.1), there are in general two methods for optically measuring the distance: light transit time estimation and triangulation. In the former method, time of light traveling in the medium can be estimated either directly via timer or indirectly via phase measurement in continuous wave lasers.

Time-of-fight measurement The assumption behind a time-of-fight (TOF) ranging system is that light waves travel with a known velocity in the specific medium. Thus, the distance ρ between sensor and reflective target surface is estimated as the product of the specific propagation speed of light and the runtime

$$\rho = \frac{c}{n} \frac{\tau}{2} \tag{2.1}$$

where $c = 299792.458$ km/s is the light propagation velocity in a vacuum. It is characterized by the refractive index n which mainly depends on the wave length, air temperature, pressure, and humidity. The time delay is assumed as half of the round trip duration τ from the sensor to reflective target surface and back to the senors. It is obvious that the determination of τ is the essential part of TOF ranging systems. The time detector will generate a time-tagged trigger pulse depending on the implemented criterion, i.e. when the echo reaches a

---

[1]The terms horizontal and vertical angles are strictly only defined for leveled instruments. For the non-leveled ones this is different. In the following, these terms should be continued throughout the thesis for both the leveled and non-leveled instruments

peak, certain threshold or constant fraction with the maximum amplitude (cf. Vosselman and Maas, 2010, pp. 3ff.).

The standard deviation σ_{r-p} of the range measurement for a single pulse buried in additive white noise is approximately given by

$$\sigma_{r-p} \approx \frac{c}{2} \frac{t_r}{\sqrt{SNR}} \tag{2.2}$$

where t_r is the rise time of the laser pulse and the SNR is the power ratio of signal over noise. Generally the pulse-based TOF systems are characterized by a long range (several hundred meters) but, commonly, lower data rates.

Phase measurement techniques As an alternative approach to directly record the light transit duration, the time delay can be estimated by the phase difference $\Delta\varphi$ of the emitted and received signal,

$$\tau = \frac{\Delta\varphi}{2\pi} \frac{\lambda_m}{c/n} \tag{2.3}$$

where λ_m is the wavelength of the amplitude modulation and hence the range is found using Equation (2.1). The standard deviation of the range measurement by this approach σ_{r-AM} is approximately given by

$$\sigma_{r-AM} \approx \frac{1}{4\pi} \frac{\lambda_m}{\sqrt{SNR}} \tag{2.4}$$

It is indicated by Equation (2.4) that a smaller wavelength makes the phase detection more precise and in consequence lead to a more accurate distance measurement. Applying the wave characterized with a small wavelength would in fact result in a smaller ambiguity interval which means the distance always includes N full wavelengths λ_m. In that case, the multiples of wavelength $N\lambda_m$ have to be added to the fractional part recorded by phase difference ($\Delta\rho = \frac{\Delta\varphi \cdot \lambda_m}{2\pi}$), however, it is not possible to determine N by a single phase measurement. In order to solve this problem, various wavelengths are applied: the large-length wave is in charge of a potentially large ambiguity interval while a small wave length ensures a desirable precision. Typical commercial phase-based measurement systems are characterized with high data rates but shorter operating ranges (cf. Vosselman and Maas, 2010, pp. 5ff.), which is much improved by nowadays scanners. For instance, the Zoller+Fröhlich IMAGER 5016 laser scanner has been extended up to 360 m while it has maximum measurement rate of more than 1 million points per second, which guarantees a high resolution of object even for long distances.

Triangulation While the light transit time estimation approaches are usually applied for mid- and long-range TLS, the triangulation principal is popular in close range measurements smaller than 5 m. The triangulation method is based on the cosine law by constructing a triangle and calculating the distance using the baseline length as well as the interior angles of illumination and reflection lines relative to the baseline. Since the triangulation-based systems usually find their application in medical and industrial measurements instead of engineering surveying, it is beyond the scope of this thesis. Interested readers are referred to Blais (2004) and Kanade (2012, pp. 63-97).

2.1.2 Beam deflection system

Scanning the object requires the single laser beam to move over the surface, hence, the laser beam is deflected in horizontal and vertical direction. For TLS, the beam deflection can be done in one of the following ways (cf. Reshetyuk, 2009, pp. 16ff.):

1. Two orthogonally mounted mirrors are included so that both horizontal and vertical deflections are realized by mirror oscillations as shown in Figure 2.1 top left. This is typical for TLS with a camera-like (or window-like) field of view (FOV) which can only capture data within a certain field. This mechanism is common for pulse-based TOF systems, which are characterized by a slower range measurement compared with phase-based techniques.

2. The laser beam is deflected in vertical direction by rotating or oscillating a mirror combined with a horizontal 360° rotation of a scanner head with the help of a servomotor, which is shown in Figure 2.1 top middle. This is typical for hybrid laser scanners which are characterized by the 360° horizontal FOV yet limited vertical FOV.

3. Similar with hybrid scanners, the scanning head rotates horizontally for 360°, however, the laser beam is deflected by the monogon mirror which may efficiently provide max 360° vertical FOV (Figure 2.1 top right). This mechanism is used for the panoramic scanners and is often combined with the phase-based ranging technique due to its rapid measurements.
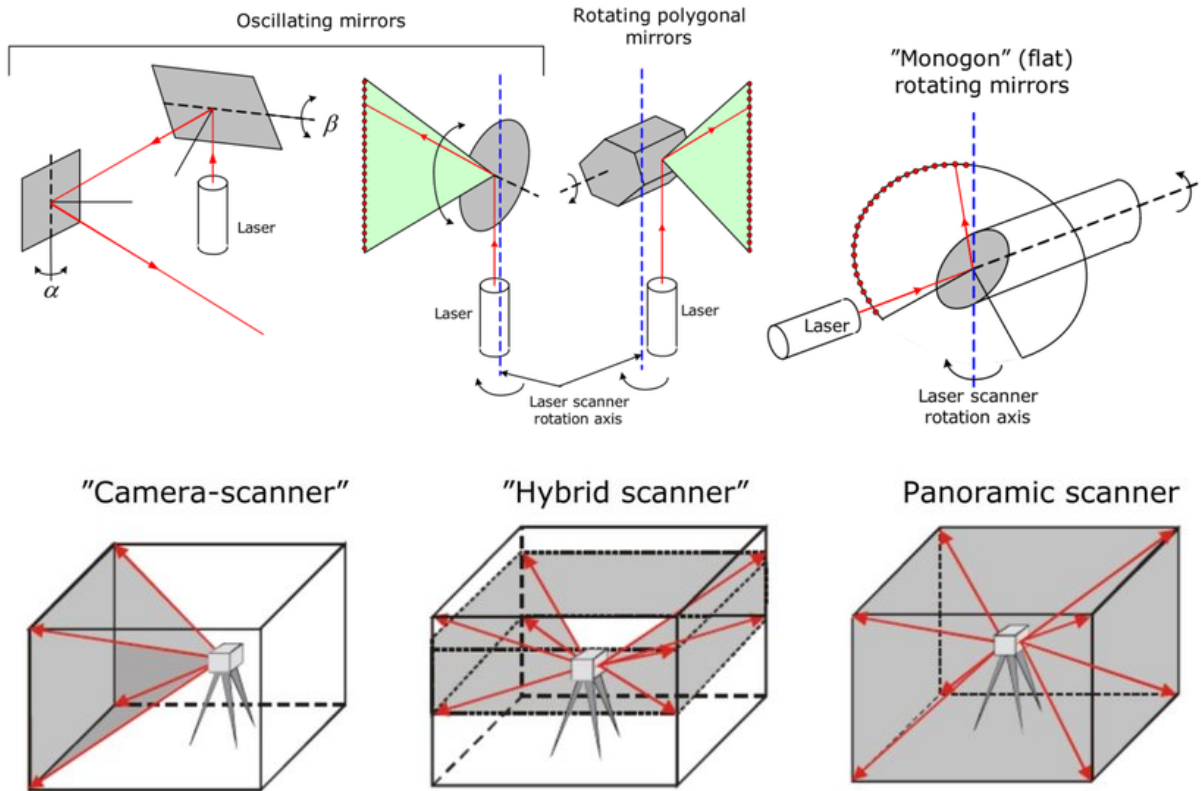
Figure 2.1: *Top: types of laser beam deflection units used in TLS. Bottom: types of TLS according to the field-of-view (FOV) (cf. Reshetyuk (2009)).*

2.2 Error sources for TLS measurements

As other surveying techniques, the TLS measurements have imperfections that give rise to errors in the measurement results. It is necessary to investigate the errors in order to evaluate the performance of the instrument and the data quality which is known as coordinate precision or accuracy of 3D points. It is indicated by many references that the single-point coordinate precision of TLS is in the sub-centimeter range which is commonly not as good as traditional geodetic surveying approach, i.e. total station. However, the high density of the scanning observations

facilitates a higher precision via supplicating of least-squares based curve or surface estimation. Consequently, in most applications of TLS, such as deformation monitoring, the measurements are approximated by certain mathematical model in a linear GMM (refer to subsection 2.3.4). A comprehensive uncertainty budget is the significant basis for the realistic stochastic model in least-squares approximation and the further deformation monitoring process.

2.2.1 Influence factors for the errors

Traditionally, the measurements are imperfect due to the outliers and errors. The outliers in the experiments can lead to serious problems in further data analyses and thus need to be detected and eliminated. In the geodetic field, the outlier detection is firmly based on the fundamentals of statistical hypotheses testing procedures (cf. Lehmann and Lösler, 2016; Teunissen and de Bakker, 2013). In this dissertation, an ideal condition is assumed that there is no outlier in the dataset. Since the robust estimation approaches for free-form curves are investigated by another colleague in our research group (Bureick et al., 2016b), it can be applied in the further research for the dataset containing outliers.

The errors are classified into two groups, namely, random and systematic errors. As defined by the Guide to the Expression of Uncertainty in Measurement (GUM): "Random error presumably arises from unpredictable or stochastic temporal and spatial variations of influence quantities" (JCGM, 2008, subsection 3.2.2). Since the expectation of a random error is assumed as zero, according to the law of large numbers, the influence of random errors can usually be reduced by increasing the number of observations. By contrast, the systematic error is assumed as constant and usually "arises from a recognized effect of an influence quantity on a measurement result" (JCGM, 2008, subsection 3.2.3). The systematic error can be quantified through calibration procedures and a correction is applied to compensate for the effect. Specifically, the errors of TLS measurements can be divided into instrumental, object-related, and atmospheric influence factor (cf. Reshetyuk 2009, Chapter 3; Soudarissanane 2016, subsection 2.3).

Instrumental influence factors The imperfections in instrument manufacturing and assembling give rise to errors in the measurements. For example, the vertical, horizontal and collimation axes of the TLS are assumed to be mutually orthogonal and to intersect at a common point. However, these conditions are in general hardly met in a real system which leads to the axis errors.

In the range measurement system, besides the random error for time-of-flight and phase measurement techniques (refer to equation (2.2) and (2.4)), there are additional systematic errors such as the zero-offset error which is due to the discrepancy between electrical and mechanical zero positions at the scanner, scale error which is a scale factor in the measured distance, and time discriminator errors.

Moreover, the beam deflection system has influences on the accuracy of the angle measurements. Although the scanners with polygonal and oscillating mirrors have separate error sources, the angle measurements of both types are influenced by the quality of the angular position sensors, the imperfections of the rotating mirrors and the misalignment of mirrors, and encoders.

Atmospheric influence factors Between the emitter and reflective target surface, the laser beam travels through the air. Thus, the atmospheric conditions, e.g. ambient temperature, pressure, relative humidity, illumination, vibration etc., will affect the laser beam propagation.

Specifically, on the one hand, laser power can be attenuated, i.e. the signal intensity becomes weaker as it travels through the medium, due to molecular absorption and scattering (Weichel, 1990, Chapter 2 and Chapter 3). On the other hand, the atmospheric turbulences

caused by temperature differences and involved particles give rise to beam wander, i.e. the beam displacement from the initial propagation direction, and beam distortion, i.e. a pulse would be elongated or shortened and thus the wavelength is changed (Blais, 2004; Borah and Voelz, 2007). In normal applications of TLS, the influence of atmospheric turbulence is not significant in the distance range of up to some hundreds of meters if the atmospheric parameters are additionally measured (Hejbudzka et al., 2010).

For the long-range measurements up to a few kilometers, the atmospheric refraction would significantly affect the measurements by leading to artifacts that are not relevant in close-range cases. These artifacts are generally caused by instabilities of instruments, e.g. caused by wind, and atmospheric refraction. It is suggested by Friedli et al. (2019) that the monitoring over long ranges should be carried out in the evening after the sunset.

Object-related influence factors Since the TLS is characterized by reflectorless measurement technologies, the performance is affected and limited by the reflectance which is defined as the ratio between reflected and incident laser power (cf. Ingensand et al. (2003)). The reflectance is highly dependent on the emitted and reflected beam which essentially depends on the wavelength, incidence angle, and object properties (Soudarissanane and Lindenbergh, 2011; Zámečníková et al., 2015), e.g. optical properties of materials, surface color, roughness and temperature (Lichti and Harvey, 2002; Nyland, 1998; Zámečníková et al., 2014; Schäfer, 2017, Chapter 5). Although object-related influences are clearly detected, it is still challenging to model them separately due to the unclear correlation with other influence factors. Furthermore, the objects properties are usually unknown, which increases the difficulty to specify the object-related errors.

Additionally, there are methodological errors, also named as scanning geometry errors. They are related to the methods which are employed to collect and register multiple point clouds into a common coordinate system. Since this type of errors is not generated during scanning procedure where our focus lies on, the interested readers are referred to Lichti and Gordon (2004), Wujanz and Neitzel (2016), Soudarissanane (2016, subsection 2.3), Reshetyuk (2009, subsection 3.5) and Schäfer (2017, Chapter 4).

2.2.2 State of the art in TLS calibration

As mentioned previously, the random errors of TLS are assumed to be reduced by adjusting the highly dense observations, whereas the systematic errors are quantified through calibration procedures. In general, the TLS can be calibrated either in the individual components or as a complete system.

Since a TLS is the combination of ranging and angular measurement systems which are used in existing instruments, i.e. electronic distance meters (EDM), theodolite and total stations, the component calibration can in principal make use of the procedures in calibrating these traditional instruments. However, problems of direct applying the existing calibration procedures for TLS lie in the inability of exactly centering the scanner in a known point as well as repeatedly scanning the same point in a non-target observation procedure (cf. Vosselman and Maas, 2010, pp. 122ff.). These limitations are treated by hardware developments and adjusting geometry parameters, e.g. center points or diameters of spherical targets, as references. These procedures have been used for calibrating various TLS systems. Schulz (2008) designed several experiments to calibrate the distance and angle measurement systems of a Zoller+Fröhlich IMAGER 5003 TLS in both statistic and scanning mode through comparing the scanning measurements with the references, i.e. measurements from interferometer, total station and theodolite. Salo et al. (2008) calibrated the ranging system of a TLS Faro LS880 HE80 by comparing the scanning measurement with results obtained with a robot tacheometer, while Neitzel (2007) calibrated the axis errors for Zoller+Fröhlich IMAGER 5003 laser scanner. The manufactures also undertake the obligations of calibrating TLS

and offering prior to delivery and offering the datasheet to users. Among all the manufactures, the calibration procedures of P- and C-series laser scanners from Leica Geosystems are available for users and are explained in Walsh (2014), where several telescopes are employed to calibrate the angle and ranging systems.

On the contrast, the system calibration procedure usually requires no special equipment or facilities, such as total station and theodolite which are used in the component calibration. The systematic errors, which are treated as additional parameters involved in a observation model, are estimated simultaneously with coordinates of the target points in the adjustment procedure. Summaries on the subject are presented by Lichti (2007), Schneider and Schwalbe (2008) and by Pareja et al. (2013). Furthermore, the problems involved in the self-calibration approaches are investigated in the latter literatures, e.g. Chow et al. (2011), Al-Manasir and Lichti (2015), and Muralikrishnan et al. (2018). Since high correlations are present between the estimated parameters, Lichti (2010) and Reshetyuk (2010) were searching for solutions to decorrelate them. Meanwhile, Li et al. (2018) updated the self-calibration experiment by omitting auxiliary targets and presented a background target-based autonomous method for TLS self-calibration. Apart from the traditional network-based calibration methods, Holst and Kuhlmann (2014) and Medić et al. (2017) proposed a two-face self-calibration method using only one single station. Ge (2016, Chapter 4) studied on the experiment configuration, i.e. reasonable number of targets and scanning strategies, during calibration procedure. Wang (2013b, subsection 5.4) proposed a combined model to solve the point registration and calibration parameters simultaneously.

2.3 Deformation monitoring with TLS measurements

Deformation monitoring of structures is a common application and one of the major tasks of engineering geodesy. A number of artificial and natural objects require monitoring, such as dams, tunnels, high-rise buildings, bridges, industrial complexes, slopes, glaciers, areas of landslides, subsidence, and crustal motion (cf. Ogundare, 2015, p. 1). Traditional geodetic monitoring technologies, i.e. total stations, precise levels and GNSS positioning, are characterized by point-wise deformation analysis in a ground surface network. In contrast, TLS has significant advantage in deformation monitoring due to its high precision and spatial resolution in capturing 3D point clouds. Although the single-point precision of TLS is inferior to traditional geodetic technologies, i.e. in the sub-centimeter range, the high density of the scanning observations facilitates a higher precision via the application of least-squares based curve or surface estimation and, hence, an adequate precision of the estimated deformation parameters can be obtained (Monserrat and Crosetto, 2008; Gordon and Lichti, 2007; Neuner et al., 2016).

There are plenty of references on the topic of TLS-based deformation monitoring, among which only some exemplary very important references are cited in this section. In the tunnel deformation monitoring, Lindenbergh et al. (2009), Nuttens et al. (2010), Jian et al. (2012) and Xie and Lu (2017) offered various strategies which are illustrated on a series of experiments. The bridge deformation monitoring is conducted by Zogg and Ingensand (2008), Neitzel et al. (2012), Neuner et al. (2014), Lõhmus et al. (2018) and Truong-Hong and Lindenbergh (2019), while Bitelli et al. (2004) and Herrero-Huerta et al. (2016) applied the TLS to quantify the geomorphological change caused by landslides. For other large structures, Alba et al. (2006) and Eling (2009) presented the procedures and results of TLS-based deformation monitoring of large concrete dams, while Pesci et al. (2015), Camarda et al. (2010), Dutescu (2006), and Tapete et al. (2013) monitored the changes of historical buildings based on TLS for the purpose of protection.

For the above mentioned TLS-based deformation monitoring projects, the typical workflow and data processing steps involved are introduced in the following subsections.

2.3.1 Design of measurement scheme

In the design stage of deformation monitoring, the setup for scanning, i.e. location and number of view points, should be arranged to balance two aspects. On the one hand, it is necessary to ensure that the scanning object is within the measurement range of the scanner and there are sufficient overlaps between the individual scans for the further georeferencing process. On the other hand, too many scanning stations are computationally intensive to register the point clouds and are inefficient from an economic point of view. A trade-off between the number of acquisitions and the computational efforts and costs needs to be defined (Soudarissanane and Lindenbergh, 2011; Wujanz and Neitzel, 2016).

If the traditional indirect georeferencing approach is used in the pre-processing procedure, the positions of control points should be obtained in this step. Since the changes of control points may cause a biased estimation of the transformation parameters and thus affect the deformation detection, it is necessary to ensure the stability of the control points in all measurement campaigns.

2.3.2 Data collection

After a comprehensive design of the view points, the TLS is set up at the defined locations for data collection. The scan settings, e.g. resolution and scanning mode, are depending on the specific application. Generally speaking, the higher the spatial resolution, the lower the temporal resolution. The traditional mode of TLS is the 3D mode (spatial mode), where the maximum spatial resolution as well as minimum temporal resolution is available (Paffenholz et al., 2008). For smaller scanning windows, the temporal resolution can be increased. When the deformation happens in one major direction, the 2D mode (profiler mode) is applied to improve the efficiency of field work (Hesse et al., 2006). In the profiler mode, the rotation of the scanner about its vertical axis is disabled. The reduced spatial dimension facilitates a higher temporal resolution. Besides, the 1D mode (statistic mode) allows the highest sampling rate so that it finds its application in the monitoring kinematic processes (Neitzel et al., 2012).

As introduced in section 2.1, the raw measurements of TLS are polar coordinates with range and angles, which are automatically converted by the internal software of TLS into Cartesian coordinates. Thus, the typical outcome of laser scanners are 3D coordinates, intensity information and echo waveform. The nowadays generation of TLS has often also a camera included which provides color information for the 3D point cloud.

2.3.3 Data pre-processing

Georeferencing/registrition of point clouds After data collection, the initial operation is to transform several epochs point clouds into a common reference coordinate system, which is the so called georeferencing or registration process. The main difference between them is that the common reference frame in georeferencing process is absolutely established by additional geodetic observations while the registration process only focus on the collected point clouds and is referred to as a relative orientation (cf. Paffenholz 2012, Chapter 2; Vosselman and Maas 2010, subsection 3.3). Both strategies are realized by transformation parameters, i.e. rotation matrix and translation vector. Consequently, the process typically involves two distinct steps: determination of the transformation parameters and transformation of all the point clouds into an identical coordinate system. Figure 2.2 shows the commonly-used georeferencing approaches, which are based on the overview of Neitzel and Neumann (2013).

Generally speaking, there are direct and indirect (object space-based) georeferencing approaches. The former are characterized by using additional sensors, such as inclinometers, compasses, inertial measurement units (IMU), GNSS systems and laser trackers (Zimmermann et al., 2018; Paffenholz, 2012; Ehm, 2012; Kersten et al., 2009; Schuhmacher and Böhm,
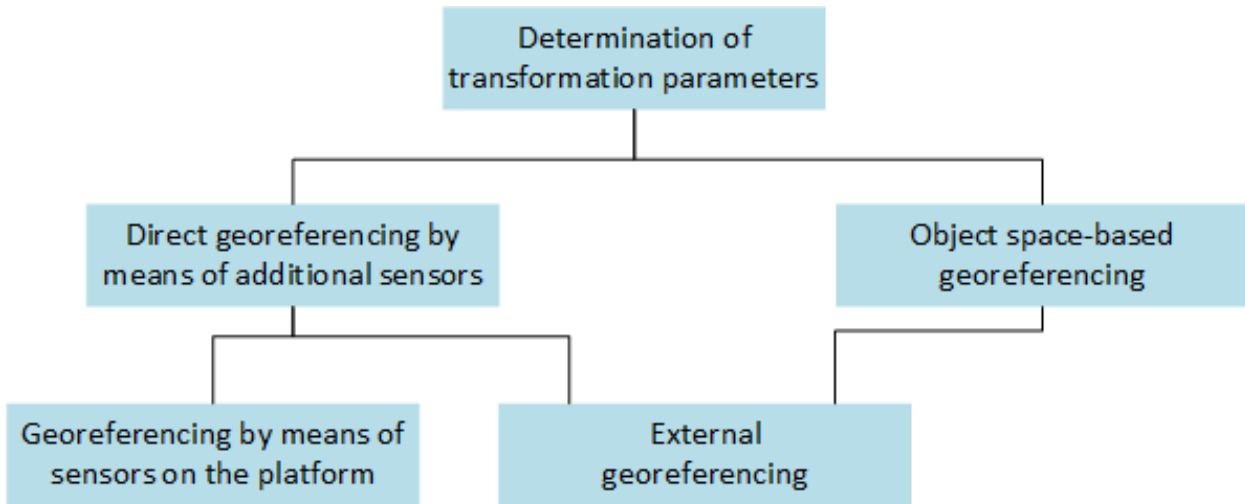
Figure 2.2: *Overview of the georeferencing approaches.*

2005), which are employed to position the laser scanner directly. These sensors can be attached in the same platform with TLS as a multi-sensor system or placed externally to track the movement of a TLS. For instance, Paffenholz (2012) (see Chapter 5) proposed a multi-sensor system consisting of a TLS, a GNSS-antenna as well as two inclinometers. An adaptive extended Kalman filter is introduced, which allows the combination with the inclinometer data and the determination of all desired transformation parameters. The position and orientation information of the TLSs are simultaneously acquired without using extra control points. An alternative approach is indirectly georeferencing, which is also named as object space-based georeferencing. Traditionally, the TLS uses extra artificial targets which coordinated by other geodetic approach, e.g. total station or GNSS systems. Specifically, at least three targets, which serve as control points, are surveyed by TLS located in two view points. Thus, their coordinates are know in both coordination system and the transformation parameters can be estimated.

The registration process works mainly on the point clouds themselves rather than additional measurements. The matching algorithms are always used to obtain the transformation parameters. The iterative closest point (ICP) algorithm is one of the most commonly used method in registering two or more point clouds (Besl and McKay, 1992). It is characterized by searching pairs of nearest points in the two point clouds and estimating the transformation parameters based on the defined corresponding point pairs. Then, the transformation parameters are applied to the points of one set, and the procedure is iterated until convergence. The classical ICP-based registration approach is improved by the later researchers (Wujanz et al., 2014; Wang, 2013a; Gressin et al., 2013; Bae, 2009; Gruen and Akca, 2005; Grant, 2013, Chapter 3 and Chapter 4). Besides, the intensity-based approach (Böhm and Becker, 2007) and geometric feature-based approach, i.e. searching for corresponding edges (Lichtenstein and Benning, 2009) or planes (Rietdorf, 2007, Chapter 4), serve as alternative strategies to solve the registration problems, which are improved by the further investigations (Kang et al., 2009; Weinmann and Jutzi, 2015; Ge and Wunderlich, 2016; Burger et al., 2018) and applied in various projects (Dold and Brenner, 2008; Watanabe et al., 2016; Wujanz et al., 2018).

Point cloud segmentation In this step, the registered point clouds are grouped, commonly by judging if they are on the same plane, sphere or cylinder, for further analysis (Vosselman and Maas, 2010, p. 63). Here, only a very brief introduction is given in this subsection since it is not the main scope of the thesis.

The Hough transform, which is a well-known method in detecting lines in a 2D image, is, e.g.

extended to detect surface geometries in 3D point clouds (Vosselman, 1999). It is used to detect planes (Vosselman et al., 2004), cylinders and spheres (Rabbani et al., 2006). Alternatively, the random sample consensus (RANSAC) algorithm (Fischler and Bolles, 1981) is an easy-operating method in point cloud segmentation. It is initiated by a randomly picked minimal point set to uniquely define a model, e.g. three points for a plane and four for a sphere. Then, the rest points are searched for model compatible points. The RANSAC algorithm is improved and applied in many further literatures (Barnea and Filin, 2013; Chen et al., 2014).

Another alternative method is the surface growing approach. The surface growing approach is similar with the region growing algorithm used in image processing. Specifically, after selecting an ideal seed region which is characterized with smallest standard deviation in surface estimation, the neighbor point of the seed region is one-by-one judged whether it fits to the same surface. Once a set of coplanar points has been found, the seed surface is expanded by adding this set of points.

Besides these geometry feature-based segmentation strategies, additional information, e.g. intensity values, are in some cases used to segment the point clouds (Niemeyer et al., 2012; Burger et al., 2018). Due to the combination of TLS with high-resolution digital cameras, the colorimetric information from cameras can also serve as an additional criterion for segmentation (Douillard et al., 2011).

2.3.4 General methodology in TLS-based deformation monitoring

As summarized by Ohlmann-Lauber and Schäfer (2011), deformation detection from scatter point clouds can be based on different comparison methods: point-, point cloud-, surface-, geometry- and parameter-based strategies.

Point-based strategy is a common approach to describe deformations captured by conventional point-wise surveying techniques, for example, total station and GNSS. However, there are seldom TLS data-based applications, since the finding of a reference point between two epochs is challenging. As a compromise scheme, the local neighborhood points are used to estimate a representative point as reference for comparison (Little, 2006). Another solution is to apply a spherical target in scanning and extract the centers of the sphere as references (Ogundare, 2015).

Point cloud-based strategy is in most applications characterized by using an octree structure which is often used to partition a 3D space by recursively subdividing it into eight octants. Specifically, the registered point clouds of various epochs are subdivided into cubes with equal size. The ICP algorithm is applied to determine the transformation parameters from stable cubes and the deformation is defined by the coordinate difference of points involved in the "homologous" cubes of various epochs (Teza et al., 2007; Wujanz, 2016, Chapter 4; Eling, 2009, pp. 96-98).

Surface-based strategy respectively cloud to mesh/model is to compare the point clouds with the reference surface model consisting of point grids. The gridded point sets are compared to generate a digital elevation model (DEM) for coordinate differences, which reduce the spatial information from 3D to 2.5D (Mukupa et al., 2017). This procedure is commonly used in commercial software for point cloud processing, since it is a efficient approach in producing color coded inspection maps (Tsakiri et al., 2006; Lague et al., 2013).

Geometry-based strategy approximates the point clouds by analytic functions such as planes, spheres, cylinders and the free-form curves or surfaces. The approximated models of different

epochs are compared to detect the geometry changes (Vezočnik et al., 2009; Wang, 2013a; Bureick et al., 2016a,b). Compared with the cloud to mesh/model approach, the geometry-based strategy facilitates a higher precision through parameter estimation with large redundancy without losing any spatial information.

Parameter-based strategy shares the same approximation approach with the geometry-based strategy. However, in the parameter-based strategy, the deformation is characterized by comparing the corresponding estimated parameters from the approximated analytic functions, e.g. radius, focal length of the rotational paraboloids (Holst et al., 2015), normal vector of planes (Lindenbergh and Pfeifer, 2005), center point of circles (Schneider, 2006).

In this thesis, our focus lies on the geometry-based strategy, where the deformation is characterized by comparing the continuous model functions from the scattered point samples so that continuous differences between epochs can be obtained. The key point of the geometry-based strategy is to approximate the scattered points by a mathematical model and, in most cases, the unknown parameters of the approximated model are estimated by a least-squares adjustment. Consequently, we are devoted to increase the reliability of geometry-based deformation monitoring results by improving two main points of the adjustment: on the one hand, trying to specify the stochastic model of TLS measurements and statistically evaluating its performance; on the other hand, selecting a proper parametric function as functional model by means of hypothesis testing.

As a summary, the procedure of TLS-based deformation monitoring introduced in this chapter is depicted by the following flowchart diagram.
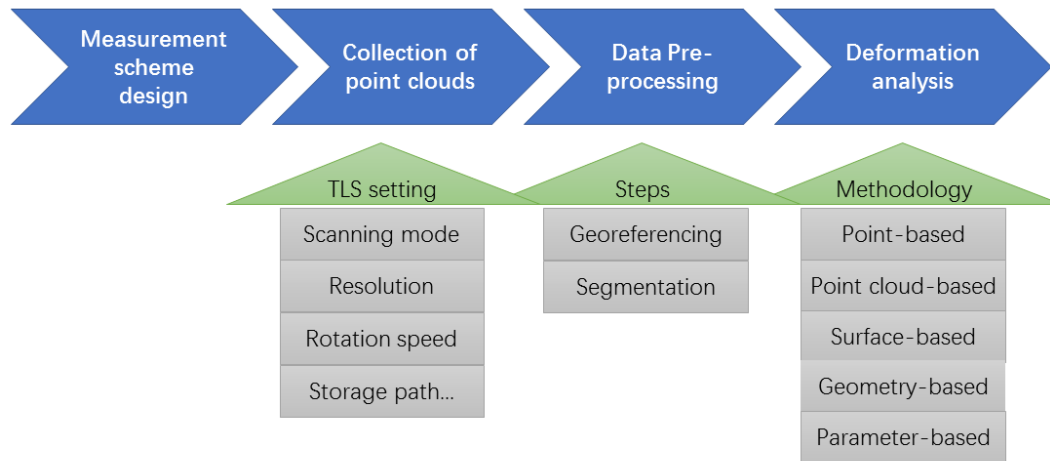

Figure 2.3: *Flowchart of TLS-based deformation analysis.*

3 The influence of a simplified stochastic model on a congruence based deformation analysis

After data acquisition and pre-processing, the subsequent step is to model the deformations. According to Heunecke et al. (2013, p. 78), the deformation can be modeled either descriptively or causally. An extensive introduction of deformation modelling will be given in subsection 3.1. The congruence model, as one of the descriptive models, is the most popular one in the geodetic field since it purely focuses on the geometric state of the object in various epochs and the deformation is described by coordinate changes. For this reason, the congruency model is also in the main focus of this thesis. A vital assumption of the congruency model is that some portion of an observed area remains geometrically stable, which is judged by statistical tests. The implementation of the congruency test is described in subsection 3.2. It is noticeable that the results of the congruency test are highly depending on the stochastic model. The influence of a simplified stochastic model on the test result is analyzed in subsection 3.3.

3.1 Modelling the deformation

3.1.1 Conventional deformation model (Descriptive model)

Conventionally, the continuum object is characterized by discrete points in geodetic modelling, thus, the movement of these points represents the deformation of the object. It is refereed to as "congruency model" where only the geometry changes is modeled without explicitly considering the time intervals between the epochs or the causes for the deformation.

The automatic measurement approaches felicitate the observation of the deformation process in certain time intervals in order to properly model temporal changes of the deformation. It is referred to as "kinematic model" where the geometry changes of characteristic points are described with time variable (Welsch and Heunecke, 2001).

Either the congruency model or kinematic model describe the deformation process as an phenomenon without analyzing the potential causes. Thus, these two models are summarized as "descriptive models" Heunecke et al. (2013, p. 78).

3.1.2 Advanced deformation model (Causal model)

For many interdisciplinary cooperation projects, the deformation need to be modeled regarding to the causes, i.e. internal and external forces, instead of only being described in a phenomenological manner as in the conventional deformation models. This kind of cause-response models are refereed to as "advanced deformation models" or "causal models", which are further classified into static and dynamic models depending on the consideration of the time as variable.

For an object, if the functional relationship between stress, i.e. loads or forces, and geometry changes, needs to be revealed, and meanwhile the object is sufficiently stable during the measurement procedure, the "static model" can be applied. In the static models, the movements and distortions of the object are considered as function of only the load but not the time (Welsch and Heunecke, 2001). Static models are frequently applied, if the load-carrying capacity of structures like bridges, pylons etc. have to be tested (Hesse et al., 2000).

When the time is additionally considered as a variable into the load-deformation relationship, it turns to be a "dynamic model". The time-varying loads lead to the corresponding time-varying geometry changes. The dynamic model is the most general and comprehensive modelling of deformations where the movements and distortions of the object are considered as function of both load and time.

The deformation models are summarized by Heunecke et al. (2013, p. 78) by Table 3.1.

Table 3.1: *The estimation models for deformation measurements (Heunecke et al., 2013, p. 78)*

Deformation models	Congruence model	Kinematic model	Static model	Dynamic model
Time	Not explicitly modelled	Movement as function of time	Not explicitly modelled	Movement as function of time and load
Load	Not modelled	Not modelled	Distortion as function of load	
State of the measured object	Sufficiently stable	Moved	Sufficiently stable under load	Moved under load

3.2 Hypothesis test for congruency

In the traditional geodetic field, the focus of deformation monitoring lies on the detection of geometry changes of an object, i.e. the coordinate variation of the characteristic points between the two epochs. Hence, the congruency model, which is the most popular strategy, is exemplarily applied in this dissertation. The strategy of congruency model is to statistically judge the identity of point coordinates between two or more epochs. More specifically, we have for each epoch an observation vector $\mathbf{l}^{(1)}$ and $\mathbf{l}^{(2)}$ to be approximated by $\mathbf{A}^{(1)}\mathbf{x}^{(1)}$ and $\mathbf{A}^{(2)}\mathbf{x}^{(2)}$ separately. We assume the corresponding random deviations $\mathbf{e}^{(1)}$ and $\mathbf{e}^{(2)}$ to be normally distributed with zero mean and the corresponding VCMs are $\mathbf{\Sigma}_{ll}^{(1)}$ and $\mathbf{\Sigma}_{ll}^{(2)}$. We assume that each random deviation of the first epoch and their second epoch are uncorrelated. Thus, a linear GMM is obtained:

$$\begin{bmatrix} \mathbf{l}^{(1)} \\ \mathbf{l}^{(2)} \end{bmatrix} = \begin{bmatrix} \mathbf{A}^{(1)} & \mathbf{0} \\ \mathbf{0} & \mathbf{A}^{(2)} \end{bmatrix} \begin{bmatrix} \mathbf{x}^{(1)} \\ \mathbf{x}^{(2)} \end{bmatrix} + \begin{bmatrix} \mathbf{e}^{(1)} \\ \mathbf{e}^{(2)} \end{bmatrix} \tag{3.1}$$

and

$$\mathbf{\Sigma}_{\mathbf{l}^{(1)},\mathbf{l}^{(2)}} = \begin{bmatrix} \mathbf{\Sigma}_{ll}^{(1)} & \mathbf{0} \\ \mathbf{0} & \mathbf{\Sigma}_{ll}^{(2)} \end{bmatrix} = \sigma_0^2 \begin{bmatrix} \mathbf{Q}_{ll}^{(1)} & \mathbf{0} \\ \mathbf{0} & \mathbf{Q}_{ll}^{(2)} \end{bmatrix} = \sigma_0^2 \begin{bmatrix} \mathbf{P}^{(1)} & \mathbf{0} \\ \mathbf{0} & \mathbf{P}^{(2)} \end{bmatrix}^{-1} = \sigma_0^2 \mathbf{P}_{\mathbf{l}^{(1)},\mathbf{l}^{(2)}} \tag{3.2}$$

The hypotheses tests are in most cases formulated on the basis of $\mathbf{x}$ ($\mathbf{x} = \begin{bmatrix} \mathbf{x}^{(1)} & \mathbf{x}^{(2)} \end{bmatrix}^\top$) when the deformation is defined as the changes on the parameter level.

Given the matrix $\mathbf{H} = \begin{bmatrix} -\mathbf{I} & \mathbf{I} \end{bmatrix}$, we define the null hypothesis H_0 that no deformation occurred based on the form of a general linear hypothesis:

$$H_0 : \mathbf{H}\mathbf{x} = \begin{bmatrix} -\mathbf{I} & \mathbf{I} \end{bmatrix} \begin{bmatrix} \mathbf{x}^{(1)} \\ \mathbf{x}^{(2)} \end{bmatrix} = \mathbf{0} \tag{3.3}$$

we also formulate an alternative hypothesis by the following equation:

$$H_1 : \mathbf{Hx} = \begin{bmatrix} -\mathbf{I} & \mathbf{I} \end{bmatrix} \begin{bmatrix} \mathbf{x}^{(1)} \\ \mathbf{x}^{(2)} \end{bmatrix} \neq \mathbf{0} \tag{3.4}$$

According to Pelzer (1971), the test statistics T follows a χ_h^2 distribution with h degrees of freedom ($h = rank(\mathbf{H\Sigma_{\hat{x}\hat{x}}H^\top})$):

$$T = \hat{\mathbf{x}}^\top \mathbf{H}^\top \left(\mathbf{H\Sigma_{\hat{x}\hat{x}}H^\top} \right)^{-1} \mathbf{H}\hat{\mathbf{x}} \sim \chi_h^2 \tag{3.5}$$

with

$$\mathbf{\Sigma_{\hat{x}\hat{x}}} = \left(\begin{bmatrix} \mathbf{A}^{(1)} & \mathbf{0} \\ \mathbf{0} & \mathbf{A}^{(2)} \end{bmatrix}^\top \mathbf{\Sigma}^{-1}_{\mathbf{l}^{(1)},\mathbf{l}^{(2)}} \begin{bmatrix} \mathbf{A}^{(1)} & \mathbf{0} \\ \mathbf{0} & \mathbf{A}^{(2)} \end{bmatrix} \right)^{-1} \tag{3.6}$$

We obtain the test decision via the comparison of the numerical value of T with the quantile $k_{1-\alpha}^{\chi_h^2}$ of the χ_h^2 distribution at the specified significance level α.

1. The congruence (or identity) assumption is plausible based on the present data in case of

$$T \leq k_{1-\alpha}^{\chi_h^2}$$

2. The congruence (or identity) assumption is untenable based on the present data in case of

$$T > k_{1-\alpha}^{\chi_h^2}$$

In the aforementioned general form of a linear hypothesis test, the congruence between the estimated unknown parameters $\mathbf{x}^{(1)}$ and $\mathbf{x}^{(2)}$ of two epochs are tested. However, in the geometry-based deformation monitoring strategy which the thesis focus on, the deformation $\mathbf{\Delta}$ is always defined as the difference of adjusted measurements

$$\mathbf{\Delta} = \mathbf{H}_A\mathbf{x} = \begin{bmatrix} -\mathbf{A}^{(1)} & \mathbf{A}^{(2)} \end{bmatrix} \begin{bmatrix} \mathbf{x}^{(1)} \\ \mathbf{x}^{(2)} \end{bmatrix} \tag{3.7}$$

Consequently, the congruency test should be accordingly reformulated. Specifically, we can write (3.3) and (3.4) simpler as $H_0 : \mathbf{\Delta} = \mathbf{0}$ and $H_1 : \mathbf{\Delta} \neq \mathbf{0}$. The matrix $\mathbf{H}$ in the equations (3.3)(3.4)(3.5) is replaced by $\mathbf{H}_A = \begin{bmatrix} -\mathbf{A}^{(1)} & \mathbf{A}^{(2)} \end{bmatrix}$. The replacement lead to a new statistic T_A following a $\chi_{h_A}^2$ distribution with h_A degrees of freedom ($h_A = rank(\mathbf{H}_A\mathbf{\Sigma_{\hat{x}\hat{x}}}\mathbf{H}_A^\top)$)

$$T_A = \hat{\mathbf{x}}^\top \mathbf{H}_A^\top \left(\mathbf{H}_A\mathbf{\Sigma_{\hat{x}\hat{x}}}\mathbf{H}_A^\top \right)^{-1} \mathbf{H}_A\hat{\mathbf{x}} \sim \chi_h^2 \tag{3.8}$$

The test statistic T_A is compared with the quantile $k_{1-\alpha}^{\chi_{h_A}^2}$ to obtain the conclusion that whether there is significant deformation according to the adjusted measurements. For more details of the reformulated congruency test the readers is referred to the attached Paper 1, section 2.2.2.

3.3 Influence of simplified VCMs on the congruency test

In the normal GMM, the test for congruency is proofed as the UMPI test for discriminating between the null hypothesis of zero deformation and its alternative hypothesis on condition of (cf. Kargoll, 2012, Chapter 3)

1. a known design matrix $\mathbf{H}$ (or $\mathbf{H}_A$) of full rank and

2. a known positive definite weight matrix $\mathbf{P}$.

In practice, however, neither the design matrix nor the weight matrix, i.e. the stochastic characteristics, are known exactly, and they need to be determined by experience or other testing approaches. The functional model is in most cases determined through model selection approaches based on information criterion or statistical tests. As another prerequisite of the UMPI property, the stochastic model is even more challenging to be specified due to the limited knowledge on internal and external measurement uncertainties of TLS. The weight matrix is in most cases determined according to experience or simply assumed as identity matrix. The misspecified stochastic model theoretically weakens the power of the congruency test. This view is addressed in this thesis and mainly presented in the attached Paper 1.

As initial investigation, the impact of neglecting the heteroscedasticity and mathematical correlations of a VCM in the B-spline surface approximation (refer to chapter 5 for details) on the congruency test is investigated based on Monte Carlo simulations. The procedures of this study are illustrated by a flowchart diagram in Figure 3.1. Generally, four main steps are involved:

Data simulation Since it is challenging to obtain the exact VCM in practice, especially its covariance information, we created sample points from given mathematical reference surfaces. Within the simulation, a noise vector with known VCM is added to each point cloud of an epoch. The simulated point clouds are from different mathematic surfaces and are assumed as belonging to two epochs, between which the geometry changes happened. In our study, three pairs of point clouds are simulated by $10,000$ repetitions regarding to small (case I), middle (case II) and large (case III) deformation magnitudes. These procedures are blocked by red dot-dash lines in the flowchart diagram and more details are explained in Paper 1, section 3.1.

B-spline surface approximation In order to guarantee the adequacy of functional models in approximating the simulated point clouds, the model selection procedure is employed for each dataset of an epoch. The selected B-spline surfaces are applied to approximate points with the reference VCM or two simplified ones, i.e. neglecting the mathematical correlation or assuming as a homoscedastic VCM (see Paper 1, section 3.2). These procedures are blocked by green dot-dash lines in the flowchart diagram. For more details on B-spline model selection and approximation methodology the reader is referred to Paper 1, section 2.1 and section 2.2.1.

Congruency test The least-squares adjustment results with reference or simplified VCMs are the input parameters for the congruency tests, which are carried out for each stochastic model with $10,000$ repetitions. The rejection rates of the null hypothesis in the congruency test are employed to reflect the impact of unspecified VCMs on the power of the congruency test. These procedures are blocked by yellow dot-dash lines in the flowchart diagram and more details on the congruency test are presented Paper 1, section 2.2.2.

Analysis result According to the results, the rejection rates are not sensitive to the simplification of the stochastic models in the larger deformation area with higher point precision, while they are obviously influenced in the smaller deformation area with unfavorable geometries, i.e. larger uncertainties. In order to offer some hints—whether the results of the congruency

test are reliable when using homoscedastic VCM—for further analysis, we summarize the rejection rates from the studied cases and use the following criterion: the ratio of estimated differences to the relative standard deviations. When this ratio is larger than the threshold, the congruency test results are not impacted by the simplification of VCMs (see Paper 1, section 4.3). It is concluded that the simplification of the stochastic model has a significant impact on the power of the congruency test, especially in the smaller deformation areas with larger uncertainties. These procedures are blocked by gray dot-dash lines in the flowchart diagram and for more details on the result analysis the reader is referred to Paper 1, section 3.4 and section 4.
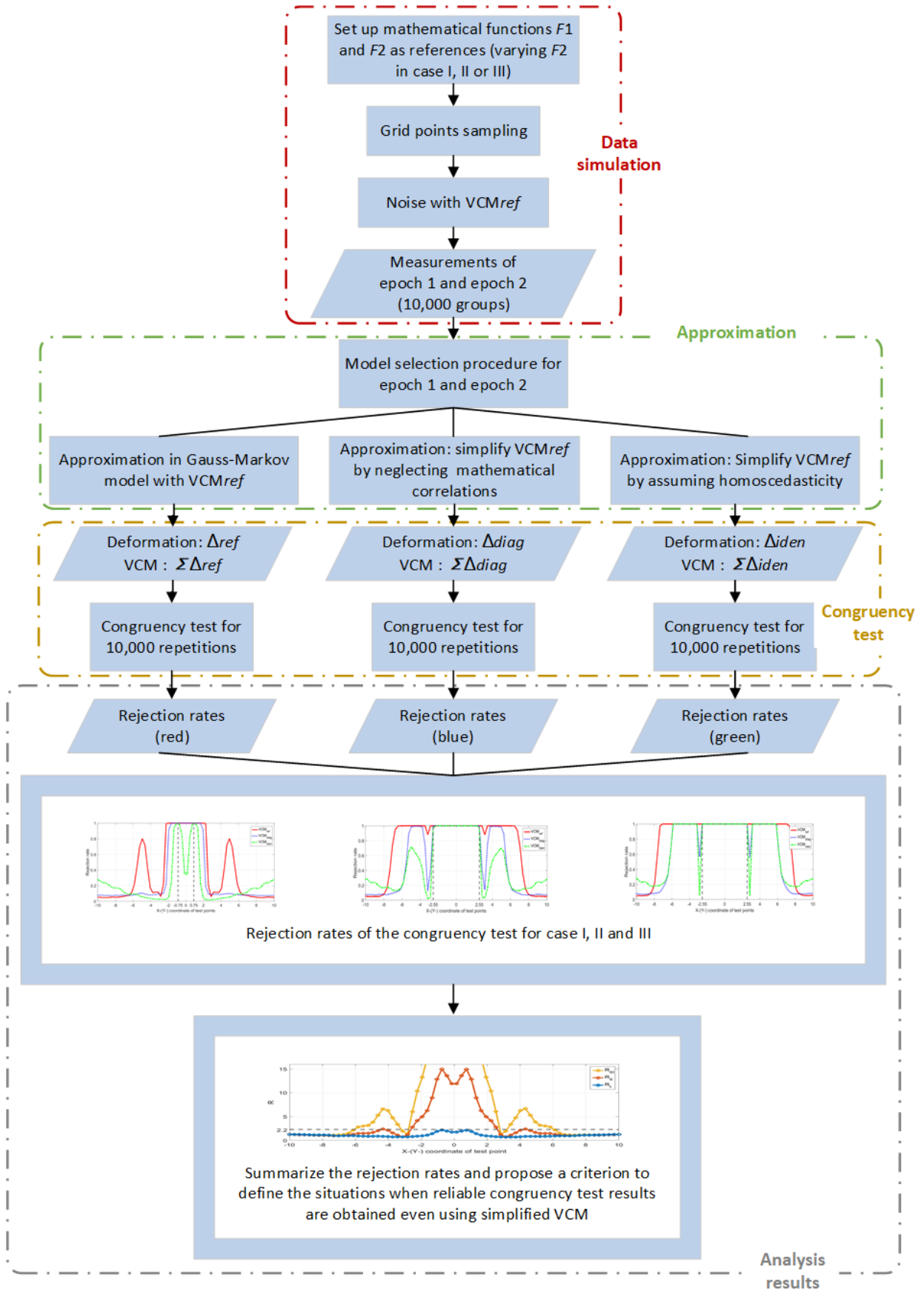
Figure 3.1: *Flowchart of the study on the influence of the simplified stochastic models on the congruency test*

4 On the stochasticity of TLS measurement

The strong significant influence of a misspecified stochastic model on the congruency test motivates the further investigation on the stochasticity of TLS measurements. Many researchers devoted efforts in specifying the stochastic models for TLS, among which the most important references for the thesis are introduced in subsection 4.1. However, it is still challenging in specifying the VCM for TLS measurements due to the limited knowledge on the internal structure of laser scanner as well as the complex influence resources for reflector-less distance measurement systems. These problems are summarized in subsection 4.2. Finally, our efforts are put on the specification of comprehensive VCM and the statistical evaluation of the refined stochastic model in the context of a given dataset (see subsection 4.3).

4.1 State of the art for the stochastic models of TLS measurements

In practice, the true values of observations, i.e. raw measurements and the corrections, are unknown. Thus, the error which is defined as the difference between measurement and the truth is an idealized concept and cannot be known exactly. Consequently, the term "uncertainty" is introduced to reflect the lack of exact knowledge of the value of the measurand. For the evaluation of uncertainties in measurements, GUM has been internationally accepted as the standard. GUM groups the uncertainties according to evaluation method into Type A and Type B. Random and systematic errors are both modeled and treated as random variables in the uncertainty propagation. Type A components are determined by statistical analysis from repeated observations, whereas Type B components are evaluated by other means such as experience, manufacturer's specification and calibration information. Both type A and type B uncertainties can have random and systematic deviations determined by probabilistic approaches.

In most cases, the law of propagation of uncertainty (LOP) is used in linear and linearized models to estimate the output uncertainty. Besides the normal distribution, GUM recommends further types of distributions for the input quantities, e.g. rectangular distribution, triangular distribution and trapezoidal distribution, which make a more exact description of the uncertainties. However, in many cases the models are neither linear nor can be linearized using Taylor series expansions. Thus, for the strongly nonlinear cases, the GUM framework will not be satisfied (Hennes, 2007). To solve this problem, the extension of GUM (JCGM, 2008) recommends the propagation of uncertainties using a probabilistic approach, e.g. Monte Carlo techniques. In this field, Koch (2008b) models the uncertainties of independent measurements by Bayesian confidence intervals using Monte Carlo simulation in the context of the extension of GUM. The approach was extended to correlated measurements in the further literature (Koch, 2008a). Alternatively, fuzzy techniques are used to model the uncertainties which are in many cases too optimistically evaluated by pure probabilistic approaches (cf. Alkhatib et al. (2009)). The investigation on fuzzy techniques in the context of GUM can be found in Mauris et al. (2001). Alkhatib et al. (2009) compared the uncertainty modeling approach based on LOP, Monte Carlo and fuzzy techniques in a numerical example.

A novel approach in establishing stochastic models based on intensity values was proposed by Wujanz et al. (2017). Since the intensity values, which are collected as extra information besides Cartesian coordinates, reflect the effects that are caused by "acquisition configuration as well as interdependencies between emitted signal and object surface". They serve as an index of signal strength which is highly related with the noise of a range-finder. The uncertainty of the range

is empirically modeled as a function of the intensity value, where the object-related influences on the range measurements are involved. Similar work was carried out by Zámečníková et al. (2014), where the distance uncertainty is modeled by a bivariate quadratic polynomial function of measured distance and signal strength.

4.2 Challenge of specifying variance-covariance values

Although a number of references are focusing on the stochasticity of TLS measurements, it is still challenging in specifying a comprehensive and sophisticated VCM. The key problems include:

- An accurate observation model including the raw observations and all the systematic errors, which is necessary to propagate uncertainties, is absent. The uncertainties of output variables, which are obtained either through the LOP or the Monte Carlo propagation approach, rely on the function specified between output, i.e. Cartesian coordinates, and input, i.e. raw observations and systematic errors. However, even if the existence of some influences is validated by experiments, e.g. the object-related influences, the modeling of these effects still needs more investigation. So that they can hardly be specified in the observation model.

- The correlation among TLS measurements is mostly unclear so that the covariance elements in VCMs are always misspecified (Kauker et al., 2016). It is claimed by Lichti (2010) that the estimates of systematic error parameters are hindered by high correlations between model variables. The solution of the author is to de-correlate some variables through a special design of experiments. Alternatively, Kauker and Schwieger (2017) approximated the spatial correlations of Cartesian coordinates by an exponential function related to the distances between points. A similar investigation was shown in Jurek et al. (2017), where the covariances of range measurements are modeled as a function of the color noise ratio. However, the correctness of covariance modeling needs further experimental investigations in the future.

- The statistical approaches in discriminating between candidate stochastic models are missing. Alkhatib and Kutterer (2013) validated the correctness of input stochasticity by simply comparing the statistic parameters of output variables with real dataset, i.e. skewness and kurtosis. The global test (Niemeier, 2008, pp. 167ff.), also known as the overall model test (Teunissen, 2000), is always conducted, e.g. by Wujanz et al. (2017) and Jurek et al. (2017), to judge if the chosen stochastic models in least-squares adjustment are appropriate. However, the global test (overall model test) only offers decision in an absolute way at a certain type I error rate, while during the investigation of specifying VCM, we are always exposed to the question which candidate model is more suitable for the given datasets.

4.3 Statistical evaluation of stochastic model

Although it is challenging to specify the VCM of TLS measurements, the significance of the correct stochastic model in the deformation monitoring, here i.e. for the congruency test, motivates our further investigation on this subject. In the subsequent study (Paper 2), we tried to consider all the influence factors and established a diagonal heteroscedastic VCM for N independent measurements

$$\boldsymbol{\Sigma} = \mathrm{diag}(\sigma_1^2, \ldots, \sigma_N^2) \tag{4.1}$$

It is noticeable that, as an initial attempt in specifying the stochastic model, in this study the correlation of measurements are not considered. Since the applied hypothesis tests are based on the assumption of identical and independent variables, the correlation of measurements will be considered in the further studies with considerable improvement of the testing procedures. In the

comprehensive stochastic model, the intensity-based range uncertainties are involved so that the work on specifying the object-related influences is economized. Other uncertainties related to the instrument and atmosphere are specified according to the manufacturer's data sheet (Zoller+Fröhlich, 2007) as well as the previous investigations on TLS calibration (Gordon, 2008, Chapter 5; Schulz, 2008, Chapter 3; Neitzel, 2007) and Barrel-Sears formula (Barrell and Sears, 1939; Joeckel et al., 2008; Borah and Voelz, 2007; Rüeger, 1990, Chapter 5). The reason for the relatively old references lies on the limited investigations of the Zoller+Fröhlich IMAGER 5006 laser scanner. The general procedures are the same for other instruments. The refined stochastic model is used in approximating bridge measurements in a linear GMM, while the B-spline curve is employed as the functional model. More details on the specification of the VCM and data approximation are given in Paper 2, section 2-4.

Comparisons are made between the estimated B-spline curves using on the one hand a homoscedastic VCM and on the other hand the refined VCM. To assess the statistical significance of the differences displayed by the estimates for the two stochastic models, a nested model misspecification test and a non-nested model selection test are developed, described and applied.

A nested test for heteroscedasticity The first testing approach addresses the question whether a given data set provides sufficient evidence for rejecting the simple, homoscedastic structure $\mathbf{\Sigma}_0$ ($\mathbf{\Sigma}_0 = \sigma^2 \mathbf{I}$) in favor of some heteroscedastic diagonal matrix $\mathbf{\Sigma}$ (4.1), which is reformulated as

$$\mathbf{\Sigma} = \sigma^2 \mathbf{I} + \gamma \mathbf{V}, \tag{4.2}$$

where σ^2 is chosen to be the least variance within $\mathbf{\Sigma}$ and where $\mathbf{V}$ is a non-negative diagonal matrix constituting the difference of corresponding variances $V_i = \sigma_i^2 - \sigma^2$ ($i = 1, 2, ..., N$). The model (4.2) represents a GMM with two overlapping variance components σ^2 and γ (Kargoll, 2012, p. 76). A test about the hypotheses

$$H_0 : \gamma = 0 \qquad versus \qquad H_1 : \gamma > 0 \tag{4.3}$$

is carried out which give rise to two possible test decisions:

i. $\mathbf{\Sigma}_0$ is inadequate for the given dataset when the null hypothesis H_0 is rejected;

ii. $\mathbf{\Sigma}_0$ is adequate for the given dataset when the alternative hypothesis H_1 is rejected.

The test is most conveniently based on Rao's Score statistic, which avoids computation of the additional parameters γ. For more details about the test procedures the reader is referred to Paper 2, section 5.1.

However, the nested test only answers the question whether we could use the homoscedastic structure $\mathbf{\Sigma}_0$ in the given dataset, while the adequacy of the refined heteroscedastic stochastic model is not evaluated. The discrimination between the two stochastic models will be done by a non-nested test.

A non-nested discrimination test of stochastic models Since the heteroscedastic covariance matrix $\mathbf{\Sigma}$ is fully specified, it is actually not necessary to use the overlapping model where the null hypothesis is nested inside the alternative one. It could be processed as a model selection problem where (log-) likelihood ratio tests are commonly employed for comparing the goodness of two models.

The simple model describes the observables by means of the log-likelihood function $L_0(\mathbf{x}, \sigma^2; \mathbf{l})$ with unknown parameters $\boldsymbol{\theta}_0 = [\mathbf{x}; \sigma^2]$ ($\boldsymbol{\Theta}_0 = \mathbb{R}^{n+1} \times \mathbb{R}_+$), and the refined model is based on the log-likelihood function $L_1(\mathbf{x}; \mathbf{l})$ with unknowns $\boldsymbol{\theta}_1 = \mathbf{x}$ ($\boldsymbol{\Theta}_1 = \mathbb{R}^{n+1}$). Under the previous

assumptions, the logarithmized likelihood ratio

$$L_{0,1} = L_0(\hat{\mathbf{x}}, \hat{\sigma}^2; \mathbf{l}) - L_1(\tilde{\mathbf{x}}; \mathbf{l}) \tag{4.4}$$

can be used to test the adequacy of the simple model against the refined model (see the equations (15) and (46) in Cox, 1961). Here, the maximum likelihood estimates $\hat{\mathbf{x}}$, $\hat{\sigma}^2$ and $\tilde{\mathbf{x}}$ may be obtained via least-squares adjustments. According to Cox (1961, sections 8 and 9), the quantity $L_{0,1}$ approximately follows a normal distribution with expectation $\mu_{\hat{\theta}_0}$ and standard deviation $\sigma_{\hat{\theta}_0}$ if the homoscedastic model $\boldsymbol{\Sigma}_0$ is true, or with expectation $\mu_{\tilde{\theta}_1}$ and standard deviation $\sigma_{\tilde{\theta}_1}$ if the heteroscedastic model $\boldsymbol{\Sigma}$ is true.

Since the logarithm of the likelihood function is computed, which leads to a strong non-linearity, unfortunately, the variances $\sigma_{\hat{\theta}_0}$ and $\sigma_{\hat{\theta}_1}$ can not be obtained by normal variance propagation. We carried out Monte Carlo simulation to determine empirical arithmetic means $(\mu_{\hat{\theta}_0},\ \mu_{\tilde{\theta}_1})$ and empirical standard deviations $(\sigma_{\hat{\theta}_0},\ \sigma_{\tilde{\theta}_1})$, similar as the approach used in Williams (1970). More details are given in Paper 2, section 5.2, thus, there is no further detailed description in this chapter. The two assumptions lead to two consecutive tests of the hypotheses

H_0 : the homoscedastic model $\boldsymbol{\Sigma}_0$ is true;

H_1 : the heteroscedastic model $\boldsymbol{\Sigma}$ is true.

which give rise to four possible, mutually exclusive test decisions:

i. $\boldsymbol{\Sigma}_0$ is rejected and the $\boldsymbol{\Sigma}$ is not rejected, i.e. the specific heteroscedastic model is true while homoscedastic model is not. Thus, the heteroscedastic model is sufficient for our dataset;

ii. $\boldsymbol{\Sigma}$ is rejected and $\boldsymbol{\Sigma}_0$ is not rejected, i.e. the homoscedastic model is true while the specific heteroscedastic model is not. Thus, the homoscedastic model is sufficient for our dataset;

iii. Both $\boldsymbol{\Sigma}_0$ and $\boldsymbol{\Sigma}$ are rejected, i.e. neither the homoscedastic nor the specific heteroscedastic model is sufficient. Thus, the stochastic modelling has to be further refined;

iv. Neither $\boldsymbol{\Sigma}_0$ nor $\boldsymbol{\Sigma}$ is rejected, i.e. both homoscedastic and the specific heteroscedastic model are sufficient. Thus, there is no significant difference between the two stochastic models and either of them can be selected for our dataset.

According to the test decisions in our application, the homoscedastic VCM should be replaced by a heteroscedastic VCM in the direction of the suggested VCM. However, the tests also indicated that our specified VCM is still inadequate in light of the given dataset and should therefore be improved. That probably can be due to the misspecification of the variance values and neglecting correlations of the measurements which lead to an unrealistic stochastic model in this regard.

The study presented the statistical approaches in evaluating stochastic models. The nested test for heteroscedasticity is used to judge whether we can use the homoscedastic structure in the given dataset, while the non-nested discrimination test serves as a model selection approach and is able to answer the question that which candidate model is more suitable for the given datasets. It is a systematic and mathematically sophisticated approach to select the stochastic models. The general idea can be transformed to other applications in the future. However, the testing procedures are based on the assumption that the measurements are independent and identically distributed, which should be extended in the further study in accordance with the correlated measurements.

5 Approximating the 3D point clouds with B-spline models for deformation monitoring

As introduced in subsection 2.3.4, the point clouds are restructured in different ways according to various deformation monitoring strategies. Among them, the geometry-based strategy is the most popular one since it facilitates a higher precision through parameter estimation with large redundancies. In this strategy, the point clouds are approximated by mathematical functions for each epoch, whose changes serve as indicator for the object deformation. There are many mathematical functions, e.g. in implicit, explicit, or parametric form. Parametric functions are usually employed to fit point clouds in applications such as deformation monitoring and reverse engineering. Different parametric models find their proper application in various projects which are introduced in subsection 5.1. Among the parametric models, our focus lies in B-splines which offer a great flexibility and can be used to fit nearly every object scanned with TLS. The procedure of approximating point clouds by B-splines is introduced in subsection 5.2. Since the choice of the model would definitely affect the power of congruency test (see subsection 3.3), we made additional research on the parametric model selection approaches based on hypothesis tests which are introduced in subsection 5.3. The performance of B-splines is compared with that of commonly used polynomial models with similar coefficients. The results are explained and discussed in detail in subsection 5.4.

5.1 State of the art on the approximation of 3D point clouds

In the field of engineering geodesy, there are plenty of references on the topic of 3D point cloud approximation, from which some of the most related ones are introduced in this subsection. As summarized by Wunderlich et al. (2016), the object is represented by various functional models according to their geometry characteristics. In general, regular surfaces with defined boundaries are approximated by polynomial functions with various degrees. While the irregular or higher order surfaces which are common in real world applications are more often to be approximated by free-form curves or radial basis functions. The selection of functional models also depends on the further deformation analysis strategy, i.e. based on the segmentations or integral objects. For instance, among the applications of analyzing deformation of tunnels, Walton et al. (2014) and Delaloye (2012) represented the tunnel by a series of cross profiles approximated by ellipses, while Chmelina et al. (2012) and Van Gosliga et al. (2006) approximated the measurements integrally by a cylinder. Both the approximated ellipses and cylinder serve as the idealized models to express the tunnels. Similar application is conducted by Eling (2009), in which the general structure of the dam was parameterized by a quadratic, i.e. ellipsoid function. In the bridge deformation monitoring, Erdélyi et al. (2017) and Kopačik et al. (2013) segmented the superstructure into square-shaped elements, where planes are applied to approximate the points contained in an element. The feature of the individual elements is represented by that of the central points; while Neuner et al. (2014) approximated the point clouds obtained by TLS profile mode globally by free-form curves, i.e. B-spline and Bézier. Similarly, Schill et al. (2019) applied B-spline curves in approximating the measurements of profile scanner in the application of monitoring the noise barriers along railway tracks. The free-form surfaces also find their additional application in modeling the cooling tower (Ioannidis et al., 2006), a leaf surface (Dupuis and Kuhlmann, 2016) and a concrete shell (Schmitt et al., 2019). The benefit of such a space-continuous modeling lies in the continuous representation of deformation at any point of the superstructure (Neuner et al., 2016).

From the above introduced applications, it can be seen that polynomials and free-form curves or surfaces are the most popular parametric models in deformation monitoring. The mathematical basis from polynomial, Bézier, B-Spline functions to Non-uniform rational B-Splines (NURBS) is described by Bureick et al. (2016a). It is pointed out by the authors that in addition to being popular in automobile industry and a standard tool in computer aided geometric design, the free-form curves and surfaces are increasingly used in geodesy fields due to their great flexibility to approximate objects scanned with TLS. A lot of recent research regarding the parametrization of the measurements (Harmening and Neuner, 2015) or determination of the optimal knot vector regarding the scattered point clouds (Bureick et al., 2016b) highlight the high interest of the geodetic community in B-splines approximation.

When selecting the mathematical function for the object, it is, in most cases unclear, whether the surface is smooth enough to be described by a simple model (e.g., as a low-order, global polynomial surface) or not. This is especially in the cases of deformation monitoring where local geometry changes might happen. This motivates the study on the model selection approaches in order to select the most parsimonious, yet sufficiently accurate and statistically reasonable, parametric description of the structure based on TLS measurements. Generally speaking, the model selection methodology can be divided into two main paradigms: information-theoretic approaches and more traditional approaches based upon hypothesis testing (Lewis et al., 2011). Two well-known information-theoretic approaches are the AIC and BIC which are comprehensively explained and compared by Burnham and Anderson (2004). Harmening and Neuner (2016, 2017) investigated statistical methods based on information criteria and statistical learning theory for selecting the optimal number of control points within B-spline surface estimation. Another possibility is to compare the (log-)likelihoods of competing models directly by means of the general testing principle by Cox (1961) and Vuong (1989). Such hypothesis tests offer the advantage that significant probabilistic differences between models can be detected, whose information is not provided by the previously mentioned methods.

5.2 B-spline approximation in a linear Gauss-Markov model

Since the B-splines are increasingly applied in deformation monitoring due to the flexibility in modeling the local geometry changes, the procedures of B-spline surface approximation are introduced in this subsection.

The mathematical description of a B-spline surface point $\begin{bmatrix} X_k & Y_k & Z_k \end{bmatrix}^\top$ ($k = 1, 2, ..., \mathrm{K}$) is as follows

$$\begin{bmatrix} X_k & Y_k & Z_k \end{bmatrix}^\top = \mathbf{S}(\bar{u}_k, \bar{v}_k) = \sum_{i=0}^{n} \sum_{j=0}^{m} \mathbf{N}_{i,p}(\bar{u}_k) \mathbf{N}_{j,q}(\bar{v}_k) \mathbf{C}_{i,j} \tag{5.1}$$

here $\bar{\mathbf{u}} = \{\bar{u}_k\}$ is the location parameter vector in the u-direction and $\bar{\mathbf{v}} = \{\bar{v}_k\}$ is the location parameter vector in the v-direction which is perpendicular to the u-direction. The surface point is obtained by the totalised linear combinations of the basis function $\mathbf{N}_{i,p}(\bar{u}_k)$, $\mathbf{N}_{j,q}(\bar{v}_k)$ and control points $\mathbf{C}_{i,j} = \begin{bmatrix} C_{X_{i,j}} & C_{Y_{i,j}} & C_{Z_{i,j}} \end{bmatrix}^\top$. The control points are located at the mutually perpendicular directions, i.e. u- and v-directions, with the number of $(n+1)$ and $(m+1)$ respectively. The control points, in most cases, serve as unknown parameters $\mathbf{x}$ which are estimated by means of a linear GMM.

The B-spline surface approximation involves three main steps, as summarized by Bureick et al. (2016a):

1. Parametrization of the measurements located in the u- and v directions into location param-

eter vectors $\bar{\mathbf{u}}$ and $\bar{\mathbf{v}}$.

2. Determination of the knot vectors $\mathbf{U}$ and $\mathbf{V}$ in the u- and v-direction.

3. Estimation of the $(n+1) \times (m+1)$ control points by means of a linear GMM: $\mathbf{l} + \mathbf{v} = \mathbf{Ax}$.

The location parameters and knot vectors of step 1 and 2 are used for the derivation of the basis functions $\mathbf{N}_{i,p}$, $\mathbf{N}_{j,q}$. The corresponding information is summarized into a design matrix $\mathbf{A}$ for the final estimation step, i.e. the estimation of the positions of the $(n+1) \times (m+1)$ control points by least-square adjustment, where $\mathbf{v}$ denotes the vector of residuals regarding the observations $\mathbf{l}$. The steps of B-spline surface approximation are summarized by the following flowchart diagram. More details are given in the attached Paper 3, section 2.2.
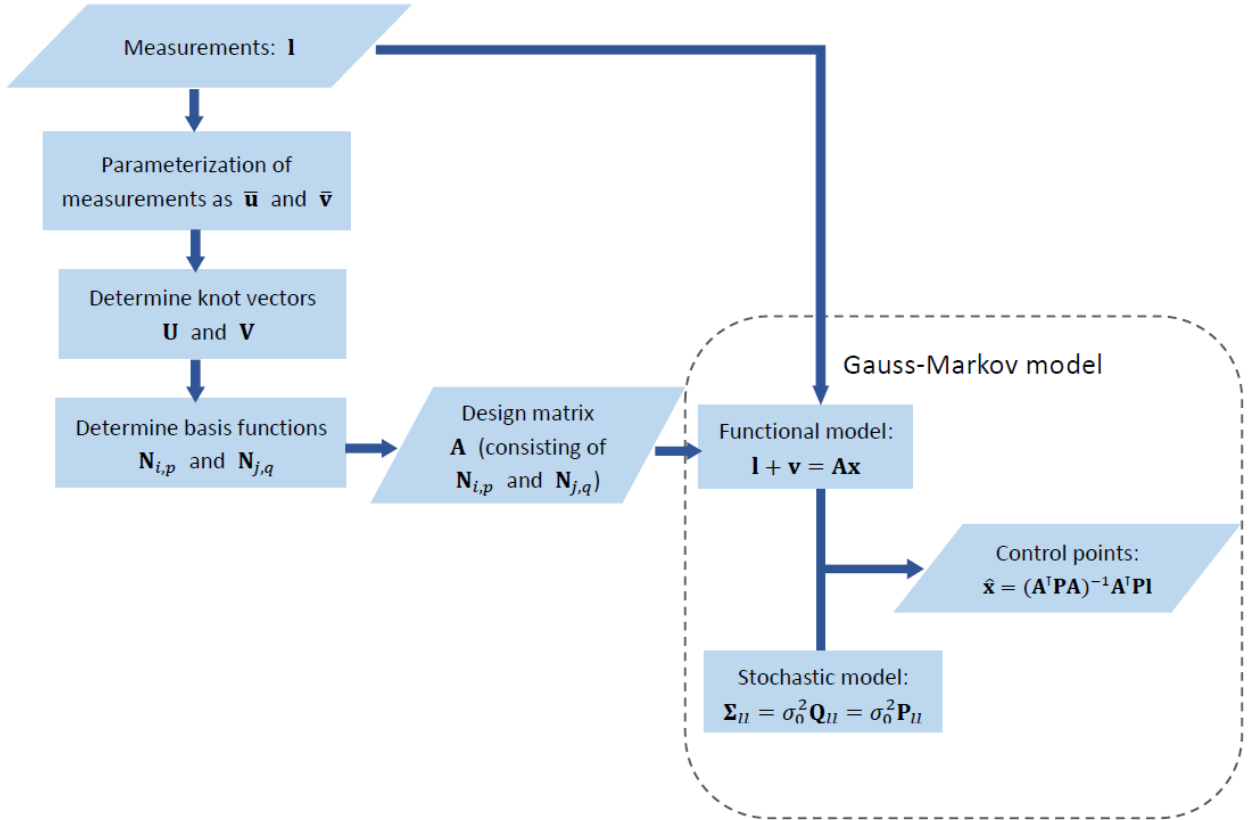
Figure 5.1: *Approximation of a B-spline surface in a linear GMM.*

On the B-spline surface approximation procedure, there are further explanations on the following three points that help to understand the attached 4 papers in more detail:

- The selection of the parameterization method highly depends on the characteristics of the measurements. If the point clouds represented as a grid structure with s rows and t columns, the points on each row can be parameterized with respect to the u-direction while that on each column being parameterized with respect to the v-direction. The parameterization approaches in this case are analogous to that used in B-spline curve parameterization, e.g. equally spaced, chord length and centripetal method (Piegl and Tiller, 2012, p. 365). Compared with the grid data, the parameterization of unorganized point clouds is much more complex. In this case, the Coons patch is a common approach which is characterized by setting up the patch network with boundary points and projecting the measured points on the approximated base surface to find the parameters. Since it is beyond the scope of this thesis, the reader is referred to Ma and Kruth (1995) and Harmening and Neuner (2015).

- In order to simplify the parameterization procedure, we assume that the measurements in our numerical examples have the grid structure. In Paper 1, the measurements are simulated based on the grid points while in Paper 3 the unorganized point clouds are resampled as grid structure for the approximation procedure. The chord length approach is applied in parameterizing the measurements with respect to each row and column, since it is "the most widely used method and generally adequate" (Piegl and Tiller, 2012, p. 365). Alternatively, according to the same reference, the variables can be parametrized by either equal space or centripetal method. The selection of the parameterization method, which may lead to different knot vectors and further influence on the estimation of control points, depends on the homogeneity and the existence of sharp turns in the measurements. Here, taking the datasets of Paper 1 (epoch 1) and Paper 3 (segment I) as two examples, the differences of the control points and B-spline surface points caused by using chord length and equal space parameterization method are shown in the following Figure 5.2.
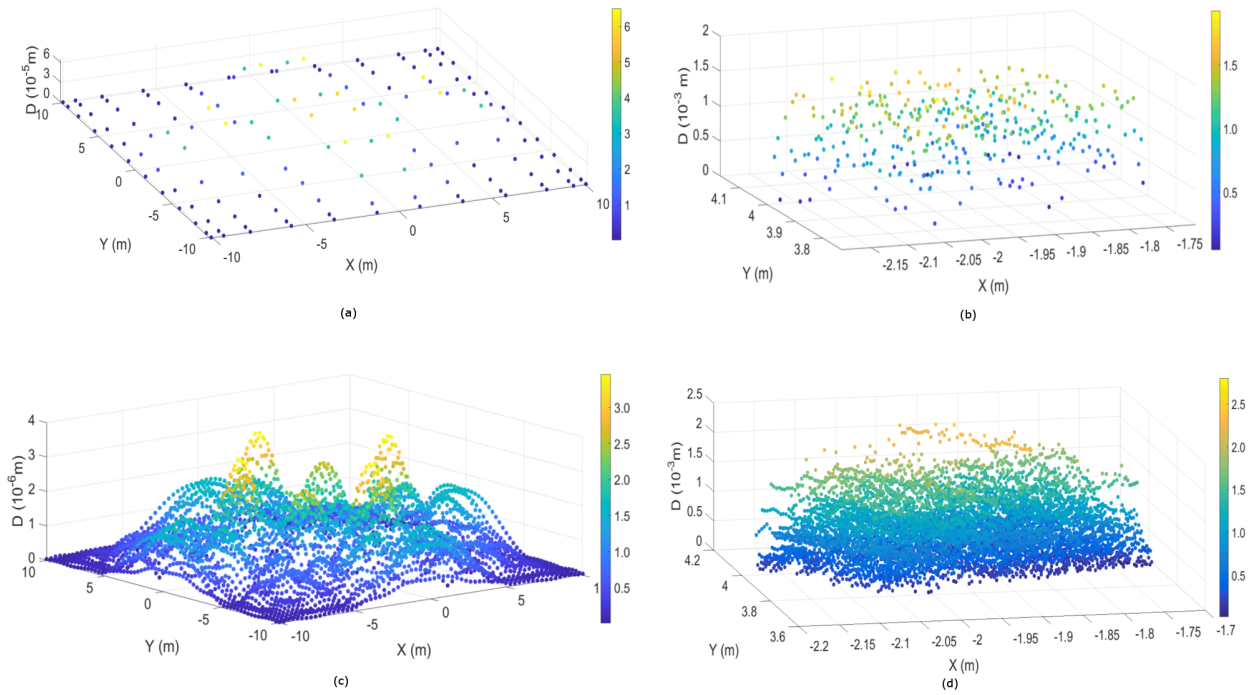
Figure 5.2: *The differences of control points (upper) and surface points (lower) caused by applying the two parameterization methods. (a)(c): dataset of Paper 1 (epoch 1); (b)(d): dataset of Paper 3 (segment I).*

It is indicated by the figure that this kind of control point position differences of dataset 1 are ranging from 10^{-8} m to 10^{-5} m, while that of dataset 2 are ranging from 10^{-4} m to 10^{-3} m. The influences of applying the two parameterization methods on the surface point estimation are at the similar levels as that on the control points. Since the X- and Y-coordinates of the two datasets are evenly distributed as grid structure, the influence of parameterization method are mainly caused by the change of Z-coordinates, i.e. the area of yellow points is corresponding to a larger partial derivative with respective to the Z-coordinates. However, the influences of the different parameterization methods on the *a posteriori* variance factor of approximated B-spline surfaces are not significant (see Table 5.1), so that, in both datasets, the model selection results are identical while applying different parameterization methods. The relatively strong influence on dataset 2, compared with dataset 1, is due to the drastic changes of Z-coordinates within a relatively small area.

Table 5.1: *Comparison of the a posteriori variance factor of approximated B-spline surfaces using different parameterization method*

Parameterization method	*a posteriori* variance factor	
	Dataset of Paper 1 (epoch 1)	Dataset of Paper 3 (segment I)
Chord length	1.04×10^{-6}	8.07×10^{-7}
Equal space	1.05×10^{-6}	5.31×10^{-7}

- The control points are estimated by means of a linear GMM under the assumption that the parameter vectors $\bar{\mathbf{u}}$ and $\bar{\mathbf{v}}$ are error-free. However, in most cases, the determination of the parameters depends on the location of measurements so that the parameter vectors are subject to random errors. Considering the measurement uncertainties, a comprehensive errors-in-variables (EIV) model should be set up and the unknown parameters are estimated through a Gauss-Helmert model (GHM) instead of linear GMM. In the field of approximating the Spline curves with EIV model and a total least squares solution, interested reader is referred to Borges and Pastva (2002) and Neitzel et al. (2019).

5.3 Model selection methodology based on hypothesis testing

As summarized by Lewis et al. (2011), the model selection methodology can be divided into information-theoretic and hypotheses test-based approaches. The main difference between the two is that the former compare sets of models and each model is treated as an equivalent candidate, whereas the later discriminate pairs of models by assuming the null model is valid unless the data shows there is significant evidence to reject it in favor of the alternative model. There are ongoing debates on the merits and drawbacks of the two methodologies (Burnham and Anderson, 2004; Stephens et al., 2005). One of the argued drawback of hypotheses test-based approaches is that they are only suitable for discriminating the nested models, i.e. one model is a special case of another one. On this subject, Cox (1961) modified the likelihood ratio tests, thus, they can be applied to non-nested model comparisons. The Cox's test is improved by Williams (1970) based on the use of Monte Carlo simulation, which is more straightforward to implement. Alternatively to the standard likelihood ratio test, Vuong (1989) provides a non-nested hypothesis test based on the Kullback-Leibler information criterion (KLIC) which measure the closeness of two models.

In the parametric model selection process, the two non-nested hypothesis tests, i.e. simulation-based Cox's test and Vuong's test, are employed to discriminate between the polynomial and B-spline models in paper 3. The most parsimonious, yet sufficiently accurate parametric model is selected through the testing procedure. Since the simulation-based Cox's test is explained in the subsection 4.3 for the application of discriminating between two stochastic models, we will not repeat that but briefly introduce the testing procedure of Vuong's non-nested test in this subsection.

The Vuong's test is based on the KLIC which measure the closeness of two models and uses the likelihood-ratio based statistics to test the null hypothesis that the competing models are equally close to the true data against the alternative hypothesis that one model is closer (Vuong, 1989). Specifically, the two competing models are given as $\mathbf{F}_\theta = \{\mathbf{f}(\mathbf{l}; \boldsymbol{\theta}); \boldsymbol{\theta} \in \boldsymbol{\Theta}\}$ and $\mathbf{G}_\gamma = \{\mathbf{g}(\mathbf{l}; \boldsymbol{\gamma}); \boldsymbol{\gamma} \in \boldsymbol{\Gamma}\}$, where $\mathbf{l}$ denote observations and $\boldsymbol{\theta}, \boldsymbol{\gamma}$ are the relative unknown parameters. Specifically in our case, $\mathbf{l}$ are the acquired 3D points while $\boldsymbol{\theta}$ and $\boldsymbol{\gamma}$ are parameters for the competing models, i.e. control points of the B-spline model, coefficients of the polynomial model and their respective *a posteriori* variance factors. According to Vuong (1989), the two models' Kullback-Leibler distances from the true density $\mathbf{h}_0(\mathbf{l})$ are $E_0[\ln \mathbf{h}_0(\mathbf{l})] - E_0[\ln \mathbf{f}(\mathbf{l}; \boldsymbol{\theta}_*)]$ and $E_0[\ln \mathbf{h}_0(\mathbf{l})] - E_0[\ln \mathbf{g}(\mathbf{l}; \boldsymbol{\gamma}_*)]$ respectively, where E_0 denote the expectation under the true model and $\boldsymbol{\theta}_*, \boldsymbol{\gamma}_*$ are the pseudo-true value

of $\boldsymbol{\theta}$, $\boldsymbol{\gamma}$. It is clear that the model with a minimum KLIC value is closer to the truth, which is however hard to quantify. Thus, an equivalent selection criterion can be based on the quantities $E_0[\ln \mathbf{f}(\mathbf{l}; \boldsymbol{\theta}_*)]$ and $E_0[\ln \mathbf{g}(\mathbf{l}; \boldsymbol{\gamma}_*)]$, the better model being the one with larger quantity.

There are three possible cases when comparing the competing models with each other and we propose the hypothesis as follows:

H_0 : The two models have equal expectation values so that they are equivalent;

H_f : $E_0[\ln \mathbf{f}(\mathbf{l}; \boldsymbol{\theta}_*)] > E_0[\ln \mathbf{g}(\mathbf{l}; \boldsymbol{\gamma}_*)]$ meaning $\mathbf{F}_\theta$ is the better model;

H_g : $E_0[\ln \mathbf{f}(\mathbf{l}; \boldsymbol{\theta}_*)] < E_0[\ln \mathbf{g}(\mathbf{l}; \boldsymbol{\gamma}_*)]$ meaning $\mathbf{G}_\gamma$ is the better model.

Since the quantity $E_0[\ln \mathbf{f}(\mathbf{l}; \boldsymbol{\theta}_*)] - E_0[\ln \mathbf{g}(\mathbf{l}; \boldsymbol{\gamma}_*)]$ is still hard to quantify, Vuong consistently estimates it by $(1/n)$ times the log-likelihood ratio. Thus, similar to Cox's test, the statistic of Vuong's test is also based on the log-likelihood ratio (4.4). Vuong's test is potentially sensitive to the number of estimated parameters on condition that the log-likelihood ratio $L_{0,1}$ is adjusted by a correction factor K.

$$\tilde{L}_{0,1} \equiv L_{0,1} - K \tag{5.2}$$

Vuong (1989) suggests that K corresponds to the penalty term of AIC or BIC. According to the former $K = p_0 - p_1$ and according to latter $K = (p_0/2) \ln N - (p_1/2) \ln N$, where p_0 and p_1 are the numbers of parameters in the competing models. The BIC generally penalizes free parameters more strongly than AIC. Here, we prefer the BIC correction factor in order to avoid an overfitting problem. The adjusted likelihood ratio is further normalized and assumed to converge, asymptotically to a standard normal distribution. More details on Vuong's non-nested hypothesis test are given in Paper 3, section 2.3 so that there is no further detailed description in this chapter.

5.4 Comparison between B-splines and polynomial approximation

As already introduced in subsection 5.1, the parametric models are usually employed in approximating point clouds. Among the parametric models, polynomials and B-splines are widely applied in various projects. In the Paper 3 and Paper 4, we focus on discriminating between polynomial and B-spline models in two case studies. It is notable that the general strategy is also possible for the comparison of other surfaces. In general, polynomials are used to model the regular geometries or segmentations, since the complex geometry which need higher degree polynomial functions may lead to large computation burden as well as numerical instability of polynomials. On contrast, the B-splines are characterized as piecewise polynomial which can approximate complex geometry section by section with a lower degree. In order to give a clear explanation, the creation of a B-spline curve is illustrated by the following figures. The measurements is shown in Figure 5.3 as gray points which are approximated by a cubic B-spline curve (red solid and dashed line) with 11 control points (yellow). Figure 5.4 shows the piecewise basis functions by alternating the solid and dashed line corresponding to the knot spans generated by the internal knot points U_i (in our example $i = 5, 6, ..., 11$). The piecewise basis functions are linearly combined with the control points and the sum of the results lead to a piecewise polynomial, which is a B-spline curve.

In order to compare the performance of B-splines and polynomials in approximating point clouds, we carried out two case studies. The data used in the two numerical examples are the measurements of a Zoller+Fröhlich IMAGER 5006 laser scanner for a concrete arch structure with a length of about 2 m and a thickness of 0.1 m (Figure 5.5). In the experiment, loads were periodically placed on top of the arch's surface to probe the load-caused deformation of the arch structure. After pre-processing of the measurements, two top surface segments and boundary edge of the arch are extracted from the point cloud, which are used in the numerical examples (Figure 5.6).
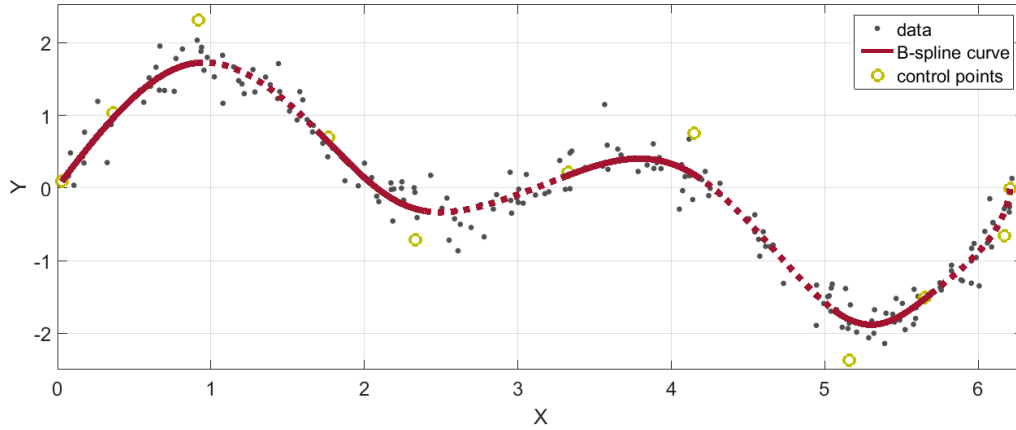
Figure 5.3: *Cubic B-spline curve using the basis function depicted in Figure 5.4.*
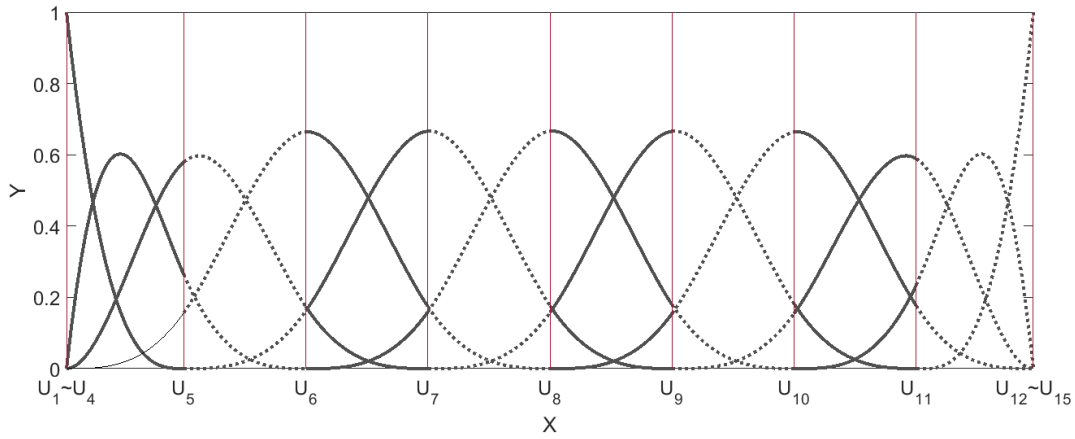

Figure 5.4: *Cubic basis functions corresponding to the knot spans.*

Case study I: comparison of approximated B-spline and polynomial curves In the first step, the extracted boundary edge points are approximated globally by polynomial and B-spline curves with similar model complexity, i.e. number of parameters. The *a posteriori* variance factor serves as an index of fitting precision. The results indicate that the B-spline curve has a more satisfying fitting precision due to the reason that the *a posteriori* variance is 90% smaller than that of the polynomial curve. As a second step, the boundary points were segmented and approximated locally. The fitting precision improved by B-spline is not as much as that of polynomial curves.

Since the B-spline curve is a piecewise polynomial, it has a great flexibility in reflecting detailed geometries even in global fitting. A smaller *a posteriori* variance is within the expectation in this numerical example. Although several polynomial curves can also be used in piecewise-approximation of the boundary edge, it is no longer a continuous curve as B-spline curves. Only the combination of individual polynomials by restrictions in the transition region (e.g. some functional vaules or inclinations) can form a continuous curve which is then a B-spline curve. More details related to the case study I are given in Paper 4.

Case study II: Model selection between B-spline and polynomial surfaces In this case, two segments of the top surface measurements (Figure 5.6) are extracted and each segment is approximated by both polynomial and B-spline surfaces for comparison. The simulation-based Cox's test and Vuong's non-nested test are employed to select the better model. It is no-
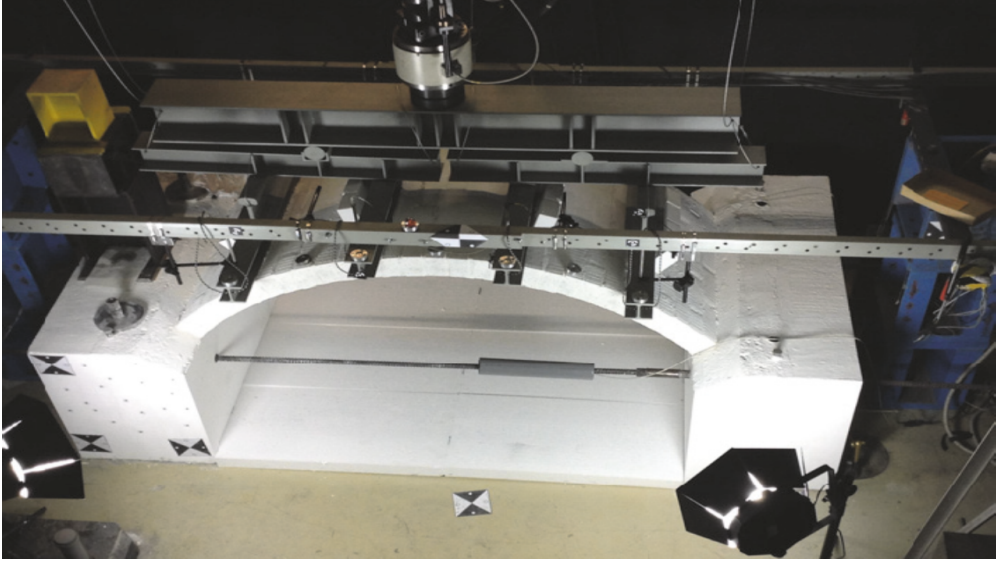
Figure 5.5: *The measured concrete arch structure under load.*
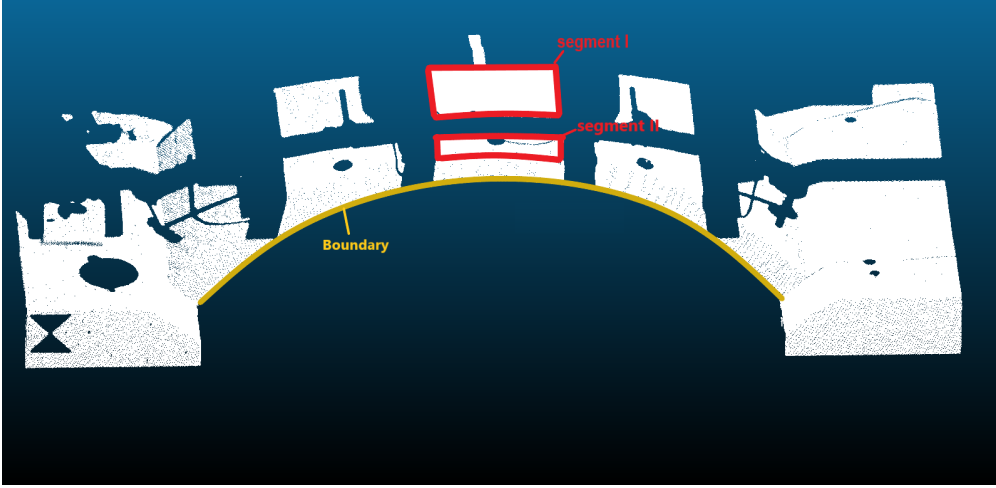
Figure 5.6: *The boundary edge for case I (yellow) and two top surface segments for case II (within the red boundary) shown by the software CloudCompare.*

ticeable that in this numerical example the load is placed on top of the arch's surface and the geometry changes happens mainly on the vertical direction, hence, our focus lies on the changes of Z-coordinates. In order to define the reference points of different epochs, also to regularize the point clouds for further B-spline surface approximation, we resampled the high-density point clouds based on a grid structure of XOY plane, i.e. calculating the plane distance d_{p-g} $(d_{p-g} = \sqrt{\triangle x_{p-g}^2 + \triangle y_{p-g}^2})$ from each measured points to the grid points and the closest ones are selected. Due to the resampling procedure, we assume the X- and Y-coordinates of selected points as error-free. Then, the resampled points are approximated by either polynomial or B-spline surfaces in a linear GMM.

According to the testing results, for segment I, the B-spline surface has better performance than polynomials with same number of parameters. The higher degree polynomials lead to a unstable normal equations which prohibit the approximated polynomials surface to reflect detailed geometrical changes of the target segment. Consequently, B-splines are recommended. However, the model selection results of segment II are quite different from the previous one. The data gap leads to numerical instabilities in determining the knot vector and therefore

resulting the oscillation effects of B-splines. It is noticeable that the conclusions are draw from this case study. That can be various when using other datasets. However, the general model selection strategy is still applicable for other cases. More details related to the case study II are given in Paper 3.

It can be concluded from the two case studies I and II, that the B-splines, as piecewise polynomials, are powerful in approximating geometry details and offers a continuous information for the objects. However, the traditional knot vector determination procedure is sensitive to data gaps which also needs more study on the robust and reliable parameter estimation approaches.

Our focus lies not only on the discrimination of B-spline and polynomial models in the given numerical example, but also presenting two of the hypotheses-based approaches for model selection problem, which can be used in further studies. The simulation-based Cox's test and Vuong's non-nested test are developed and applied in the case study II to solve the model selection problems. The results of the hypothesis tests are compared with that of information-theoretic approaches, i.e. AIC and BIC (see Paper 3, section 4). According to the comparison, we found that the decision of Vuong's non-nested testis is consistent with that of BIC. Actually, there are close connections between AIC, BIC, the simulation-based Cox's likelihood ratio test and Vuong's test, since the maximum value of likelihood function for candidate model are involved in all of the four strategies. However, due to no penalized terms, the parsimony of models is neglected in simulation-based Cox's testing procedure, i.e. the more complex and accurate models are always selected. Thus, this approach is suitable to discriminate models with similar parameters. It can be concluded from the comparison of the model selection approaches that the results obtained via hypotheses tests can, in certain circumstances and when interpreted carefully, assist in the interpretation of the results obtained using information criterion.

6 Conclusion and Outlook

In this thesis, the key problems of data analysis in TLS-based deformation monitoring are investigated. The characteristics of high precision and spatial resolution in capturing 3D point clouds make the TLS become powerful instruments for data collection. However, due to the non-reproducible scanning measurements, it is challenging to find the reference points between two epochs. That facilitates many strategies for TLS-based deformation monitoring, among which the geometry-based method is the most popular one. The key procedure in this strategy is to approximate the point clouds by analytic functions. The geometry changes of objects are detected by comparing the approximated models of various epochs. If the deformation is purely described by geometry changes of the object, regardless of the causes and time, the congruence model, as one of the the most popular descriptive models in geodetic field, are usually employed in this case. The key point in this model is to decide whether geometry changes occur between two or more measuring epochs, where the congruency tests proposed by Pelzer (1971) are usually employed to judge this kind of congruency problem.

The thesis carries out the investigation in the above background. Specifically, the contributions can be summarized as the following four points.

1. Studying the influence of a simplified stochastic model, i.e. neglecting the mathematical correlations and assuming homoscedasticity, on the results of a congruency test. The research, on the one hand, generate an indication which can be used to judge whether the result of a congruency test is free of influence by the simplified VCMs and is able to offer the reliable testing results in deformation analysis. On the other hand, the risk of the simplification of the stochastic models on congruency tests is highlighted, especially in the smaller deformation area with larger uncertainties.

2. Developing and applying two innovative statistical approaches in discriminating between homoscedastic and heteroscedastic stochastic models. The first procedure is based on Rao's score statistic and nests the homoscedastic model as a special case of the fully specified heteroscedastic model. It addresses the question whether the homoscedastic structure should be rejected in the context of the given dataset. The second procedure is based on the Cox's non-nested likelihood ratio test, in which the homoscedastic and the fully specified heteroscedastic model are tested independently against each other. The two statistical approaches can be used to validate further attempts at improving the stochastic model for TLS measurements.

3. Applying two hypotheses-based approaches, i.e. simulation-based Cox's test and Vuong's non-nested test, for functional model selection and comparison of the results with that of information-theoretic approaches, i.e. AIC and BIC. Among the four procedures, the simulation-based Cox's test is more suitable to discriminate the candidate models with similar parameters due to the absence of a penalty term related to model parsimony. The Vuong's non-nested test can serve as an alternative approach to assist in the interpretation of the results obtained using information criterion in the further studies.

4. The superiority and limitation of B-spline models are revealed in the numerical examples. The B-splines, as piecewise polynomials, offer a great flexibility in approximating geometry details with continuous information for the objects. However, the traditional knot vector determination procedure is sensitive to data gaps which would lead to a numerical instability problem.

The research mainly highlighted the importance of specified stochastic models and adequate functional models in geometry-based deformation monitoring and proposed some alternative solutions based on hypothesis testing procedure for model selection problem. However, there are still open questions and recommendations arising from this work which should be pursued in the further research.

1. The extended uncertainty budget in specifying the heteroscedastic VCM (see Paper 2) is based on the previous literatures, which may be not consistent with the properties of our specific TLS. That leads to the misspecification of variance factors. In addition, the correlations of the influences and the measurements is not considered. Therefore, the specification of VCM also needs more further experimental investigations in the future.

2. The hypothesis testing procedures are mostly based on the assumption that the measurements are independent and identically distributed, which should be extended in the further study in accordance with the correlated measurements.

3. The B-splines approximated by means of traditional procedures (Piegl and Tiller, 2012) might be sensitive to data gaps, which can be found in our numerical example (subsection 5.4, case II). Therefore, the optimization of B-splines by robust and reliable parameter estimation approaches needs more investigations.

4. The linear GMM is applied in the surface and curve approximation under the assumption that the parameter vectors are error-free, which is actually not the truth. A comprehensive model, e.g. EIV model, should be set up to solve this problem in the further studies.

5. The congruency deformation model is only exemplarily used in our research. The general idea and conclusion of the thesis can be also transferred to other deformation models in the future work.

Contributions of authors

Paper 1

The first paper aims at analyzing the impact of simplified VCMs, i.e. neglecting the mathematical correlations and heteroscedasticity, on the congruency test based on Monte Carlo simulation. More specifically, we generate grids points from two given mathematical reference surfaces. Within the simulation, a noise vector with known VCM is added to each point cloud of an epoch. The procedure repeats for $10,000$ times and offer us the simulation dataset for the next step. A B-spline surface model, which is proofed by AIC and BIC approaches as the adequate expression of the dataset, is applied to approximate the simulated points in a GMM with reference VCM and its simplified ones. Then, the congruence testing procedure is repeated for $10,000$ times based on adjusted points of two epochs and the difference of the rejection ratios serves as an indication to reflect the influence of the simplified VCMs on the congruency test.

In this paper, Xin Zhao proposed the initial research idea on investigating the risk of misspecified stochastic model on the congruency test. Dr. Gaël Kermarrec, Dr. Boris Kargoll, Dr. Hamza Alkhatib and Prof. Ingo Neumann improved the conception and give suggestions on the implementation. Xin Zhao designed the computation, performed the analysis, drafted the manuscript and designed the figure. The computations and the manuscript were improved under suggestions of Dr. Gaël Kermarrec; Dr. Boris Kargoll improved the theory of the congruency test for our application and contributed the section 2.2 of the manuscript; Dr. Hamza Alkhatib contributed the selection of functional model; Prof. Ingo Neumann offered suggestions step by step and controlled the overall direction and plan.

Paper 2

According to the conclusions of Paper 1, the strong significant impact of misspecified stochastic models should not be underestimated in deformation analysis. Thus, the further investigation on specifying the VCM for geometry-based deformation analysis is motivated. In Paper 2, a more detailed uncertainty budget, which is summarized from the previous literature, is considered in the context of GUM and thus, a refined heteroscedastic VCM of TLS measurements is generated. Furthermore, a bridge measured in 2D profile mode is approximated by B-spline curves. Comparisons are made between the estimated B-spline curves using on the one hand a homoscedastic VCM and on the other hand the refined VCM. To assess the statistical significance of the differences displayed by the estimates for the two stochastic models, a nested model misspecification test and a non-nested model selection test are described and applied. In our study, the test decisions indicate that the homoscedastic VCM should be replaced by a heteroscedastic VCM in the direction of the suggested VCM. However, the tests also indicate that the considered VCM is still inadequate in light of the given data set and should therefore be improved in the future.

In this paper, Xin Zhao established the uncertainty budget of TLS measurements based on the comprehensive literature review and modeled the object through B-spline curve approximation with the refined stochastic model; Dr. Hamza Alkhatib offered MATLAB files from his previous research on constructing VCM through LOP approach and gave suggestions in the whole procedure; Dr. Boris Kargoll proposed and implemented the statistical tests to evaluate the specified stochastic model; After obtaining the computation results, Xin Zhao drafted the manuscript and designed the figures, while Dr. Hamza Alkhatib and Dr. Boris Kargoll revised and improved the manuscript;

Prof. Ingo Neumann motivated the study and supervised the procedure.

Paper 3

The motivation of paper 3 lies in the selection of the most parsimonious, yet sufficiently accurate, parametric description of an object based on TLS measurements, whose model is applied to geometry-based deformation analysis. Beyond standard model selection procedures based on information criteria, i.e. AIC and BIC, we applied two hypotheses-based approaches, i.e. simulation-based Cox's test and Vuong's non-nested test, which are instantiated in numerical examples to discriminate statistically between the widely used polynomial and B-spline surfaces as models for TLS point clouds. Finally, the results of hypotheses-based approaches are compared with that of AIC and BIC. It is indicated by the results that the hypotheses test-based approaches can serve as an alternative approach to assist the interpretation of the decisions from information-theoretic approaches. In addition, the superiority and limitation of B-spline and polynomial models are revealed in the case studies.

In this paper, Xin Zhao designed the research, conducted the approximation, analyzed the test results, and drafted the manuscript. Dr. Boris Kargoll suggested the statistical test approaches, contributed to the theoretical parts and revised the manuscript; Mohammad Omidalizarandi contributed to the data pre-processing; Dr. Xiangyang Xu helped to conceive the numerical example; Dr. Hamza Alkhatib organized the discussion and revised the manuscript.

Paper 4

This paper aims at comparing the performance of B-spline and polynomial curves in approximating the arch boundary edge. The edge points are extracted through the window-neighborhood method and are approximated by B-spline and polynomial curves with similar parameters. The *a posteriori* standard deviation is selected as an indicator to reflect the performance of the approximations. According to the result, the B-spline curve has a more satisfying fitting precision due to the reason that the *a posteriori* variance is 90% smaller than that of the polynomial curve. However, in the local approximation, the polynomial fitting precision is much improved. The fitting precision improved by B-spline is not as much as that of polynomial curves. This paper serves as an additional numerical example for this thesis on the topic of comparing the performance of two widely-used parametric curves.

Dr. Xiangyang Xu conceived the study, performed the analysis, drafted the manuscript and designed the figures; Xin Zhao implemented the B-spline approximation and contributed the relative paragraph on B-splines; Dr. Hao Yang did the proofreading and offered suggestion on the data processing; Prof. Ingo Neumann reviewed the manuscript and supervised the project.

Paper 1

Xin Zhao*, Gaël Kermarrec, Boris Kargoll, Hamza Alkhatib, and Ingo Neumann

Influence of the simplified stochastic model of TLS measurements on geometry-based deformation analysis

Abstract: Terrestrial laser scanners (TLS) are powerful instruments that can be employed for deformation monitoring due to their high precision and spatial resolution in capturing 3D point clouds. Deformation detections from scatter point clouds can be based on different comparison methods, among which the geometry-based method is one of the most popular. Compared with approximating surfaces with predetermined geometric primitives, such as plane or sphere, the B-splines surface approximation offers a great flexibility and can be used to fit nearly every object scanned with TLS. However, a variance-covariance matrix (VCM) of the observations involved in approximating the scattered points to B-spline surfaces impact the results of a congruency test, which is the uniformly most powerful invariant (UMPI) test for discriminating between the null hypothesis of zero deformation and its alternative hypotheses. Consequently, simplified stochastic models may weaken the UMPI property. Based on Monte Carlo simulations, the impact of the heteroscedasticity and mathematical correlations often neglected in B-splines approximation are investigated. These correlations are specific in approximating TLS measurements when the raw measurements are transformed into Cartesian coordinates. The rates of rejecting the null hypothesis in a congruency test is employed to reflect the impact of unspecified VCMs on the power of the congruency test. The rejection rates are not sensitive to the simplification of the stochastic models, in the larger deformation area with higher point accuracy, while they are obviously influenced in the smaller deformation area with unfavourable geometries, i. e. larger uncertainties. A threshold ratio of estimated differences to the relative standard deviation highlights whereas the

results of congruency test are reliable when using simplified VCMs. It is concluded that the simplification of the stochastic model has a significant impact on the power of the congruency test, especially in the smaller deformation area with larger uncertainties.

1 Introduction

Deformation monitoring of structures is a common application and one of the major tasks of engineering surveying. Terrestrial laser scanning (TLS) has become a powerful method among all the data acquisition approaches for deformation detection due to its high precision and spatial resolution in capturing 3D point clouds. As summarized by Ohlmann-Lauber and Schäfer [35], deformation detection from scatter point clouds can be based on different comparison methods: point-, point cloud-, surface-, geometry- and parameter-based strategies. The point-based strategy is a common approach to describe deformations captured by conventional point-wise surveying techniques, for example, total station and the Global Navigation Satellite System. However, there are seldom TLS data-based applications, since the finding of a reference point between two epochs may be challenging. As an alternative, the point cloud-based strategies are characterized by using octree structure which is often used to partition a 3D space by recursively subdividing it into eight octants. Specifically, the registered point clouds of various epochs are subdivided into cubes with equal size and the deformation is defined by coordinates transformation of points involved in the "homologous" cubes of various epochs [8, 29, 41]. The surface-based strategies allow the modelling of one epoch of the point clouds by a surface consisting of meshes. Consequently, the deformation is defined as the distance between points of the second epoch to the relative meshes [25, 42]. The geometry-based strategy, instead of representing the point clouds by meshes, approximates them by analytic functions, such as planes, spheres, cylinders and

*Corresponding author: Xin Zhao, Geodätisches Institut, Leibniz Universität Hannover, Nienburger Str. 1, 30167 Hannover, Germany, e-mail: zhao@gih.uni-hannover.de, ORCID: https://orcid.org/0000-0001-5265-6659
Gaël Kermarrec, Boris Kargoll, Hamza Alkhatib, Ingo Neumann, Geodätisches Institut, Leibniz Universität Hannover, Nienburger Str. 1, 30167 Hannover, Germany, e-mails: kermarrec@gih.uni-hannover.de, kargoll@gih.uni-hannover.de, alkhatib@gih.uni-hannover.de, neumann@gih.uni-hannover.de, ORCID: https://orcid.org/0000-0001-5986-5269 (G. Kermarrec)

the free-form curves or surfaces and compares the approximated analytic functions of different epochs [4, 5, 44, 45, 50]. The geometry-based method shares the same approximations approach with the parameter-based strategy. In the latter, however, the deformation is characterized by comparing the corresponding estimated parameters from the approximated analytic functions [13, 27, 38].

In this contribution, our focus lays on the geometry-based methods. The deformation is characterized by comparing the continuous model functions from the scatter point samples so that continuous differences between epochs can be obtained. In most cases, the unknown parameters of the approximated model are estimated by least squares (LS) adjustment, i. e. the zero-mean residuals obtained by subtracting the overdetermined measurements and their approximation are minimized in the LS sense, in the metric of the variance–covariance matrix (VCM) of the observations [24]. Consequently, the trustworthiness of the adjusted results depends on both the validity of the selected functional model, i. e. the relationship between the parameters to be estimated and the observations, and the stochastic model, i. e. the description of a realistic VCM. Free-form curves and surfaces, such as B-splines, among parametric functions are a powerful tool to obtain an analytical model of the object. In addition to being popular in automobile industry and a standard tool in computer aided geometric design [7, 11], B-splines are increasingly used in geodesy fields due to their great flexibility to approximate objects scanned with TLS. The drawback of using a Gauss–Helmert model to fit an object with restrictive standard surfaces, such as a plane or cylinder, can be overcome. Interested readers could refer to Bureick et al. [4] for a comparison of the most popular parametric surfaces in geodetic applications from polynomial to non-uniform rational B-splines. A lot of recent research regarding the parametrization of the surface [10] or determination of the optimal knot vector regarding the scattered point clouds [5] highlight the high interest of the geodetic community in B-splines approximation. Improving the functional model is of main importance as the major application is to quantify and analyse deformations. Exemplarily, Koch [23] made use of the B-spline surface in deformation analysis by modelling a plastic sheet under increasing pressure. Neuner et al. [32] detected the deflection of a bridge by TLS in a profile mode. The point profiles obtained were approximated by B-spline curves. Xu et al. [49] offered a robust and time-efficient solution to approximate the point cloud of a tunnel with B-spline curves. Consequently, improvements regarding the functional model remain indispensable if not vital to avoid wrong or inaccurate modelization of deformations.

However, the second pillar of the LS adjustment should not be underestimated: the stochastic model can strongly influence the efficiency of the parameters estimated; here, the control points of the B-splines surface. Earlier literature related to geodetic fields has already discussed the effect of an incorrect stochastic model on adjusted results [9, 28, 46]. Indeed, in addition to biasness of the *a posteriori* variance factor [48], the LS solution become less efficient when the VCM involved is misspecified [19]. The description of uncertainties often relies on the "Guide to the Expression of Uncertainty in Measurement" [14]. In addition to the classical law of error propagation, the uncertainties can be propagated via Monte Carlo approach [21, 22] or fuzzy techniques [2]. Alternatively, empirical methods are used to describe the stochasticity of TLS measurements. Wujanz et al. [47] developed an intensity-based stochastic model which makes use of the intensity values to account for the impact of surface and the acquisition configuration of the uncertainties. Kauker and Schwieger [17] generated a synthetic VCM by integrating the functional correlated, stochastic correlated and non-correlated errors. In evaluating the stochastic model, Zhao et al. [50] used simulation-based Cox's and Rao's score tests to discriminate between homoscedastic and heteroscedastic VCMs. Jurek et al. [15] evaluated the impact of spatial correlations, with various correlation lengths and colour noise ratios, on the surface estimation by global and parameter tests.

The key point in deformation analysis is to decide whether a deformation occurs between two or more measuring epochs. In other words, the congruency problem for these repeatedly measured epochs has to be solved. The congruency tests proposed by Pelzer [36] are usually applied to judge the possible changes in the geometry, which has proved to be the most powerful test in Gauss–Markov models with normal distributed variants and specified VCM [16]. Niemeier [33] presented a rigorous mathematical procedure for this congruency analysis of multiple measured networks. Neumann and Kutterer [30, 31] considered the remaining systematic deviations in the stochastic model, which is involved in the congruency test, by fuzzy intervals. Velsink [43] improved the iterative procedure by non-iterative hypothesis tests, where all the subsets of the non-congruent points considered were tested. Lehmann and Lösler [26] interpreted the detection of unstable points within the congruence analysis as a model selection problem, where comparisons with the classic information criterion approach were made. The congruency test is further widely applied in global positioning system (GPS) deformation networks [6, 39, 40]. Baselga et al. [3] searched for a maximum number of stable points by means of a con-

gruency test in a relative control networks for deformation determination. However, the test statistic of the congruency test is not only based on the detected difference between the points' coordinates at the two epochs, but also depends on their stochastic characteristics. Consequently, any misspecification of the VCM leads to an untrustworthy test result [12].

When approximating the point clouds by B-splines and using the surface points' differences in a congruency test, accounting for mathematical correlations of Cartesian coordinates in the stochastic model is unavoidable, in addition to an accurate description of the variance by taking heteroscedasticity of the raw measurements into account. In this contribution, a Monte Carlo simulation-based study is carried out to analyze the impact of a simplified VCM. More specifically, we investigate neglecting mathematical correlations and heteroscedasticity on geometry-based deformation analysis, where the geometry is expressed by B-splines. In addition to the true deformation, the true VCM that generates the noisy observations has to be determined exactly to assess whether and when the simplified stochastic models affect the rejection rate of the null hypothesis that no deformation occurs. They remain, thus, unavoidable, as real data analysis cannot provide the truth.

The paper is organised as follows. In Section 2, the methodology of B-spline surface approximation and congruency analysis procedures is reviewed and explained. This methodology is instantiated in Section 3, based on simulation, to detect the influence of misspecified VCMs on the power of the congruency test. The subsequent Section 4 provides a further discussion on the results and deduces a threshold ratio which highlights the area of reliable congruency test results when using simplified VCMs. Finally, conclusions are drawn in Section 5.

2 Methodology

In this section, the procedure of the B-spline surface approximation and congruency test are introduced.

2.1 B-spline surface approximation with VCM

The purpose of surface fitting is to estimate a continuous model function from the scatter point samples, which can be implemented by a LS adjustment in the case of redundant measurements. The B-splines are usually employed

to fit point clouds due to their flexibility in modelling complicated objects.

The mathematical description of a B-spline surface point $\begin{bmatrix} X_k & Y_k & Z_k \end{bmatrix}^\top$ ($k = 1, 2, ..., K$) is as follows

$$\begin{aligned} \begin{bmatrix} X_k & Y_k & Z_k \end{bmatrix}^\top &= \mathbf{S}(\bar{u}_k, \bar{v}_k) \\ &= \sum_{i=0}^{n} \sum_{j=0}^{m} N_{i,p}(\bar{u}_k) N_{j,q}(\bar{v}_k) \mathbf{C}_{i,j} \end{aligned} \quad (1)$$

here $\bar{\mathbf{u}} = \bar{u}_k$ is the location parameter vector in the u-direction and $\bar{\mathbf{v}} = \bar{v}_k$ is the location parameter vector in the v-direction which is perpendicular to the u-direction. The surface point builds upon the bidirectional combination of the basis function $N_{i,p}(\bar{u}_k)$, $N_{j,q}(\bar{v}_k)$ with the degree p, q and control points $\mathbf{C}_{i,j} = \begin{bmatrix} C_{X_{i,j}} & C_{Y_{i,j}} & C_{Z_{i,j}} \end{bmatrix}^\top$, which are located on a bidirectional net with the number of $(n+1)$ and $(m+1)$ in the u- and v-directions, respectively.

The B-spline surface approximation involves three main steps, as summarized by Bureick et al. [4]:
(i)   Parametrization of the measurements located in the u- and v directions into location parameter vector $\bar{\mathbf{u}}$ and $\bar{\mathbf{v}}$.
(ii) Determination of the knot vectors $\mathbf{U}$ and $\mathbf{V}$ in the u- and v-direction.
(iii) Estimation of the $(n + 1) \times (m + 1)$ control points by means of a linear Gauss–Markov model.

The location parameter and knot vectors of step 1 and 2 are used for the derivation of the basis function $\mathbf{N}_{i,p}$, $\mathbf{N}_{j,q}$. The corresponding information is summarized into a design matrix for the final estimation step, i. e. the estimation of the positions of the $(n+1) \times (m+1)$ control points by LS-adjustment. Interested readers are referred to [5], [4] and [37].

Given the points observed with the number K located on a grid defined by s rows and t columns, they also can be arranged in matrix form as

$$\mathbf{l} = \begin{bmatrix} \mathbf{l}_1 \\ \vdots \\ \mathbf{l}_K \end{bmatrix} = \begin{bmatrix} X_1 \\ Y_1 \\ Z_1 \\ \vdots \\ X_K \\ Y_K \\ Z_K \end{bmatrix} \quad (2)$$

The functional model (1) then gives rise to the (pointwise) observations equations

$$\mathbf{l}_k + \mathbf{v}_k = \mathbf{S}(\bar{u}_k, \bar{v}_k) = \sum_{i=0}^{n} \sum_{j=0}^{m} N_{i,p}(\bar{u}_k) N_{j,q}(\bar{v}_k) \mathbf{C}_{i,j} \quad (3)$$

where $\mathbf{v}_k$ denotes the vector of residuals or random deviations regarding the observations $\mathbf{l}_k$ for point k. These con-

stitute a linear model which can be jointly written in the form

$$\mathbf{l} + \mathbf{v} = \mathbf{A}\mathbf{x} \tag{4}$$

$$\mathbf{A} = \begin{bmatrix} N_{0,p}(\bar{u}_1)N_{0,q}(\bar{v}_1) & 0 & 0 & \cdots & N_{n,p}(\bar{u}_1)N_{m,q}(\bar{v}_1) & 0 & 0 \\ 0 & N_{0,p}(\bar{u}_1)N_{0,q}(\bar{v}_1) & 0 & \cdots & 0 & N_{n,p}(\bar{u}_1)N_{m,q}(\bar{v}_1) & 0 \\ 0 & 0 & N_{0,p}(\bar{u}_1)N_{0,q}(\bar{v}_1) & \cdots & 0 & 0 & N_{n,p}(\bar{u}_1)N_{m,q}(\bar{v}_1) \\ & & & \vdots & & & \\ N_{0,p}(\bar{u}_K)N_{0,q}(\bar{v}_K) & 0 & 0 & \cdots & N_{n,p}(\bar{u}_K)N_{m,q}(\bar{v}_K) & 0 & 0 \\ 0 & N_{0,p}(\bar{u}_K)N_{0,q}(\bar{v}_K) & 0 & \cdots & 0 & N_{n,p}(\bar{u}_K)N_{m,q}(\bar{v}_K) & 0 \\ 0 & 0 & N_{0,p}(\bar{u}_K)N_{0,q}(\bar{v}_K) & \cdots & 0 & 0 & N_{n,p}(\bar{u}_K)N_{m,q}(\bar{v}_K) \end{bmatrix} \tag{5}$$

$$\mathbf{x} = \begin{bmatrix} \mathbf{C}_{0,0} \\ \vdots \\ \mathbf{C}_{n,m} \end{bmatrix} = \begin{bmatrix} C_{X_{0,0}} \\ C_{Y_{0,0}} \\ C_{Z_{0,0}} \\ \vdots \\ C_{X_{n,m}} \\ C_{Y_{n,m}} \\ C_{Z_{n,m}} \end{bmatrix} \tag{6}$$

are readily assembled. In addition to the functional model, we generically define the stochastic model of measurements in terms of $\boldsymbol{\Sigma}_{ll}$, where σ_0^2 is the *a priori* variance factor, $\mathbf{Q}_{ll}$ and $\mathbf{P}$ are the cofactor matrix and weight matrix respectively.

$$\boldsymbol{\Sigma}_{ll} = \sigma_0^2 \mathbf{Q}_{ll} = \sigma_0^2 \mathbf{P}^{-1} \tag{7}$$

The LS estimates of the control points may then be obtained through the well-known inverted normal equations

$$\hat{\mathbf{x}} = (\mathbf{A}^\top \boldsymbol{\Sigma}_{ll}^{-1} \mathbf{A})^{-1} \mathbf{A}^\top \boldsymbol{\Sigma}_{ll}^{-1} \mathbf{l} \tag{8}$$

The residuals should have zero-mean for an unbiased generalized LS estimator. To derive the statistical distribution of test statistic, the Gaussian assumption for the residuals is further necessary. Although the unbiasedness of the generalized LS estimator (i. e. here the coordinates of the control points) is still given when the VCM are misspecified, the solution is less efficient and the VCM of the adjusted surface points is biased in case of misspecification.

2.2 Optimal tests in Gauss-Markov models with normal random deviations and known VCM

2.2.1 Adequacy evaluation of the functional model

In situations where the observables of a Gauss–Markov model are known to be truly normally distributed and to

for all the points with a $(3K \times 3(n+1)(m+1))$ design matrix $\mathbf{A}$ is shown in (5) and the total $(3(n+1)(m+1) \times 1)$ parameter vector $\mathbf{x}$ is shown in (6).

truly have the fully specified VCM $\boldsymbol{\Sigma}_{ll}$, it might still happen that the functional model $\mathbf{Ax}$ within the observation equations (4) is misspecified and erroneous. Therefore, it makes sense to carry out a model selection procedure that evaluates different candidate models and indicates the optimal one either through relative testing or absolute minimization of an information measure. Both kinds of procedure are based on the log-likelihood function L of the observation model. Under the aforementioned 'normal' distributional assumption $\mathbf{l} \sim N(\mathbf{Ax}, \boldsymbol{\Sigma}_{ll})$, the corresponding likelihood function is defined to be the probability density function (pdf) of that multivariate normal distribution [24], that is,

$$f(\mathbf{l}; \mathbf{x}) = \frac{1}{(2\pi)^{n_{\text{obs}}/2}(\det \boldsymbol{\Sigma}_{ll})^{1/2}} \cdot$$
$$\exp\left\{-\frac{1}{2}(\mathbf{l} - \mathbf{Ax})^\top \boldsymbol{\Sigma}_{ll}^{-1}(\mathbf{l} - \mathbf{Ax})\right\} \tag{9}$$

Since we assume the VCM to be (truly) known, we may compute its Cholesky decomposition $\boldsymbol{\Sigma}_{ll} = \mathbf{R}^\top \mathbf{R}$ and transform the observation equations (4) via left-multiplication by $(\mathbf{R}^\top)^{-1}$, resulting in

$$\bar{\mathbf{l}} + \bar{\mathbf{v}} = \bar{\mathbf{A}}\mathbf{x} \tag{10}$$

with $\bar{\mathbf{l}} = (\mathbf{R}^\top)^{-1}\mathbf{l}$, $\bar{\mathbf{v}} = (\mathbf{R}^\top)^{-1}\mathbf{v}$ and $\bar{\mathbf{A}} = (\mathbf{R}^\top)^{-1}\mathbf{A}$. The point of this transformation is that the (possibly fully populated) VCM $\boldsymbol{\Sigma}_{ll}$ of $\mathbf{l}$ reduces to the identity VCM $\mathbf{I}$ for $\bar{\mathbf{l}}$, so that, on the one hand, the LS estimate (8) can be replaced by the simpler formula

$$\hat{\mathbf{x}} = (\bar{\mathbf{A}}^\top \bar{\mathbf{A}})^{-1} \bar{\mathbf{A}}^\top \bar{\mathbf{l}} \tag{11}$$

On the other hand, the log-likelihood now takes the form

$$L(\mathbf{x}; \bar{\mathbf{l}}) = -\frac{n_{\text{obs}}}{2} \log(2\pi) - \frac{1}{2} \sum_{i=1}^{n_{\text{obs}}} (\bar{\mathbf{A}}_i \mathbf{x} - \bar{\mathbf{l}}_i)^2 \tag{12}$$

and is conditioned by the independently distributed observations $\bar{\mathbf{l}}$. Based on this model, the Akaike information criterion (AIC) and the Bayesian information criterion (BIC) read (cf. [1, 51])

$$\text{AIC} = -2L(\hat{\mathbf{x}}; \bar{\mathbf{l}}) + 2n_{\text{par}}, \tag{13}$$

$$\text{BIC} = -2L(\hat{\mathbf{x}}; \bar{\mathbf{l}}) + n_{\text{par}} \log(n_{\text{obs}}) \tag{14}$$

The smaller the AIC/BIC value, the better the parameterization $\mathbf{Ax}$. Therefore, we should choose among all models that have the smallest AIC/BIC value. Alternatively, we could carry out statistical model selection tests in the spirit of Vuong or Clarke (cf. [1, 51]) to identify the best model. Once adequate B-spline models have been fitted to point clouds of two or more epochs, these models can be safely used within a congruence or deformation test.

2.2.2 Test for congruency

The key point in deformation analysis is to decide whether significant changes between the two epochs measured occur or not. More specifically, we have in epoch $N_e \in \{1, 2\}$ an observation vector $\mathbf{l}^{(N_e)}$ to be approximated by a B-spline model $\mathbf{A}^{(N_e)}\mathbf{x}^{(N_e)}$. We assume the corresponding random deviations $\mathbf{e}^{(1)}$ and $\mathbf{e}^{(2)}$ to be normally distributed with zero mean and the corresponding VCMs are $\boldsymbol{\Sigma}_{ll}^{(1)}$ and $\boldsymbol{\Sigma}_{ll}^{(2)}$. We assume that each random deviation of the first epoch and the second epoch are uncorrelated. We, thus, have the linear Gauss–Markov model:

$$\begin{bmatrix} \mathbf{l}^{(1)} \\ \mathbf{l}^{(2)} \end{bmatrix} = \begin{bmatrix} \mathbf{A}^{(1)} & \mathbf{0} \\ \mathbf{0} & \mathbf{A}^{(2)} \end{bmatrix} \begin{bmatrix} \mathbf{x}^{(1)} \\ \mathbf{x}^{(2)} \end{bmatrix} \tag{15}$$

and

$$\begin{aligned} \boldsymbol{\Sigma}_{\mathbf{l}^{(1)},\mathbf{l}^{(2)}} &= \begin{bmatrix} \boldsymbol{\Sigma}_{ll}^{(1)} & \mathbf{0} \\ \mathbf{0} & \boldsymbol{\Sigma}_{ll}^{(2)} \end{bmatrix} = \sigma_0^2 \begin{bmatrix} \mathbf{Q}_{ll}^{(1)} & \mathbf{0} \\ \mathbf{0} & \mathbf{Q}_{ll}^{(2)} \end{bmatrix} \\ &= \sigma_0^2 \begin{bmatrix} \mathbf{P}^{(1)} & \mathbf{0} \\ \mathbf{0} & \mathbf{P}^{(2)} \end{bmatrix}^{-1} = \sigma_0^2 \mathbf{P}_{\mathbf{l}^{(1)},\mathbf{l}^{(2)}} \end{aligned} \tag{16}$$

We will not formulate the hypotheses concerning the (total) deformation between the two epochs at the level of the associated control points $\mathbf{x}^{(1)}$ and $\mathbf{x}^{(2)}$, but at the level of the surface points $\mathbf{F}^{(1)}\mathbf{x}^{(1)}$ and $\mathbf{F}^{(2)}\mathbf{x}^{(2)}$ defined by (3). There are two reasons for comparing the surface points instead of the control points. Firstly, because of the changes in the geometry, the model complexity of B-splines may vary between two epochs, which leads to different numbers of control points. In that case, it is complex to define reference control points between two epochs on which the

congruency could be based meaningfully. Moreover, compared with the large number of surface points, the control points are relatively small in number and sparsely distributed in the approximated B-spline surface. Thus, the detailed deformation cannot be reflected and located sufficiently well by the reference control points. We correspondingly define the null hypothesis H_0 that no deformation occurred by the equation:

$$H_0 : \mathbf{F}^{(2)}\mathbf{x}^{(2)} - \mathbf{F}^{(1)}\mathbf{x}^{(1)} = \begin{bmatrix} -\mathbf{F}^{(1)} & \mathbf{F}^{(2)} \end{bmatrix} \begin{bmatrix} \mathbf{x}^{(1)} \\ \mathbf{x}^{(2)} \end{bmatrix} = \mathbf{0} \tag{17}$$

Since we intend to analyse the power function of the congruency test, we also formulate an alternative hypothesis, which is adequately described by the inequalities

$$H_1 : \begin{bmatrix} -\mathbf{F}^{(1)} & \mathbf{F}^{(2)} \end{bmatrix} \begin{bmatrix} \mathbf{x}^{(1)} \\ \mathbf{x}^{(2)} \end{bmatrix} \neq \mathbf{0} \tag{18}$$

Under the assumptions that the model (15)–(16) is correctly specified (up to the unknown, true parameter values) and that the number h of rows of the matrix $\mathbf{H} = \begin{bmatrix} -\mathbf{F}^{(1)} & \mathbf{F}^{(2)} \end{bmatrix}$ is less than or equal to the total number of parameters in $\boldsymbol{\beta} = \begin{bmatrix} \mathbf{x}^{(1),\top} & \mathbf{x}^{(2),\top} \end{bmatrix}^{\top}$, a *uniformly most powerful invariant* (UMPI) test exists (cf. [16], Chapter 3), based on the test statistic

$$\begin{aligned} T = \frac{1}{\sigma_0^2} \hat{\boldsymbol{\beta}}^{\top} \mathbf{H}^{\top} \Bigg(\mathbf{H} \Bigg(\begin{bmatrix} \mathbf{A}^{(1)} & \mathbf{0} \\ \mathbf{0} & \mathbf{A}^{(2)} \end{bmatrix}^{\top} \cdot \\ \mathbf{P}_{\mathbf{l}^{(1)},\mathbf{l}^{(2)}} \begin{bmatrix} \mathbf{A}^{(1)} & \mathbf{0} \\ \mathbf{0} & \mathbf{A}^{(2)} \end{bmatrix} \Bigg)^{-1} \mathbf{H}^{\top} \Bigg)^{-1} \mathbf{H}\hat{\boldsymbol{\beta}} \sim \chi_h^2 \end{aligned} \tag{19}$$

Here, $\hat{\boldsymbol{\beta}}$ comprises the LS (or equivalently maximum-likelihood) estimates

$$\begin{aligned} \hat{\boldsymbol{\beta}} = \begin{bmatrix} \hat{\mathbf{x}}^{(1)} \\ \hat{\mathbf{x}}^{(2)} \end{bmatrix} &= \Bigg(\begin{bmatrix} \mathbf{A}^{(1)} & \mathbf{0} \\ \mathbf{0} & \mathbf{A}^{(2)} \end{bmatrix}^{\top} \boldsymbol{\Sigma}_{\mathbf{l}^{(1)},\mathbf{l}^{(2)}}^{-1} \begin{bmatrix} \mathbf{A}^{(1)} & \mathbf{0} \\ \mathbf{0} & \mathbf{A}^{(2)} \end{bmatrix} \Bigg)^{-1} \cdot \\ &\quad \begin{bmatrix} \mathbf{A}^{(1)} & \mathbf{0} \\ \mathbf{0} & \mathbf{A}^{(2)} \end{bmatrix}^{\top} \boldsymbol{\Sigma}_{\mathbf{l}^{(1)},\mathbf{l}^{(2)}}^{-1} \begin{bmatrix} \mathbf{l}^{(1)} \\ \mathbf{l}^{(2)} \end{bmatrix} \end{aligned} \tag{20}$$

of the control points for both epochs, and

$$\begin{aligned} \boldsymbol{\Sigma}_{\hat{\boldsymbol{\beta}}\hat{\boldsymbol{\beta}}} &= \Bigg(\begin{bmatrix} \mathbf{A}^{(1)} & \mathbf{0} \\ \mathbf{0} & \mathbf{A}^{(2)} \end{bmatrix}^{\top} \boldsymbol{\Sigma}_{\mathbf{l}^{(1)},\mathbf{l}^{(2)}}^{-1} \begin{bmatrix} \mathbf{A}^{(1)} & \mathbf{0} \\ \mathbf{0} & \mathbf{A}^{(2)} \end{bmatrix} \Bigg)^{-1} \\ &= \frac{1}{\sigma_0^2} \Bigg(\begin{bmatrix} \mathbf{A}^{(1)} & \mathbf{0} \\ \mathbf{0} & \mathbf{A}^{(2)} \end{bmatrix}^{T} \mathbf{P}_{\mathbf{l}^{(1)},\mathbf{l}^{(2)}} \begin{bmatrix} \mathbf{A}^{(1)} & \mathbf{0} \\ \mathbf{0} & \mathbf{A}^{(2)} \end{bmatrix} \Bigg)^{-1} \end{aligned} \tag{21}$$

constituting the corresponding VCM. As we assumed all cross-correlations between the two measurement epochs to be zero, we can compute the estimates $\hat{\mathbf{x}}^{(1)}$ and $\hat{\mathbf{x}}^{(2)}$ by

evaluating (8) for both epochs separately. We now reparameterize the testing problem by setting

$$\boldsymbol{\Delta} = \mathbf{H}\boldsymbol{\beta} \qquad (22)$$

so that we can write (17) and (18) simpler as $H_0 : \boldsymbol{\Delta} = \mathbf{0}$ and $H_1 : \boldsymbol{\Delta} \neq \mathbf{0}$. Denoting the deformation estimates by $\hat{\boldsymbol{\Delta}} = \mathbf{H}\hat{\boldsymbol{\beta}}$, we obtain the corresponding VCM via the variance-covariance propagation law:

$$\boldsymbol{\Sigma}_{\hat{\Delta}\hat{\Delta}} = \mathbf{H}\boldsymbol{\Sigma}_{\hat{\beta}\hat{\beta}}\mathbf{H}^{\top} \qquad (23)$$

Thus, the test statistic (19) simplifies to

$$T = \hat{\boldsymbol{\Delta}}^{\top}\boldsymbol{\Sigma}_{\hat{\Delta}\hat{\Delta}}^{-1}\hat{\boldsymbol{\Delta}} \qquad (24)$$

whose form resembles the test statistic introduced by Pelzer [36]. We obtain the test decision via the comparison of the numerical value of T (associated with the actual measurement results $\mathbf{l}^{(1)}$ and $\mathbf{l}^{(2)}$) with the quantile $k_{1-\alpha}^{\chi_h^2}$ of the χ_h^2 test distribution at the specified significance level α. We accept H_0 in the case of $T \leq k_{1-\alpha}^{\chi_h^2}$, and we reject H_0 in the case of $T > k_{1-\alpha}^{\chi_h^2}$. We can apply the preceding UMPI test either 'globally' to $h \leq n_{\text{par}}$ surface points that represent the object of interest surveyed, or 'locally' to a single point ($h = 3$ for the X-, Y- and Z-coordinate). If more than n_{par} are to be tested, then the VCM (23) becomes rank-deficient, in which case its inverse in (24) can be replaced by the pseudo-inverse, as for the Pelzer test (cf. [34]; p. 439). However, it is unknown whether such a test still possesses the UMPI property.

Another situation in which this optimality criterion will no longer apply is when the true VCM $\boldsymbol{\Sigma}_{\mathbf{l}^{(1)},\mathbf{l}^{(2)}}$ is replaced by a numerically different matrix, for example, by ignoring significant covariances. Such a modified test can be theoretically expected to have less power than the UMPI test, i. e. less sensitivity to actual deformations than the optimal test. We use numerical simulations for this purpose because a quantification of the degradation of test power has not yet been achieved analytically.

3 Numerical example

Unfortunately, both the deformation and the true VCM of the observations are unknown in real data analysis. Consequently, we focus in this paper on Monte Carlo simulations to assess the impact of neglecting mathematical correlations and heteroscedasticity on the power of the congruency test. The surfaces to approximate and the stochasticity of the observations can be perfectly controlled and gradually misspecified by neglecting correlations or assuming equal variances of the measurements.

3.1 Simulation of measurement points

3.1.1 Reference VCM set up

When performing B-splines approximations with LS adjustment, we obtain the Cartesian coordinates of the control points so that the TLS measurements, expressed originally in polar coordinates (i. e. distance r, horizontal angel φ and vertical angel θ), must be firstly transformed into Cartesian coordinates $[X \quad Y \quad Z]$. Consequently, the VCM used in LS adjustment must account for the mathematical correlations induced by the transformation between polar and Cartesian coordinates.

The geometrical relationship between point in polar coordinates and in Cartesian coordinates is given by

$$\begin{bmatrix} X \\ Y \\ Z \end{bmatrix} = r \begin{bmatrix} \sin\theta\cos\varphi \\ \sin\theta\sin\varphi \\ \cos\theta \end{bmatrix} \qquad (25)$$

The VCM $\boldsymbol{\Sigma}_{r\varphi\theta}$ for the observation is fixed here because the uncertainties of raw measurements σ_r, σ_φ and σ_θ could be estimated from previous experience or the manufacturer's data sheet.

$$\boldsymbol{\Sigma}_{r\varphi\theta} = \begin{bmatrix} \sigma_r^2 & 0 & 0 \\ 0 & \sigma_\varphi^2 & 0 \\ 0 & 0 & \sigma_\theta^2 \end{bmatrix} \qquad (26)$$

We assume that the standard deviations of the TLS raw measurements are $\sigma_r = 10^{-4} \, m$ and $\sigma_\varphi = \sigma_\theta = 10^{-4} \, rad$. The units are neglected in the following sections for the sake of simplicity. Through the law of propagation of uncertainties, the transformed VCM reads.

$$\boldsymbol{\Sigma}_{XYZ} = \mathbf{J}\boldsymbol{\Sigma}_{r\varphi\theta}\mathbf{J}^{\top} = \begin{bmatrix} \sigma_X^2 & \sigma_{XY} & \sigma_{XZ} \\ \sigma_{YX} & \sigma_Y^2 & \sigma_{YZ} \\ \sigma_{ZX} & \sigma_{ZY} & \sigma_Z^2 \end{bmatrix} \qquad (27)$$

where $\mathbf{J}$ is the Jacobian matrix containing the derivatives of the Cartesian coordinates regarding r, φ and θ. The elements in $\boldsymbol{\Sigma}_{XYZ}$ are

$$\sigma_X^2 = (r\cos\varphi\sin\theta)^2\sigma_\varphi^2 + (r\sin\varphi\sin\theta)^2\sigma_\theta^2 + (\cos\varphi\sin\theta)^2\sigma_r^2$$
$$\sigma_Y^2 = (r\sin\varphi\cos\theta)^2\sigma_\varphi^2 + (r\cos\varphi\sin\theta)^2\sigma_\theta^2 + (\sin\varphi\sin\theta)^2\sigma_r^2$$
$$\sigma_Z^2 = (r\sin\theta)^2\sigma_\varphi^2 + \cos^2\varphi\sigma_r^2$$
$$\sigma_{XY} = \sigma_{YX} = (\cos\varphi\sin\varphi\sin^2\theta)\sigma_r^2 + (r^2\cos\varphi\sin\varphi\cos^2\theta)\sigma_\varphi^2$$
$$\qquad - (r^2\sin\varphi\cos\varphi\sin^2\theta)\sigma_\theta^2$$
$$\sigma_{XZ} = \sigma_{ZX} = (-r^2\cos\varphi\sin\theta\cos\theta)\sigma_\varphi^2 + (\cos\varphi\sin\theta\cos\theta)\sigma_r^2$$
$$\sigma_{YZ} = \sigma_{ZY} = (-r^2\sin\varphi\cos\theta\sin\theta)\sigma_\varphi^2 + (\sin\varphi\sin\theta\cos\theta)\sigma_r^2$$
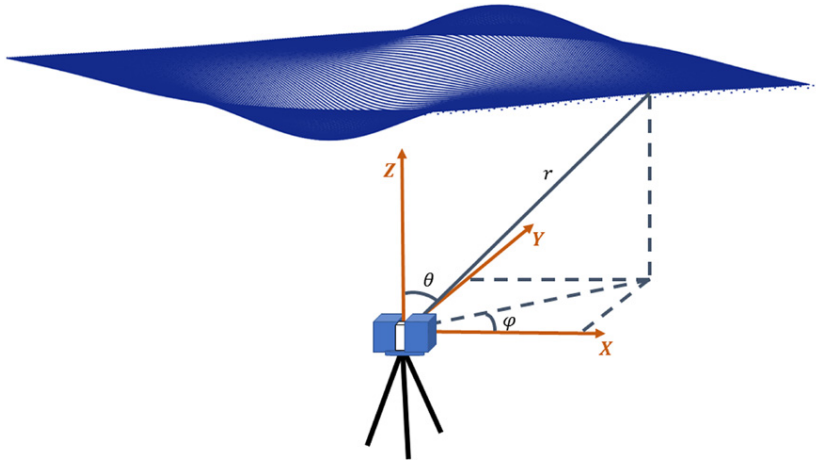$$\qquad (28)$$

Figure 1: Scan geometry of the simulated scanning scene.

The non-diagonal elements of the symmetric matrix Σ_{XYZ} are the mathematical correlation of the Cartesian coordinates for one point. The effect of neglecting them will, thus, depend on both the geometry by means of the angles and the respective variances of the measurements. Except for favourable geometries, i. e. when the angles are close to zero, it is, thus, difficult to predict how the omission will propagate in the deformation analysis, so that simulations allow one to investigate on the importance of their consideration.

3.1.2 Data simulation

The procedure of data simulation involves two main steps:
(i)   creation of the sample points from a given mathematical reference surface, and
(ii) addition of a noises vector with a known VCM corresponding to Σ_{XYZ} (27).

The points of the reference surface can be sampled from any mathematical function. Because of its smooth properties, which allow an accurate approximation with B-splines without being influenced by an inaccurate determination of the knot vector, the joint normal distribution function with independent random variables X_0 and Y_0 was retained. For one epoch, given the mean vector $\mathbf{a} = [a_{x_0} \quad a_{y_0}]^\top$ and VCM $\mathbf{b} = diag[b_{x_0}^2 \quad b_{y_0}^2]$, the pdf of bivariate normal distribution is shown as follows.

$$Z_0 = f(X_0, Y_0)$$
$$= \frac{1}{2\pi b_{x_0} b_{y_0}} exp\left(-\frac{1}{2}\left[\frac{(X_0 - a_{x_0})^2}{b_{x_0}^2} + \frac{(Y_0 - a_{y_0})^2}{b_{y_0}^2}\right]\right) \quad (29)$$

The laser scanner in our numerical example is assumed to be located in the centre of the object with a distance around 10 and the sample points are assumed as grid points located in the area of $[-10.05 \leq X \leq 10.05]$ and $[-10.05 \leq Y \leq 10.05]$ with a grid length 0.3. A relatively large grid length (0.3) is selected to avoid the great computational burden. The specific boundaries of the interval guarantee that the X- and Y-coordinates of sample points are symmetrical regarding the origin. Based on these parameters, i. e. $\mathbf{a}$, $\mathbf{b}$, X- and Y-coordinates, the Z-coordinates of the sample points are calculated through (29). Consequently, we obtain 68×68 sample points uniformly located on the reference surface.

At least two epochs of point clouds are necessary to simulate the deformation. The points sampled of each epoch share the identical X- and Y-coordinates due to the same sampling resolution. We simulate the deformation of Z-coordinates between two epochs by setting a different VCM for the pdfs. Exemplarily, assuming $\mathbf{a}_1 = [0 \quad 0]^\top$, $\mathbf{b}_1 = diag[10 \quad 10]$ and $\mathbf{a}_2 = [0 \quad 0]^\top$, $\mathbf{b}_2 = diag[9 \quad 9]$, the points sampled of epoch 1 and epoch 2 are shown in Figure 2.

Additionally, two other deformation magnitudes were simulated by varying the $\mathbf{b}_2$ of probability density function of epoch 2, corresponding to smaller and larger changes in the center part of the surface. Figure 3 shows the simulated deformation with various $\mathbf{b}_2$:
I.   small magnitude (blue curve):
     $\mathbf{b}_2 = diag[9.85 \quad 9.85]$,
II. middle magnitude (red curve):
     $\mathbf{b}_2 = diag[9.0 \quad 9.0]$, and
III. large magnitude (yellow curve):
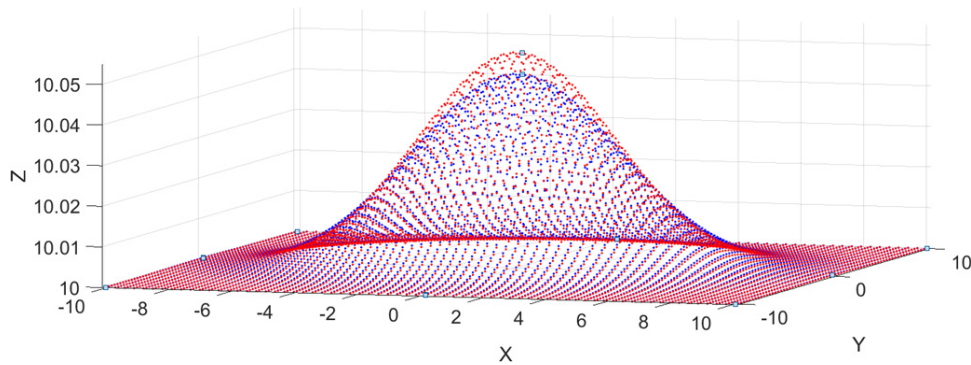 $\mathbf{b}_2 = diag[7.5 \quad 7.5]$.

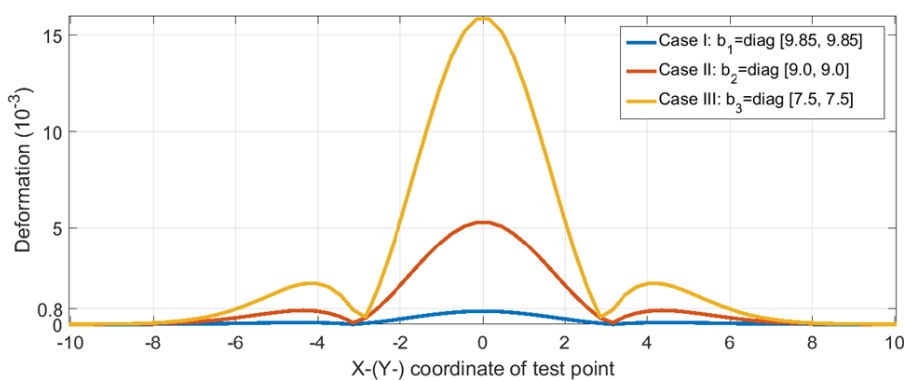**Figure 2:** Sampled points of epoch 1 (red) and epoch 2 (blue).

Figure 3: Simulated deformation magnitudes in the case I, II and III.

Please notice that the deformation here refers to the distance between the reference test points belongs to various epochs.

In the next step, a noise vector is added to the true sampled points. For one point, the noisy Cartesian coordinates are as follows:

$$\begin{bmatrix} X \\ Y \\ Z \end{bmatrix} = \mathbf{G}^\top \cdot randn(\boldsymbol{\mu}_0, \boldsymbol{\Sigma}_0) + \begin{bmatrix} X_0 \\ Y_0 \\ Z_0 \end{bmatrix} \tag{30}$$

where $\boldsymbol{\mu}_0 = \begin{bmatrix} 0 & 0 & 0 \end{bmatrix}^\top$ and $\boldsymbol{\Sigma}_0 = diag \begin{bmatrix} 1 & 1 & 1 \end{bmatrix}$. $\mathbf{G}^\top$ denote a regular lower triangular matrix of the Cholesky factorization $\boldsymbol{\Sigma}_{XYZ} = \mathbf{G}^\top \cdot \mathbf{G}$ (cf. [20]). A total of 10,000 simulations for each point were carried out using the Monte Carlo approach.

3.2 Simplified VCMs

The *a posteriori* VCM and the simplified matrices are applied in a B-spline surfaces approximation to detect the impact of the inadequate VCMs on the geometry-based de-formation analysis. The three VCM models retained, which correspond to usual misspecification, are

(i) VCM model 1: considering the mathematic correlation among Cartesian coordinates within one point. $\boldsymbol{\Sigma}_{ref}$ is a block diagonal matrix and it is exactly the *a priori* VCM of the measurements simulated (Section 3.1).

$$\boldsymbol{\Sigma}_{ref} = \begin{bmatrix} \sigma_{x_1}^2 & \sigma_{x_1y_1} & \sigma_{x_1z_1} & & & & & & \\ \sigma_{y_1x_1} & \sigma_{y_1}^2 & \sigma_{y_1z_1} & & \mathbf{0} & & \cdots & & \mathbf{0} \\ \sigma_{z_1x_1} & \sigma_{z_1y_1} & \sigma_{z_1}^2 & & & & & & \\ & & & \sigma_{x_2}^2 & \sigma_{x_2y_2} & \sigma_{x_2z_2} & & & \\ & \mathbf{0} & & \sigma_{y_2x_2} & \sigma_{y_2}^2 & \sigma_{y_2z_2} & & \mathbf{0} & \\ & & & \sigma_{z_2x_2} & \sigma_{z_2y_2} & \sigma_{z_2}^2 & & & \\ & \vdots & & & & & \ddots & & \vdots \\ & & & & & & \sigma_{x_K}^2 & \sigma_{x_Ky_K} & \sigma_{x_Kz_K} \\ & \mathbf{0} & & & \cdots & & \sigma_{y_Kx_K} & \sigma_{y_K}^2 & \sigma_{y_Kz_K} \\ & & & & & & \sigma_{z_Kx_K} & \sigma_{z_Ky_K} & \sigma_{z_K}^2 \end{bmatrix} \tag{31}$$

(ii) VCM model 2: considering the measurements as independent but with different variances. $\boldsymbol{\Sigma}_{diag}$ is exactly the diagonal matrix from (31).

$$\mathbf{\Sigma}_{diag} = \begin{bmatrix} \sigma_{x_1}^2 & 0 & 0 \\ 0 & \sigma_{y_1}^2 & 0 & \quad \mathbf{0} & \cdots & \mathbf{0} \\ 0 & 0 & \sigma_{z_1}^2 \\ & & & \sigma_{x_2}^2 & 0 & 0 \\ & \mathbf{0} & & 0 & \sigma_{y_2}^2 & 0 & & \mathbf{0} \\ & & & 0 & 0 & \sigma_{z_2}^2 \\ \vdots & & & & \ddots & & \vdots \\ & & & & & \sigma_{x_K}^2 & 0 & 0 \\ & \mathbf{0} & & \cdots & & 0 & \sigma_{y_K}^2 & 0 \\ & & & & & 0 & 0 & \sigma_{z_K}^2 \end{bmatrix} \quad (32)$$

(iii) VCM model 3: considering the measurements as independent and with equal variances. $\mathbf{\Sigma}_{iden}$ is a diagonal matrix with variance $\sigma_I^2 = 7.98e^{-7}$, which is exactly the mean of the diagonal elements of (32).

$$\mathbf{\Sigma}_{iden} = \begin{bmatrix} \sigma_I^2 & 0 & 0 \\ 0 & \sigma_I^2 & 0 & \quad \mathbf{0} & \cdots & \mathbf{0} \\ 0 & 0 & \sigma_I^2 \\ & & & \sigma_I^2 & 0 & 0 \\ & \mathbf{0} & & 0 & \sigma_I^2 & 0 & & \mathbf{0} \\ & & & 0 & 0 & \sigma_I^2 \\ \vdots & & & & \ddots & & \vdots \\ & & & & & \sigma_I^2 & 0 & 0 \\ & \mathbf{0} & & \cdots & & 0 & \sigma_I^2 & 0 \\ & & & & & 0 & 0 & \sigma_I^2 \end{bmatrix}$$
$$(33)$$

3.3 Selection of the B-spline model

The investigation of the stochastic model's impact on the congruency test should be based on an appropriate functional model which is sufficient to describe the geometrical features of each epoch. It is expected that the specification of knot vectors and the number of control points contribute to the goodness of the approximation. In our numerical example, the knot vectors $\mathbf{U}$ and $\mathbf{V}$ in u- and v-direction are determined by the Piegl and Tiller approach [37], since it is a fast and easy algorithm to align the knot vectors to the location parameters. Thus, the goodness of the approximation replied mainly on the complexity of B-spline model, i. e. the number of control points. Due to the symmetry of the area simulated, the number of control points are assumed to be identical in the u- and v-

directions, i. e. $m = n$. We compared the bi-cubic B-spline models with a control point number from $m = n = 5$ to $m = n = 20$.

The model selection procedures based on the information criterion are employed to help us in selecting the optimal functional model. The optimal number of control points of the bi-cubic B-spline model selected by AIC and BIC procedures are summarized in Table 1.

Since the AIC and BIC values are quite similar between the models $m, n = 10$ and $m, n = 11$ for epoch 1, which is also the same case for epoch 2 between the models $m, n = 11$ and $m, n = 13$, we would follow the BIC conclusion to choose the most parsimonious B-spline model to save the computation burden. Consequently, the optimal bi-cubic B-spline model for epoch 1 is $m, n = 10$ while that for epoch 2 in all three cases is $m, n = 11$.

3.4 Results of the congruency test

Based on the three VCMs, the surface points of the two epochs are adjusted as $\hat{\mathbf{S}}_1$ and $\hat{\mathbf{S}}_2$. Both global and local congruency tests were carried out on all 10,000 repetitions. The number of null hypotheses rejected (N_{rej}) divided by the number of repetitions (M) is defined as the rejection rate (N_{rej}/M). We selected 68 representative points in the global congruency test to avoid the aforementioned rank-deficiency problem in section 2.2.2 and due to the symmetry of the points sampled. The locations of the representative points are shown in Figure 4 in the context of the simulated surface of epoch 1.

3.4.1 Case 1: Zero deformation

The reference surfaces in the first simulation, are the same in the two epochs, i. e. $\mathbf{b}_1 = \mathbf{b}_2 = diag\,[10 \quad 10]$.

The null hypothesis H_0 is in none of the 10,000 repetitions rejected in the global scale. In the local scale, the rejection rates of the three stochastic models are various. Figure 5 presents the corresponding results for the zero deformation case, where the red curve, indicating the rejection rate of the estimated deformation with Σ_{ref}, stabilizes at 5 %, which is consistent with the assumed type-I error

Table 1: The optimal bi-cubic B-spline model evaluated by model selection procedures.

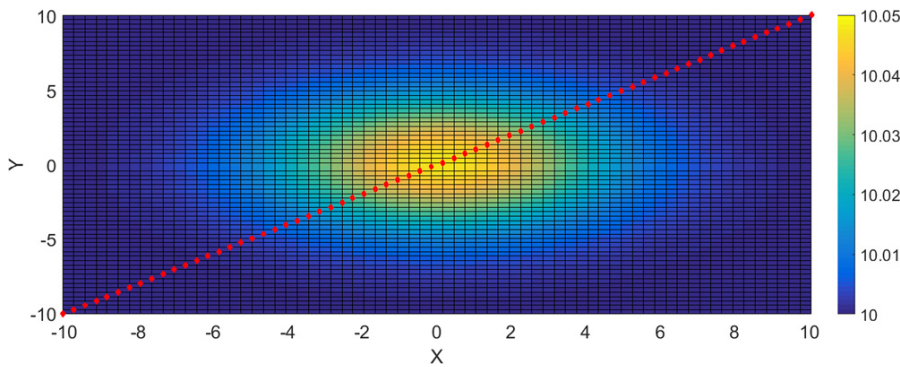| Dataset	epoch 1	epoch 2 (case I)	epoch 2 (case II)	epoch 2 (case III)
AIC	$m, n = 11$	$m, n = 13$	$m, n = 13$	$m, n = 13$
BIC	$m, n = 10$	$m, n = 11$	$m, n = 11$	$m, n = 11$

Figure 4: Location of the test points (red points) in the context of the simulated surface of epoch 1.
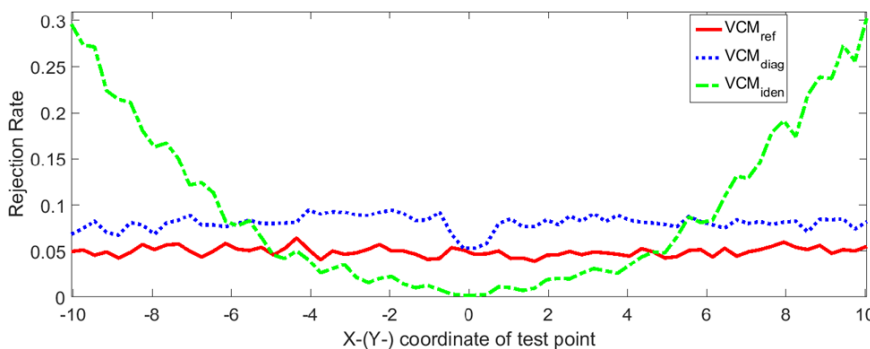

Figure 5: The rejection rate of the local congruency test for the case of zero deformation within 10,000 repetitions.

rate $\alpha = 0.05$. The blue dotted curve fluctuates slightly at a higher rejection rate (6–10 %), whereas the green dashed curve, unlike the other two, shows a small rejection rate in the centre part, which increases and reaches 30 % towards both edges.

The estimated surface points with the reference VCM accounting for mathematical correlations are congruent with the true values. High rejection rates are obtained in the two other cases, especially at the edge points estimated with the identity VCM. For the VCM accounting only for heteroscedasticity (Σ_{diag}) the rejection rate is similar to the one obtained for the reference VCM up to a variate inflation factor of approximately 2–4 %, Thus, the fact that correlations decrease the variance of the estimated parameter is confirmed (see e. g. [18]).

3.4.2 Case 2: Deformation

Three magnitudes of deformation are simulated (see Figure 3) and investigated. The null hypothesis in the global congruency test was rejected for all the 10,000 repetitions at type-I error rate $\alpha = 0.05$. This is consistent with the actual differences between the simulated two epochs. How-

ever, the test static values T of the three models differ significantly. Table 2 shows the range of test statistic values in the global test of the three stochastic models for case II exemplarily, while the quantile value with type-I error rate $\alpha = 0.05$ is $k^{\chi_h^2}_{1-\alpha} = 233.98$ ($h = 204$ for X-, Y- and Z-coordinate of 68 test points).

The local congruency tests were additionally carried out to find the individual points responsible for the rejection of the general null hypothesis. The rejection rate of 10,000 repetitions at type-I error rate $\alpha = 0.05$ for 68 test points are shown in Figure 6, 7 and 8 for the three deformation magnitudes. The red curve denotes the rejection rate of the deformation estimated with Σ_{ref}, while the blue dotted curve and green dashed curve correspond to Σ_{diag} and Σ_{iden} as the stochastic model, respectively.

The test results of the deformation estimated with Σ_{ref}, i. e. the true stochastic model, are consistent with the simulated deformations. Larger deformation occurs in the centre part in all three cases and the rejection rates should stabilize at 100 %. However, for smaller deformation (case I shown in Figure 6), using Σ_{iden} does not provide the correct rejection of the null hypothesis even in the centre part of the surface, which is actually deformed. During the deformation decreasing to the local minimum

Table 2: Global congruency test statistics of case II with the quantile value with type-I error rate $\alpha = 0.05$ $k_{1-\alpha}^{\chi_h^2} = 233.98$.

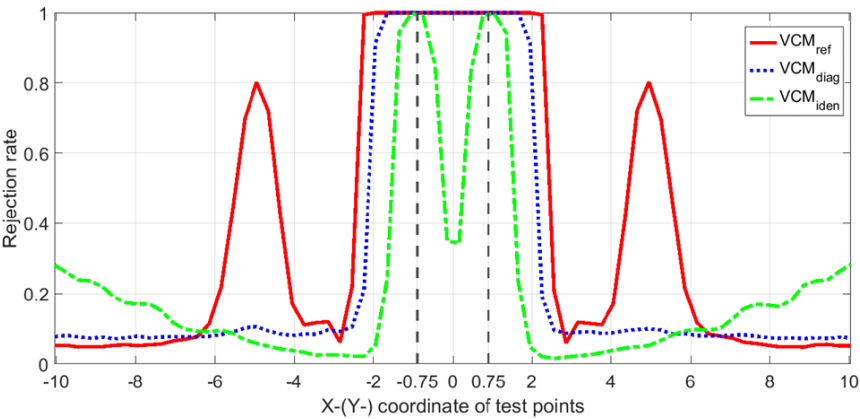| Test statistic	T_{ref}	T_{diag}	T_{iden}
Range	$(1.57-1.62) \times 10^5$	$(5.91-6.12) \times 10^4$	$(5.02-5.28) \times 10^3$

Figure 6: Rejection rate of the local congruency test for 68 points in 10,000 repetitions using various VCMs (case I).
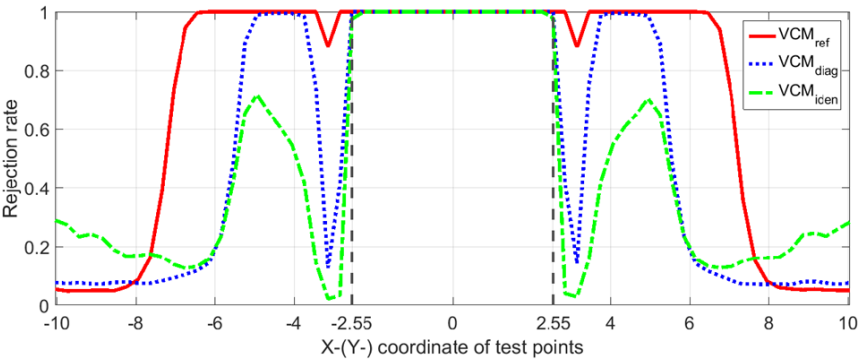

Figure 7: Rejection rate of the local congruency test for 68 points in 10,000 repetitions using various VCMs (case II).
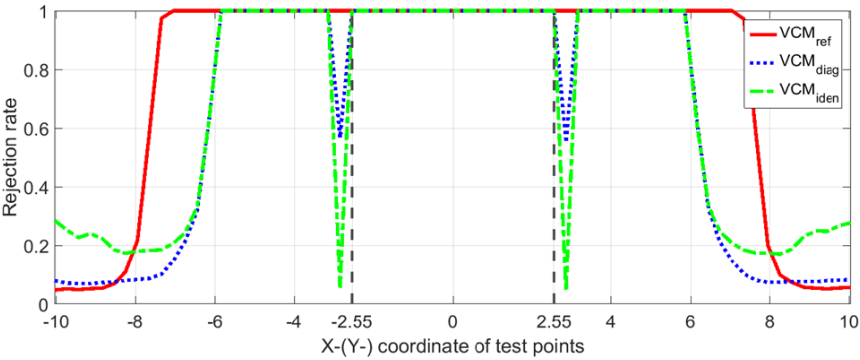

Figure 8: Rejection rate of the local congruency test for 68 points in 10,000 repetitions using various VCMs (case III).

values, the green and blue curves of case I and II (Figure 7) change faster than the red one with lower rejection rates. For case III (Figure 8), the green and blue curves highlights that the null hypothesis is wrongly accepted for point $X(Y) = -2.85$ and $X(Y) = 2.85$, whereas the rejection rate is constant at a 100 % level for the red curve. When deformation increases after the local minimum points, the green and blue curves of case I perform as they do in the zero-deformation case (Figure 5) and indicate a false lower rejection rates. For case II, slower changes with lower rejection rates can be found in the green and blue curves. For the three deformation magnitudes under consideration, the rejection rates on the edge part where no deformation occurs ($-10.05 \leq X(Y) < -8.25$ and $8.25 \leq X(Y) < 10.05$) are comparable with the zero-deformation case (Figure 5), which is expected.

4 Discussion

Although the congruency tests in the global scale are consistent with the simulated truth, the local test results, in the two cases, i. e. zero-deformation and deformation, vary significantly (see Figure 5, 6, 7 and 8). In this section, these results are put into perspective, focusing on the balance between heteroscedasticity, geometry and mathematical correlations.

4.1 The approximated results

Because of the unbiasedness of the LS estimator, the VCM chosen – either the true or a simplified matrix – will not impact the approximated surface points $\hat{S}_1$ and $\hat{S}_2$, provided that the safety of the functional model is guaranteed by the model selection procedure. However, the accuracy of approximation varies from the center to the edges. Ex-

emplarily, Figure 9 shows 95 % confidence interval radius of test points' residuals ($\hat{v}_x$, $\hat{v}_y$ and $\hat{v}_z$) in 10,000 repetitions. As expected, the estimated points are concentrated in the center, which is reflected by the small radius of 95 % confidence interval (at the level of 10^{-6}). The approximation becomes inaccurate at the edges since the radius surges up to 10^{-4} level, which has to be related both to the angle uncertainties contribution and the larger variances due to the lack of neighbouring points. The same behaviour holds true for the estimated deformation.

4.2 Congruency test for the case of zero deformation

In the congruency test, the rejection rate depends on the value of the test statistics T (see (24)) and, thus, on the quantities $\hat{\Delta}$ and $\Sigma_{\hat{\Delta}\hat{\Delta}}$. The reason for the different rejection rates in case of zero deformation, found in Figure 5, are to be searched for in the structure of the VCMs themselves.

The standard deviation of the estimated deformation for each point $\sigma_{\hat{\Delta}}$ is derived as

$$\sigma_{\hat{\Delta}} = \sqrt{\sigma_\alpha^2 + \sigma_\beta^2 + \sigma_\gamma^2} \tag{34}$$

where σ_α^2, σ_β^2 and σ_γ^2 are eigenvalues of the VCM for each test point. Figure 10 shows the standard deviation of the estimated deformation, i. e. $\sigma_{\hat{\Delta}_{ref}}$ (red curve), $\sigma_{\hat{\Delta}_{diag}}$ (blue curve) and $\sigma_{\hat{\Delta}_{iden}}$ (green curve), which are correspondingly obtained with three VCM models (see (31), (32), (33)). The red and blue curves have a similar shape, i. e. smaller values in the center part increasing on both edges, the blue one having lower magnitudes than the red one, i. e. accounting for correlations is similar to increasing the variance. The green curve, different from the other two, keeps a fluctuation in a steady range around $(3 \sim 5) \times 10^{-4}$ in most regions ($-8.85 \leq X(Y) < 8.85$). That is due to the initial assumption of homoscedasticity, i. e. all measurements have
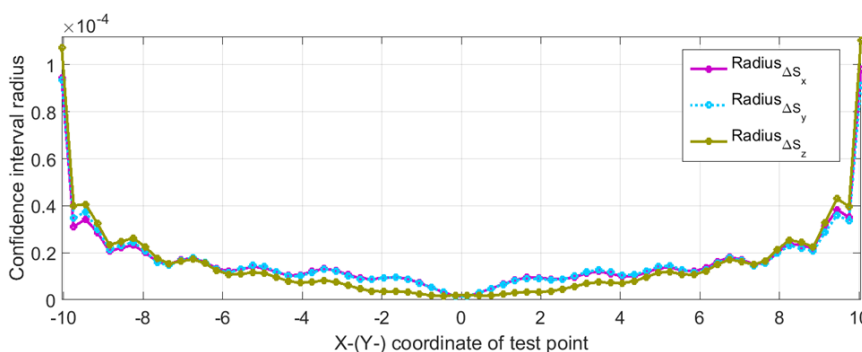

Figure 9: The radius 95 % confidence interval of residuals in terms of $\Delta_{\hat{S}_x}$, $\Delta_{\hat{S}_y}$ and $\Delta_{\hat{S}_z}$.
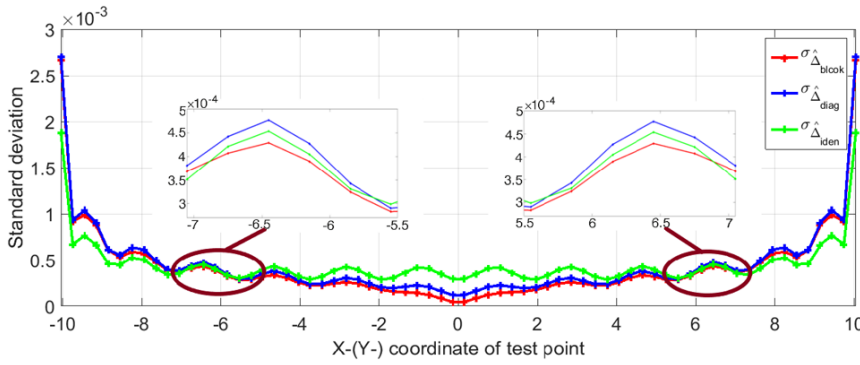
Figure 10: Standard deviation of the deformation estimated by the three VCMs.

equal accuracy. It surges to 1.9×10^{-3} at the edges due to the aforementioned border influence of the approximation.

The difference of the rejection rate shown in Figure 5 can be thus attributed to the heteroscedasticity of the TLS measurements and the impact of the mathematical correlations.

4.3 Congruency test for the case of deformation

The statistics T in case of deformation do not only depend on $\Sigma_{\hat{\Delta}\hat{\Delta}}$ but also on the deformation magnitudes $\hat{\Delta}$ (see (24)).

When the magnitude of deformation is strong enough, for example, in the centre part of case II and III, a large T is obtained, i. e. a high rejection rate is independent of the VCMs chosen in the approximation. However, the VCM plays a dominant role in determining T for smaller deformation magnitudes (case I). Thus, neglecting the heteroscedasticity and mathematical correlation leads to different rejection rates.

As the deformation decreases toward both edges, T decreases as the impact of mathematical correlations increases (see (28)). This corresponds to an increase of the heteroscedasticity, i. e. a less favorable geometry. Thus, the effect of heteroscedasticity and mathematical correlation of VCMs are non-negligible in this region.

Indeed, taking a closer look at Figure 7, the turning points ($X(Y) = \pm 2.55$) can be identified, where the variance increase due to heteroscedasticity is not strong enough to compensate for the impact of neglecting the mathematical correlations. This effect was shown in Section 4.2 leading to an inflations factor on the rejection rate (see Figure 5 blue and red curves). Consequently, it remains indispensable to account for mathematical correlations for deformations with small magnitudes, particularly under un-

favourable scanning conditions with increasing incidence angles. Additionally, homoscedasticity is a bad alternative. The rejection rate with Σ_{iden} increases at the edge regarding Σ_{ref} and Σ_{diag} due to the non-consideration of the uncertainty changes due to the geometry, i. e. larger range and incidence angles, and indicate lower rejection rates when the deformation magnitude is small, due to both the homoscedasticity assumption and the neglection of mathematical correlations.

The ratio of the estimated deformation to its standard deviation $R = \hat{\Delta}_{iden}/\sigma_{\hat{\Delta}_{iden}}$ also provides an indication of the points that are not influenced by simplification of the VCM. In all the cases, the points with R larger than 2.2 have not been influenced by the homoscedastic VCM, as shown in Figure 11. However, improving the stochastic model by means of taking heteroscedasticity and mathematical correlations into account becomes increasingly important when the ratio is lower than the threshold. Since the measurements are considered as equal accurate in most cases, which is actually untrue, this threshold of ratio helps to fix the appropriate scope for applying the homoscedastic VCM.

5 Conclusion

In the B-splines approximation geometry-based method which is used to detect deformations of objects scanned with TLS, both the functional as well as the stochastic model impacts the power of the congruency test. This test is proposed by Pelzer [36] and is normally used to judge whether the differences of two approximations between two epochs are significant or not.

When the powerful B-splines approximation is used, the Cartesian coordinates of the control points can be estimated by LS adjustment. Because the raw measurements of TLS consist of range and angles, mathematical correla-
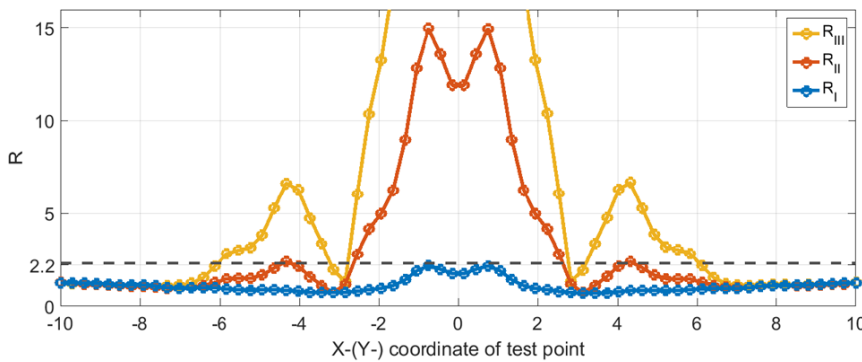
Figure 11: Ratio of the estimated deformation to its standard deviation in the three cases.

tions have to be considered when specifying the stochastic model of the observations. They are, however, mostly neglected and the transformed Cartesian coordinates are simply considered as being independent with equal accuracy.

In this contribution, we aimed to highlight the risk of not accounting for this specific type of correlations, by simultaneously showing the impact of heteroscedasticity on the results of the congruency test for deformation analysis. Monte Carlo simulations were used since both the reference surfaces of the two epochs and their stochastic properties have been known exactly. The model selection procedures were employed to guarantee the adequacy of the functional model. The VCM was gradually misspecified, neglecting in a first step mathematical correlations and assuming homoscedasticity in a second one. The stochastic characters of points contribute to different rejection rates in the congruency test for zero-deformation. The most popular identity VCM, which assumes all measurements as independent with equal accuracy, leads to higher rejection rates on the edges due to underestimating the points position errors. Diagonal VCM with specified variances is better, however, it induces higher rejection rates, especially under unfavourable geometries. Indeed, in the congruency test for deformation case, when the differences between two epochs are large enough to play the dominant role in test statistics, the effect of a misspecified stochastic model is insignificant. However, the stochastic models become increasingly important when the deformation magnitudes decrease. Consequently, although it is tempting to reduce the computational burden, the effect of mathematical correlations and heteroscedasticity should not be underestimated in the deformation analysis using B-splines modelization and congruency tests. The ratio of the estimated difference to its standard deviation helps to judge whether the simplified VCM is able to offer the reliable results in deformation analysis.

It can be concluded that, according to our simulation example, the simplification of the stochastic model has a significant impact on the B-spline-based deformation analysis, especially in the smaller deformation area with larger uncertainties. The variance inflation factor remains to be studied in more detail to potentially simplify the fully populated VCM into diagonal matrices when congruency tests are employed.

References

[1] Alkhatib, H., Kargoll, B., Paffenholz, J., and Bureick, J. Terrestrial laser scanning for deformation monitoring. In *Proceedings of the XXVI FIG congress* (Istanbul, Turkey, 6–11 May, 2018).

[2] Alkhatib, H., Neumann, I., and Kutterer, H. Uncertainty modeling of random and systematic errors by means of Monte-Carlo and fuzzy techniques. *J. Appl. Geod. 3*, 2 (2009), 67–79.

[3] Baselga, S., García-Asenjo, L., and Garrigues, P. Deformation monitoring and the maximum number of stable points method. *Measurement 70* (2015), 27–35.

[4] Bureick, J., Alkhatib, H., and Neumann, I. Robust spatial approximation of laser scanner point clouds by means of free-form curve approaches in deformation analysis. *J. Appl. Geod. 10*, 1 (2016), 27–35.

[5] Bureick, J., Neuner, H., Harmening, C., and Neumann, I. Curve and surface approximation of 3D point clouds. *avn. 123*, 11–12 (2016), 315–327.

[6] Denli, H. H., and Deniz, R. Global congruency test methods for GPS networks. *J. Surv. Eng. 129*, 3 (2003), 95–98.

[7] Farin, G. From conics to NURBS: A tutorial and survey. *IEEE Comput. Graph. 12*, 5 (1992), 78–86.

[8] Girardeau-Montaut, D., Roux, M., Marc, R., and Thibault, G. Change detection on points cloud data acquired with a ground laser scanner. *ISPRS J. Photogramm. Remote Sens. 36*, part 3 (2005), 30–35.

[9] Gotthardt, E. Die Auswirkung unrichtiger Annahmen über Gewichte und Korrelationen auf die Genauigkeit von Ausgleichungen. *Z. Vermess. 87* (1962), 65–68.

[10] HARMENING, C., AND NEUNER, H. A constraint-based parameterization technique for B-spline surfaces. *J. Appl. Geod. 9*, 3 (2015), 143–161.

[11] HOFFMANN, M., LI, Y., AND WANG, G. Paths of C-Bézier and CB-spline curves. *Comput. Aided Geom. Des. 23*, 5 (2006), 463–475.

[12] HOLST, C., AND KUHLMANN, H. Challenges and present fields of action at laser scanner based deformation analyses. *J. Appl. Geod. 10*, 1 (2016), 17–25.

[13] HOLST, C., NOTHNAGEL, A., BLOME, M., BECKER, P., EICHBORN, M., AND KUHLMANN, H. Improved area-based deformation analysis of a radio telescopes main reflector based on terrestrial laser scanning. *J. Appl. Geod. 9*, 1 (2015), 1–14.

[14] JCGM. *Uncertainty of measurement–Part 3: Guide to the expression of uncertainty in measurement (GUM:1995 with minor corrections)*. 2008.

[15] JUREK, T., KUHLMANN, H., AND HOLST, C. Impact of spatial correlations on the surface estimation based on terrestrial laser scanning. *J. Appl. Geod. 11*, 3 (2017), 143–155.

[16] KARGOLL, B. *On the theory and application of model misspecification tests in geodesy*. PhD thesis, Deutsche Geodätische Kommission, 2012.

[17] KAUKER, S., AND SCHWIEGER, V. A synthetic covariance matrix for monitoring by terrestrial laser scanning. *J. Appl. Geod. 11*, 2 (2017), 77–87.

[18] KERMARREC, G., AND SCHÖN, S. Taking correlations in GPS least squares adjustments into account with a diagonal covariance matrix. *J. Geod. 90*, 9 (2016), 793–805.

[19] KERMARREC, G., AND SCHÖN, S. A priori fully populated covariance matrices in least-squares adjustment-case study: GPS relative positioning. *J. Geod. 91*, 5 (2017), 465–484.

[20] KOCH, K.-R. *Introduction to Bayesian Statistics*. Springer Science & Business Media, 2007.

[21] KOCH, K.-R. Determining uncertainties of correlated measurements by Monte-Carlo simulations applied to laserscanning. *J. Appl. Geod. 2*, 3 (2008), 139–147.

[22] KOCH, K.-R. Evaluation of uncertainties in measurements by Monte-Carlo simulations with an application for laserscanning. *J. Appl. Geod. 2*, 2 (2008), 67–77.

[23] KOCH, K.-R. NURBS surface with changing shape. *avn. 117* (2010), 83–89.

[24] KOCH, K.-R. *Parameter Estimation and Hypothesis Testing in Linear Models*. Springer Science & Business Media, 2013.

[25] LAGUE, D., BRODU, N., AND LEROUX, J. Accurate 3D comparison of complex topography with terrestrial laser scanner: Application to the Rangitikei canyon (N-Z). *ISPRS J. Photogramm. Remote Sens. 82* (2013), 10–26.

[26] LEHMANN, R., AND LÖSLER, M. Congruence analysis of geodetic networks-hypothesis tests versus model selection by information criteria. *J. Appl. Geod. 11*, 4 (2017), 271–283.

[27] LINDENBERGH, R., AND PFEIFER, N. A statistical deformation analysis of two epochs of terrestrial laser data of a lock. In *Proceedings of the 7th Conference on Optical 3D Measurement Techniques* (Vienna, Austria, 3–5 October 2005).

[28] LINKWITZ, K. Über den Einfluß verschiedener Gewichtsannahmen auf das Ausgleichsergebnis bei bedingten Beobachtungen. *Z. Vermess. 86* (1961), 179–186.

[29] MEAGHER, D. J. *Octree encoding: A new technique for the representation, manipulation and display of arbitrary 3D objects by computer*. Tech. Rep. IPL-TR-80-111, Rensselaer Polytechnic Institute, Image Processing Laboratory, 1980.

[30] NEUMANN, I., AND KUTTERER, H. Congruence tests and outlier detection in deformation analysis with respect to observation imprecision. *J. Appl. Geod. 1*, 1 (2007), 1–7.

[31] NEUMANN, I., AND KUTTERER, H. The probability of type I and type II errors in imprecise hypothesis testing with an application to geodetic deformation analysis. *Int. J. Reliab. Saf. 3*, 1–3 (2009), 286–306.

[32] NEUNER, H., SCHMITT, C., AND NEUMANN, I. Zur Bestimmung der verkehrsseitig verursachten Dehnung an einem Brückentragwerk mittels terrestrischem Laserscanning. In *A. Wieser (ed.): Ingenieurvermessung' 14. Beiträge zum 17. Internationalen Ingenieurvermessungskurs* (Zürich, Switzerland, 2014).

[33] NIEMEIER, W. Statistical tests for detecting movements in repeatedly measured geodetic networks. *Tectonophysics 71*, 1–4 (1981), 335–351.

[34] NIEMEIER, W. *Ausgleichungsrechnung: Statistische Auswertemethoden*. Walter de Gruyter, 2008.

[35] OHLMANN-LAUBER, J., AND SCHÄFER, T. Ansätze zur Ableitung von Deformationen aus TLS-Daten. In *DVW Seminal Terrestrisches Laserscanning-TLS 2011 mit TLS-Challenge* (Fulda, Germany, 2011).

[36] PELZER, H. *Zur Analyse geodatischer Deformations-messungen*. Reihe c, Deutsche Geodätische Kommission, 1971.

[37] PIEGL, L., AND TILLER, W. *The NURBS Book*. Springer Science & Business Media, 2012.

[38] SCHNEIDER, D. Terrestrial laser scanning for area based deformation analysis of towers and water damns. In *Proceedings of 3rd IAG/12th FIG Symposium* (Baden, Austria, 22–24 May, 2006).

[39] SETAN, H., AND SINGH, R. Deformation analysis of a geodetic monitoring network. *Geomatica 55*, 3 (2001), 333–346.

[40] TAŞCCEDIL, L. Analysis of dam deformation measurements with the robust and non-robust methods. *Sci. Res. Essays 5*, 14 (2010), 1770–1779.

[41] TEZA, G., GALGARO, A., ZALTRON, N., AND GENEVOIS, R. Terrestrial laser scanner to detect landslide displacement fields: a new approach. *Int. J. Remote Sens. 28*, 16 (2007), 3425–3446.

[42] TSAKIRI, M., LICHTI, D., AND PFEIFER, N. Terrestrial laser scanning for deformation monitoring. In *Proceedings of 3rd IAG/12th FIG Symposium* (Baden, Austria, 22–24 May, 2006).

[43] VELSINK, H. On the deformation analysis of point fields. *J. Geod. 89*, 11 (2015), 1071–1087.

[44] VEZOČNIK, R., AMBROŽIČ, T., STERLE, O., BILBAN, G., PFEIFER, N., STOPAR, B., ET AL. Use of terrestrial laser scanning technology for long term high precision deformation monitoring. *Sensors 9*, 12 (2009), 9873–9895.

[45] WANG, J. Block-to-point fine registration in terrestrial laser scanning. *Remote Sens. 5*, 12 (2013), 6921–6937.

[46] WOLF, H. Der Einfluss von Gewichtsänderungen auf die Ausgleichungsergebnisse. *Z. Vermess. 86* (1961), 361–362.

[47] WUJANZ, D., BURGER, M., METTENLEITER, M., AND NEITZEL, F. An intensity-based stochastic model for terrestrial laser

scanners. *ISPRS J. Photogramm. Remote Sens. 125* (2017), 146–155.

[48] Xu, P. The effect of incorrect weights on estimating the variance of unit weight. *Stud. Geophys. Geod. 57*, 3 (2013), 339–352.

[49] Xu, X., Kargoll, B., Bureick, J., Yang, H., Alkhatib, H., and Neumann, I. TLS-based profile model analysis of major composite structures with robust B-spline method. *Compos. Struct. 184* (2018), 814–820.

[50] Zhao, X., Alkhatib, H., Kargoll, B., and Neumann, I. Statistical evaluation of the influence of the uncertainty budget on B-spline curve approximation. *J. Appl. Geod. 11*, 4 (2017), 215–230.

[51] Zhao, X., Kargoll, B., Omidalizarandi, M., Xu, X., and Alkhatib, H. Model selection for parametric surfaces approximating 3D point clouds for deformation analysis. *Remote Sens. 10*, 4 (2018), 634.

Paper 2

Xin Zhao*, Hamza Alkhatib, Boris Kargoll, and Ingo Neumann

Statistical evaluation of the influence of the uncertainty budget on B-spline curve approximation

Abstract: In the field of engineering geodesy, terrestrial laser scanning (TLS) has become a popular method for detecting deformations. This paper analyzes the influence of the uncertainty budget on free-form curves modeled by B-splines. Usually, free-form estimation is based on scanning points assumed to have equal accuracies, which is not realistic. Previous findings demonstrate that the residuals still contain random and systematic uncertainties caused by instrumental, object-related and atmospheric influences. In order to guarantee the quality of derived estimates, it is essential to be aware of all uncertainties and their impact on the estimation.

In this paper, a more detailed uncertainty budget is considered, in the context of the "Guide to the Expression of Uncertainty in Measurement" (GUM), which leads to a refined, heteroskedastic variance covariance matrix (VCM) of TLS measurements. Furthermore, the control points of B-spline curves approximating a measured bridge are estimated. Comparisons are made between the estimated B-spline curves using on the one hand a homoskedastic VCM and on the other hand the refined VCM. To assess the statistical significance of the differences displayed by the estimates for the two stochastic models, a nested model misspecification test and a non-nested model selection test are described and applied. The test decisions indicate that the homoskedastic VCM should be replaced by a heteroskedastic VCM in the direction of the suggested VCM. However, the tests also indicate that the considered VCM is still inadequate in light of the given data set and should therefore be improved.

Keywords: Terrestrial laser scanning, deformations, uncertainty budget, GUM, B-spline approximation, Gauss-Markov model, model misspecification test, model selection test

*Corresponding author: Xin Zhao, Geodetic Institute, Leibniz Universität Hannover, Nienburger Str. 1, 30167 Hannover, Germany, e-mail: zhao@gih.uni-hannover.de
Hamza Alkhatib, Boris Kargoll, Ingo Neumann, Geodetic Institute, Leibniz Universität Hannover, Nienburger Str. 1, 30167 Hannover, Germany, e-mails: alkhatib@gih.uni-hannover.de, kargoll@gih.uni-hannover.de, neumann@gih.uni-hannover.de

1 Introduction

In the field of engineering geodesy, terrestrial laser scanning (TLS) has become a popular method for the purpose of detecting deformations and displacements, with three possible measurement modes (1D, 2D and 3D) under various conditions. In this paper, the focus is on the 2D case, in which the laser scanner carries out profile measurements. This kind of measurement is important, e.g., for load tests and deformation analysis of elongated objects such as wind energy turbines, bridges and high rise buildings. To detect the deflection for instance of bridges, the 2D profile mode is chosen, and oftentimes B-Spline estimation is used to increase the accuracy of approximated displacements. In many cases, however, the measurements are considered with equal accuracies, which assumption is not realistic. Indeed, the residuals of free-form curves were found to contain both random and systematic uncertainties caused by instrumental, object-related as well as atmospheric influences [cf. 1]. In order to guarantee the quality of measurements and to obtain realistic analysis results, it is essential to be aware of all uncertainties and their impact on the measurements.

For this reason, the sophisticated consideration of all occurring uncertainties sources is necessary [4]. These sources can be divided into different influencing areas and into different effects (random, systematic) on the result. Some of the earlier accuracy investigations were carried out by Lichti et al. [29], Lichti and Harvey [28], Lichti et al. [27] and Balzani et al. [5]. Calibration and analysis of errors occurring in measurements from pulsed and phase ranging TLS were carried out by Reshetyuk [35] and Schulz [37], respectively. Specifically, axes errors were investigated by Neitzel [31] and Gordon [12]. The influence caused by the incidence angle were investigated by Eling [10], Soudarissanane and Lindenbergh [39], Soudarissanane et al. [40], Zámečníková et al. [43], and Zámečníková et al. [44]. Environmental influences were studied by Hejbudzka et al. [15] and Borah and Voelz

[7]. As for comprehensive evaluation of data quality, Gumus and Erkaya [13] carried out investigations of the positioning accuracy of TLS using 3D models obtained from point cloud data, and Fernández Pareja et al. [11] presented a procedure for assessing the observational quality and estimated uncertainty values of TLS measurements.

Based on the uncertainty budget, a refined VCM for observations is necessary in order to model the impacts of the main error sources on the data quality. Kauker and Schwieger [21] and Harmening et al. [14] developed a procedure for a synthetic covariance matrix based on an elementary error model containing different groups of correlations. Their approach allows for the modeling of correlations both between the different coordinate components of a single laser scanner point and between different points. We take a slightly different approach which is based on The "Guide to the Expression of Uncertainty in Measurement (GUM)" [18, 17].

GUM has been internationally accepted as the standard for the evaluation of uncertainties in measurements [38]. GUM groups the uncertainties according to evaluation method into Type A and Type B instead of random and systematic errors, which make it possible to consider both types of uncertainties as random variables. Type A components are determined by statistical analysis from repeated observations, whereas Type B components are evaluated by other means such as experience, manufacturer's specification and calibration information. Furthermore, the law of propagation of uncertainty is used in linear and linearized models to estimate the output uncertainty. Besides the normal distribution, GUM recommends further types of distributions for the input quantities, e.g. rectangular, triangular and trapezoidal distributions. Koch [24] and Alkhatib and Kutterer [1] presented a method for setting up the combined uncertainty model based on GUM, applying error propagation via Monte Carlo simulation instead of using the law of propagation of uncertainty. Alkhatib et al. [2] applied the GUM to K-TLS vertical profile scans and combined it with a deterministic approach based on fuzzy sets. Alkhatib et al. [3] took a few influence factors into consideration and applied the uncertainty model to B-spline estimation.

In this paper, we analyze an extended uncertainty budget for TLS measurements based on the GUM in the context of bridge measurements in 2D profile mode. This budget will be used to derive covariance matrices for the measured TLS coordinates. These covariance matrices, which are characterized by non-uniform variances (i.e., heteroskedasticity) will serve as a 'refined' stochastic model in approximating the measured bridge profile

by a B-spline curve. In order to obtain a feasible estimation and testing procedure, correlations between coordinate components and between different TLS points are currently neglected. The adjustment results will be compared to the results from an approximation based on a simple homoskedastic model. In order to evaluate the effect of the use of the refined covariance matrix on the adjustment (in comparison to the simple covariance matrix), we propose two different testing procedures. The first procedure, which utilizes a Rao's score test proposed in Kargoll [20], tests the homoskedastic model (as the null hypothesis) against an unspecified multiple of a fully specified diagonal matrix, based on the aforementioned heteroskedastic covariance matrix. The second procedure, which is based on a well-known non-nested testing principle by Cox [9], tests the homoskedastic and the fully specified heteroskedastic model independently against each other. The extension of this estimation and testing procedure to the more realistic scenario of correlated coordinates and points constitutes a formidable task which will be undertaken in future research.

The paper is organized as follows. In Section 2 we summarize typical influence factors affecting TLS measurements in three domains: instrumental, object-related and atmospheric influences. In Section 3, the law of propagation of uncertainties is used to derive a refined, heteroskedastic covariance matrix. The B-spline curve model according to Piegl and Tiller [34] will be briefly outlined in Section 4. The focus of the current contribution lies on the development of the two aforementioned procedures for testing the validity of a specified covariance matrix. Section 5 explains the theory behind these statistical hypothesis tests. Section 6 gives the estimation and testing results with respect to a TLS profile of a bridge, modeled as a B-spline curve.

2 Uncertainty budget

The qualitative and quantitative uncertainty budget of a laser scanner needs to be individually investigated for every instrument and measurement setup. According to the error sources, the uncertainties of TLS measurements can be divided into instrumental, object-related and atmospheric influences. As mentioned above, the Z+F Imager 5006 was used within the current study to obtain the numerical examples. Therefore, the exemplified values of the measurement uncertainties are mostly given for this type of scanner.

Table 1: Uncertainty budget of the instrumental influence for the Z+F Imager 5003 and 5006.

Source of uncertainty	Evaluation	Distribution	Expected value	Standard uncertainty
range noise (Z+F 5006)	type B	normal	variable	$u_r = 0.4$ mm
scale error (Z+F 5003)	type B	normal	1 pm	$u_{k_0} = 0.5$ pm
zero point error (Z+F 5003)	type B	triangular	4 mm	$u_{m_0} = 0.8$ mm
angle noise (Z+F 5006)	type B	normal	variable	$u_\theta = u_\varphi = 7.7$ mgon
resolution for zenith angle (Z+F 5006)	type B	rectangular	1.0 mgon	$u_{\xi_\theta} = 0.6$ mgon
resolution for horizontal angle (Z+F 5006)	type B	rectangular	1.0 mgon	$u_{\xi_\varphi} = 0.6$ mgon
collimation axis error (Z+F 5003)	type B	normal	-37.8 mgon	$u_c = 5.4$ mgon
horizontal axis error (Z+F 5003)	type B	normal	-30.2 mgon	$u_h = 1.9$ mgon
vertical index error (Z+F 5006)	type B	normal	-17.7 mgon	$u_{\xi_v} = 5.3$ mgon

2.1 Instrumental influences

The best way to quantify instrumental influences are calibrations. As no standard for the calibration of TLS systems exists and since the working principle is similar to that of total stations, it seems natural to tentatively use the standard for traditional geodetic instruments, e.g. "Optics and optical instruments – field procedures for testing geodetic and surveying instrument – Part 5: Total stations" [16].

The following error budget in Table 1 for instrumental influences is mainly based on the technical data sheet of Z+F Imager 5006 [46], and some are from the previous calibration result of Z+F Imager 5003. The GUM recommends certain standard types of probability density functions (pdfs) as probabilistic models (e.g., normal, trapezoidal, uniform and triangular pdfs) for input quantities. Following this approach we assign to each influence factor a specific pdf and standard uncertainty according to the following list:

- range noise is assumed as normally distributed [1], the standard uncertainty (u_r) is given by Zoller+Fröhlich [46].
- scale error is assumed as normally distributed [24], both the expected value and standard uncertainties (u_{k_0}) of scale error are according to Gordon [12].
- zero point error is assumed as triangularly distributed [24], both the expected value and standard uncertainty of zero point error (u_{m_0}) are according to Gordon [12].
- angle noise is assumed as normally distributed [1], the standard uncertainties of angle noise (u_θ/u_φ) are given by Zoller+Fröhlich [46].
- resolution for zenith/horizontal angle are assumed as rectangularly distributed [2]. Zoller+Fröhlich [46] indicates the upper-boundary is 2 mgon so that the errors can be assumed to be uniformly distributed on

the interval $[0, 2]$ mgon. The expected values and uncertainty ($u_{\xi_\theta}/u_{\xi_\varphi}$) of angular resolution are calculated according to (2).
- collimation axis error, horizontal axis error and vertical index error are all assumed to be normally distributed, the corresponding expected values and the standard uncertainties ($u_c/u_h/u_{\xi_v}$) are given by Neitzel [31].

The equations for calculating expected values and uncertainties of triangular and rectangular distributions are shown in the following. We have for a triangular distribution [18]

$$E_{\text{tri}} = \frac{a_+ + a_-}{2}$$
$$U_{\text{tri}} = \sqrt{\frac{a^2}{6}} \tag{1}$$

with $a = (a_+ - a_-)/2$, where a_+ and a_- is the upper and the lower bound, respectively.

For the rectangular distribution, the expected values and standard uncertainty are calculated as [18]

$$E_{\text{rec}} = \frac{a_+ + a_-}{2}$$
$$U_{\text{rec}} = \sqrt{\frac{a^2}{3}} \tag{2}$$

The standard uncertainty of the angular resolution, which obeys a rectangular distribution, is calculated as $u_{\xi_\theta} = u_{\xi_\varphi} = 0.6$ mgon. All information of the instrumental errors used for creating the corresponding VCMs are shown in Table 1.

2.2 Object-related influence

The measurement quality does not only depend on the TLS measurements' precision and accuracy. The object proper-

Table 2: Uncertainty budget of atmospheric influence.

Source of uncertainty	Evaluation	Distribution	Expected influence of value	Standard uncertainty
Temperature	type B	normal	1.00 (ppm/ °C)	$u_{\Delta t} = 0.5$ °C
Pressure	type B	normal	0.29 (ppm/hPa)	$u_{\Delta p} = 1$ hPa
Partial water vapor pressure	type B	normal	0.04 (ppm/hPa)	$u_{\Delta e} = 19$ hPa

ties, e.g., the type of material, the surface color, the reflectivity as well as the incidence angle (IA) also significantly influence the data quality.

Mazalová et al. [30] claimed that the color of the target contributes to the uncertainty of a measured distance. However, in the current paper, the influence of color is not considered because it was found to be insignificant in comparison to the whole uncertainty budget of TLS. Zámečníková et al. [43] and Zámečníková et al. [44] investigated the influence of the IA and drew the conclusion that at close ranges of 3.5 m – 5.2 m other influence are more relevant than the IA, while at 30 m, significant influences are detected. However, the stochastic properties of the uncertainty could not be quantified because the reference distances are too noisy. As for the influence of surface reflectivity, Zámečníková et al. [45] assumed that the signal strength depends linearly on the target reflectance, and presented the function of distance uncertainty with respect to distance and signal strength.

Although object-related influences are clearly detected, it is still difficult to model them separately due to the unclear correlation with other influence factors. According to Soudarissanane and Lindenbergh [39], Soudarissanane et al. [40], Zámečníková et al. [43] and Zámečníková et al. [44], the influence of the IA and the range are closely related to each other, but an exact correlation between the two is actually not known. Kauker and Schwieger [22] consider for the object-related component of their synthetic covariance matrix, on the one hand, the IA and the distance between object and scanner as sources of uncertainty. On the other hand, they modeled jointly, as a group of surface-related sources of uncertainty, the influence of color, penetration depth, roughness and reflectivity.

Wujanz et al. [42] proposed an alternative approach to modeling object-related influences, based directly on recorded intensity values. These reflect influences that are caused by the acquisition configuration as well as by interdependencies between the signal and object surface. In other words, the intensity is representative of all the object-related influences as well as of the range noise. Wujanz et al. [42] determined the standard uncertainty u_I of a range, including object-related influences, from the measured in-

tensity through the regression

$$u_I = k_1 \cdot \text{intensity}^{k_2}, \tag{3}$$

where the unknown parameters k_1 and k_2 are estimated via least squares adjustment, resulting in the estimates $k_1 = 1.61715$ and $k_2 = -0.57069$ for the Z+F Imager 5006. Since the uncertainty of the range noise u_r in Table 1 is included in u_I, which also comprises object-related influences, the former is replaced by the latter intensity-based in Section 3.

2.3 Atmospheric influence

The atmosphere also has an influence on the data quality through affecting the propagation speed of electromagnetic waves, which depends mainly on the refractive index, the density of atmospheric layer and the wavelength (see Table 2). Gordon [12] and Kauker and Schwieger [22] have considered the atmospheric influence on the respective covariance matrix. The following compilation of results follows the latter exposition.

The Barrel-Sears formula [6] is recommended by the Association of Geodesy General Assembly to calculate the group index of refraction n_g according to

$$(n_g - 1) \cdot 10^6 = 287.604 + \frac{4.886}{\lambda^2} + \frac{0.068}{\lambda^4} \tag{4}$$

where λ denotes the specific wavelength in micrometers. To calculate the specific atmospheric influence, the standard atmosphere should be reduced to real atmospheric conditions (see Joeckel et al. [19]) by using

$$(n_a - 1) \cdot 10^6 = N_g \cdot \frac{273.15}{1013.25} \cdot \frac{P}{T} - \frac{11.27}{T \cdot e} \tag{5}$$

with $N_g = (n_g - 1) \cdot 10^6$, where T, P, e denote temperature, pressure and partial water vapor pressure, respectively. Based on (5), the total differential can be calculated; Joeckel et al. [19] give the corresponding coefficients of the mean atmosphere for a temperature of 17 °C (T = 290.15 K), a pressure of 1000 hPa and a water vapor pressure of 11 hPa. Finally, the atmospheric influence on distance measurements can be approximated according to Rüeger [36] by

$$\Delta n_a \cdot 10^6 = -1.00 \cdot \Delta t + 0.29 \cdot \Delta p - 0.04 \cdot \Delta e, \tag{6}$$

where Δt, $\triangle p$ and Δe represent, respectively, the changes of temperature, pressure and partial water vapor pressure, compared with the standard atmosphere (at temperature $t = 0$ °C, pressure $p = 1013.25$ hPa, partial water vapor pressure $e = 0$ hPa, and CO_2 content 0.0375% = 375 ppm). Range measurements are corrected by the product of measured range and Δn_a, that is,

$$\xi_A = r \cdot \Delta n_a. \tag{7}$$

The uncertainties of atmospheric corrections are linked to the accuracies of the atmospheric measurements (Δt, Δp, Δe) given by Rüeger [36]. The results are summarized in Table 2, based on the distributions given in ISO [16]. Specifically, $u_{\Delta t}$, $u_{\Delta p}$ and $u_{\Delta e}$ depend on the accuracies of the pocket barometers, the electronic thermistor thermometers and the hygrometer. There are several laser scanners that do not allow one to correct for atmospheric effects. For such scanners, the uncertainties related to the atmosphere are larger, with typical values of $u_{\Delta t} = 20$ °C and $u_{\Delta p} = 20$ hPa.

Based on the equations (4) and (5), the uncertainty u_{ξ_A} caused by atmospheric factors can be calculated as

$$u_{\xi_A}^2 = \mathbf{B}^T \Sigma_{\text{atm}} \mathbf{B} = \mathbf{B}^T \begin{bmatrix} u_{\Delta t}^2 & 0 & 0 \\ 0 & u_{\Delta p}^2 & 0 \\ 0 & 0 & u_{\Delta e}^2 \end{bmatrix} \mathbf{B} \tag{8}$$

with coefficient matrix $\mathbf{B}^T = r[-1.00, 0.29, -0.04]$ and the VCM Σ_{atm} of the atmospheric factors. This model is valid only for short distances, as considered in our current application (see Section 6). We refer to Kauker and Schwieger [21] for an atmospheric model that is generally adequate also for long distances.

3 Uncertainty modeling by means of the law of propagation of uncertainty

After the preceding analysis, the uncertainty budget is summarized for all influence factors. The subsequent steps have the goal to obtain the observations' VCM and weight matrix in order to study the influence of the uncertainty budget on B-Spline curve estimation. To calculate the VCM, the law of propagation of uncertainty [cf. 18, p. 55] is used here.

The geometrical relationships between an observation in polar coordinates (r, θ, φ) and in Cartesian coordinates (X, Y, Z) are given by

$$\begin{bmatrix} X \\ Y \\ Z \end{bmatrix} = r \begin{bmatrix} \sin(\theta)\cos(\varphi) \\ \sin(\theta)\sin(\varphi) \\ \cos(\theta) \end{bmatrix}, \tag{9}$$

where r is the measured range, φ the measured horizontal rotation angle and θ the measured vertical rotation angle.

According to the influences studied in Section 2, corrections should be added respectively to r, θ and φ, which corrections influence the Cartesian coordinates by means of the law of propagation of uncertainty. The corrected formulas read

$$X = (r(1 + k_0) + m_0 + \xi_A)\sin(\theta + \xi_\theta + \xi_v)$$
$$\times \cos(\varphi + \xi_\varphi + c/\sin\theta + h\cot\theta) \tag{10}$$

$$Y = (r(1 + k_0) + m_0 + \xi_A)\sin(\theta + \xi_\theta + \xi_v)$$
$$\times \sin(\varphi + \xi_\varphi + c/\sin\theta + h\cot\theta), \tag{11}$$

$$Z = (r(1 + k_0) + m_0 + \xi_A)\cos(\theta + \xi_\theta + \xi_v), \tag{12}$$

The components are defined as follows:

k_0 ... scale factor

m_0 ... zero point error

ξ_φ ... horizontal resolution

ξ_θ ... vertical resolution

c ... collimation axis error

h ... horizontal axis error

ξ_v ... vertical index error

ξ_A ... atmospheric influence on distance measurements

A 3×3 covariance matrix Σ_{p_k}, which reflects the uncertainty of one measurement point (X_k, Y_k, Z_k), can be determined for every $k = 1, 2, \ldots, N$ (with N the number of measured points) by means of the law of propagation of uncertainty as

$$\Sigma_{p_k} = \mathbf{F}_k^T \Sigma_{\text{fac}.k} \mathbf{F}_k = \begin{bmatrix} u_{X_k}^2 & u_{X_k Y_k} & u_{X_k Z_k} \\ u_{Y_k X_k} & u_{Y_k}^2 & u_{Y_k Z_k} \\ u_{Z_k X_k} & u_{Z_k Y_k} & u_{Z_k}^2 \end{bmatrix}, \tag{13}$$

where $\mathbf{F}_k$ is the Jacobian matrix containing the derivatives of (X_k, Y_k, Z_k) with respect to the influence factors and where

$$\Sigma_{\text{fac}.k} = \begin{bmatrix} u_{l_k}^2 & & & & & & & & & & \\ & u_{k_{0_k}}^2 & & & & & & & & & \\ & & u_{m_{0_k}}^2 & & & & & & & & \\ & & & u_{\theta_k}^2 & & & & & & & \\ & & & & u_{\varphi_k}^2 & & & & & & \\ & & & & & u_{\xi_{\theta_k}}^2 & & & & & \\ & & & & & & u_{\xi_{\varphi_k}}^2 & & & & \\ & & & & & & & u_{c_k}^2 & & & \\ & & & & & & & & u_{h_k}^2 & \\ & & & & & & & & & u_{\xi_A}^2 \end{bmatrix} \tag{14}$$

denotes the VCM of the influence factors. Because the range noise is considered together with the object-related influences (see Section 2), the intensity-based uncertainty u_I is used in the calculations instead of the range noise u_r in Table 1.

Based on equation (7), the standard uncertainty for one point in 3D is obtained. This procedure yields then the uncertainty of the entire point cloud.

4 B-spline curve approximation

In light of their flexibility, accuracy, numerical stability and structural simplicity, B-spline curves are popular functions for approximating point clouds of geometrically intricate objects, as well as for detecting (partly changing) deformations and displacements of such objects. Former applications to TLS in engineering geodesy have shown that residuals resulting from B-spline curve approximations still contain random and systematic effects [3], arising from the sensor itself, from the surface structure of the object, from the model, as well as from the environment. These effects occur due to the lack of stochastic and uncertainty information for the observations when B-Spline estimation is carried out by means of the least squares method. In this paper, such information will be included in the estimation of B-splines via a refined VCM or weight matrix based on the uncertainty budget stated in the previous two sections.

The setup of the B-Spline model largely follows the description given by Piegl and Tiller [34] [see also 25, 8, for further explanations and details]. Although we focus in the sequel on the use of B-spline curves, an extension to surfaces would be straightforward [cf. 26, for a detailed description of B-spline surfaces]. The basic idea is to view the set of three-dimensional points on some curve as values $X(\bar{u})$, $Y(\bar{u})$ and $Z(\bar{u})$ of real-valued functions X, Y and Z on some interval (commonly taken to be the unit interval $[0,1]$). These coordinate functions are usually parametrized with respect to given basis functions $f_0, \dots, f_n$ having properties that are beneficial to the tasks of geometrical approximation and numerical computation. Then, each point is represented by a row vector

$$
\begin{aligned}
\mathbf{C}(\bar{u}) &= [X(\bar{u})\ Y(\bar{u})\ Z(\bar{u})] \\
&= \left[\sum_{i=0}^{n} f_i(\bar{u}) P_{i,X} \quad \sum_{i=0}^{n} f_i(\bar{u}) P_{i,Y} \quad \sum_{i=0}^{n} f_i(\bar{u}) P_{i,Z} \right] \\
&= \sum_{i=0}^{n} f_i(\bar{u}) \mathbf{P}_i,
\end{aligned} \tag{15}
$$

where $\mathbf{P}_i = [P_{i,X}\ P_{i,Y}\ P_{i,Z}]$ is the vector of component-

dependent (usually unknown) coefficients with respect to the i-th basis function. The employment of power functions $u^0, \dots, u^n$ or Bernstein polynomials $B_{0,p}, \dots, B_{n,p}$ as basis functions yields a globally defined Bézier curve. However, more suitable for our purposes are the p-th degree basis (B-)splines $N_{0,p}, \dots, N_{n,p}$, which are defined piecewise on the interval $[0,1]$, so that the resulting B-spline curve adapts to geometrically varying objects in a highly flexible manner. The B-spline coefficients $\mathbf{P}_0, \dots, \mathbf{P}_n$, which are often called *control points* or *de Boor points*, constitute 3D points themselves. Thus, any point $[X(\bar{u})\ Y(\bar{u})\ Z(\bar{u})]$ on a B-spline curve may be viewed as a linear combination of the control points. The basis functions can be evaluated (for every $i \in \{0, \dots, n\}$ and any $\bar{u} \in [0,1]$) by the *Cox-de Boor recursion formulas* [cf. 34, Chapter 2]

$$
N_{i,0}(\bar{u}) = \begin{cases} 1, & \text{if } u_i \le \bar{u} \le u_{i+1} \\ 0, & \text{otherwise} \end{cases} \tag{16}
$$

$$
N_{i,p}(\bar{u}) = \frac{\bar{u} - u_i}{u_{i+p} - u_i} N_{i,p-1}(\bar{u}) + \frac{u_{i+p+1} - \bar{u}}{u_{i+p+1} - u_{i+1}} N_{i+1,p-1}(\bar{u}), \tag{17}
$$

which involve $m + 1$ so-called *knots* $u_0, \dots, u_m$, where m is taken to be $m = n + p + 1$. One approach of defining these knots is based on the equations

$$
\begin{cases} u_0 = \dots = u_p = 0, \\ u_{p+j} = (1-k)\bar{u}_{i-1} + k\bar{u}_i & (j = 1, 2, \dots, n-p), \\ u_{n+1} = \dots = u_m = 1 \end{cases} \tag{18}
$$

with $i = \text{int}(jd)$, $k = jd - i$ and $d = \frac{m+1}{n-p+1}$ [cf. 34, p. 412]. The knots then give rise to the *knot vector* $\mathbf{U} = [0, \dots, 0, u_{p+1}, \dots, u_{m-p-1}, 1, \dots, 1]^T$.

Given N measured points $[X_1\ Y_1\ Z_1], \dots, [Y_N\ Y_N\ Z_N]$, we may form the observation matrix

$$
\mathbf{l} = \begin{bmatrix} \mathbf{l}_1 \\ \vdots \\ \mathbf{l}_N \end{bmatrix} = \begin{bmatrix} X_1 & Y_1 & Z_1 \\ \vdots & \vdots & \vdots \\ X_N & Y_N & Z_N \end{bmatrix}. \tag{19}
$$

The addition of a corresponding matrix of suitable residuals $\mathbf{v}$ to the observation matrix yields the adjusted observations, which can be represented by the functional B-spline model. This identification of the model with the (adjusted) observations requires that the individual B-splines are evaluated for the N 'locations' $\bar{u}_1, \dots, \bar{u}_N$ (in $[0,1]$) associated with the measured points. We determine these *location parameters* according to the standard method of *chord length*, setting [cf. 34, Section 9.2]

$$
\bar{u}_k = \begin{cases} 0 & \text{if } k = 1 \\ \bar{u}_{k-1} + \dfrac{\sqrt{(\mathbf{l}_k - \mathbf{l}_{k-1})^T (\mathbf{l}_k - \mathbf{l}_{k-1})}}{\sum_{j=2}^{N} \sqrt{(\mathbf{l}_j - \mathbf{l}_{j-1})^T (\mathbf{l}_j - \mathbf{l}_{j-1})}} & \text{if } k \ge 2, \end{cases} \tag{20}
$$

which gives for the last location parameter $\bar{u}_N = 1$. These evaluations turn (15) into the N observation equations

$$\mathbf{l}_k + \mathbf{v}_k = \mathbf{C}(\bar{u}_k) = \sum_{i=0}^{n} N_{i,p}(\bar{u}_k)\mathbf{P}_i, \qquad (21)$$

which we write jointly in the form $\mathbf{l} + \mathbf{v} = \mathbf{A}\mathbf{x}$ with design matrix

$$\mathbf{A} = \begin{bmatrix} N_{0,p}(\bar{u}_1) & \cdots & N_{n,p}(\bar{u}_1) \\ \vdots & & \vdots \\ N_{0,p}(\bar{u}_N) & \cdots & N_{n,p}(\bar{u}_N) \end{bmatrix} \qquad (22)$$

and unknown parameter matrix

$$\mathbf{x} = \begin{bmatrix} \mathbf{P}_0 \\ \vdots \\ \mathbf{P}_n \end{bmatrix} = \begin{bmatrix} P_{0,X} & P_{0,Y} & P_{0,Z} \\ \vdots & \vdots & \\ P_{n,X} & P_{n,Y} & P_{n,Z} \end{bmatrix} \qquad (23)$$

We see now that (19)–(23) form the observation equations of a multivariate Gauss-Markov model [cf. 23, Section 3.7], for which the least-squares estimates of the unknown parameters $\mathbf{x}$ are readily obtained. If the X-, the Y- and the Z-components of the measured points are all mutually uncorrelated, then the multivariate model can be adjusted by separately adjusting the three univariate Gauss-Markov models that arise by considering only one particular column of $\mathbf{l}$ and the corresponding column within $\mathbf{x}$. This means that the data for each of the measured coordinate components determines the estimates for the corresponding coordinate component of the control points, independently of the other coordinate components. The separation of the models implies also that component-wise adjustments are possible even in case the measured X-, Y- and Z-coordinates have different covariance matrices Σ_X, Σ_Y and Σ_Z, as long as their inverses are used as metrics in the formation of the corresponding normal equations, that is, in the solution for the X-component

$$\begin{bmatrix} \hat{P}_{0,X} \\ \vdots \\ \hat{P}_{n,X} \end{bmatrix} = (\mathbf{A}^T\Sigma_X^{-1}\mathbf{A})^{-1}\mathbf{A}^T\Sigma_X^{-1} \begin{bmatrix} X_1 \\ \vdots \\ X_N \end{bmatrix}, \qquad (24)$$

the solution for the Y-component

$$\begin{bmatrix} \hat{P}_{0,Y} \\ \vdots \\ \hat{P}_{n,Y} \end{bmatrix} = (\mathbf{A}^T\Sigma_Y^{-1}\mathbf{A})^{-1}\mathbf{A}^T\Sigma_Y^{-1} \begin{bmatrix} Y_1 \\ \vdots \\ Y_N \end{bmatrix}, \qquad (25)$$

and the solution for the Z-component

$$\begin{bmatrix} \hat{P}_{0,Z} \\ \vdots \\ \hat{P}_{n,Z} \end{bmatrix} = (\mathbf{A}^T\Sigma_Z^{-1}\mathbf{A})^{-1}\mathbf{A}^T\Sigma_Z^{-1} \begin{bmatrix} Z_1 \\ \vdots \\ Z_N \end{bmatrix}. \qquad (26)$$

5 Testing for heteroskedasticity

We will now outline two different approaches to testing the validity of the covariance matrix of a linear Gauss-Markov model with generic observation equations $\mathbf{l} + \mathbf{v} = \mathbf{A}\mathbf{x}$, where $\mathbf{A}$ is an $(n \times m)$-matrix of full rank. As a basic reference, we will consider a simple stochastic model in the form of a homoskedastic covariance matrix

$$\Sigma_0 = \sigma^2\mathbf{I} \qquad (27)$$

with generally unknown variance factor σ^2. Furthermore, we assume that the vector of observables follows a multivariate normal distribution.

5.1 A nested test for heteroskedasticity

The first testing approach addresses the question whether a given data set provides sufficient evidence for rejecting the simple, homoskedastic structure (27) in favor of some heteroskedastic diagonal matrix

$$\Sigma = \sigma^2\mathbf{I} + \gamma\mathbf{V}, \qquad (28)$$

where σ^2 and γ are treated as unknown parameters and where $\mathbf{V}$ constitutes a given, non-negative diagonal matrix; thus, the i-th variance can be written as the sum

$$\sigma_i^2 = \sigma^2 + \gamma V_{ii}. \qquad (29)$$

The additive form (28) represents a possible decomposition of an arbitrary diagonal covariance matrix

$$\Sigma = \mathrm{diag}(\sigma_1^2, \ldots, \sigma_n^2), \qquad (30)$$

where σ^2 is chosen to be the least variance within Σ.

Under the null hypothesis $H_0 : \gamma = 0$, Σ reduces to the homoskedastic covariance matrix (27), whereas the alternative $H_1 : \gamma > 0$ imposes a heteroskedastic structure onto $\sigma^2\mathbf{I}$ according to the fully specified diagonal matrix $\mathbf{V}$. Evidently, the homoskedastic model under H_0 represents a special case of the heteroskedastic model (28) under H_1, so that the former is nested into the latter. Under the initial normality assumption, a reasonable and computationally convenient test statistic can be based on Rao's score. More specifically, due to the assumed uncorrelatedness of the observables, the log-likelihood function can be written in the form

$$L(\mathbf{x}, \sigma^2, \gamma; \mathbf{l}) = \ln \prod_{i=1}^{n} \frac{1}{\sqrt{2\pi\sigma_i^2}} \exp\left\{ -\frac{1}{2}\left(\frac{\mathbf{A}_i\mathbf{x} - l_i}{\sigma_i}\right)^2 \right\}$$

$$= -\frac{n}{2}\ln(2\pi) - \frac{1}{2}\sum_{i=1}^{n}\ln(\sigma^2 + \gamma V_{ii})$$

$$- \frac{1}{2}\sum_{i=1}^{n}\frac{(\mathbf{A}_i\mathbf{x} - l_i)^2}{\sigma^2 + \gamma V_{ii}}. \tag{31}$$

Introducing then for brevity of expressions the $(n \times 1)$-vectors $\mathbf{1} = [1 \cdots 1]^T$,

$$\hat{\mathbf{v}} = \begin{bmatrix} \hat{v}_1 \\ \vdots \\ \hat{v}_n \end{bmatrix} = \begin{bmatrix} \mathbf{A}_1\hat{\mathbf{x}} - l_1 \\ \vdots \\ \mathbf{A}_n\hat{\mathbf{x}} - l_n \end{bmatrix}$$

and

$$\bar{\mathbf{v}} = \begin{bmatrix} \bar{v}_1 \\ \vdots \\ \bar{v}_n \end{bmatrix} = \begin{bmatrix} (\hat{v}_1/\hat{\sigma})^2 - 1 \\ \vdots \\ (\hat{v}_n/\hat{\sigma})^2 - 1 \end{bmatrix}$$

based on the restricted maximum likelihood estimates $\hat{\mathbf{x}}$, $\hat{\sigma}^2 = \hat{\mathbf{v}}'\hat{\mathbf{v}}/n$ and $\hat{\gamma} = 0$, Rao's score statistic reads

$$T_{RS} = \frac{1}{2}\bar{\mathbf{v}}'\mathbf{V}\mathbf{1}\left(\mathbf{1}'\mathbf{V}\left[\mathbf{I} - \mathbf{1}(\mathbf{1}'\mathbf{1})^{-1}\mathbf{1}'\right]\mathbf{V}\mathbf{1}\right)^{-1}\mathbf{1}'\mathbf{V}\bar{\mathbf{v}} \tag{32}$$

and approximates a chi-square distribution with one degree of freedom (χ_1^2) for large numbers n of observations [cf. 20, Section 4.3]. As the test is one-sided, the null hypothesis of homoskedasticity is rejected if the test statistic takes a value larger than the critical value $k_{1-\alpha}^{\chi_1^2}$, where α is the preset probability of committing a type-I error. In view of the design of the test, this event is likely to happen if the prescribed diagonal structure in $\mathbf{V}$ (and thus in Σ) is reflected by the given data.

5.2 A non-nested discrimination test of stochastic models

In case a heteroskedastic covariance matrix Σ is fully specified (as described in Section 3), it is actually neither necessary to nest the null hypothesis (27) inside the refined model (28), nor to treat σ^2 and γ as unknown parameters. For instance, we may specify σ^2 to be the least variance of the heteroskedastic covariance matrix Σ (which fixes $\sigma^2\mathbf{I}$) and choose nonnegative numbers in $\gamma\mathbf{V}$ in such a way that Σ is obtained. Instead of testing (27) versus (28), we can therefore alternatively perform a model selection test where the first model is based on the covariance matrix (27) and the second model on the specified diagonal, heteroskedastic covariance matrix Σ (without introducing a parameter γ for the purpose of nesting decomposition). The simple model describes the observables by means of

the log-likelihood function

$$L_0(\mathbf{x}, \sigma^2; \mathbf{l}) = \ln\prod_{i=1}^{n}\frac{1}{\sqrt{2\pi\sigma^2}}\exp\left\{-\frac{1}{2}\left(\frac{\mathbf{A}_i\mathbf{x} - l_i}{\sigma}\right)^2\right\}$$

$$= -\frac{n}{2}\ln(2\pi) - \frac{n}{2}\ln(\sigma^2) - \frac{1}{2}\sum_{i=1}^{n}\frac{(\mathbf{A}_i\mathbf{x} - l_i)^2}{\sigma^2} \tag{33}$$

with unknown parameters $\boldsymbol{\theta}_0 = [\mathbf{x}; \sigma^2]$, and the refined model is based on the log-likelihood function

$$L_1(\mathbf{x}; \mathbf{l}) = \ln\prod_{i=1}^{n}\frac{1}{\sqrt{2\pi\sigma_i^2}}\exp\left\{-\frac{1}{2}\left(\frac{\mathbf{A}_i\mathbf{x} - l_i}{\sigma_i}\right)^2\right\}$$

$$= -\frac{n}{2}\ln(2\pi) - \frac{1}{2}\sum_{i=1}^{n}\ln(\sigma_i^2) - \frac{1}{2}\sum_{i=1}^{n}\frac{(\mathbf{A}_i\mathbf{x} - l_i)^2}{\sigma_i^2} \tag{34}$$

with unknowns $\boldsymbol{\theta}_1 = \mathbf{x}$. Clearly, the unknown functional parameters $\mathbf{x}$ are finite (real) numbers, and the variance within the simple model is assumed to satisfy $\sigma^2 > 0$ as usual, so that all of the occurring parameters are interior points of the corresponding parameter spaces $\Theta_0 = \mathbb{R}^{n+1} \times \mathbb{R}_+$ and $\Theta_1 = \mathbb{R}^{n+1}$. Furthermore, the homoskedastic covariance matrix Σ_0 and the heteroskedastic covariance matrix Σ are numerically different, so that the observables are modeled by different sets of multivariate normal distributions. Therefore, both distribution sets are non-nested in the sense that none of the distributions of either set constitutes a special case of the other set. Under the previous assumptions, the logarithmized likelihood ratio

$$L_{0,1} = L_0(\hat{\mathbf{x}}, \hat{\sigma}^2; \mathbf{l}) - L_1(\tilde{\mathbf{x}}; \mathbf{l}) \tag{35}$$

$$= -\frac{n}{2}\ln(\hat{\sigma}^2) + \frac{1}{2}\sum_{i=1}^{n}\ln(\sigma_i^2) - \frac{1}{2}\sum_{i=1}^{n}\frac{(\mathbf{A}_i\hat{\mathbf{x}} - l_i)^2}{\hat{\sigma}^2}$$

$$+ \frac{1}{2}\sum_{i=1}^{n}\frac{(\mathbf{A}_i\tilde{\mathbf{x}} - l_i)^2}{\sigma_i^2} \tag{36}$$

can be used to test the adequacy of the simple model against the refined model [see the equations (15) and (46) in 9]. Here, the maximum likelihood estimates $\hat{\mathbf{x}}$, $\hat{\sigma}^2$ and $\tilde{\mathbf{x}}$ may be obtained via least-squares adjustments [see Section 3.2.4 23]. According to Cox [9, see the sections 8 and 9], the quantity $L_{0,1}$ approximately follows a normal distribution

(i) with expectation $\mu_{\hat{\theta}_0}$ and standard deviation $\sigma_{\hat{\theta}_0}$ if the homoskedastic model is true, as well as

(ii) with expectation $\mu_{\tilde{\theta}_1}$ and standard deviation $\sigma_{\tilde{\theta}_1}$ if the heteroskedastic model is true.

Consequently, standardizing the observed value $L_{0,1}$ accordingly yields (approximately) standard normally distributed statistics T_0 and T_1 for carrying out two consecutive tests of the hypotheses

(i) H_0 : the homoskedastic model is true
(ii) H_1 : the heteroskedastic model is true

at significance level (i.e., type-I error rate) α. It is beyond the scope of the current paper to make an attempt to derive the required quantities $\mu_{\hat{\theta}_0}$, $\sigma_{\hat{\theta}_0}$, $\mu_{\tilde{\theta}_1}$ and $\sigma_{\tilde{\theta}_1}$ analytically. Instead, we carried out a Monte Carlo simulation to determine empirical arithmetic means and empirical standard deviations as consistent estimates of these moments, given the least-squares estimates $\hat{\boldsymbol{\theta}}_0 = [\hat{\mathbf{x}}; \hat{\sigma}^2]$ and $\tilde{\boldsymbol{\theta}}_1 = \tilde{\mathbf{x}}$ based on the measurements $\mathbf{l}$. A similar simulation approach was previously applied by Williams [41] in the context of testing two types of functional models against each other. Note that the expectations and standard deviations that we simulate by means of Monte Carlo simulation are unknown since we currently do not have analytical expressions for them. The latter can, unfortunately, not be obtained by normal variance propagation because the difference (35) is formed with the log-likelihoods L_0 in (33) and L_1 in (34), which are the logarithms of normal distributions.

Adapting this approach to our problem of testing two competing stochastic models, we first generate a large number M observation vectors by using the multivariate normal distribution $N(\mathbf{A}\hat{\mathbf{x}}, \hat{\sigma}^2 \mathbf{I})$. These samples are in turn used to compute M samples of least-squares estimates of $\boldsymbol{\theta}_0 = [\mathbf{x}; \sigma^2]$ in the homoskedastic model as well as M samples of least-squares estimates of $\boldsymbol{\theta}_1 = \mathbf{x}$ in the heteroskedastic model. Based on the sampled observation vectors and parameter estimates, the corresponding log-likelihood functions (33) and (34) are each evaluated M times, resulting in M realizations of the logarithmized likelihood ratio (35). Under the current generating distribution $N(\mathbf{A}\hat{\mathbf{x}}, \hat{\sigma}^2 \mathbf{I})$, the empirical mean and standard deviation of the sampled $L_{0,1}$ constitute consistent estimates of $\mu_{\hat{\theta}_0}$ and $\sigma_{\hat{\theta}_0}$, allowing us to compute the standardized statistic T_0 with respect to the test of the homoskedastic model. Addressing next the test of the heteroskedastic model, we generate M observation vectors from the multivariate normal distribution $N(\mathbf{A}\tilde{\mathbf{x}}, \boldsymbol{\Sigma})$ and compute again the least-squares estimates for both models. Evaluation of the corresponding log-likelihood functions L_0 and L_1 at the sampled observations and estimates gives us another M samples of $L_{0,1}$, whose mean and standard deviation we estimate subsequently, as numerical approximations of $\mu_{\tilde{\theta}_1}$ and $\sigma_{\tilde{\theta}_1}$. We are thus in a position to calculate also the statistic T_1 (with respect to the test of the heteroskedastic model). We will show in Section 6 that the sampled $L_{0,1}$ for both models are indeed closely described by normal distributions having the corresponding simulated means and standard deviations, as indicated earlier.

Cox [9] recommends to apply one-sided tests in the sense that
(i) H_0 is rejected if $T_0 < k_\alpha^{N(0,1)}$ and
(ii) H_1 is rejected if $T_1 > k_{1-\alpha}^{N(0,1)}$.

These two tests give rise to four possible, mutually exclusive test decisions:
(i) The homoskedastic model is rejected and the heteroskedastic model is not rejected in case of

$$T_0 < k_\alpha^{N(0,1)} \ \wedge \ T_1 \le k_{1-\alpha}^{N(0,1)}. \tag{37}$$

(ii) The heteroskedastic model is rejected and the homoskedastic model is not rejected in case of

$$T_0 \ge k_\alpha^{N(0,1)} \ \wedge \ T_1 > k_{1-\alpha}^{N(0,1)}. \tag{38}$$

(iii) Both the homoskedastic and the heteroskedastic model are rejected in case of

$$T_0 < k_\alpha^{N(0,1)} \ \wedge \ T_1 > k_{1-\alpha}^{N(0,1)}. \tag{39}$$

(iv) Neither the homoskedastic nor the heteroskedastic model are rejected in case of

$$T_0 \ge k_\alpha^{N(0,1)} \ \wedge \ T_1 \le k_{1-\alpha}^{N(0,1)}. \tag{40}$$

6 Numerical example

Based on the analysis steps in former sections, a numerical example is analyzed. The aim of the application is to detect the vertical displacements of a prestressed concrete bridge under load, which are induced by car traffic and train crossings. The data were collected in the framework of the interdisciplinary project "Application of life cycle concepts to civil engineering structures" [described in more detailed in 33] at the Leibniz Universität Hannover. The geodetic contribution was to provide an independent methodology for computing strain values derived from the approximated deflections [32]. The bridge is an overpass for several tracks and streets, connecting the city with the adjoining villages. Its total width measures 14 m and the width of the two mutual lanes is 10 m. The total length is 404.55 m segmented into 13 sections. In the third section, denoted as MQ3, the TLS for this study was installed (see the top part of Fig. 1 and Fig. 2). For the measurements, the TLS was positioned under the middle of the bridge segment and aligned along the main axis (Y-axis) of the bridge (see Fig. 2 red dotted line) so that the outside bottom of the box beam could be scanned at the shortest distance (in the direction of the Z-axis) of 4.7 m. As measuring type the 2D profile mode was chosen with a sampling interval of 0.08 seconds per profile, which corresponds to a sampling rate
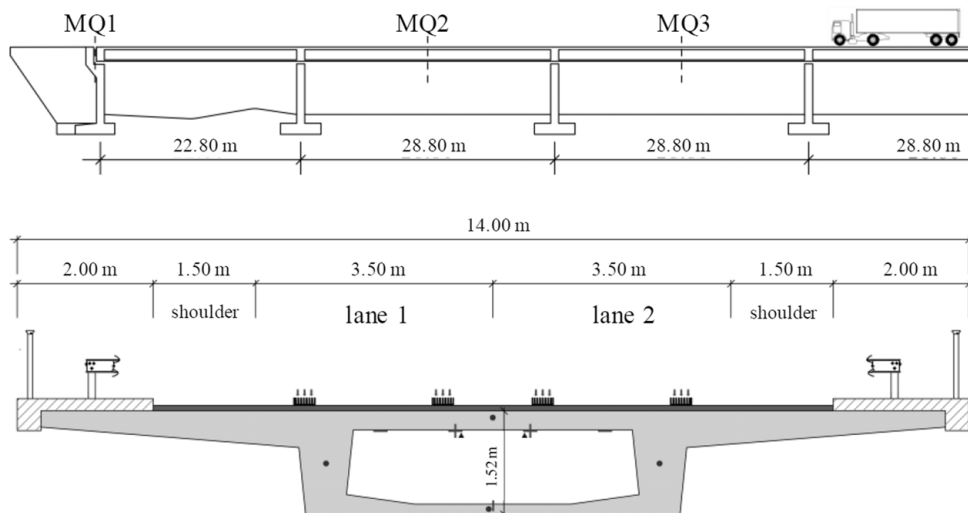
Figure 1: Bridge structure longitudinal section (above), cross section (below) [32].
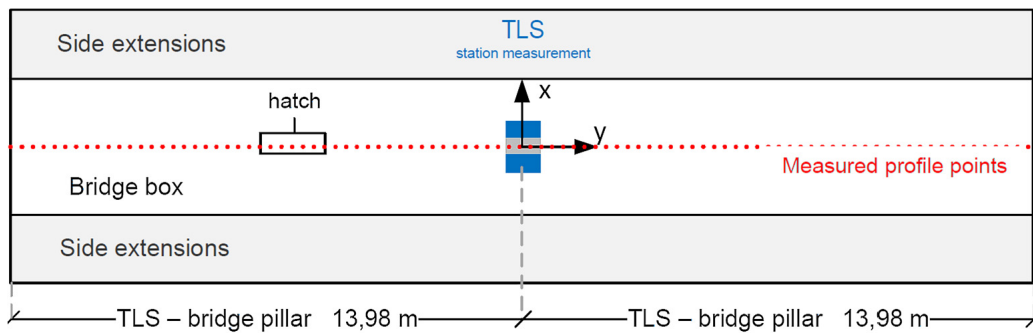

Figure 2: Layout of the measurement setup-bridge section at MQ3, TLS station (blue-gray) and the profile direction (red dotted line) in coordinate system [32].

of 12.5 Hz. The point sampling rate was 500,000 points per second and results in 2,539 points within each profile.

6.1 The observation model

Because the 2D mode was chosen in our specific numerical example, only Y- and Z-coordinates including their uncertainties are considered (the X-coordinates were all identical to 0). Furthermore, the correlations between the measured Y- and Z-coordinates are neglected. Consequently, the X-coordinates of the estimated control points of any B-spline model approximating these data are also identical to 0 in view of (24). It therefore suffices to consider (11) and (12) as models for correcting the measured Y- and Z-coordinates. Thus, the pointwise covariance matrix (13) can be reduced to

$$\Sigma_{p_k} = \begin{bmatrix} u_{Y_k}^2 & 0 \\ 0 & u_{Z_k}^2 \end{bmatrix}. \tag{41}$$

Reducing the Jacobian matrix $\mathbf{F}_k$ accordingly and splitting it into the two parts $\mathbf{F}_{Y,k}$ and $\mathbf{F}_{Z,k}$ with respect to the remaining two coordinate components, we find that $u_{Y_k}^2$ and $u_{Z_k}^2$ can be calculated separately by

$$u_{Y_k}^2 = \mathbf{F}_{Y,k}^T \Sigma_{\mathrm{fac}.k} \mathbf{F}_{Y,k}, \tag{42}$$

$$u_{Z_k}^2 = \mathbf{F}_{Z,k}^T \Sigma_{\mathrm{fac}.k} \mathbf{F}_{Z,k}. \tag{43}$$

The uncertainties caused by the collimation axis error and the horizontal axis error in $\Sigma_{\mathrm{fac}.k}$ can be excluded since there is no horizontal rotation angle influence on Z-coordinates. Thus, the component-wise Jacobian matrices read

$$\mathbf{F}_{Y,k}^T = \left[\frac{\partial Y_k}{\partial r}, \frac{\partial Y_k}{\partial k_0}, \frac{\partial Y_k}{\partial m_0}, \frac{\partial Y_k}{\partial \xi_A}, \frac{\partial Y_k}{\partial \theta}, \frac{\partial Y_k}{\partial \xi_\theta}, \frac{\partial Y_k}{\partial \xi_v} \right]$$

$$\mathbf{F}_{Z,k}^T = \left[\frac{\partial Z_k}{\partial r}, \frac{\partial Z_k}{\partial k_0}, \frac{\partial Z_k}{\partial m_0}, \frac{\partial Z_k}{\partial \xi_A}, \frac{\partial Z_k}{\partial \theta}, \frac{\partial Z_k}{\partial \xi_\theta}, \frac{\partial Z_k}{\partial \xi_v} \right]$$
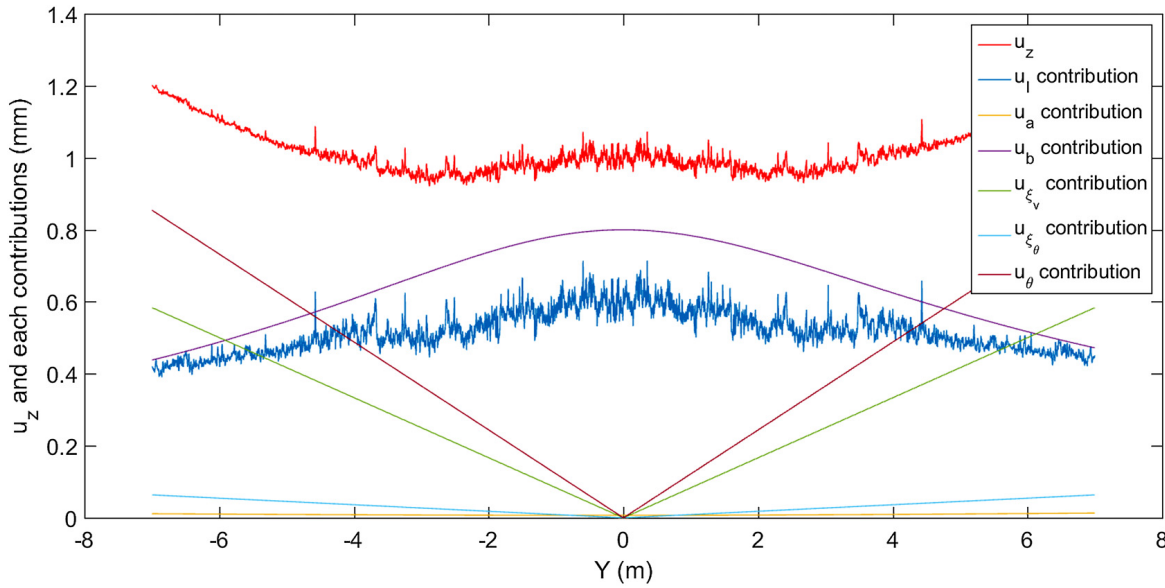
Figure 3: Standard uncertainty of Z-coordinates and individual contributions to its magnitude.

$$\begin{cases} \dfrac{\partial Y_k}{\partial r} = (1 + k_0) \cdot \sin(\theta_k + \xi_\theta + \xi_v) \\[2mm] \dfrac{\partial Y_k}{\partial k_0} = r_k \cdot \sin(\theta_k + \xi_\theta + \xi_v) \\[2mm] \dfrac{\partial Y_k}{\partial m_0} = \sin(\theta_k + \xi_\theta + \xi_v) \\[2mm] \dfrac{\partial Y_k}{\partial \xi_A} = \sin(\theta_k + \xi_\theta + \xi_v) \\[2mm] \dfrac{\partial Y_k}{\partial \theta} = (r_k \cdot (1 + k_0) + m_0 + \xi_A) \cdot \cos(\theta_k + \xi_\theta + \xi_v) \\[2mm] \dfrac{\partial Y_k}{\partial \xi_\theta} = (r_k \cdot (1 + k_0) + m_0 + \xi_A) \cdot \cos(\theta_k + \xi_\theta + \xi_v) \\[2mm] \dfrac{\partial Y_k}{\partial \xi_v} = (r_k \cdot (1 + k_0) + m_0 + \xi_A) \cdot \cos(\theta_k + \xi_\theta + \xi_v) \end{cases} \quad (44)$$

$$\begin{cases} \dfrac{\partial Z_k}{\partial r} = (1 + k_0) \cdot \cos(\theta_k + \xi_\theta + \xi_v) \\[2mm] \dfrac{\partial Z_k}{\partial k_0} = r_k \cdot \cos(\theta_k + \xi_\theta + \xi_v) \\[2mm] \dfrac{\partial Z_k}{\partial m_0} = \cos(\theta_k + \xi_\theta + \xi_v) \\[2mm] \dfrac{\partial Z_k}{\partial \xi_A} = \cos(\theta_k + \xi_\theta + \xi_v) \\[2mm] \dfrac{\partial Z_k}{\partial \theta} = -(r_k \cdot (1 + k_0) + m_0 + \xi_A) \cdot \sin(\theta_k + \xi_\theta + \xi_v) \\[2mm] \dfrac{\partial Z_k}{\partial \xi_\theta} = -(r_k \cdot (1 + k_0) + m_0 + \xi_A) \cdot \sin(\theta_k + \xi_\theta + \xi_v) \\[2mm] \dfrac{\partial Z_k}{\partial \xi_v} = -(r_k \cdot (1 + k_0) + m_0 + \xi_A) \cdot \sin(\theta_k + \xi_\theta + \xi_v) \end{cases} \quad (45)$$

Having computed the covariance matrix (41), we are now in a position to set up the component-wise covariance matrices Σ_Y and Σ_Z in order to determine the solutions (25)–(26) for the control points.

Consequently, the covariance matrix Σ, is reduced to a simple block matrix (24) comprising only the uncertainty of Y-and Z-coordinates.

$$\Sigma_Y = \mathrm{diag}(u_{Y_1}^2, \dots, u_{Y_N}^2), \quad (46)$$

$$\Sigma_Z = \mathrm{diag}(u_{Z_1}^2, \dots, u_{Z_N}^2). \quad (47)$$

6.2 Evaluation of the results

This section gives the results for the aforementioned numerical example. According to the uncertainty budget given in Section 2, the standard uncertainties of the Z-coordinates are shown jointly with the individual uncertainty factors in Fig. 3. It can be concluded that instrumental influences, e.g., the uncertainties of the zero point error, the object-related influence, the angle noise and the vertical index error, play a dominant role. The atmospheric uncertainty, which is in micrometer range, is too tiny to show in this figure. The same characteristics are found with respect to the Y-coordinates.

We used the resulting covariance matrices (46)–(47) as the stochastic model in a multivariate Gauss-Markov model to approximate the measured profile by a B-spline model, as shown in Section 4. In addition, we carried out the same adjustment using the homoskedastic covariance matrix (27) as the stochastic model. The chosen parameters for the B-Spline are in both cases fixed to $p = 3$ and $n = 30$. The resulting two adjusted B-spline models are
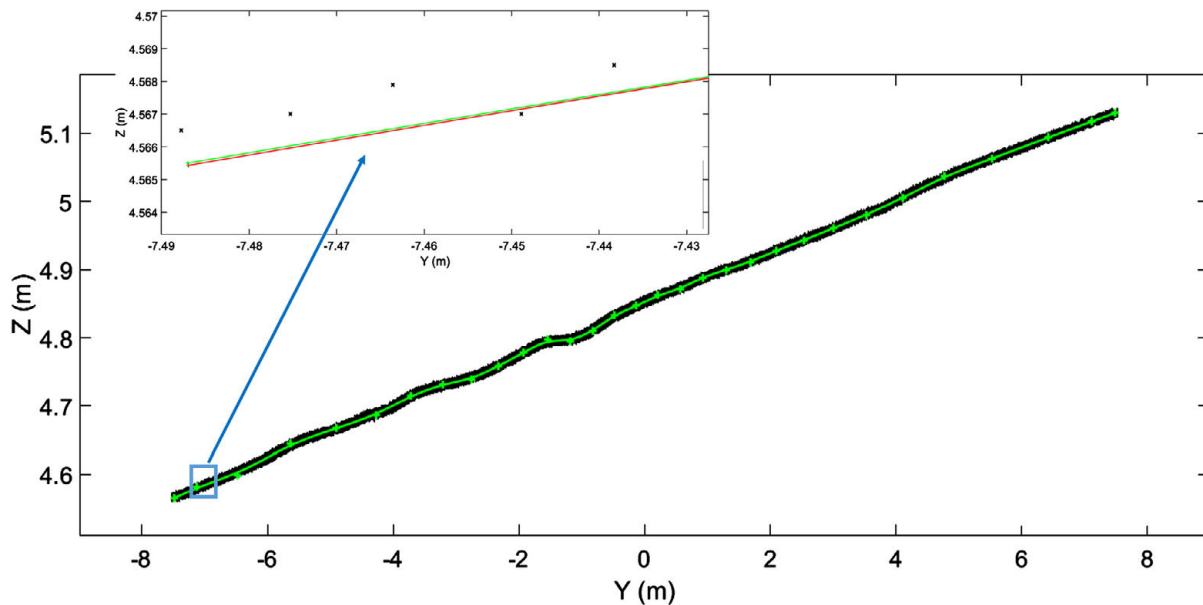
Figure 4: Estimated B-splines based on the heteroskedastic model (green) and based on the homoskedastic model (red), shown for the entire profile and for a short segment in the left part of the profile (see the zoomed area). The corresponding control points as well as the measured data are also displayed (in red and green, respectively); the measurements are indicated by black crosses.
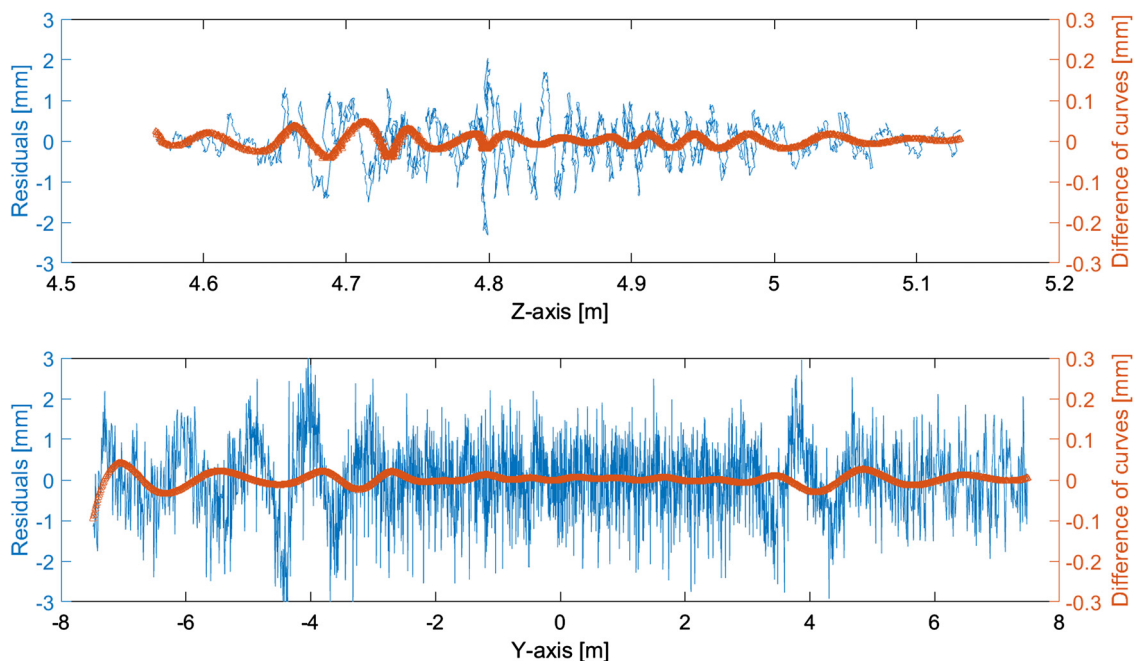

Figure 5: Difference between the two estimated B-spline curves in comparison to the estimated residuals of the B-spline model based on the homoskedastic covariance matrix, shown with two different scales for the Y- and Z-coordinates.

shown in Fig. 4 (for the entire profile and for a selected window within the left part of the profile). It can be seen that both estimated B-spline models coincide almost perfectly in the center of the profile and to a lesser extent at the edges.

Figure 5 shows on the one hand the estimated residuals for the B-spline model based on the unit covariance matrix, and on the other hand the difference between the two estimated B-spline models. The residuals are generally one magnitude larger than the model differences. Further-
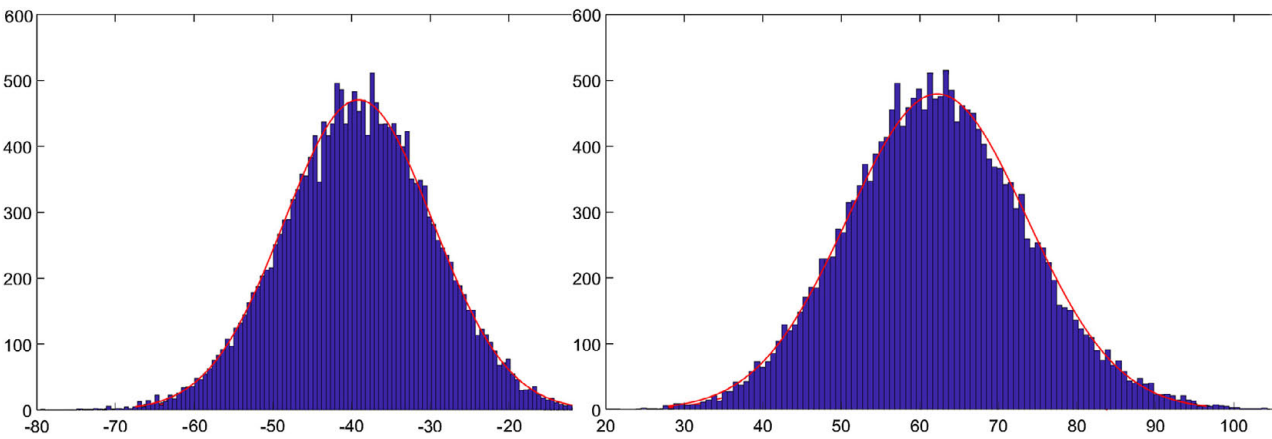
Figure 6: Histogram of the sampled log-likelihood differences $L_{0,1}$ under the homoskedastic (left) and heteroskedastic model (right), approximated by a Gaussian density functions (in red).

more, the model differences in the Z-component are significantly larger than in the Y-component.

In order to test if the refined stochastic model (46)–(47) has a significant and beneficial influence on the B-spline estimation, we evaluated first the test statistic (32). Comparison with the critical value at the type-I error rate $\alpha = 0.05$ leads to the rejection of the null hypothesis that $\gamma = 0$ is true (see Table 3). Thus, the given measurements $\mathbf{l}$ suggest the inadequacy of the homoskedastic covariance matrix (27).

Table 3: Result for the nested test for heteroskedasticity ("Test 1") for the measured profile.

T_{RS}	$k_{0.95}^{\chi^2(1)}$	rejected
18.57	3.84	homoskedastic model (H_0)

We can however not automatically infer from the preceding test result that the heteroskedastic covariance matrix (30) is correct since the null hypothesis could in principle have been rejected also for other heteroskedastic models. Therefore, we carried out in addition the non-nested discrimination test described in Section 5.2 (see Table 4). On the one hand, since T_0 is less than the α-quantile of $N(0,1)$, the homoskedastic model is rejected. On the other hand, T_1 takes a large positive value, so that the specific heteroskedastic model (30) should also be rejected.

Figure 6 demonstrates that the 10,000 sampled log-likelihood differences (35) approximately follow a Gaussian distribution both under the simple and under the refined stochastic model. Thus, it is justified to standardize the log-likelihood difference computed from the actual measurements by means of the sample mean and standard

Table 4: Results for the two non-nested model discrimination tests ("Test 2a" and "Test 2b") for the measured profile.

T_0	$k_{0.05}^{N(0,1)}$	rejected
−3.27	−1.64	homoskedastic model

T_1	$k_{0.95}^{N(0,1)}$	rejected
22.24	1.64	heteroskedastic model

Table 5: Rejection rates for the nested and the non-nested tests with respect to all 376 measured profiles.

Test	Test 1	Test 2a	Test 2b
Rejection rate	0.65	0.40	1.00

deviation under each of the two stochastic models (resulting in the values for T_0 and T_1 as shown in Table 4).

In order to assess whether the test results obtained for the specific profile is representative, the tests were repeated for 375 further profiles. Table 5 shows the rejection rates for the nested heteroskedasticity test ("Test 1") and for the two non-nested model discrimination tests ("Test 2a" and "Test 2b"). The homoskedastic model is rejected in 65% of the cases by the first test and in 40% of the cases by the second test. Thus, Test 1 rejects that model for an additional 25% of the profiles, which shows that the two test procedures are not equivalent. In all cases, the specified heteroskedastic model was rejected by the second test. We also determined the rejection rate for the event that both tests concurrently reject the homoskedastic model. We found that the non-nested test did not confirm the rejection of the homoskedastic model by the nested test in only 4% of the cases. Therefore, we may conclude that

rejection of the homoskedastic model by the non-nested test practically implies the rejection of that model by the nested test.

In summary, we see from the application of the previous hypothesis tests that both the homoskedastic and the specific form of heteroskedastic model are inadequate. As the large rejection rate of the nested test points towards accepting the alternative hypothesis $y > 0$, it is possible that a rescaling of the heteroskedastic diagonal covariance matrix by some (currently unknown) y-value leads to a more realistic stochastic model. But this work should be carried out in the future research.

7 Conclusion and outlook

In this paper, an extended uncertainty budget for terrestrial laser scanning (TLS) measurements, based on the Guide to the Expression of Uncertainty in Measurement (GUM), was investigated in the context of bridge measurements in 2D profile mode. It was shown for short-range measurements that instrumental and object-related influences play a dominant role in comparison to atmospheric influence. The extended uncertainty budget was used to derive covariance matrices for the Y- and Z-coordinates. These covariance matrices served as the stochastic model within a multivariate Gauss-Markov model, which was used to approximate the measured bridge profile by a B-spline model. The same adjustment was also made by employing simple, homoskedastic covariance matrices for the stochastic model. The two resulting B-spline models were shown to coincide closely in the central part of the profile, and to coincide to a lesser extent in the edges of the profile. The model differences turned out to be one magnitude smaller than the estimated residuals with respect to the homoskedastic model, indicating insignificant differences between the two B-spline curves. The effect of the extended, heteroskedastic covariance matrix on the adjustment was also assessed by means of two testing procedures. The first procedure was based on Rao's score statistic in order to test the homoskedastic model against an unspecified multiple of a fully specified diagonal matrix, which was constructed from the extended uncertainty budget. The second procedure tests the homoskedastic and the fully specified heteroskedastic model independently against each other, where each model takes the role of the null hypothesis once and the other model the role the alternative. The two testing procedures led to the rejection of both the simple homoskedastic and the extended heteroskedastic models. The tests were repeated

in total for 376 measured profiles; the simple stochastic model was rejected in the majority of cases, and the extended model was rejected in all cases. We can therefore conclude that both forms of stochastic model are inadequate. The presented testing procedures will in the future be used to validate further attempts at improving the stochastic model for TLS measurements. The correlations of the influences and the measurements will also be considered since the currently used stochastic model is not realistic in this regard. These improvements will require considerable extensions of the B-spline estimation and testing procedure. Moreover, we intend to apply the extensions to GUM concerning the Monte Carlo propagation of uncertainties in order to further evaluate the stochastic modeling approach based on GUM, and to enable realistic comparisons to the approach based on synthetic covariance matrices.

References

[1] Alkhatib, H. and Kutterer, H. (2013). Estimation of measurement uncertainty of kinematic TLS observation process by means of Monte-Carlo methods. *Journal of Applied Geodesy*, 7(2):125–134.

[2] Alkhatib, H., Neumann, I., and Kutterer, H. (2009). Uncertainty modeling of random and systematic errors by means of Monte Carlo and fuzzy techniques. *Journal of Applied Geodesy*, 3(2):67–79.

[3] Alkhatib, H., Schmitt, C., and Neumann, I. (2014). Spatial approximation of terrestrial laser scanner profiles by considering observations with stochastic information. In *Proceedings of the XXV FIG Congress. Engaging the Challenges, Enhancing the Relevance*, Kuala Lumpur.

[4] Baltsavias, E. P. (1999). Airborne laser scanning: basic relations and formulas. *ISPRS Journal of photogrammetry and remote sensing*, 54(2):199–214.

[5] Balzani, M., Pellegrinelli, A., Perfetti, N., and Uccelli, F. (2001). A terrestrial laser scanner: accuracy tests. In *18th International Symposium CIPA*, Potsdam, Germany.

[6] Barrell, H. and Sears, J. (1939). The refraction and dispersion of air for the visible spectrum. *Philosophical Transactions of the Royal Society of London. Series A, Mathematical and Physical Sciences*, 238(786):1–64.

[7] Borah, D. K. and Voelz, D. G. (2007). Estimation of laser beam pointing parameters in the presence of atmospheric turbulence. *Applied Optics*, 46(23):6010–6018.

[8] Bureick, J., Alkhatib, H., and Neumann, I. (2016). Robust spatial approximation of laser scanner point clouds by means of free–form curve approaches in deformation analysis. *Journal of Applied Geodesy*, 10(1):27–35.

[9] Cox, D. R. (1961). Tests of separate families of hypotheses. In *Proceedings of the Fourth Berkeley Symposium on Mathematical Statistics and Probability, Volume 1: Contributions to the Theory of Statistics*, pages

105–123, Berkeley, Calif., University of California Press.

[10] Eling, D., 2009 *Terrestrisches Laserscanning für die Bauwerksüberwachung*, Ph.D. thesis, Leibniz Universität Hannover.

[11] Fernández Pareja, T., García Pablos, A., and de Vicente y Oliva, J. (2013). Terrestrial laser scanner (TLS) equipment calibration. *Procedia Engineering*, 63:278–286.

[12] Gordon, B. (2008). *Zur Bestimmung von Messunsicherheiten terrestrischer Laserscanner*, Ph.D. thesis, Technische Universität Darmstadt.

[13] Gumus, K. and Erkaya, H. (2011). Analyzing the geometric accuracy of simple shaped reference object models created by terrestrial laser scanners. *International Journal of Physical Sciences*, 6(28):6529–6536.

[14] Harmening, C., Kauker, S., Neuner, H.-B., and Schwieger, V. (2016). Terrestrial laserscanning–modeling of correlations and surface deformations. In *FIG Working Week 2016 Recovery from Disaster*, Christchurch, New Zealand.

[15] Hejbudzka, K., Lindenbergh, R., Soudarissanane, S., and Humme, A. (2010). Influence of atmospheric conditions on the range distance and number of returned points in Leica Scanstation 2 point clouds. In *Proceedings ISPRS Commission V Mid-Term Symposium-Close Range Image Measurement Techniques*, Newcastle upon Tyne, UK, 21–24 June 2010; IAPRS, XXXVIII (5), 2010.

[16] ISO (2005). *Optics and optical instruments–Field procedures for testing geodetic and surveying instruments–Part 5: Electronic tacheometers*. International Organization of Standardization.

[17] ISO/IEC (2008a). *Evaluation of Measurement Data–Supplement 1 to the "Guide to the Expression of Uncertainty in Measurement"–Propagation of distributions using a Monte Carlo method*. Geneva.

[18] ISO/IEC (2008b). *Uncertainty of measurement – Part 3: Guide to the expression of uncertainty in measurement (GUM:1995 with minor corrections)*. Geneva.

[19] Joeckel, R., Stober, M., and Huep, W. (2008). *Elektronische Entfernungsmessung und ihre Integration in aktuelle Positionierungsverfahren*. Wichmann.

[20] Kargoll, B. (2012). *On the Theory and Application of Model Misspecification Tests in Geodesy*. Ph.D. thesis, Deutsche Geodätische Kommission, Series C, No. 674.

[21] Kauker, S. and Schwieger, V. (2016). First investigations for a synthetic covariance matrix for monitoring by terrestrial laser scanning. In *3rd Joint International Symposium on Deformation Monitoring, Volume 30*.

[22] Kauker, S. and Schwieger, V. (2017). A synthetic covariance matrix for monitoring by terrestrial laser scanning. *Journal of Applied Geodesy*, 11(2):77–87.

[23] Koch, K.-R. (1999). *Parameter Estimation and Hypothesis Testing in Linear Models*. Springer.

[24] Koch, K.-R. (2008). Evaluation of uncertainties in measurements by Monte Carlo simulations with an application for laserscanning. *Journal of Applied Geodesy*, 2(2):67–77.

[25] Koch, K.-R. (2009). Fitting free-form surfaces to laserscan data by NURBS. *Allgemeine Vermessungs-Nachrichten*, 116:134–140.

[26] Koch, K.-R. (2015). Minimal detectable outliers as measures of reliability. *Journal of Geodesy*, 89:483–490.

[27] Lichti, D. D., Gordon, S. J., and Tipdecho, T. (2005). Error models and propagation in directly georeferenced terrestrial laser scanner networks. *Journal of Surveying Engineering*, 131(4):135–142.

[28] Lichti, D. D. and Harvey, B. (2002). The effects of reflecting surface material properties on time-of-flight laser scanner measurements. In *Symposium on Geospatial Theoty, Processing and Applications*, Ottawa, Canada, Vol. 2.

[29] Lichti, D. D., Stewart, M., Tsakiri, M., and Snow, A. (2000). Calibration and testing of a terrestrial laser scanner. *International archives of Photogrammetry and Remote sensing*, 33(B5/2; PART 5):485–492.

[30] Mazalová, J., Valentová, K., and Vlčková, L. (2010). Testing of accuracy of reflectorless distance measurement of selected Leica and Topcon total stations. *GeoScience Engineering*, 56(1):19–26.

[31] Neitzel, F. (2007). Investigation of axes errors of terrestrial laser scanners. In *Fifth International Symposium Turkisch-German Joint Geodetic Days*, Berlin, Germany.

[32] Neuner, H., Schmitt, C., and Neumann, I. (2014). Zur Bestimmung der verkehrsseitig verursachten Dehnung an einem Brückentragwerk mittels terrestrischem Laserscanning. In A. Wieser (ed.): *Ingenieurvermessung'14. Beiträge zum 17. Internationalen Ingenieurvermessungskurs Zürich*, pages 231–243. Wichmann.

[33] NTH-BAU (2010). *Life Cycle Enginnering for Enginnering Structures and Buildings Strategies and Methods*. Topic 6: Application of life cycle concepts to civil engineering structures, 2010–2013, www.nth-bau.de.

[34] Piegl, L. and Tiller, W. (1997). *The NURBS book*. Springer Science & Business Media.

[35] Reshetyuk, Y. (2006). *Investigation and calibration of pulsed time-of-flight terrestrial laser scanners*. Ph.D. thesis, Royal Institute of Technology (KYH).

[36] Rüeger, J. M. (1990). *Electronic distance measurement*. Springer.

[37] Schulz, T. (2007). *Calibration of a terrestrial laser scanner for engineering geodesy*. Ph.D. thesis, ETH ZURICH.

[38] Sommer, K. and Siebert, B. (2004). Praxisgerechtes Bestimmen der Messunsicherheit nach GUM. *Technisches Messen*, 71:52–60.

[39] Soudarissanane, S. and Lindenbergh, R. (2011). Optimizing terrestrial laser scanning measurement set-up. In *ISPRS Workshop Laser Scanning 2011*, Calgary, Canada, 29–31 August 2011; IAPRS, XXXVIII (5/W12), 2011.

[40] Soudarissanane, S., Lindenbergh, R., Menenti, M., and Teunissen, P. (2011). Scanning geometry: influencing factor on the quality of terrestrial laser scanning points. *ISPRS Journal of Photogrammetry and Remote Sensing*, 66(4):389–399.

[41] Williams, D. A. (1970). Discrimination between regression models to determine the pattern of enzyme synthesis in synchronous cell cultures. *Biometrics*, 26(1):23–32.

[42] Wujanz, D., Mettenleiter, M., Burger, M., and Neitzel, F. (2016). Viewpoint planning for terrestrial laser scanning utilising an intensity based stochastic model. In *3rd Joint International Symposium on Deformation Monitoring (JISDM)*.

[43] Zámečníková, M., Neuner, H., and Pegritz, S. (2014a). Influence of the incidence angle on the reflectorless distance measurement in close range. In *INGEO 2014 – 6th International Conference on Engineering Surveying*, Prague, Czech Republic.

[44] Zámečníková, M., Neuner, H., Pegritz, S., and Sonnleitner, R. (2015). Investigation on the influence of the incidenceangle on the reflectorless distance measurement of a terrestrial laser scanner. *Vermessung & Geoinformation*, 2(3):208–218.

[45] Zámečníková, M., Wieser, A., Woschitz, H., and Ressl, C. (2014b). Influence of surface reflectivity on reflectorless

electronic distance measurement and terrestrial laser scanning. *Journal of Applied Geodesy*, 8(4):311–326.

[46] Zoller+Fröhlich (2007). *Technical datasheet IMAGER 5006*. Zoller+Fröhlich GmbH.

Paper 3

Model Selection for Parametric Surfaces Approximating 3D Point Clouds for Deformation Analysis

Xin Zhao * [ID]**, Boris Kargoll** [ID]**, Mohammad Omidalizarandi** [ID]**, Xiangyang Xu and Hamza Alkhatib** [ID]

Geodetic Institute, Leibniz Universität Hannover, Nienburger Str. 1, 30167 Hannover, Germany; kargoll@gih.uni-hannover.de (B.K.); zarandi@gih.uni-hannover.de (M.O.); xu@gih.uni-hannover.de (X.X.); alkhatib@gih.uni-hannover.de (H.A.)

* **Correspondence:** zhao@gih.uni-hannover.de; Tel.: +49-511-7622466

Abstract: Deformation monitoring of structures is a common application and one of the major tasks of engineering surveying. Terrestrial laser scanning (TLS) has become a popular method for detecting deformations due to high precision and spatial resolution in capturing a number of three-dimensional point clouds. Surface-based methodology plays a prominent role in rigorous deformation analysis. Consequently, it is of great importance to select an appropriate regression model that reflects the geometrical features of each state or epoch. This paper aims at providing the practitioner some guidance in this regard. Different from standard model selection procedures for surface models based on information criteria, we adopted the hypothesis tests from D.R. Cox and Q.H. Vuong to discriminate statistically between parametric models. The methodology was instantiated in two numerical examples by discriminating between widely used polynomial and B-spline surfaces as models of given TLS point clouds. According to the test decisions, the B-spline surface model showed a slight advantage when both surface types had few parameters in the first example, while it performed significantly better for larger numbers of parameters. Within B-spline surface models, the optimal one for the specific segment was fixed by Vuong's test whose result was quite consistent with the judgment of widely used Bayesian information criterion. The numerical instabilities of B-spline models due to data gap were clearly reflected by the model selection tests, which rejected inadequate B-spline models in another numerical example.

Keywords: terrestrial laser scanning; surface modeling; B-spline; polynomial; Gauss-Markov model; simulation-based Cox's test; Vuong's test

1. Introduction

Deformation monitoring of engineering structures such as bridges, tunnels, dams, and tall buildings is a common application of engineering surveying [1]. As summarized in Mukupa et al. [2], deformation analysis can be based on different comparison objects, namely, point-to-point, point-to-surface, or surface-to-surface. The point-to-point-based analysis is a common approach to describe deformations that are captured by conventional point-wise surveying techniques. Examples of such techniques are the total station and the global navigation satellite system; however, in many cases, these have been surpassed by the use of LiDAR technology, especially terrestrial laser scanning (TLS) [3,4]. Although the single-point precision of TLS is in the sub-centimeter range (± 2 to ± 25 mm), the high redundancy of the scanning observations facilitates a higher precision via the application of least-squares based curve or surface estimation and, hence, an adequate precision of the estimated deformation parameters [5].

A point-to-surface-based analysis is carried out to represent a deformation by the distance between the point cloud in one epoch and the surface estimated from measurements in another epoch. Such a surface can be constructed as a polygonal model (mesh) [6–8] or as a regression model (e.g., a polynomial or B-spline surface model) [9–13]. The procedure of a surface-to-surface-based deformation analysis, which is appropriate in certain situations, is to divide the point clouds into cells and to compare the parameters of fitted planes based on cell points in two epochs. This method is applied in Lindenbergh et al. [14], where the different positions of the laser scanner and strong wind contribute to the change of the coordinate system. The aforementioned three approaches to deformation analysis are complemented by the "point-cloud-based" approach, in which a deformation is reflected by the parameters of a coordinate transformation between sets of point clouds in various epochs. The common algorithm for determining the transformation matrix is the iterative closest point algorithm. The authors of Girardeau-Montaut et al. [15] presented three simple cloud-to-cloud comparison techniques for detecting changes in building sites or indoor facilities within a certain time.

Aiming at rigorous deformation detection from scatter point clouds, it is crucial to describe the geometrical features of the object accurately by an appropriate curve or surface regression model, and emphasis is put on the latter model in this paper. The purpose of surface fitting is to estimate the continuous model function from the scatter point samples, which can be implemented by approximation in the case of redundant measurements. There are many approximation approaches for working with surfaces based on an implicit, explicit, or parametric form. Parametric models are usually employed to fit point cloud data in applications such as deformation monitoring and reverse engineering. Different parametric models perform differently in terms of accuracy and number of coefficients when fitted to a dataset. Among the many methods utilized in various applications for approximating point clouds, polynomial model fitting is usually applied to smooth and regular objects due to its simple operation. In [16], the authors assumed a concrete arch as regular and analyzed the deformation behavior through comparing fitted second-degree polynomial surfaces. The more involved fitting of B-splines and non-uniform rational basis splines is often preferred for modeling geometrically complicated objects. In this context, much research has focused on the optimization of the mathematical and stochastic models. In Bureick et al. [17], the authors optimized free-form curve approximation by means of an optimal selection of the knot vector. Furthermore, in Harmening and Neuner [18], the authors improved the parametrization process in B-spline surface fitting by using an object-oriented approach instead of focusing on a superior coordinates system, thereby enabling the generated parameters to reflect the features of the object realistically. Moreover, in Zhao et al. [19], the authors suggested a new stochastic model for TLS measurements and used the resulting covariance matrix within the least-squares estimation of a B-spline curve.

The need for model selection and statistical validation was emphasized in Wunderlich et al. [20], the authors of which described the deficiencies in current areal deformation analysis and presented possible strategies to improve this situation. Typically, the selection of surface model depends on the object features—for example, whether the surface is regular or irregular. However, in most cases, it is unclear whether the object is smooth enough to be described by a simple model (e.g., as a low-order, global polynomial surface) or not. This limitation serves as the motivation for discriminating between estimated surface models in order to select the most appropriate one. In the context of model selection, Harmening and Neuner [21,22] investigated statistical methods based on information criteria and statistical learning theory for selecting the optimal number of control points within B-spline surface estimation. Another possibility is to compare the (log-)likelihoods of competing models directly by means of the general testing principle by D.R. Cox [23]. In Williams [24], the authors improved the Cox's test based on the use of Monte-Carlo simulation, which is straightforward to implement. This kind of test has already been used in Zhao et al. [19] to select the best fitting stochastic model for B-spline curve estimation. In Vuong [25], the authors use likelihood-ratio-based statistics to discriminate the competing models based on Kullback–Leibler information criterion. Such hypothesis

tests offer the advantage that significant probabilistic differences between models can be detected, which is information that has not been provided by the methods mentioned previously.

The motivation of this paper lies in the selection of the most parsimonious, yet sufficiently accurate, parametric description of structure based on TLS measurements, whose model is applied to reflect the surface-based deformation of measured objects. Different from standard model selections procedures based on information criteria, we introduce two likelihood-ratio tests from D.R. Cox and Q.H. Vuong, which are instantiated in numerical examples to discriminate statistically between widely used polynomial and B-spline surfaces as models of given TLS point clouds. The selected surface model's performance in reflecting deformation is compared with the result of the block-means approach. The paper is organized as follows. In Section 2, the methodology of surface approximation and model selection is reviewed and explained. This methodology is instantiated in two numerical examples by discriminating between widely used polynomial and B-spline surfaces. The evaluation of approximated surface models as well as their performance in deformation analysis are given as results in Section 3. The subsequent Section 4 provides a further discussion on the results and a comparison with results obtained by some well-known penalization information criterion approaches. Finally, conclusions are drawn in Section 5.

2. Methodology

2.1. Experiment Design

An experiment was conducted jointly with the Institute of Concrete Construction of the Leibniz Universität Hannover to probe the load-caused behavior and ultimate bearing capacity of a concrete arch structure with a length of about 2 m and thickness of 0.1 m. Loads were placed on top of the arch's surface for 13 epochs, within which the load was exerted with a uniform speed (2 kN/min) of about 20 min followed by a break of approximately 10 min for data capture [9]. The weight of load was increased continuously and reached 520 kN at the end of the 13th epoch.

A multi-sensor-system (MSS) consisting of a TLS (here Z+F Imager 5006), laser tracker (here Leica AT960LR) and digital camera (here Nikon D750) were used to acquire the data from the deformable arch structure. The positions of the MSS relative to the arch structure are shown in Figure 1 (see also [16]). TLS data were acquired in "super high" resolution mode with normal quality. The vertical and horizontal resolution was $0.0018°$ and vertical and horizontal accuracy was $0.007°$ rms. The TLS scanned the top and the side surfaces of the arch. The laser tracker was used as a reference sensor for the validation purpose, which allows sub-millimeter accuracy with a maximum permissible error of $15 \, \mu m + 6 \, \mu m/m$ [26]. In addition, a digital camera was used to capture the feature points with a high resolution (thus exploiting their strength in discrete feature point extraction). Targets were mounted in the surroundings and on the arch (see Figure 1) to perform the external calibration between the sensors.

Among various datasets, the focus of this literature lies in capturing the data by the TLS to use a large number of 3D point clouds with a high accuracy in approximating a surface model, which is important in rigorous deformation monitoring. In our experiment, the top surface of the arch is of great interest since it is under load pressure in the consecutive 13 epochs and has obvious movements compared to the other parts of the structure. However, as can be seen from Figure 1, the top surface is partially occluded by the steel beams. Consequently, it is necessary to extract the top-surface points in order to enable an accurate surface model. As a preliminary step to separate the obstructions and the arch-shape part of the object, the reflectance image was generated by using the reflectivity values of the raw TLS data. It was performed by assigning the reflectivity values of each point cloud to one pixel based on the scan resolution [27] (see Figure 2). Since the occluded objects such as the beams on top of the arc shape object were darker compared to the arc shape part, it could be discarded by means of the OpenCV threshold function and by setting the threshold value manually to 80 from a range of 0–255. Therefore, those values greater than 80 were set to 0. However, before performing the

thresholding, OpenCV GaussianBlur function with a size of 5 was applied to reduce the image noise. Next, the morphological opening and closing filters were applied to discard the very small segments. As previously, the position and orientation of the global coordinate system was defined in Figure 1, the Z-axis was in the zenith direction. Therefore, the Pass Through filter of the Point Cloud Library was applied to cut off those 3D point clouds below or greater than the predefined threshold in the Z-axis direction. Then the "setFilterLimits" member function of this filter was set to (−4.50 m, −3.75 m) to select the 3D point clouds within the boundaries. Subsequently, the StatisticalOutlierRemoval filter of the Point Cloud Library was applied to remove the outliers of the 3D point clouds. In this filter, the k nearest neighbor points were used to estimate the mean distance. Therefore, its "setMeanK" member function was set to 20. Next, the "setStddevMulThresh" member function of this filter was set to 3.0 to reject the outliers by means of the 3σ test. The extracted arch surface data is shown in Figure 3. As an example, only two representative segments of the point cloud within the red boundary are separately investigated since the middle area has significant deviations compared to the other parts of the surface. The same methodology is applicable in modeling other segments.
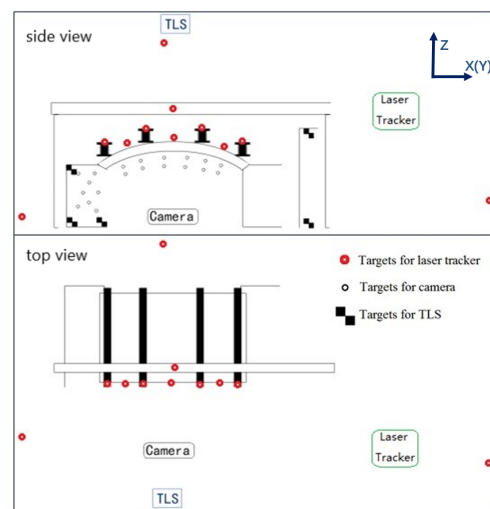

Figure 1. Sketch map of the experimental design concerning the locations of the instruments and relevant targets in side view (**upper**) and top view (**bottom**) [16].
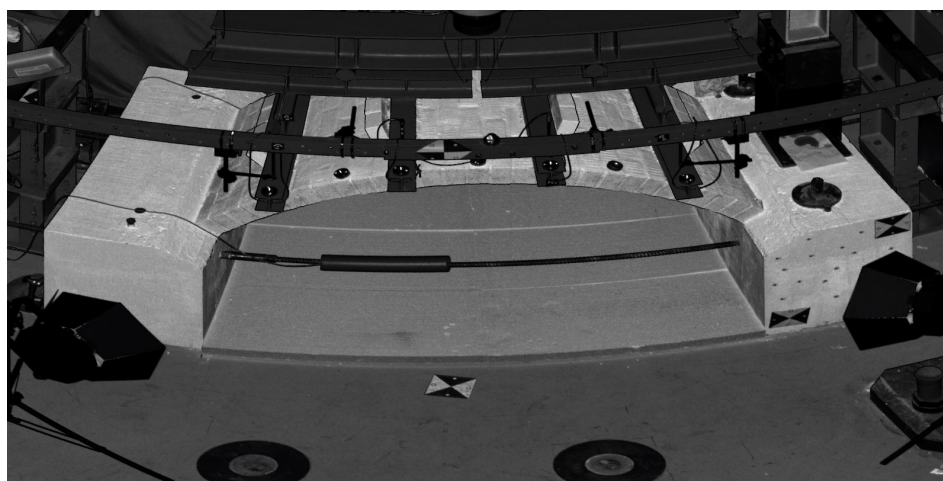

Figure 2. Reflectance image generated by reflectivity values of TLS data [16].
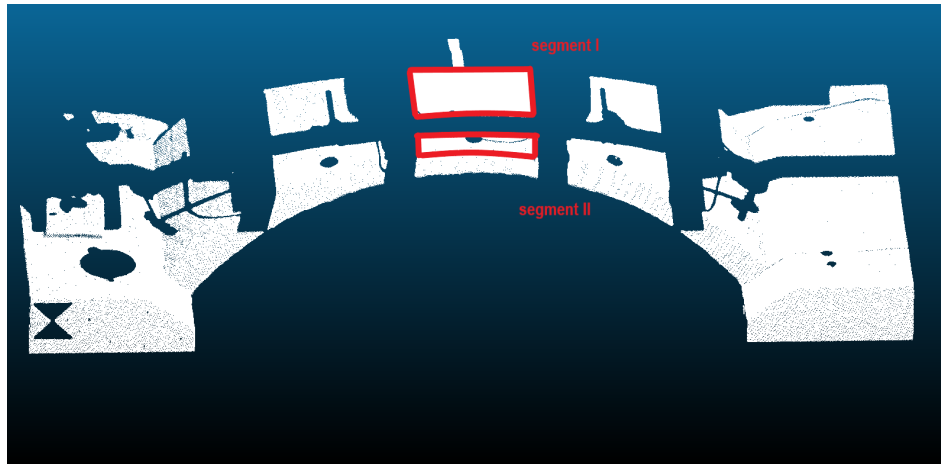
Figure 3. Extracted Arc-shape object and the target segments in our numerical example (within the red boundary) shown by the software CloudCompare.

2.2. Surface Approximation

In surface-based deformation analysis, an appropriate surface model is required as a representation of each deformation status. Among the various parametric models, polynomial surface fitting are the most common approach due to its easy implementation [9,16], while free-form surfaces, especially B-splines, have become relevant to deformation analysis due to their capacity to accurately model more detailed geometrical features including sharp edges, cusps, and leaps [28]. The functional relationships behind B-splines and polynomials, as two of the most commonly used types of surface model, as well as the corresponding approximation steps, are described in this subsection.

2.2.1. B-Spline Surface Approximation

The mathematical description of a 3D point

$$\mathbf{S} = [X \, Y \, Z] = \sum_{i=0}^{n} \sum_{j=0}^{m} \mathbf{N}_{i,p}(\bar{u}) \mathbf{N}_{j,q}(\bar{v}) \mathbf{P}_{i,j} \tag{1}$$

on a B-spline surface is based on the bidirectional combination of basis functions $\mathbf{N}_{i,p}(\bar{u})$, $\mathbf{N}_{j,q}(\bar{v})$ and 3D control points $\mathbf{P}_{i,j} = [P_{X_{i,j}} \, P_{Y_{i,j}} \, P_{Z_{i,j}}]$, which are located on a bidirectional net with the number of $n+1$ and $m+1$ in u- and v-directions.

B-spline surface approximation builds upon B-spline curve fitting in the two directions. Following Bureick et al. [17], this procedure can be carried out in three steps:

1. Parametrization of the measurements with s rows and t columns with respect to the u- and v-direction.
2. Determination of the knot vectors $\mathbf{U}$ and $\mathbf{V}$ in the u- and v-direction.
3. Estimation of the control points by means of a linear Gauss–Markov model.

The first two steps consist of the parameterization and computation of knot vectors, which serve as input parameters for the final estimation. Since the calculation of B-spline parameters are beyond the scope of this paper, the interested reader is referred to Bureick et al. [17] and Piegl and Tiller [29]. The final step of B-spline approximation is to estimate the positions of the control points, which is done essentially by adjusting a linear Gauss–Markov model (cf. [29,30]). Given measured points located on a grid defined by s rows and t columns, they also can be arranged in matrix form as

$$\mathbf{l} = \begin{bmatrix} \mathbf{l}_1 \\ \vdots \\ \mathbf{l}_{s \cdot t} \end{bmatrix} = \begin{bmatrix} X_1 & Y_1 & Z_1 \\ \vdots & \vdots & \vdots \\ X_{s \cdot t} & Y_{s \cdot t} & Z_{s \cdot t} \end{bmatrix}. \tag{2}$$

The addition of a corresponding matrix **v** of residuals to the observation matrix yields the adjusted observations, which can be represented by the functional B-spline model in Equation (1). We thus have for a particular observation the equation

$$\mathbf{l}_{k_u k_v} + \mathbf{v}_{k_u k_v} = \mathbf{S} = \sum_{i=0}^{n} \sum_{j=0}^{m} \mathbf{N}_{i,p}(\bar{u}_{k_u}) \mathbf{N}_{j,q}(\bar{v}_{k_v}) \mathbf{P}_{i,j} \tag{3}$$

where $k_u = 2, ..., s$ and $k_v = 2, ..., t$. We can write all of the equations jointly in the form $\mathbf{l} + \mathbf{v} = \mathbf{A}_0 \mathbf{x}$ with a design matrix within which the basis functions $\mathbf{N}_{i,p}(\bar{u})$, $\mathbf{N}_{j,q}(\bar{v})$ are calculated based on the parameterization and knot vectors

$$\mathbf{A}_0 = \begin{bmatrix} N_{0,p}(\bar{u}_1) \cdot N_{0,q}(\bar{v}_1) & \cdots & N_{n,p}(\bar{u}_1) \cdot N_{m,q}(\bar{v}_1) \\ \vdots & & \vdots \\ N_{0,p}(\bar{u}_s) \cdot N_{0,q}(\bar{v}_t) & \cdots & N_{n,p}(\bar{u}_s) \cdot N_{m,q}(\bar{v}_t) \end{bmatrix} \tag{4}$$

and (unknown) parameter matrix **x**. We assume all of the measured point coordinates to have identical accuracies and to be uncorrelated, so that we obtain for the least squares estimates of these parameters:

$$\hat{\mathbf{x}} = \begin{bmatrix} \hat{P}_{X_{0,0}} & \hat{P}_{Y_{0,0}} & \hat{P}_{Z_{0,0}} \\ \vdots & \vdots & \vdots \\ \hat{P}_{X_{n,m}} & \hat{P}_{Y_{n,m}} & \hat{P}_{Z_{n,m}} \end{bmatrix} = (\mathbf{A}_0^T \mathbf{A}_0)^{-1} \mathbf{A}_0^T \mathbf{l}. \tag{5}$$

2.2.2. Polynomial Surface Approximation

Denoting a generic surface point by $\mathbf{S} = (X, Y, Z)$, the Z-component can be expressed as the two-fold linear combination

$$Z = \sum_{i=0}^{p} \sum_{j=0}^{q} a_{i,j} X^i Y^j = a_{0,0} + a_{1,0} X + a_{0,1} Y + a_{2,0} X^2 + a_{1,1} XY + a_{0,2} Y^2 + \ldots$$

$$+ a_{p,0} X^p + a_{p-1,1} X^{p-1} Y + \ldots + a_{1,q-1} XY^{q-1} + a_{0,q} Y^q \tag{6}$$

where $\mathbf{a} = [a_{0,0}, a_{1,0}, \ldots, a_{p,q}]$ is the coefficient vector having $(p+1)(q+1) - 1$ elements, and where p and q represent the polynomial degrees with respect to the X- and Y-components, respectively.

Polynomial surface fitting consists of the estimation of the coefficient vector **a**, which we carry out again in the least-squares sense by minimizing the sum of squared ("vertical") residuals

$$\Omega^2 = \sum_{n=1}^{N} \left(l_n - \sum_{i=0}^{p} \sum_{j=0}^{q} a_{i,j} X_n^i Y_n^j \right)^2 \tag{7}$$

where $\mathbf{l} = [l_1, l_2, ..., l_N]$ is now an observation vector consisting of the N measured Z-coordinates. The design matrix

$$\mathbf{A}_1 = \begin{bmatrix} X_1^0 \cdot Y_1^0 & \cdots & X_1^i \cdot Y_1^j & \cdots & X_1^p \cdot Y_1^q \\ \vdots & & & & \vdots \\ X_N^0 \cdot Y_N^0 & \cdots & X_N^i \cdot Y_N^j & \cdots & X_N^p \cdot Y_N^q \end{bmatrix} \tag{8}$$

is computed by exponentiation (where $i = 0, 1, 2, \ldots, p$, $j = 0, 1, 2, \ldots, q$) and multiplication of the X- and Y-components, which are considered as error-free. Under the assumption again of homoskedastic and uncorrelated measurements, the estimated parameters are given by

$$\tilde{\mathbf{x}} = \begin{bmatrix} \tilde{a}_{0,0} \\ \vdots \\ \tilde{a}_{p,q} \end{bmatrix} = (\mathbf{A}_1^T \mathbf{A}_1)^{-1} \mathbf{A}_1^T \mathbf{l}. \tag{9}$$

2.2.3. Parameter Number of Competing Models

The approximation quality of a surface model is related to its complexity embodied in the number of parameters. Hence, when choosing pairs of models to be compared, we should pay attention to the parameter numbers.

In the initial comparison, the target segments of the point cloud of the first epoch are modeled by means of polynomial and B-spline surface functions with similar numbers of parameters in order to minimize the effect of model complexity. As the most basic description of a surface, the second degree polynomial function ($p = q = 2$) with six unknown parameters is approximated. A B-spline surface with the same parameter number ($n = 1$, $m = 2$) is modeled as a competitor. In order to facilitate a comprehensive analysis, polynomial functions of higher degrees are adjusted and compared to other estimated B-spline surface models. According to the general polynomial model Equation (6), a third-degree polynomial model is based on the specification of $p = q = 3$, resulting in 10 unknown parameters to be estimated. It is reasonable to compare this model with the adjusted B-spline surface involving nine parameters ($m = n = 2$). Further comparisons are carried out between the fourth-degree polynomial and B-spline surface models with 15 and 16 unknown parameters, respectively. Table 1 lists the candidate surface models mentioned above, where N_{poly} and N_B represent the number of parameters of the polynomial and of the B-spline models, respectively.

Table 1. The numbers of parameters for the various employed polynomial and B-spline surface models.

Pairs	Polynomial Model		B-Spline Model	
	Degree	N_{poly}	n, m	N_B
I	2nd	6	$n = 1, m = 2$	6
II	3rd	10	$n = 2, m = 2$	9
III	4th	15	$n = 3, m = 3$	16

It should be mentioned that polynomial functions of degrees higher than four are useless in our numerical example, since the resulting normal equation matrices within parameter estimation Equation (9) would be ill-conditioned. In this case, on the one hand, it is quite interesting to compare the best-fitting fourth-degree polynomial model with a higher-quality yet more complex B-spline surfaces when considering the complexity of models as penalization. It is predicted that the latter would be superior to the former in initial comparison pairs, but the superiority is expected to be offset by penalization due to increasing parameters. The comparison results of Segment I will be presented in Section 3.1 in Table 3 and in Appendix in Table A1. It helps to judge in which situation the B-spline models are recommended compared with the polynomial model. On the other hand, in practice, among the recommended B-spline models, we need the optimal one for further deformation analysis, which motivates the comparison within B-spline models. The comparison results of Segment I will be shown in Section 3.2 in Table 5 and in Appendix in Table A2.

2.3. Model Selection Method

The aim of model selection is to find a balance between the parsimony of the model and its approximation quality [21]. Unlike the trial-and-error procedures and information theoretic criterion

model selection approaches, we adopt the likelihood-ratio-based hypotheses testing framework to discriminate between the competing models. The likelihood ratio tests are generally used to compare two nested models; however, in our case, the polynomial surface model and B-spline model are non-nested because neither model can be reduced to the other by imposing a set of parametric restrictions or limiting process.

Regarding the non-nested models selection problem, in Cox [23] and Vuong [25], the authors proposed respective approaches to extend the likelihood ratio test into non-nested cases. In this subsection, both a simulation-based version of Cox's test and Vuong's test, which will be instantiated later with the experiment data, are explained.

2.3.1. Simulation-Based Version of Cox's Test

Under the assumption of normally distributed, uncorrelated and homoskedastic random deviations, the observation models can be defined in terms of the generic log-likelihood function

$$
\begin{aligned}
L(\mathbf{x}, \sigma^2; \mathbf{l}) &= \ln \prod_{n=1}^{N} \frac{1}{\sqrt{2\pi\sigma^2}} \exp\left\{ -\frac{1}{2} \left(\frac{l_n - \mathbf{A}_n \mathbf{x}}{\sigma} \right)^2 \right\} \\
&= -\frac{N}{2} \ln(2\pi) - \frac{N}{2} \ln(\sigma^2) - \frac{1}{2} \sum_{n=1}^{N} \frac{(l_n - \mathbf{A}_n \mathbf{x})^2}{\sigma^2}
\end{aligned}
\tag{10}
$$

where the variance factor σ^2 is treated as an unknown parameter alongside the functional parameters. Let us define $L_0(\mathbf{x}, \sigma^2; \mathbf{l})$, and $L_1(\mathbf{x}, \sigma^2; \mathbf{l})$ to be the specific log-likelihood functions with respect to the design matrices Equations (4) and (8), respectively. Both types of design matrix define different types of functions where neither is a special case of the other one. Thus, the two sets of multivariate normal distributions defined by L_0 and L_1 are non-nested, so that the likelihood ratio test cannot be applied in its usual form ([31] cf.) (pp. 276–278).

According to Cox [23], we may, however, use the logarithmized likelihood ratio

$$
\begin{aligned}
L_{0,1} &= L_0(\hat{\mathbf{x}}, \hat{\sigma}^2; \mathbf{l}) - L_1(\tilde{\mathbf{x}}, \tilde{\sigma}^2; \mathbf{l}) \\
&= -\frac{N}{2} \ln(\hat{\sigma}^2) - \frac{1}{2\hat{\sigma}^2} \sum_{n=1}^{N} (l_n - \mathbf{A}_{0n}\hat{\mathbf{x}})^2 + \frac{N}{2} \ln(\tilde{\sigma}^2) + \frac{1}{2\tilde{\sigma}^2} \sum_{n=1}^{N} (l_n - \mathbf{A}_{1n}\tilde{\mathbf{x}})^2
\end{aligned}
\tag{11}
$$

for testing the adequacy of the polynomial model against the B-spline model. Note that the substituted least squares solutions Equations (5) and (9) are identical to the maximum likelihood estimates; furthermore, the two occurring maximum likelihood estimates of the variance factor σ^2 are given by $\hat{\sigma}^2 = \frac{1}{N} \sum_{n=1}^{N} (l_n - \mathbf{A}_{0n}\hat{\mathbf{x}})^2$ and $\tilde{\sigma}^2 = \frac{1}{N} \sum_{n=1}^{N} (l_n - \mathbf{A}_{1n}\tilde{\mathbf{x}})^2$ ([31] cf.) (pp. 161). The statistic $L_{0,1}$ follows approximately a normal distribution

1. with certain expectation μ_0 and standard deviation σ_0 if the polynomial model is true, and
2. with certain expectation μ_1 and standard deviation σ_1 if the B-spline model is true.

Thus, we may calculate the approximately standard normally distributed statistics $T_0 = (L_{0,1} - \mu_0)/\sigma_0$ and $T_1 = (L_{0,1} - \mu_1)/\sigma_1$ for carrying out two separate tests of the hypotheses—

1. H_0 : the polynomial model is true;
2. H_1 : the B-spline model is true—

at significance level α. We may determine the means μ_0 and μ_1 as well as the standard deviations σ_0 and σ_1 conditionally on the two parameter solutions $(\hat{\mathbf{x}}, \hat{\sigma}^2)$, and $(\tilde{\mathbf{x}}, \tilde{\sigma}^2)$ through a Monte Carlo simulation in analogy to the approach taken in Williams [24].

According to that approach, we start by generating a large number M of observation vectors $\mathbf{l}^{(1)}, \ldots, \mathbf{l}^{(M)}$ randomly from the N-dimensional Gaussian distribution $N(\mathbf{A}\hat{\mathbf{x}}, \hat{\sigma}^2 \mathbf{I}_N)$. Based on these samples, we compute the corresponding solutions $(\hat{\mathbf{x}}^{(1)}; \hat{\sigma}^{(1)}), \ldots, (\hat{\mathbf{x}}^{(M)}; \hat{\sigma}^{(M)})$ with respect to the

polynomial model and $(\tilde{\mathbf{x}}^{(1)}; \tilde{\sigma}^{(1)}), \ldots, (\tilde{\mathbf{x}}^{(M)}; \tilde{\sigma}^{(M)})$ with respect to the B-spline model. We use the first solution set to evaluate the corresponding log-likelihood functions $L_0^{(1)}, \ldots, L_0^{(M)}$, and the second set to evaluate $L_1^{(1)}, \ldots, L_1^{(M)}$, so that we may compute the realizations $L_{0,1}^{(1)}, \ldots, L_{0,1}^{(M)}$ of Equation (11). Thus, the arithmetic mean and empirical standard deviation of these sampled logarithmized likelihood ratios serve as estimates of μ_0 and σ_0, leading to the standardized Gaussian test statistic T_0 under the currently assumed polynomial model.

The second test statistic T_1 (with respect to the test of the B-spline model) is computed in analogy to the first one, sampling now M observation vectors from $N(\mathbf{A}\tilde{\mathbf{x}}, \tilde{\sigma}^2 \mathbf{I}_N)$, and using the two new sets of parameter solutions (regarding the polynomial and B-spline model) to compute the M realizations of the log-likelihood ratios, as well as the resulting estimates of μ_1 and σ_1.

Since Cox [23] suggests applying the one-sided decision rules,

1.　reject H_0 if $T_0 < k_\alpha^{N(0,1)}$, and
2.　reject H_1 if $T_1 > k_{1-\alpha}^{N(0,1)}$

(where $k_\alpha^{N(0,1)}$ is the α-quantile and $k_{1-\alpha}^{N(0,1)}$ the $1-\alpha$-quantile of the standard normal distribution), the execution of the two tests may result in four mutually exclusive decisions:

1.　The polynomial model is rejected and the B-spline model is not rejected in the case of

$$T_0 < k_\alpha^{N(0,1)} \ \wedge \ T_1 \leq k_{1-\alpha}^{N(0,1)}. \tag{12}$$

2.　The B-spline model is rejected and the polynomial model is not rejected in the case of

$$T_0 \geq k_\alpha^{N(0,1)} \ \wedge \ T_1 > k_{1-\alpha}^{N(0,1)}. \tag{13}$$

3.　Both the polynomial and the B-spline models are rejected in the case of

$$T_0 < k_\alpha^{N(0,1)} \ \wedge \ T_1 > k_{1-\alpha}^{N(0,1)}. \tag{14}$$

4.　Neither the polynomial nor the B-spline model is rejected in the case of

$$T_0 \geq k_\alpha^{N(0,1)} \ \wedge \ T_1 \leq k_{1-\alpha}^{N(0,1)}. \tag{15}$$

2.3.2. Vuong's Non-Nested Hypothesis Test

Vuong's test is based on the Kullback–Leibler information criterion (KLIC), which measures the closeness of two models and uses the likelihood-ratio-based statistics to test the null hypothesis that the competing models are equally close to the true data generating process against the alternative hypothesis that one model is closer [25]. Specifically, the two competing models are given as $\mathbf{F}_\theta = \{f(l; \theta); \theta \in \Theta\}$ and $\mathbf{G}_\gamma = \{g(l; \gamma); \gamma \in \Gamma\}$, l denotes variables, and θ and γ are their respective parameters. As defined by Vuong, the two models' Kullback–Leibler distances from the true density $h_0(l)$ are $E_0[\ln h_0(l)] - E_0[\ln f(l; \theta_*)]$ and $E_0[\ln h_0(l)] - E_0[\ln g(l; \gamma_*)]$, respectively, where E_0 denotes the expectation under the true model, and θ_* and γ_* are the pseudo-true values of θ and γ. It is clear that the model with a minimum KLIC value is closer to the truth, which is, however, hard to quantify. Thus, an equivalent selection criterion can be based on the quantities $E_0[\ln f(l; \theta_*)]$ and $E_0[\ln g(l; \gamma_*)]$, the better model being the one with larger quantity.

There are three possible cases when comparing, and we propose the null hypothesis, as the two models have equal expectation values so that they are equivalent. One alternative hypothesis is $E_0[\ln f(l; \theta_*)] > E_0[\ln g(l; \gamma_*)]$, which means $\mathbf{F}_\theta$ is the better model. The other alternative hypothesis is $E_0[\ln f(l; \theta_*)] < E_0[\ln g(l; \gamma_*)]$, meaning $\mathbf{G}_\gamma$ is better. Since the quantity $E_0[\ln f(l; \theta_*)] - E_0[\ln g(l; \gamma_*)]$ is still hard to quantify, Vuong consistently estimates it by $(1/n)$ times the likelihood ratio statistic.

In our specific case to discriminate between the polynomial and B-spline surface models, with independent and identically distributed observations **l**, the probability density functions of competing models are given as $\mathbf{P}_{\mathbf{x},\sigma} = \{p(l; \mathbf{x}, \sigma^2)\}$ and $\mathbf{B}_{\mathbf{x},\sigma} = \{b(l; \mathbf{x}, \sigma^2)\}$, in which the parameter matrix **x** is estimated in its respective Gauss–Markov models and the variance factor σ^2 for competing models is calculated in the same way as in Cox's test: $\hat{\sigma}^2 = \frac{1}{N}\sum_{n=1}^{N}(l_n - \mathbf{A_0}_n\hat{\mathbf{x}})^2$ and $\tilde{\sigma}^2 = \frac{1}{N}\sum_{n=1}^{N}(l_n - \mathbf{A_1}_n\tilde{\mathbf{x}})^2$. Thus, we propose the hypothesis in discriminating between models as follows:

1. H_0: the polynomial and B-spline models are equally close to the truth;
2. H_p: the polynomial model is better since it is closer to the truth than the B-spline model is;
3. H_b: the B-spline model is better since it is closer to the truth than the Polynomial model.

Similar to Cox's test, the statistic of Vuong's test is also based on likelihood ratio. If we define $L_0(\hat{\mathbf{x}}, \hat{\sigma}^2; \mathbf{1})$ and $L_1(\tilde{\mathbf{x}}, \tilde{\sigma}^2; \mathbf{1})$ as log-likelihood functions for competing polynomial and B-spline surface models, the logarithmized likelihood ratio $L_{0,1}$ is calculated as (11). Vuong's test is potentially sensitive to the number of estimated parameters on condition that the logarithmized likelihood ratio $L_{0,1}$ is adjusted by a correction factor K.

$$\tilde{L}_{0,1} \equiv L_{0,1} - K. \tag{16}$$

Vuong [25] suggests that K corresponds to either Akaike's information criteria (AIC) or Bayesian information criteria (BIC). According to the former, $K = p_0 - p_1$, and, according to the latter, $K = (p_0/2)\ln N - (p_1/2)\ln N$, where p_0 and p_1 are numbers of parameters in competing models. The BIC generally penalizes free parameters more strongly than AIC. Here, we prefer the BIC correction factor in order to avoid an over-fitting problem.

Then, the adjusted likelihood ratio $\tilde{L}_{0,1}$ is rescaled in statistic as $T_V = N^{-1/2}\tilde{L}_{0,1}/\hat{w}$, where $\hat{w}^2$ is the variance calculated as

$$\hat{w}^2 = \frac{1}{N}\sum_{n=1}^{N}\left[\ln\frac{p(l_n; \mathbf{A_0}_n\hat{\mathbf{x}}, \hat{\sigma}^2)]}{b(l_n; \mathbf{A_1}_n\tilde{\mathbf{x}}, \tilde{\sigma}^2)}\right]^2 - \left[\frac{1}{N}\sum_{n=1}^{N}\ln\frac{p(l_n; \mathbf{A_0}_n\hat{\mathbf{x}}, \hat{\sigma}^2)]}{b(l_n; \mathbf{A_1}_n\tilde{\mathbf{x}}, \tilde{\sigma}^2)}\right]^2. \tag{17}$$

According to Vuong [25], when N is reasonably large, the statistic T_V converges, asymptotically to a standard normal distribution, $N(0,1)$. In the decision-making process, practically, we compare T_V against the quantiles of a standard normal distribution, $C_{\alpha/2}^{N(0,1)}$, for significance level α. The models are discriminated through the following decision rules:

1. The polynomial and B-spline models are equally close to the truth in case of

$$C_{\alpha/2}^{N(0,1)} \leq T_V \leq C_{1-\alpha/2}^{N(0,1)}. \tag{18}$$

2. The polynomial model is better since it is closer to the truth than B-spline model in case of

$$T_V > C_{1-\alpha/2}^{N(0,1)}. \tag{19}$$

3. The B-spline model is better since it is closer to the truth than Polynomial model in case of

$$T_V < C_{\alpha/2}^{N(0,1)}. \tag{20}$$

2.4. Deformation Analysis

To probe the selected surface model's performance in deformation analysis, each target segment of the 1st and 13th epochs are approximated by surface models. In the specific application, loads were exerted perpendicular to the ground (in the Z-direction) so that the deformation (Δ) is defined as the difference in approximated Z-coordinates of the two epochs ($\hat{\mathbf{Z}}_{13}, \hat{\mathbf{Z}}_1$), that is,

$$\Delta = \hat{\mathbf{Z}}_{13} - \hat{\mathbf{Z}}_1. \tag{21}$$

The evaluation criterion of surface models' performance is whether they are able to reflect the actual deformation, which are recorded by the point cloud. Since it is impossible to get an exact mutual spatial referencing of points in the different epochs, we compared the point clouds through the block-mean approach used in Paffenholz et al. [32]. In this application, the blocks had a size of 5 mm × 5 mm involving 2–9 points, for which the medians of the *Z*-coordinates were computed as representative values. The high-density block-means between the two epochs were used to approximate the point-wise changes.

3. Results

3.1. Evaluation of Competing Polynomial and B-Spline Models

In order to statistically discriminate between the aforementioned polynomial and B-spline surface models listed in Table 1, the result of Cox's and Vuong's test for the two segments are given in Tables 2 and 4, respectively. It is noticeable that the observations are assumed to be following identical and independent normal distribution, which satisfy the prerequisite of both tests. In addition, Figure 4 demonstrates that the 10,000 log-likelihood ratio values of Equation (11) sampled with respect to Cox's test follow approximately a Gaussian distribution under both the polynomial and B-spline surface models. Thus, it is justified to standardize the log-likelihood ratio computed from the actual measurements by means of the sample mean and standard deviation under each of the two stochastic models (resulting in the values for T_0 and T_1 shown in Tables 2 and 4).
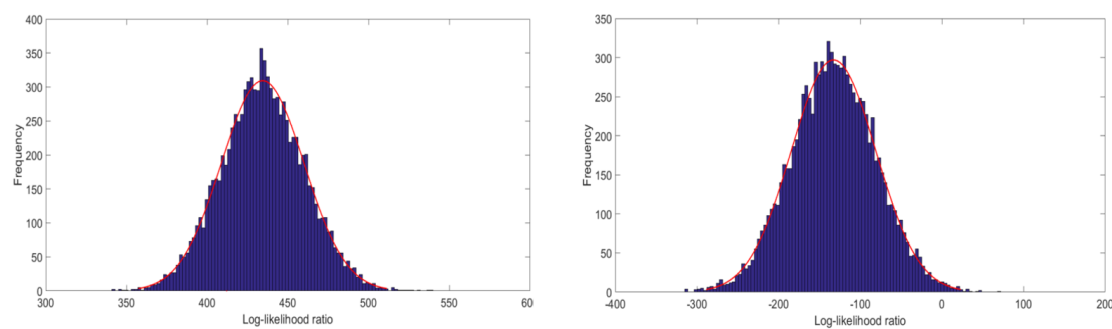

Figure 4. Histogram of the sampled log-likelihood ratio $L_{0,1}$ under the polynomial (**left**) and B-spline (**right**) surface model, approximated by a Gaussian density functions (in red).

The statistics are compared to the critical value at type-I error rate $\alpha = 0.05$. In Cox's test, the critical values are $k_{0.05}^{N(0,1)} = -1.64$ for statistic T_0, and $k_{0.95}^{N(0,1)} = 1.64$ for statistic T_1. In Vuong's test, the critical values are $C_{0.025}^{N(0,1)} = -1.96$ and $C_{0.975}^{N(0,1)} = 1.96$.

It can be clearly seen in Table 2 that, within the first pair of models, the B-spline surface model with six parameters is preferred over the second-degree polynomial model, since, in Vuong's test, the former is better verified, and, in Cox's test, the latter is rejected. This result indicates, with minor parameters, B-spline models are superior to the equivalent polynomial one. This conjecture is validated. In the second pair of models, neither the third-degree polynomial model nor the B-spline model is rejected or selected by tests, whose findings indicate that there is no significant difference between the two models. Next, further comparisons are carried out within Pair III between a fourth-degree polynomial and B-spline models with 15 and 16 unknown parameters, respectively. According to the tests results, Vuong's test indicates there is no significant superiority between the two, while the polynomial model is rejected by the Cox's test.

As mentioned before, polynomial functions of degrees greater than four become numerically unstable due to the appearance of singular matrices, so that they cannot be recommended. By contrast, approximated B-spline surface models for Segment I can describe the target segment of the point cloud

increasingly well when the parameters are increased, without producing such numerical difficulties. When comparing the increasingly accurate B-spline models with the fourth-degree polynomial surface model of Segment I by means of both hypothesis tests, as previous predicted, we find that the Cox's test always rejects the models with fewer parameters, which leads to the problem of over-fitting. By contrast, Vuong's test initially tends to prefer B-spline models due to higher approximation quality until Pair 36, in which large quantities of parameters are set ($N_B = 1600$). Table 3 offers the last five comparison pairs to show the aforementioned change in test decision. The complete test results for discriminating between fourth-degree polynomial and B-spline surface models are shown in Table A1.

Table 2. Results for Segment I of Cox's test for discriminating between polynomial and B-spline surface models at type-I error rate $\alpha = 0.05$.

Pair	Cox's Test				Vuong's Test	
	T_0	Rejected	T_1	Rejected	T_V	Preferred
I	−39.93	polynomial	−23.44	no	−29.95	B-spline
II	−0.68	no	1.44	no	0.19	no
III	−14.85	polynomial	−1.21	no	0.37	no

Table 3. Partial results for Segment I of Vuong's test and Cox's test for discriminating between fourth-degree polynomial and B-spline surface models at type-I error rate $\alpha = 0.05$.

Pair	Competing Models		Cox's Test				Vuong's Test	
	Polynomial	B-Spline	T_0	Rejected	T_1	Rejected	T_V	Preferred
32	$N_{poly} = 15$	$N_B = 1296$	−236.65	polynomial	−70.33	no	−8.99	B-spline
33	$N_{poly} = 15$	$N_B = 1369$	−213.58	polynomial	−72.86	no	−9.28	B-spline
34	$N_{poly} = 15$	$N_B = 1444$	−199.14	polynomial	−70.94	no	−5.00	B-spline
35	$N_{poly} = 15$	$N_B = 1521$	−192.05	polynomial	−84.49	no	−3.14	B-spline
36	$N_{poly} = 15$	$N_B = 1600$	−180.07	polynomial	−80.21	no	−0.36	no

The testing results for Segment II are listed in Table 4. It is indicated by the first comparison pair that both the polynomial and the B-spline surface models are rejected by Cox's test, while Vuong's test considers the polynomial model to be closer to the truth than its competitor. Within the second and third pairs, B-spline models are judged as insufficient by Cox's test, whereas the polynomial models are preferred by Vuong's test.

Table 4. Results for segment II of Cox's test for discriminating between polynomial and B-spline surface models at type-I error rate $\alpha = 0.05$.

Pair	Cox's Test				Vuong's Test	
	T_0	Rejected	T_1	Rejected	T_V	Preferred
I	−3.96	polynomial	4.46	B-spline	5.95	polynomial
II	−1.58	no	5.89	B-spline	7.43	polynomial
III	0.87	no	10.65	B-spline	11.31	polynomial

The testing result differs greatly between the two segments. These differences can be explained by the fact that Segment II contains large data gaps, which substantially distort the B-spline model estimation, in contrast to the polynomial model estimation.

3.2. Evaluation of Competing B-Spline Models with Various Parameters

The results in Table 3 motivate us to evaluate B-spline surface models with increasing parameters by means of Vuong's test in search of a balance between model complexity and its approximation

quality. Two B-spline models with different degrees or control points (Model I and Model II) are non-nested because the parameters in Model I are not a subset of the parameters in Model II. The modification of the degree or the number of control points (see Equation (1)) leads to a change in the number of knots, resulting in different basis functions. The comparison of pair setting and evaluation results are shown in Table A2, where $N_{B1} = (m_1 + 1) \cdot (n_1 + 1)$ denotes the parameter number of the first B-spline model and $N_{B2} = (m_2 + 1) \cdot (n_2 + 1)$ denotes that of the second model in the competing pair. The statistic value and test decision are shown in the last two columns. Here, we present the comparison results of B-spline models with $m_1 = n_1 = i$ and $m_2 = n_2 = i + 2$ ($i = 1, 2, 3...37$) instead of neighbor models ($m_1 = n_1 = i$, $m_2 = n_2 = i + 1$). There were large oscillations in the testing results of the pairwise neighbor models. These oscillations, which were due to the similar parameter number and model quality between neighbor models, served as noise and would confuse the result. The testing results became stable when we chose comparison models as $m_1 = n_1 = i$ and $m_2 = n_2 = i + 2$.

According to the results in Table A2, B-Spline Model II with more parameters is preferred initially; however, due to the increasing penalized term, B-Spline Model I is preferred in the final pair. The middle comparison pairs are considered to be in the overlapping region, where the test decisions swing between the two competing models. Table 5 shows the comparison pairs in the overlapping region. It can be considered that the balance sought of the model's complexity and its approximation quality is located in this region. Figure 5 offers a direct view of test statistic T_V in comparison with critics boundaries $C_{0.025}^{N(0,1)} = -1.96$ and $C_{0.975}^{N(0,1)} = 1.96$.

Table 5. Partial results of Vuong's test for discriminating B-spline surface models at type-I error rate $\alpha = 0.05$ (overlapping region).

Pair	B-Spline Model I		B-Spline Model II		Vuong's Test	
	m_1, n_1	N_{B1}	m_2, n_2	N_{B2}	T_V	Preferred
13	$m_1 = n_1 = 14$	225	$m_2 = n_2 = 16$	289	-0.57	no
14	$m_1 = n_1 = 15$	256	$m_2 = n_2 = 17$	324	-6.57	model 2
15	$m_1 = n_1 = 16$	289	$m_2 = n_2 = 18$	361	-4.06	model 2
16	$m_1 = n_1 = 17$	324	$m_2 = n_2 = 19$	400	-3.89	model 2
17	$m_1 = n_1 = 18$	361	$m_2 = n_2 = 20$	441	-4.15	model 2
18	$m_1 = n_1 = 19$	400	$m_2 = n_2 = 21$	484	3.02	model 1
19	$m_1 = n_1 = 20$	441	$m_2 = n_2 = 22$	529	9.09	model 1
20	$m_1 = n_1 = 21$	484	$m_2 = n_2 = 23$	576	0.41	no

We consider the B-spline model with 361 parameters ($n = 18, m = 18$), which lies roughly in the middle of the overlapping region, as the optimal one. Figure 6 shows the side- and top-view of this surface model.
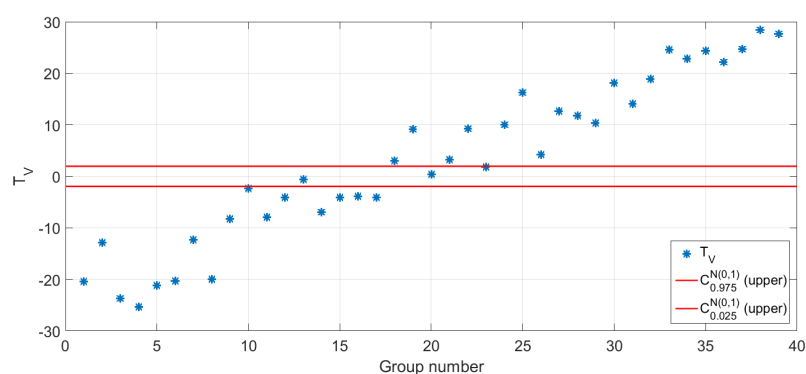

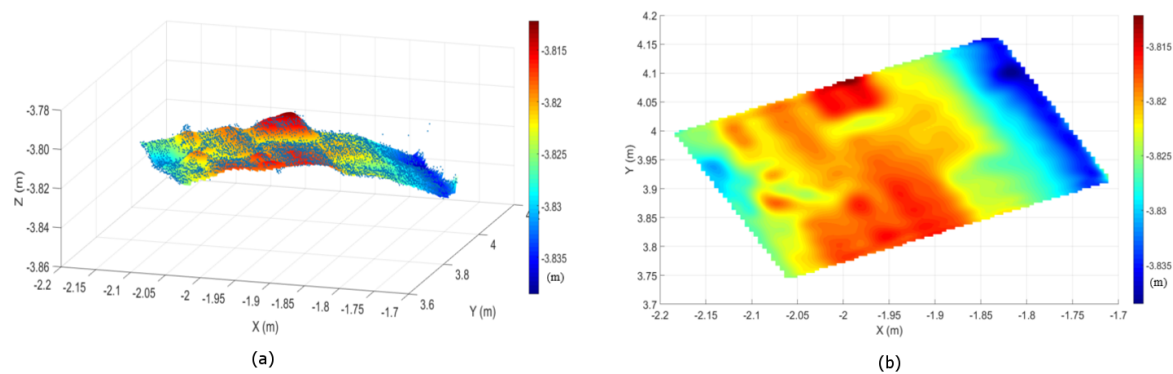**Figure 5.** Statistic values of Vuong's test in comparison with critics.

Figure 6. Side-view (**a**) and top-view (**b**) of approximated B-spline surface ($n = 18, m = 18$) with the original measurements (blue points).

3.3. Performance in Deformation Analysis

3.3.1. Deformation of Segment I

According to the model evaluation results for Segment I, the fourth-degree model is best-fitting among polynomial surface models, while the B-spline surface model with 361 parameters is optimal among all candidate models. We approximate both types of surface models for the point cloud in the 13th epoch with the same number of parameters.

Because traditional polynomial models are still the most widely used regression method in deformation analysis due to their simple operating, while the B-spline model has the potential to describe geometrically complicated objects, it is of significance to compare the performance in this numerical example between two surface models with their best-fitting parameters in reflecting deformation. In Figure 7a shows the modeled fourth-degree polynomial surfaces for the 1st (upper) and 13th (lower) epochs, while Figure 7b shows the equivalent epochs approximated by means of B-spline surfaces with 361 parameters. It is obvious that the B-spline surfaces in Figure 7b describe more detailed geometrical features than polynomial model in Figure 7a. The arch's deformation in Z-coordinates between the two epochs are shown in Figures 7c,d, by means of approximated polynomial surfaces of Figure 7a and B-spline models of Figure 7b, respectively. In order to validate that the reflected changes are the real arch's deformation recorded by the points instead of regression models, we compare the two epochs' point cloud through the block-mean approach (see Figure 8 for the differences between the two epoch's point clouds). By comparison, it is obvious that the deformation shown in Figure 7d for B-spline models reflect these differences precisely, especially in Areas A and B; in contrast, the fourth-degree polynomial surfaces in Figure 7c fail to show this deformation due to their global smoothing effect. The preceding difference and model deformation are also shown pointwise in Figure 9. The green asterisks denote the point-wise differences recorded by block-means, while the red and blue asterisks are that reflected by the fourth-degree polynomial and B-spline surfaces, respectively.
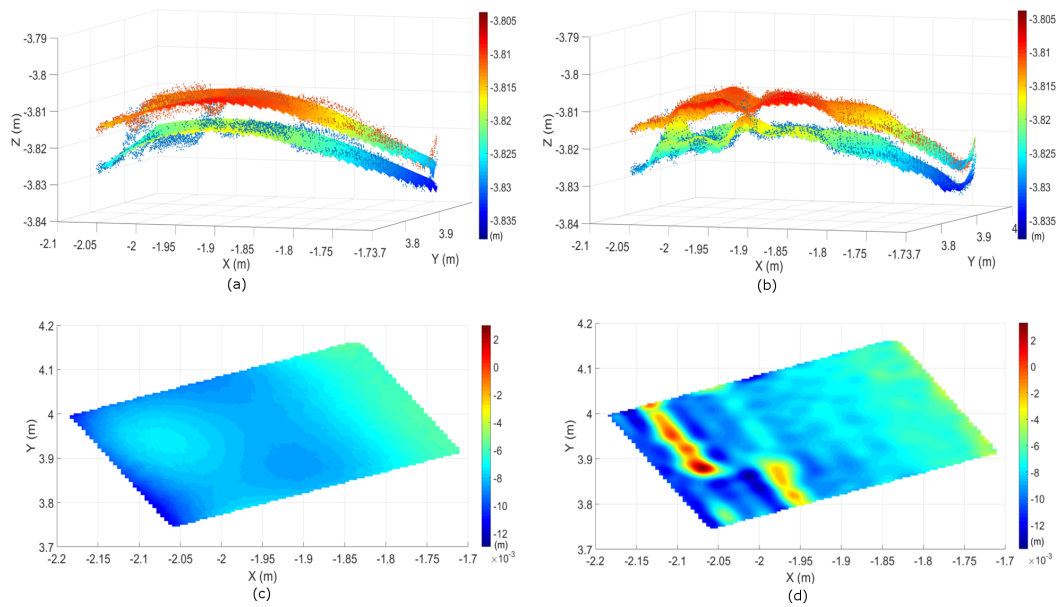
Figure 7. Polynomial (**a**,**c**) and B-spline surface models (**b**,**d**) in terms of differences of the 1st and 13th epochs in Segment I.
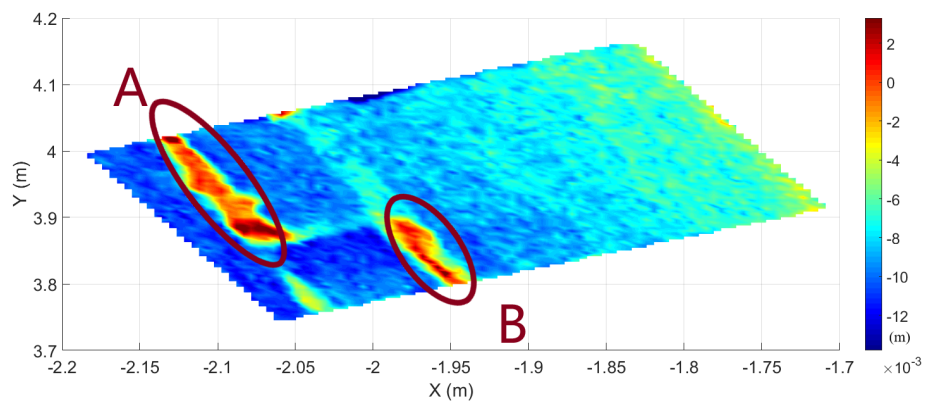

Figure 8. Deformation of segment I reflected by block means of the point cloud differences based on the 1st and 13th epochs.
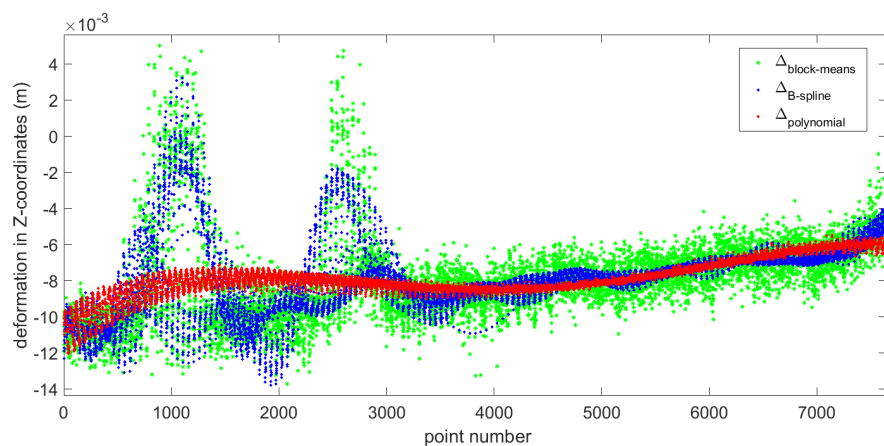

Figure 9. Deformation of Segment I between 1st and 13th epochs reflected by various approaches.

3.3.2. Deformation of Segment II

In Figure 10a shows the modeled fourth-degree polynomial surfaces for the 1st (upper) and 13th (lower) epochs, while Figure 10b shows the same epochs approximated by means of B-spline surfaces with 16 parameters.
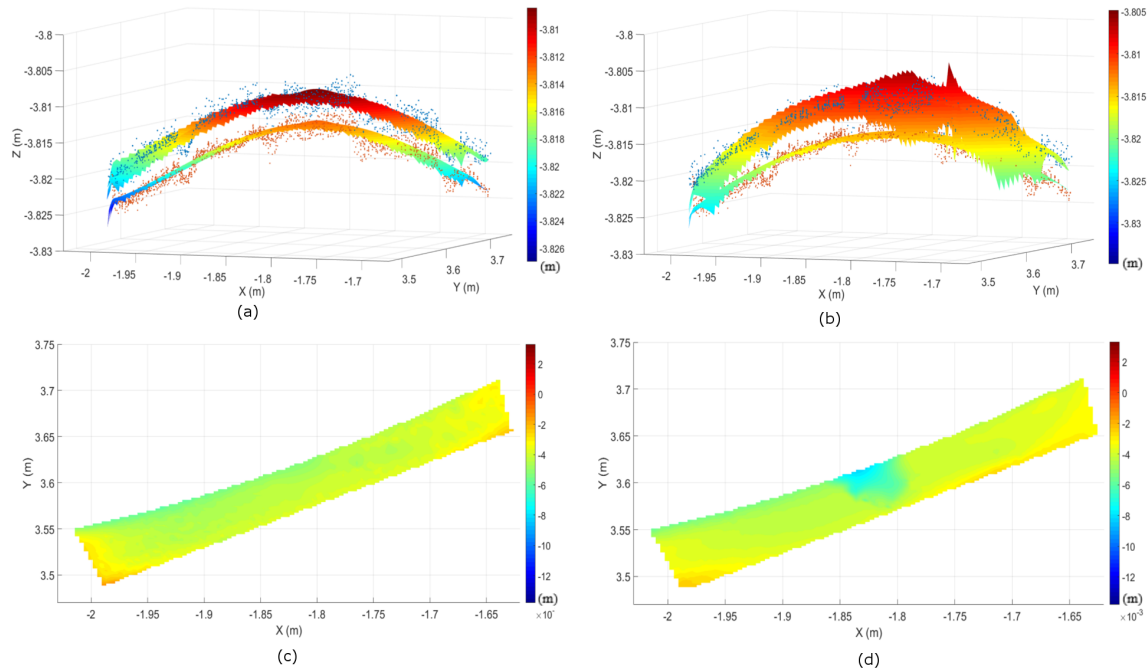

Figure 10. Polynomial (**a**,**c**) and B-spline surface models (**b**,**d**) in reflecting deformation of segment II based on the 1st and 13th epochs.

The missing data lead to oscillation, especially at the edges of the data gap (see the bounded area in Figure 11). Thus, it can be found from Figure 10d that the deformation reflected by B-splines is far from the truth. Here, the estimated B-spline surfaces clearly show the aforementioned numerical instabilities, which are caused by an inadequate specification of the knot locations with the applied classical approach to knot vector determination in Piegl and Tiller [29].
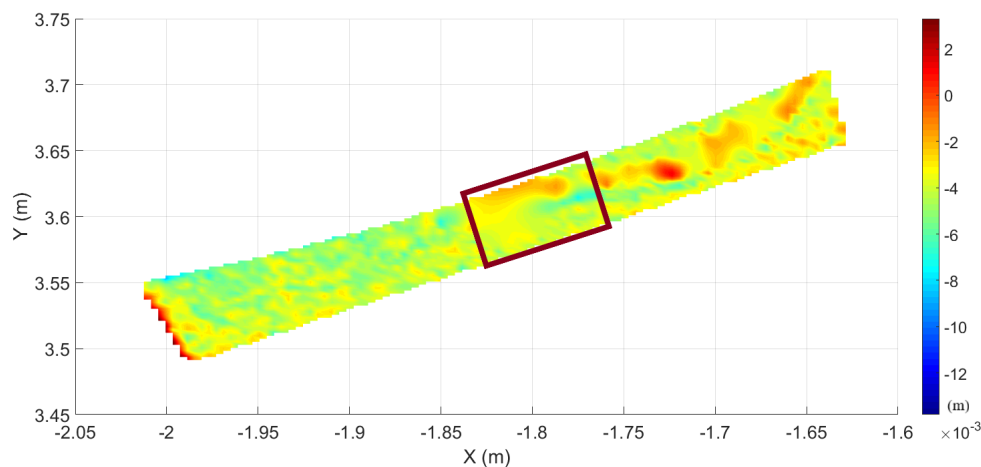

Figure 11. Deformation of Segment II reflected by block means of the point cloud differences based on the 1st and 13th epochs.

4. Discussion

In our numerical example of Segment I, the different results between the two hypothesis tests are caused by the penalized term regarding the parameter numbers. In Table 2, for example, Pair III has various test results. In Cox's test, the fourth-degree polynomial model is rejected because of the relatively poor accuracy, while the Vuong's test result recommends neither, because the improved accuracy is offset by the punishment of increasing parameters. In parallel, in Table 3, the test decision initially shows in the consistency of both tests that the B-spline models are better compared to the fourth-degree polynomial model. However, as the number of parameters increase, the improvement of model accuracy declines. Finally, in Voung's test, the advantage of the model's quality is offset again by the large penalized value and, consequently, shows results that are different from Cox's test in Pair 36.

Although Cox's test without penalized term is limited to discriminate models with similar parameters, it is practically very straightforward to implement and are able to offer more reliable decisions by simulating the test distribution, especially when the sample size is small [33]. We expect to improve the simulation-based version of Cox's test by adding a proper correction factor similar to that in Vuong's non-nested hypothesis test, which would be one of our future research projects.

Since previous geodetic literatures [21,22,28] has solved the model selection problem through well-known penalization information criteria: the AIC and BIC, it is necessary in this section to compare Vuong's non-nested hypothesis test with this widely used approach. It is noticeable that there are close connections between AIC, BIC, and Vuong's test. Taking the BIC as an example, the value of model 1 is calculated as

$$BIC_1 = -2\ln L_1 - p_1 \cdot \ln N \tag{22}$$

where L_1 is the maximum value of the likelihood function for Model 1, p_1 denotes the parameter quantity, and N is the number of measurements. The different BIC value between two models is calculated as

$$BIC_{12} = -2\ln \frac{L_1}{L_2} - (p_1 - p_2) \cdot \ln N \tag{23}$$

where the first term in the right part contains logarithmized likelihood ratio $L_{0,1}$ in Equation (16), so that BIC_{12} is equal to the (un-normalized) adjusted test statistic $\tilde{L}_{0,1}$ for Vuong's test. The main difference is that Vuong's test makes judgments in a framework of likelihood ratio hypothesis testing, which offers the advantage that significant probabilistic differences between models can be detected, which is not provided by classical penalization information criterion methods. We compared the Vuong's test results with both the AIC and BIC to discriminate between B-spline surface models, and the result is shown in Figure 12. According to the BIC's curve, the B-spline model with 361 parameters ($n = 18$, $m = 18$) is optimal, since it is associated with the smallest value. This result is quite consistent with the judgment of Vuong's test, because the BIC penalized term is used in our adjusted test statistic. By contrast, the AIC tends to prefer much larger models.

Furthermore, the performance of best-fitting polynomial and B-spline surfaces in reflecting deformation were compared. The superior model was the one able to reflect the deformation details recorded by the point clouds. In order to get an exact mutual spatial referencing of points in the different epochs, we used the block-mean approach to approximate the point-wise changes. The comparison results of Segment I indicated that the selected B-spline surfaces can reflect the actual deformation, especially in Areas A and B of Figure 8, while the best-fitting polynomial model failed to offer this information due to its global smooth effect. However, in the case of Segment II, B-spline models failed to reflect the actual deformation values, especially at the edges of the data gap.
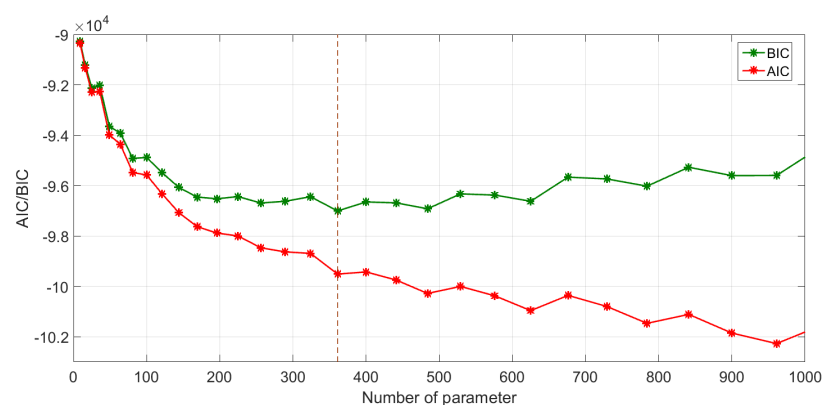
Figure 12. AIC (**red**) and BIC (**green**) values with an increasing number of parameters.

5. Conclusions

In this paper, we approximated point cloud data of a surveyed arch structure by two common surface models: polynomials and B-splines. Subsequently, we compared different adjusted surface models via Cox's test and Vuong's test to select an appropriate parametric model, which was sufficient to describe the geometrical features of the two target segments.

Regarding Segment I, in the initial comparison between lower degree polynomial and B-spline models, none of the B-spline models investigated was rejected, but only the polynomial model with degree 3 was found to be adequate in Cox's test, while Voung's test indicated no significant difference in Pairs II and III. However, none of these models could reflect detailed geometrical features of target segments. Since it was not possible to increase the degree of polynomial approximation (due to numerical instability of the normal equations) for modeling geometrical details, B-splines were recommended in the field of applications presented. That motivated us to search for an optimal model balancing between approximation quality and its complexity. According to Voung's test decisions, the B-spline surface model with $N_B = 361$ was considered as the optimal one in the specific numerical example.

The model selection testing results of Segment II were quite different from that of Segment I. All the B-spline models were rejected by Cox's test, while in Pairs II and III, the equivalent polynomial surfaces were preferred by Voung's test, as a consequence of the aforementioned numerical instabilities with the knot vector determination and the resulting oscillation effects. Such deficiencies were clearly reflected by the model selection tests, which rejected inadequate B-spline models.

A consistent model selection result was obtained by comparing Vuong's test decision with the widely used BIC in discriminating B-spline surface models. Thus, it is concluded that the alternative model selection methodology elaborated in this paper, in parallel with well-known penalization information criteria, can effectively guide practitioners in selecting a parsimonious and accurate model for structures, such as the arch in the numerical example presented. The main difference is that Vuong's test makes judgments in a framework of likelihood ratio hypothesis testing, which can detect the significant probabilistic differences between models. It was proved here that the models selected by the model selection tests have good performance in reflecting actual deformation.

The model selection methodology is applicable not only to TLS data but also to point clouds obtained by other LiDAR technology, such as airborne laser scanning and mobile laser scanning. There are also distribution-free hypothesis tests, such as Clarke's test [34], available for mixed distribution observations.

Author Contributions: Xin Zhao conducted the statistical analysis and wrote the manuscript; Boris Kargoll contributed to the analysis approach and provide advice with respect to the manuscript; Mohammad

Omidalizarandi contributed to the data processing; Xiangyang Xu helped to conceive the study and motivate the paper; Hamza Alkhatib organized the study and commented on the manuscript.

Conflicts of Interest: The authors declare no conflict of interest.

Abbreviations

The following abbreviations are used in this manuscript:

AIC	Akaike information criterion
BIC	Bayesian information criterion
KLIC	Kullback-Leibler information criterion
MSS	multi-sensor-system
RMSD	root-mean-square deviation
TLS	terrestrial laser scanning

Appendix A

Table A1. Results for Segment I of Vuong's test and Cox's test for discriminating between fourth-degree polynomial and B-spline surface models at type-I error rate $\alpha = 0.05$.

Pair	Competing Models		Cox's Test				Vuong's Test	
	Polynomial	B-Spline	T_0	Rejected	T_1	Rejected	T_V	Preferred
1	$N_{poly} = 15$	$N_B = 25$	−96.88	polynomial	−6.31	no	−14.92	B-spline
2	$N_{poly} = 15$	$N_B = 36$	−82.69	polynomial	−5.30	no	−14.59	B-spline
3	$N_{poly} = 15$	$N_B = 49$	−210.65	polynomial	−17.54	no	−13.99	B-spline
4	$N_{poly} = 15$	$N_B = 64$	−324.26	polynomial	−19.77	no	−13.37	B-spline
5	$N_{poly} = 15$	$N_B = 81$	−306.37	polynomial	−31.21	no	−12.58	B-spline
6	$N_{poly} = 15$	$N_B = 100$	−323.49	polynomial	−28.37	no	−12.75	B-spline
7	$N_{poly} = 15$	$N_B = 121$	−338.20	polynomial	−33.64	no	−13.23	B-spline
8	$N_{poly} = 15$	$N_B = 144$	−359.43	polynomial	−38.19	no	−11.79	B-spline
9	$N_{poly} = 15$	$N_B = 169$	−325.74	polynomial	−42.33	no	−10.44	B-spline
10	$N_{poly} = 15$	$N_B = 196$	−341.49	polynomial	−41.76	no	−9.68	B-spline
11	$N_{poly} = 15$	$N_B = 225$	−294.75	polynomial	−48.19	no	−11.53	B-spline
12	$N_{poly} = 15$	$N_B = 256$	−333.69	polynomial	−50.22	no	−10.59	B-spline
13	$N_{poly} = 15$	$N_B = 289$	−279.57	polynomial	−46.54	no	−11.23	B-spline
14	$N_{poly} = 15$	$N_B = 324$	−318.33	polynomial	−51.20	no	−10.02	B-spline
15	$N_{poly} = 15$	$N_B = 361$	−317.28	polynomial	−52.92	no	−9.90	B-spline
16	$N_{poly} = 15$	$N_B = 400$	−275.54	polynomial	−59.22	no	−7.43	B-spline
17	$N_{poly} = 15$	$N_B = 441$	−276.37	polynomial	−52.10	no	−8.55	B-spline
18	$N_{poly} = 15$	$N_B = 484$	−313.79	polynomial	−66.44	no	−9.12	B-spline
19	$N_{poly} = 15$	$N_B = 529$	−262.48	polynomial	−54.70	no	−7.99	B-spline
20	$N_{poly} = 15$	$N_B = 576$	−270.20	polynomial	−56.54	no	−10.10	B-spline
21	$N_{poly} = 15$	$N_B = 625$	−285.65	polynomial	−49.27	no	−6.99	B-spline
22	$N_{poly} = 15$	$N_B = 676$	−268.69	polynomial	−68.30	no	−10.59	B-spline
23	$N_{poly} = 15$	$N_B = 729$	−267.04	polynomial	−62.88	no	v8.99	B-spline
24	$N_{poly} = 15$	$N_B = 784$	−241.21	polynomial	−67.39	no	−9.54	B-spline
25	$N_{poly} = 15$	$N_B = 841$	−268.29	polynomial	−68.11	no	−8.99	B-spline
26	$N_{poly} = 15$	$N_B = 900$	−280.65	polynomial	−75.17	no	−8.70	B-spline
27	$N_{poly} = 15$	$N_B = 961$	−217.72	polynomial	−69.20	no	−6.99	B-spline
28	$N_{poly} = 15$	$N_B = 1024$	−258.19	polynomial	−84.32	no	−7.37	B-spline
29	$N_{poly} = 15$	$N_B = 1089$	−227.56	polynomial	−80.89	no	−8.67	B-spline
30	$N_{poly} = 15$	$N_B = 1156$	−240.33	polynomial	−82.54	no	−9.77	B-spline
31	$N_{poly} = 15$	$N_B = 1225$	−232.69	polynomial	−72.30	no	−7.59	B-spline
32	$N_{poly} = 15$	$N_B = 1296$	−236.65	polynomial	−70.33	no	−8.99	B-spline
33	$N_{poly} = 15$	$N_B = 1369$	−213.58	polynomial	−72.86	no	−9.28	B-spline
34	$N_{poly} = 15$	$N_B = 1444$	−199.14	polynomial	−70.94	no	−5.00	B-spline
35	$N_{poly} = 15$	$N_B = 1521$	−192.05	polynomial	−84.49	no	−3.14	B-spline
36	$N_{poly} = 15$	$N_B = 1600$	−180.07	polynomial	−80.21	no	−0.36	no

Table A2. Results of Vuong's test for discriminating B-spline surface models at type-I error rate $\alpha = 0.05$.

Pair	B-Spline Model I		B-Spline Model II		Vuong's Test	
	m_1, n_1	N_{B1}	m_2, n_2	N_{B2}	T_V	Preferred
1	$m_1 = n_1 = 2$	9	$m_2 = n_2 = 4$	25	-20.46	model 2
2	$m_1 = n_1 = 3$	16	$m_2 = n_2 = 5$	36	-12.84	model 2
3	$m_1 = n_1 = 4$	25	$m_2 = n_2 = 6$	49	-23.72	model 2
4	$m_1 = n_1 = 5$	36	$m_2 = n_2 = 7$	64	-25.30	model 2
5	$m_1 = n_1 = 6$	79	$m_2 = n_2 = 8$	81	-21.23	model 2
6	$m_1 = n_1 = 7$	64	$m_2 = n_2 = 9$	100	-20.32	model 2
7	$m_1 = n_1 = 8$	81	$m_2 = n_2 = 10$	121	-12.28	model 2
8	$m_1 = n_1 = 9$	100	$m_2 = n_2 = 11$	144	-20.03	model 2
9	$m_1 = n_1 = 10$	121	$m_2 = n_2 = 12$	169	-8.31	model 2
10	$m_1 = n_1 = 11$	144	$m_2 = n_2 = 13$	196	-2.30	model 2
11	$m_1 = n_1 = 12$	169	$m_2 = n_2 = 14$	225	-7.92	model 2
12	$m_1 = n_1 = 13$	196	$m_2 = n_2 = 15$	256	-4.11	model 2
13	$m_1 = n_1 = 14$	225	$m_2 = n_2 = 16$	289	-0.57	no
14	$m_1 = n_1 = 15$	256	$m_2 = n_2 = 17$	324	-6.57	model 2
15	$m_1 = n_1 = 16$	289	$m_2 = n_2 = 18$	361	-4.06	model 2
16	$m_1 = n_1 = 17$	324	$m_2 = n_2 = 19$	400	-3.89	model 2
17	$m_1 = n_1 = 18$	361	$m_2 = n_2 = 20$	441	-4.15	model 2
18	$m_1 = n_1 = 19$	400	$m_2 = n_2 = 21$	484	3.02	model 1
19	$m_1 = n_1 = 20$	441	$m_2 = n_2 = 22$	529	9.09	model 1
20	$m_1 = n_1 = 21$	484	$m_2 = n_2 = 23$	576	0.41	no
21	$m_1 = n_1 = 22$	529	$m_2 = n_2 = 24$	625	3.21	model 1
22	$m_1 = n_1 = 23$	576	$m_2 = n_2 = 25$	676	9.23	model 1
23	$m_1 = n_1 = 24$	625	$m_2 = n_2 = 26$	729	1.97	model 1
24	$m_1 = n_1 = 25$	676	$m_2 = n_2 = 27$	784	10.03	model 1
25	$m_1 = n_1 = 26$	729	$m_2 = n_2 = 28$	841	16.27	model 1
26	$m_1 = n_1 = 27$	784	$m_2 = n_2 = 29$	900	4.23	model 1
27	$m_1 = n_1 = 28$	841	$m_2 = n_2 = 30$	961	12.7	model 1
28	$m_1 = n_1 = 29$	900	$m_2 = n_2 = 31$	1024	11.81	model 1
29	$m_1 = n_1 = 30$	961	$m_2 = n_2 = 32$	1089	10.33	model 1
30	$m_1 = n_1 = 31$	1024	$m_2 = n_2 = 33$	1156	18.17	model 1
31	$m_1 = n_1 = 32$	1089	$m_2 = n_2 = 34$	1225	14.05	model 1
32	$m_1 = n_1 = 33$	1156	$m_2 = n_2 = 35$	1296	18.83	model 1
33	$m_1 = n_1 = 34$	1225	$m_2 = n_2 = 36$	1369	24.62	model 1
34	$m_1 = n_1 = 35$	1296	$m_2 = n_2 = 37$	1444	22.86	model 1
35	$m_1 = n_1 = 36$	1369	$m_2 = n_2 = 38$	1521	24.40	model 1
36	$m_1 = n_1 = 37$	1444	$m_2 = n_2 = 39$	1600	22.14	model 1
37	$m_1 = n_1 = 38$	1521	$m_2 = n_2 = 40$	1681	24.68	model 1
38	$m_1 = n_1 = 39$	1600	$m_2 = n_2 = 41$	1764	24.86	model 1
39	$m_1 = n_1 = 40$	1681	$m_2 = n_2 = 42$	1849	27.61	model 1

References

1. Han, J.Y.; Guo, J.; Jiang, Y.S. Monitoring tunnel profile by means of multi-epoch dispersed 3D LiDAR point clouds. *Tunn. Undergr. Space Technol.* **2013**, *33*, 186–192.
2. Mukupa, W.; Roberts, G.W.; Hancock, C.M.; Al-Manasir, K. A review of the use of terrestrial laser scanning application for change detection and deformation monitoring of structures. *Surv. Rev.* **2017**, *49*, 99–116.
3. Gordon, S.J.; Lichti, D.D. Modeling terrestrial laser scanner data for precise structural deformation measurement. *J. Surv. Eng.* **2007**, *133*, 72–80.
4. Lovas, T.; Barsi, A.; Detrekoi, A.; Dunai, L.; Csak, Z.; Polgar, A.; Berenyi, A.; Kibedy, Z.; Szocs, K. Terrestrial laser scanning in deformation measurements of structures. *Int. Arch. Photogramm. Remote Sens.* **2008**, *37*, 527–531.
5. Monserrat, O.; Crosetto, M. Deformation measurement using terrestrial laser scanning data and least squares 3D surface matching. *ISPRS J. Photogramm. Remote Sens.* **2008**, *63*, 142–154.

6. Tsakiri, M.; Lichti, D.; Pfeifer, N. Terrestrial laser scanning for deformation monitoring. In Proceedings of the 12th FIG Symposium, Baden, Germany, 22–24 May 2006.

7. Lane, S.N.; Westaway, R.M.; Murray Hicks, D. Estimation of erosion and deposition volumes in a large, gravel-bed, braided river using synoptic remote sensing. *Earth Surf. Process. Landf.* **2003**, *28*, 249–271.

8. Barnhart, T.B.; Crosby, B.T. Comparing Two Methods of Surface Change Detection on an Evolving Thermokarst Using High-Temporal-Frequency Terrestrial Laser Scanning, Selawik River, Alaska. *Remote Sens.* **2013**, *5*, 2813–2837.

9. Yang, H.; Xu, X.; Neumann, I. Deformation behavior analysis of composite structures under monotonic loads based on terrestrial laser scanning technology. *Compos. Struct.* **2018**, *183*, 594–599.

10. Ingensand, H.; Ioannidis, C.; Valani, A.; Georgopoulos, A.; Tsiligiris, E. 3D model Generation for Deformation Analysis using Laser Scanning data of a Cooling Tower. In Proceedings of the 12th FIG Symposium, Baden, Germany, 22–24 May 2006.

11. Van Gosliga, R.; Lindenbergh, R.; Pfeifer, N. Deformation analysis of a bored tunnel by means of terrestrial laser scanning. In Proceedings of the International Archives of Photogrammetry, Remote Sensing and Spatial Information Sciences, Dresden, Germany, 25–27 September 2006.

12. Vezočnik, R.; Ambrožič, T.; Sterle, O.; Bilban, G.; Pfeifer, N.; Stopar, B. Use of terrestrial laser scanning technology for long term high precision deformation monitoring. *Sensors* **2009**, *9*, 9873–9895.

13. You, L.; Tang, S.; Song, X.; Lei, Y.; Zang, H.; Lou, M.; Zhuang, C. Precise Measurement of Stem Diameter by Simulating the Path of Diameter Tape from Terrestrial Laser Scanning Data. *Remote Sens.* **2016**, *8*, 717.

14. Lindenbergh, R.; Uchanski, L.; Bucksch, A.; Van Gosliga, R. Structural monitoring of tunnels using terrestrial laser scanning. *Rep. Geod.* **2009**, *87*, 231–238.

15. Girardeau-Montaut, D.; Roux, M.; Marc, R.; Thibault, G. Change detection on points cloud data acquired with a ground laser scanner. *Int. Arch. Photogramm. Remote Sens. Spat. Inf. Sci.* **2005**, *36*, 30–35.

16. Yang, H.; Omidalizarandi, M.; Xu, X.; Neumann, I. Terrestrial laser scanning technology for deformation monitoring and surface modeling of arch structures. *Compos. Struct.* **2017**, *169*, 173–179.

17. Bureick, J.; Alkhatib, H.; Neumann, I. Robust Spatial Approximation of Laser Scanner Point Clouds by Means of Free-form Curve Approaches in Deformation Analysis. *J. Appl. Geod.* **2016**, *10*, 27–35.

18. Harmening, C.; Neuner, H. A constraint-based parameterization technique for B-spline surfaces. *J. Appl. Geod.* **2015**, *9*, 143–161.

19. Zhao, X.; Alkhatib, H.; Kargoll, B.; Neumann, I. Statistical evaluation of the influence of the uncertainty budget on B-spline curve approximation. *J. Appl. Geod.* **2017**, *11*, 215–230.

20. Wunderlich, T.; Niemeier, W.; Wujanz, D.; Holst, C.; Neitzel, F.; Kuhlmann, H. Areal deformation analysis from TLS point clouds—The challenge. *Allgemeine Vermessungs Nachrichten* **2016**, *123*, 340–351.

21. Harmening, C.; Neuner, H. Choosing the Optimal Number of B-spline Control Points (Part 1: Methodology and Approximation of Curves). *J. Appl. Geod.* **2016**, *10*, 139–157.

22. Harmening, C.; Neuner, H. Choosing the optimal number of B-spline control points (Part 2: Approximation of surfaces and applications). *J. Appl. Geod.* **2017**, *11*, 43–52.

23. Cox, D.R. Tests of Separate Families of Hypotheses. In Proceedings of the Fourth Berkeley Symposium on Mathematical Statistics and Probability, Berkeley, CA, USA, 20 June–30 July 1961.

24. Williams, D.A. Discrimination between Regression Models to Determine the Pattern of Enzyme Synthesis in Synchronous Cell Cultures. *Biometrics* **1970**, *26*, 23–32.

25. Vuong, Q.H. Likelihood ratio tests for model selection and non-nested hypotheses. *Econ. J. Econom. Soc.* **1989**, *8*, 307–333.

26. Hexagon Metrology. Leica Absolute Tracker AT960 Brochure. Available online: http://www.hexagonmi.com/products/laser-tracker-systems/leica-absolute-tracker-at960#loren (accessed on 2015).

27. Meierhold, N.; Spehr, M.; Schilling, A.; Gumhold, S.; Maas, H. Automatic feature matching between digital images and 2D representations of a 3D laser scanner point cloud. *Int. Arch. Photogramm. Remote Sens. Spat. Inf. Sci.* **2010**, *38*, 446–451.

28. Bureick, J.; Neuner, H.; Harmening, C.; Neumann, I. Curve and Surface Approximation of 3D Point Clouds. *Allgemeine Vermessungs-Nachrichten* **2016**, *123*, 315–327.

29. Piegl, L.; Tiller, W. *The NURBS Book*; Springer Science & Business Media: Berlin, Germany, 1997.

30. Koch, K. Fitting Free-Form Surfaces to Laserscan Data by NURBS. *Allgemeine Vermessungs-Nachrichten* **2009**, *116*, 134–140.

31. Koch, K. *Parameter Estimation and Hypothesis Testing in Linear Models*; Springer: Berlin, Germany, 1999.

32. Paffenholz, J.A.; Vennegeerts, H.; Kutterer, H. High frequency terrestrial laser scans for monitoring kinematic processes. In Proceedings of the INGEO 2008—4th International Conference on Engineering Surveying, Bratislava, Slovakia, 23–24 October 2008.

33. Lewis, F.; Butler, A.; Gilbert, L. A unified approach to model selection using the likelihood ratio test. *Methods Ecol. Evol.* **2011**, *2*, 155–162.

34. Clarke, K.A. A simple distribution-free test for nonnested model selection. *Polit. Anal.* **2007**, *15*, 347–363.

Paper 4

Research Article

TLS-Based Feature Extraction and 3D Modeling for Arch Structures

Xiangyang Xu,[1] Xin Zhao,[1] Hao Yang,[1,2] and Ingo Neumann[1]

[1]*Geodetic Institute, Faculty of Civil Engineering and Geodetic Science, Leibniz University Hannover, Hannover, Germany*
[2]*Jiangsu University of Science and Technology, Zhenjiang City, Jiangsu Province, China*

Correspondence should be addressed to Hao Yang; yang@gih.uni-hannover.de

Academic Editor: Mosbeh Kaloop

Terrestrial laser scanning (TLS) technology is one of the most efficient and accurate tools for 3D measurement which can reveal surface-based characteristics of objects with the aid of computer vision and programming. Thus, it plays an increasingly important role in deformation monitoring and analysis. Automatic data extraction and high efficiency and accuracy modeling from scattered point clouds are challenging issues during the TLS data processing. This paper presents a data extraction method considering the partial and statistical distribution of the point clouds scanned, called the window-neighborhood method. Based on the point clouds extracted, 3D modeling of the boundary of an arched structure was carried out. The ideal modeling strategy should be fast, accurate, and less complex regarding its application to large amounts of data. The paper discusses the accuracy of fittings in four cases between whole curve, segmentation, polynomial, and B-spline. A similar number of parameters was set for polynomial and B-spline because the number of unknown parameters is essential for the accuracy of the fittings. The uncertainties of the scanned raw point clouds and the modeling are discussed. This process is considered a prerequisite step for 3D deformation analysis with TLS.

1. Introduction

Structural health monitoring is of significant importance for the historical and architectural structures for safety reasons [1–3]. An arched structure is one of the traditional forms in western architectures, such as in churches. As the buildings age, a safety risk will occur in the arched structures which bear the load of the construction. TLS is a highly accurate, fast, and efficient technology to acquire 3D point clouds of structures [4]. An experiment was designed to simulate the load and deformation process of an arched structure and TLS was used to measure the surface-based 3D point clouds.

Morphology-oriented analysis with TLS is a new direction for deformation analysis [5]. One of the issues remaining is to assure the accuracy during modeling for deformation analysis with TLS technology. The influence factors and significance of accuracy of free-form 3D modeling for the point clouds are not reported in detail in the current literatures.

This paper presents efficient extraction and discusses accurate modeling of the boundary of an arched structure, which are prerequisite steps for deformation analysis. Data extraction is carried out by the window-neighborhood method, which is closely related to the partial and statistical distribution of the scanned point clouds. In this paper, the mathematical functions of polynomial and B-spline are adopted to model the data. A polynomial has a deficiency in describing local features, but its advantages are efficiency and simplicity, while B-spline is exactly the opposite. Four cases are discussed, including a localized segmentation, to find an efficient and accurate modeling solution for the arched structure measured. Since the number of parameters has an influence on the fitting results, the numbers of parameters of polynomial and B-spline models are proximate to emphasize the model function.

1.1. Terrestrial Laser Scanning and Data Extraction. Terrestrial laser scanning (TLS), which can capture up to millions of points per second and with a linear accuracy in the millimeter range, is one of the most efficient tools to measure 3D objects and structures. Traditional methods for monitoring,

for example, total station, inclinometer, accelerometer, and leveling are generally point-based measurements. Some low-cost sensors require preembedding or contact [6], which is difficult to maintain in the long period. TLS is area-oriented measurement which can obtain 3D coordinates information of dense point clouds. Furthermore, the measurement of TLS is contactless and not destructive. It is widely applied in the monitoring of natural and artificial constructions, for example, rock slopes, forests, coasts, and buildings [7–10].

One important task for the presteps of modeling is to detect or recognize features from the 3D data. Reference [11] extracted lithological boundaries from photographic images of rock surfaces by means of an interactive segmentation method. Reference [12] used a semiautomatic method of extracting urban road networks from point clouds to improve the detection of objects. However, automatic data extraction from point clouds data is still challenging.

1.2. Curve Fitting with Mathematical Functions. It is common to fit the data collected with geometric forms or mathematical functions [13–16]. Because the point clouds from TLS measurement contain gaps, leaps, cusps, and so on, it is necessary to construct a fitting model to investigate the 3D deformation of a structure. Complicated spatial structures especially require fitting by free-form curves and surfaces

Curve fitting is the process of constructing a curve or mathematical function with the best approximation to data points [17]. Curve fit usually means trying to find the curve that minimizes displacement of a point from the curve in vertical, orthogonal, or both axes directions [18].

Polynomial and B-spline are commonly used forms to fit a curve. Reference [19] adopted polynomial fitting with the least square method to detect the wheel set size in the railway transportation system. The polynomial surface was also considered to approximate concrete structures with gentle surfaces [20–23]. B-spline is a generalization of the Bézier curve and can be further extended to a nonuniform rational B-spline, which has the advantage of constructing an exact model; therefore, it is suitable for adoption in the high accuracy TLS measurement. Due to the properties of B-spline curves, for example, flexibility and accuracy, they are popular when estimating complex objects. Ordinary B-spline approximation involves data parameterization, knot adjustment, and control point determination. The first step is to parameterize the points measured by means of equal division, chord length, and centripetal [24]. The second step aims at knot vector adjustment. A robust method for the optimal selection of the knot vector is studied by Bureick et al. [25]. The final step is the estimation of control points by means of the Gauss-Markov model [26].

1.3. Work Flow. This paper focuses on the statistical analysis of spatial multidimensional point clouds data, which is the basis for the deformation analysis of an arched structure. The work flow of this paper is presented in Figure 1. The TLS raw data is scanned by TLS and, subsequently, the point clouds are preprocessed to outline the arched structure and
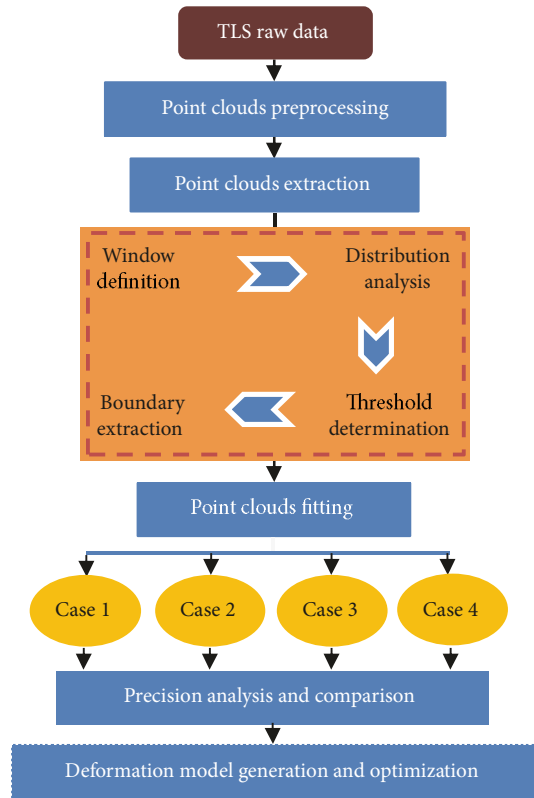

Figure 1: Work flow of data extraction and fitting analysis.

Table 1: Different methods of the fitting for whole curve and segmentation.

	Case 1	Case 2	Case 3	Case 4
Functions	P	B	P	
Points scope	Whole curve	Whole curve	Segmentation	Segmentation

eliminate the surroundings, which are not the main subject of the deformation analysis.

The arch-shaped curve is then extracted to investigate the deformation behavior where the window selection method is adopted. The latter includes four steps: window definition, distribution analysis, threshold determination, and boundary extraction.

Using the resulting extracted data, point clouds fitting is performed for four kinds of combinations, which are explained later in Table 1. The fitting precision is then analyzed and the four cases are compared. Last but not least, the deformation model of the fitting parts will be generated and optimized.

2. Experimental Setup

An experiment was carried out to investigate the deformation behavior of an arched structure using TLS point clouds. The main components are the arched structure specimen, Z + F Imager 5006, load equipment, and two supports, which are
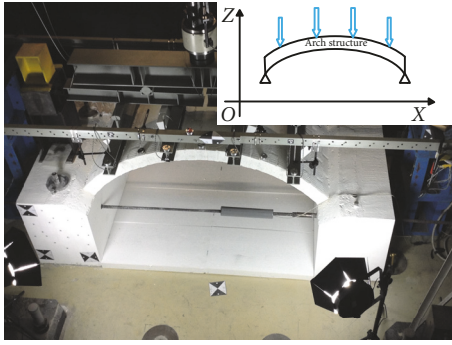
FIGURE 2: Plot of experiment.

FIGURE 3: Point clouds of side surface of the arch.

shown in Figure 2. The continuous load lasted for 20 min, under which deformation consequently formed, and then stopped for 10 min for measurements. The load is within a safety range where deformation of the arched structure is generated, but crush and failure have not begun. The lower image in Figure 2 shows the experimental setup. A coordinated system was defined to investigate the deformation behavior of the arch based on highly accurate TLS, which is shown in the upper image in Figure 2, where the y-axis direction is perpendicular to plane XOZ.

In this paper, the arch-shaped part of the object is vital for structural monitoring, because it bears the main load and shows significant deformation. The side surface of the object is taken into account for more precise deformation analysis. However, the arch-shaped object is occluded with some other objects, such as steel I-beams, and needs to be separated for more accurate analysis.

3. Data Analysis

3.1. Data Extraction. The main concern of the deformation analysis lies in the edge of the arched structure, with the motivation that the arched edge defines the border of the arched surfaces with significant deformation, and is well connected to photogrammetry, since it can also be detected from digital images. From this point of view, the edge of the arched structure should be extracted and fitted with a high accuracy taken into consideration. Point clouds are preprocessed to pick up the side surface of the arched structure, which is extracted, and the result is shown in Figure 3, with the adoption of 3D point clouds software.

As the laser beam rotates and scans with a uniform angular speed, footprints of laser beams have a theoretically close-to-even distribution considering a general surface. Suppose that each point of the surface carries a square selection window with a predefined size, which gives a reference to the neighboring points, there are mostly two cases. The first one is in the middle part of the surface, where those main points have almost the same number of neighbors, and such main points occupy the most population of all the point clouds. The second is in the boundary, with approximately half of the number of neighbors compared to the first case. A schematic diagram with a simple example is shown in Figure 4, where all the points represent footprint centers,
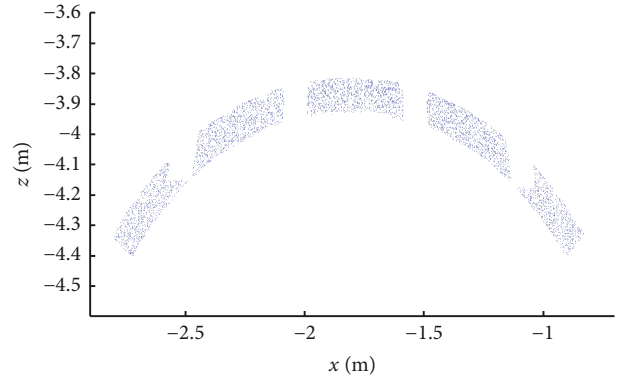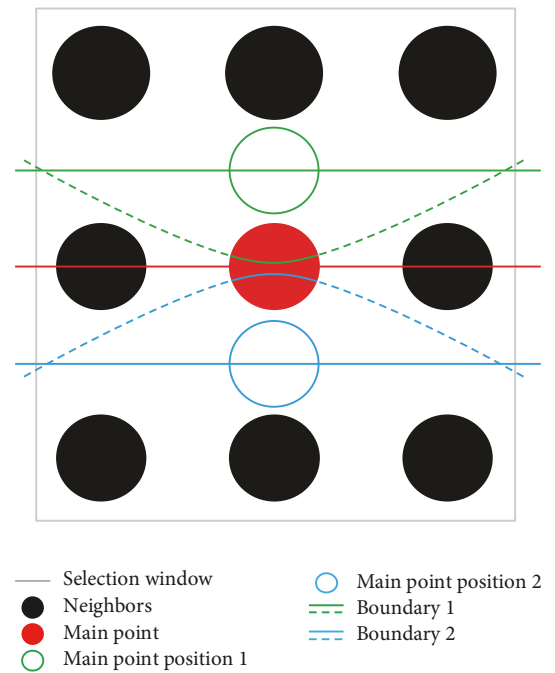

FIGURE 4: Diagrammatic sketch of the edge point picking.

which describe only the position, but not the real size of the footprints. The red point is the main point, the black ones are neighboring points, and the green and blue hollow circles are drawn for the possible relative position of the main point. The grey lines show the selection window and the red line is a simplified boundary. When the boundary inclines as dashed green and blue lines, that kind of position relationship can also be depicted with green and blue solid lines and hollow circles.

The neighboring numbers of the boundary points identified can only be within a certain range rather than an exact value, due to the inclination of the boundary line and the scattered distribution of points in the boundary area, as shown in Figure 5. The quantity Δn marked means the number of points which have escaped from the boundary, which will influence the number of neighbors shown as black points. The yellow points are virtual points, which, with the
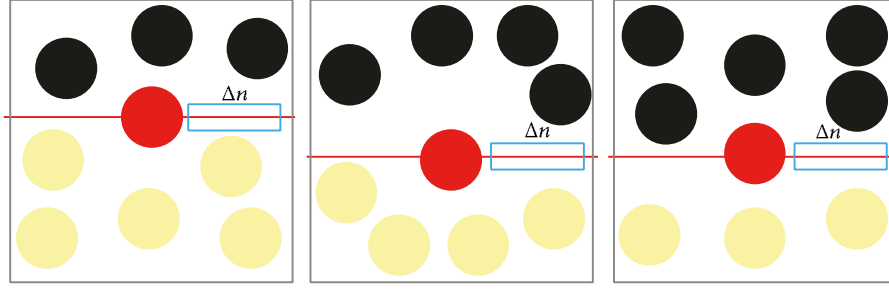
FIGURE 5: Different cases of boundary and neighboring points.

combination of black points, constitute a normal selection window as in the center of the surface.

According to the schematic diagram in Figures 4 and 5, the number of neighbors for boundary points should satisfy the function in (1), where n is the actual number of neighbors which varies for different points, N is the number of neighbors with the maximum probability in defined-size square windows, $\bar{n}$ is average neighbor number of boundary points, Δn is statistical error, that is, the number of points rejected as boundary neighbors by relative inclination of the boundary line, and s is the number of points on each side of the square window.

$$|n - \bar{n}| \leq \Delta n;$$

$$\bar{n} = \frac{N}{2};$$

$$\Delta n = N * \frac{s-1}{2(s^2-1)} = \frac{N}{2(s+1)}. \tag{1}$$

The size of the selection window has an influence on the boundary extraction. If the size is too small, the noisy point will be mistaken for a boundary point, and vice versa; if the size is too large, some boundary points will be lost. The thickness of the arched structure is 10 cm.

The threshold Nr was defined as a value with which the boundary will be filtered and represent reality. The value of Nr is determined by the actual distance of neighboring points of the point clouds. On the one hand, it is influenced by density of the point clouds depending on the scanning distance and angle, and the inner parameters of the TLS instrument used in the experiment; on the other hand, the local point clouds shapes formed by actual geometric shape of the boundary and occlusion of the point clouds also affect the value of threshold Nr. Because the various factors have undetermined influences on the point clouds of the boundary, the threshold Nr is analyzed explicitly by means of the distribution of neighboring point number by the MATLAB program. The actual number of neighboring points n is distributed as shown in Figure 6, where the maximum probability corresponds to 136 neighboring points. The threshold Nr theoretically locates at the point with the maximum distribution of the neighboring numbers.

Because the value of Nr is vital to the result of extraction, it should be carefully calculated before picking up the boundaries; therefore, the distribution of adjacent points is
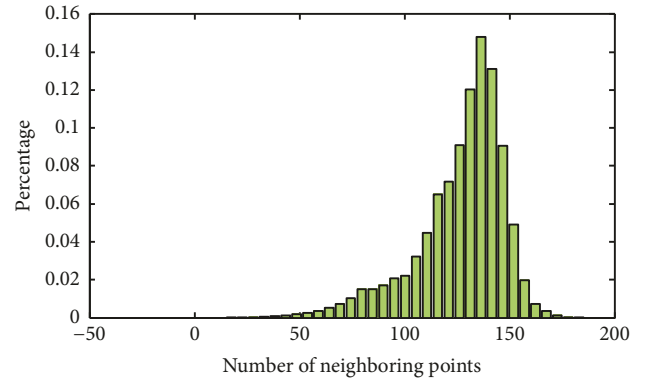

FIGURE 6: Distribution of neighboring points.

investigated and the maximum value is selected. If the Nr is too small, some valid boundaries will not be detected where the point density is large; on the contrary, if the Nr is too large, the boundary points will contain more noise, which will influence the accuracy of 3D model badly. Since the laser spots are almost uniformly distributed and most of the point clouds are in a normal area other than boundaries, we chose Nr with the maximum probability in Figure 6, which is 136. After filtering all the point clouds with (1), the boundary of the side arched surface will be extracted, as shown in Figure 7. The red point clouds correspond to the Nr value 136 and the green point clouds to 126. Blue arrows point out that when the Nr is too small, some valid boundaries are neglected. The value of the Nr is not chosen to be larger, for example, 146, because that would cause too much noise.

The extracted edges contain not only the arched-shape curves, but also shadows of the occlusions. The boundary point clouds are imported to CloudCompare® for the purpose of separation of the arched-shape curves. The open-access software CloudCompare is an independent open source project and a free software for the processing of point clouds, which provides a set of basic tools to process 3D point clouds [27]. The step adopted here is polygonal segmentation. The lower edge of the point clouds is extracted, which comprises the point clouds extracted for 3D curve fitting.

3.2. Data Fitting. The extracted point clouds are approximated by both polynomial curve and B-spline. The 3D coordinates x, y, and z can be, respectively, described as a

- · Boundary of threshold 136
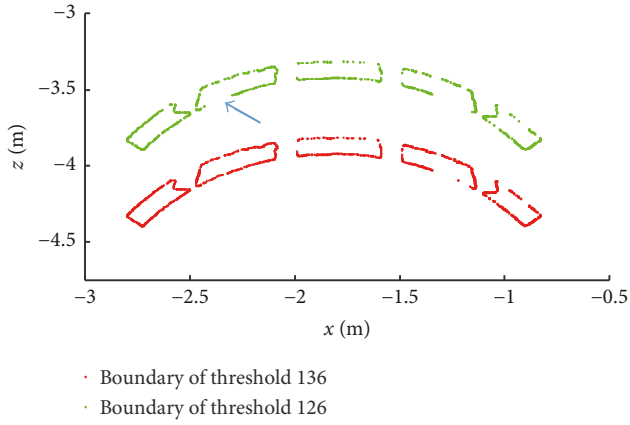- · Boundary of threshold 126

FIGURE 7: Edges extracted from MATLAB.

function of the common variable t to fit a polynomial curve. The estimation parameters for each coordinate are calculated by (2), where o represents coordinates x, y, or z, t is the common variable, v is the order of the polynomial, and $A_o(i)$ are the parameters to be estimated with index i from 1 to v. The number of unknown parameters is $(v + 1) * 3$ for kth order polynomial fitting.

$$o = \sum_{i=1}^{v} A_o(i) * t^{v+1-i}, \quad o = x, y \text{ or } z. \tag{2}$$

The functional model in (3) is described by the degree p and the pth degree B-spline basis functions $\{N_{i,p}(u)\}$ are defined on the nonperiodic knot vector U in (4), with number m to fit a 3D B-spline curve. The control points $\{P_i\}$ are the unknowns.

$$C(u) = \sum_{i=0}^{n} N_{i,p}(u) P_i, \quad u \in [0, 1], \tag{3}$$

$$U = \{0, \ldots, 0, u_{p+1}, \ldots, u_{m-p-1}, 1, \ldots, 1\}, \tag{4}$$
$$0 < u < 1.$$

The relationship between degree p, the number of control points $n + 1$, and the knot points $m + 1$ is $m = n + p + 1$. The control points are the unknowns to be estimated, which can be obtained in a least squares sense by the minimizing of

$$\sum_{k=1}^{m-1} |Q_k - C(\overline{u}_k)|^2 \sim \min \tag{5}$$

and the restriction that the B-spline passes through the first and last points measured. Q_k are the measurements and $\{U_k\}$ are parameters for each Q_k, respectively, calculated by the chord length method. Furthermore, the knot vector U is calculated with [23]

$$u_{p+j} = (1 - a)\overline{u}_{i-1} + a\overline{u}_i,$$

$$\text{with } j = 1, 2, \ldots, n - p, \ i = \text{int}(jd), \ a = jd - i, \ d = \frac{m+1}{n-p+1}. \tag{6}$$

The parameters chosen for B-spline in this case are $p = 3$ and $n = 21$, where p is the degree and $n+1$ is the number of control points. Because one direction of control points is estimated during each step; there are 22 unknown parameters in each estimation of the B-spline curve. The number of parameters matches well to that of polynomial, which is 21 parameters for 6th order approximation. This increases the reasonability of comparison between the two models, since the number of parameters has a significant influence on the accuracy of the fitting.

4. Results

The fitted curve of the polynomial and B-spline is presented in Figure 8, where the blue curve corresponds to the polynomial approximation and the red curve is B-spline fitting. The comparison between the polynomial and B-spline curves of epochs 3 and 9 corresponds to Figures 8(a) and 8(b), respectively.

Due to the displacement of z-axis being essential, the focus is on the x-z plane. The coordinate range is $[-2.75, -0.85]$ m in the x-axis direction and $[-4.35, -3.85]$ m in the z-axis direction to reduce the redundancy. According to Figure 8, the B-spline and polynomial fitting are significantly different in areas A, C, and B, corresponding to the concave piece in Figure 8(a) and the convex piece in Figure 8(b), which reveal that the B-spline has an advantage at the mutated sections. Although high order polynomial fitting can alleviate this problem, it may, however, lead to Runge's phenomenon, which is a problem at the edges of an interval that occurs when using polynomial interpolation with polynomials of a high degree over a set of equispaced interpolation points. This phenomenon was discovered by Carl David Tolmé Runge while exploring the behavior of errors when using polynomial interpolation to approximate certain functions [15].

The statistical errors of the fittings are considered to get a deeper insight into the fitting effects on the spatially scattered points. The polynomial approximation of the whole extracted line is defined as the original case/case 1 for the later comparison; the other cases are listed in Table 1, where P and B stand for polynomial and B-spline approximation, respectively.

The uncertainties of the polynomial curve fitted for epoch 3 (E3) and 9 (E9) are presented in Table 2, including deviation, standard deviation, and covariance, where $C(x, y, z)$ means covariance with x, y, and z coordinate values, diagonal element is deviation, and SD stands for standard deviation.

The number of unknown parameters is considered to compare the B-spline and polynomial for spatial point clouds more impartially. The uncertainties of the B-spline for epochs 3 and 9 are presented in Table 2.

According to Table 2, the standard deviations for the polynomial in the z-axis direction for epochs 3 and 9 are 17.51 and 12.98 mm, respectively, which are not balanced with the high accuracy of TLS measurement. Therefore, B-spline curve fitting is adopted and analyzed. For this, the standard deviations in the z-axis direction for epochs 3 and 9 are 1.45 and 1.40 mm, respectively, where the accuracy is significantly improved and the comparison is listed in Table 4.
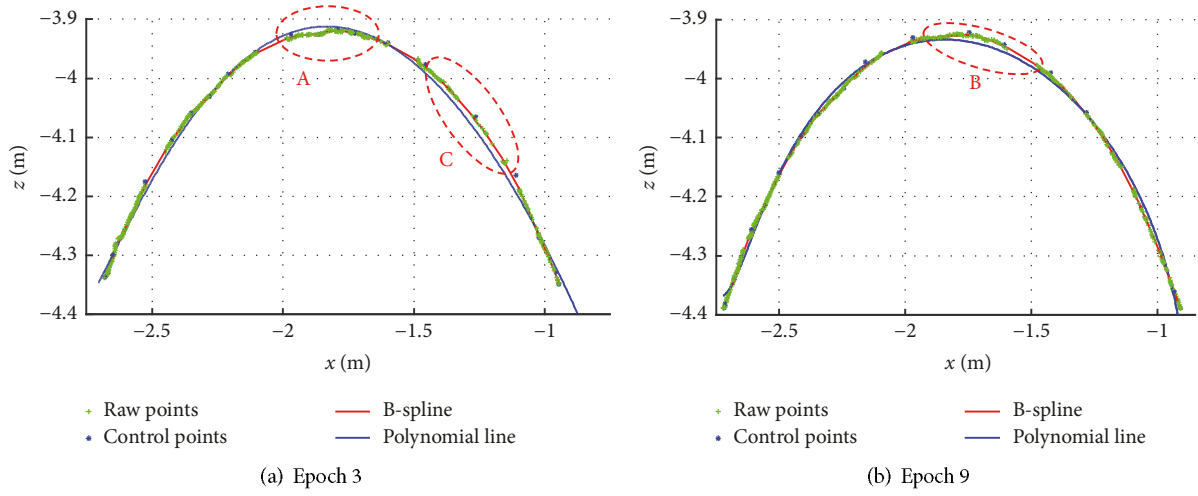
(a) Epoch 3

(b) Epoch 9

FIGURE 8: Comparison of polynomial and B-spline curves.

TABLE 2: Uncertainties of two forms of curves with unit mm.

	X	Y	Z
	P methods		
E3			
$C(X)$	1.41	$\cdots$	$\cdots$
$C(Y)$	0.62	0.28	$\cdots$
$C(Z)$	-0.18	$-8.13e-02$	0.31
SD	37.49	16.70	17.51
E9			
$C(X)$	0.61	$\cdots$	$\cdots$
$C(Y)$	0.28	0.13	$\cdots$
$C(Z)$	$-4.26e-03$	$6.67e-03$	0.17
SD	24.75	11.26	12.98
	B methods		
E3			
$C(X)$	$8.06e-03$	$\cdots$	$\cdots$
$C(Y)$	$2.73e-03$	$1.79e-03$	$\cdots$
$C(Z)$	$-1.83e-04$	$-1.83e-04$	$2.096e-03$
SD	2.84	1.34	**1.45**
E9			
$C(X)$	$6.76e-03$	$\cdots$	$\cdots$
$C(Y)$	$1.76e-03$	$1.49e-03$	$\cdots$
$C(Z)$	$-7.89e-05$	$-2.00e-04$	$1.856e-03$
SD	2.60	1.20	**1.40**

FIGURE 9: Segmentation fitting analysis of Epoch 9.

Occlusion of the laser beam in the experiment is unavoidable, because of the shelter of the loads equipment, which will cause fragmentation of the point clouds and then increase the uncertainties during the parametric estimation of the approximation. A segmentation fitting is employed for this perspective, which is presented in Figure 9, where epoch 9 is depicted.

The segmentation approximations are described in Figure 9, where the blue curve corresponds to the polynomial approximation, the gr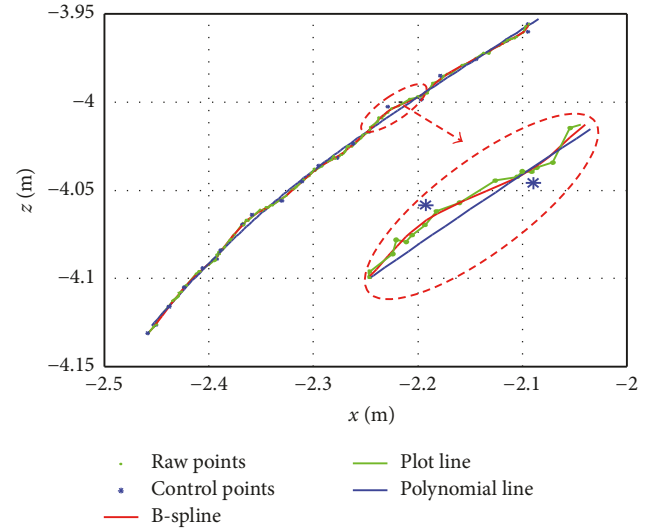een curve is an automatically plotted line, and the red curve is the B-spline fitting. The green points are raw point clouds and the blue stars are control points of the B-spline. According to the red ellipses in Figure 9, it is discovered that the B-spline is greatly improved rather than the polynomial fitting on the left side, which is succeeded through the control points and knots. However, the deviations of the two models are well matched on the right side. It is hinted that the quality of the B-spline is determined by control points and knots; thus, the optimization of the B-spline model is much more complex and costly than the polynomial. When the B-spline is used to fit a surface, the phenomenon is more prominent.

The uncertainties of polynomial lines for each epoch are listed in Table 4, where the 6th order polynomial function is advantageous through parametric model training.

The standard deviations in the z-axis direction for epochs 3 and 9 are 2.0 and 1.8 mm, respectively, according to Table 3,

Table 3: Uncertainties during segmentation with unit mm.

	X	Y	Z
	P methods		
E3			
$C(X)$	$1.53e - 02$	$\cdots$	$\cdots$
$C(Y)$	$8.21e - 03$	$5.29e - 03$	$\cdots$
$C(Z)$	$6.33e - 03$	$3.07e - 03$	$3.86e - 03$
SD	3.92	2.31	**2.00**
E9			
$C(X)$	$1.32e - 02$	$\cdots$	$\cdots$
$C(Y)$	$7.02e - 03$	$4.82e - 03$	$\cdots$
$C(Z)$	$4.31e - 03$	$2.04e - 03$	$3.38e - 03$
SD	3.61	2.23	**1.80**
	B methods		
E3			
$C(X)$	$8.00e - 04$	$\cdots$	$\cdots$
$C(Y)$	$-1.15e - 05$	$4.37e - 04$	$\cdots$
$C(Z)$	$2.37e - 04$	$-2.36e - 04$	$4.56e - 04$
SD	0.89	0.66	**0.68**
E9			
$C(X)$	$1.06e - 03$	$\cdots$	$\cdots$
$C(Y)$	$-3.13e - 05$	$5.00e - 04$	$\cdots$
$C(Z)$	$-3.88e - 04$	$-1.86e - 04$	$5.05e - 04$
SD	1.00	0.71	**0.71**

Table 4: Improvement analysis.

Ratio (%)	Epoch	X	Y	Z
	Improvement by B-spline approximation			
Whole curve	E3	**92.42**	**91.98**	**91.72**
	E9	**89.49**	**89.34**	**89.21**
Segmentation	E3	77.07	71.25	66.24
	E9	72.22	67.87	60.52
	Improvement by segmentation			
P methods	E3	**89.60**	**86.23**	**88.58**
	E9	**85.45**	**80.46**	**86.13**
B methods	E3	68.51	50.66	53.43
	E9	61.54	41.10	49.24

Table 5: Technical parameters of employed TLS.

Measurement range	0.4–79 m
Scan speed	up to 1016727 points/sec
Range noise at 10 m	
Reflectivity 10% (black)	1.2 mm rms
Reflectivity 20% (dark grey)	0.7 mm rms
Reflectivity 100% (white)	0.4 mm rms
Distance resolution	0.1 mm
Linear error (50 m)	1 mm

According to the analysis, the optimization of segmentation is shown in Table 4, where both the polynomial and B-spline have a better approximation precision after segmentation. However, the segmentation improvement using the polynomial curve is more significant, with the magnitude of increase from 80.46 to 89.60% for the polynomial compared to from 41.10 to 68.51% for the B-spline.

It is also revealed that curve fitting results have a close relation with the accuracy and reliability of the scanned point clouds. The TLS employed is Imager Z + F 5006, whose scanning precision parameters are listed in Table 5. In this experiment, the laser scanner stands about 5 m away from the arch, and the arch with shadow can be considered as grey, which means that the range noise is 0.7 mm. It agrees with the result of B method of segmentation.

5. Conclusion

This paper focuses on the comparative analysis of the B-spline and polynomial approximation based on the extraction of multidimensional data which are collected by TLS during deformation analysis. An innovative window selection method is adopted to efficiently extract the edge data of the arch structure, where the partial and statistical distribution of the scanned point clouds are considered. An optimal extraction is chosen from the aspect of noise and blank of the extracted point clouds.

The B-spline and polynomial approximation are presented and analyzed with four cases, where conclusions can be drawn as follows:

(a) For the experiment in this paper, the uncertainty ranking of the four cases is segmentation with B method (less than 1 mm), whole curve with B method and segmentation with P method (1-2 mm) and whole curve with P method (10–20 mm).

(b) It is verified experimentally, through comparing the standard deviations of the two fitting methods, that the B-spline has a more satisfactory fitting precision, where the standard deviation of the whole edge curve of the B-spline fitting is about 90% better than the polynomial approximation.

(c) However, in the case of segmented fitting, the accuracy improvement of the B-spline is not as much as the polynomial approximation. It is revealed that the B-spline has an advantage of better accuracy

and are obviously improved compared to the approximation of the whole boundary curve.

Similarly, the segmentation curve is fitted by the B-spline function. The uncertainties of the approximation are shown in Table 3, where the standard deviation in the z-axis direction for epochs 3 and 9 corresponds to 0.68 and 0.71 mm, respectively. The fittings are improved based on the segmentation approximation.

Based on the uncertainties analysis in Tables 2 and 3, the standard deviation could be abstracted as in Table 4, which describes the degree of optimization of the B-spline fitting compared with the polynomial approximation.

in complex situations, but it is also implied that the polynomial approximation can greatly improve the fitting accuracy by segmentation, simplifying the complex case.

It is indicated that, in the approximation of curves during deformation monitoring with TLS measurement, segmentation method can be adopted, where efficiency of polynomial and B-spline could be combined to construct a fast and accurate 3D model.

Conflicts of Interest

Acknowledgments

References

[1] A. Coscetta, A. Minardo, L. Olivares et al., "Wind turbine blade monitoring with brillouin-based fiber-optic sensors," *Journal of Sensors*, vol. 2017, Article ID 9175342, 5 pages, 2017.

[2] M. R. Kaloop, J. W. Hu, and M. A. Sayed, "Yonjung high-speed railway bridge assessment using output-only structural health monitoring measurements under train speed changing," *Journal of Sensors*, vol. 2016, Article ID 4869638, 15 pages, 2016.

[3] M. R. Kaloop and J. W. Hu, "Dynamic performance analysis of the towers of a long-span bridge based on gps monitoring technique," *Journal of Sensors*, vol. 2016, Article ID 7494817, 14 pages, 2016.

[4] G. Vosselman and H. Maas, *Airborne and Terrestrial Laser Scanning*, Whittles Publishing, Scotland, UK, 2010.

[5] W. Mukupa, G. W. Roberts, C. M. Hancock, and K. Al-Manasir, "A review of the use of terrestrial laser scanning application for change detection and deformation monitoring of structures," *Survey Review*, pp. 1–18, 2016.

[6] J. Zhao, T. Bao, and T. Kundu, "Wide range fiber displacement sensor based on bending loss," *Journal of Sensors*, vol. 2016, Article ID 4201870, 5 pages, 2016.

[7] A. Abellán, T. Oppikofer, M. Jaboyedoff, N. J. Rosser, M. Lim, and M. J. Lato, "Terrestrial laser scanning of rock slope instabilities," *Earth Surface Processes and Landforms*, vol. 39, no. 1, pp. 80–97, 2014.

[8] G. J. Newnham, J. D. Armston, K. Calders et al., "Terrestrial laser scanning for plot-scale forest measurement," *Current Forestry Reports*, vol. 1, no. 4, pp. 239–251, 2015.

[9] A. Costanzo, M. Minasi, G. Casula, M. Musacchio, and M. F. Buongiorno, "Combined use of terrestrial laser scanning and IR Thermography applied to a historical building," *Sensors (Switzerland)*, vol. 15, no. 1, pp. 194–213, 2014.

[10] F. Serafino, J. Horstmann, J. C. Nieto Borge, C. Lugni, and M. Brocchini, "Sensors for coastal monitoring," *Journal of Sensors*, vol. 2016, Article ID 1720563, 2 pages, 2016.

[11] Y. Vasuki, E. Holden, P. Kovesi, and S. Micklethwaite, "An interactive image segmentation method for lithological boundary detection: a rapid mapping tool for geologists," *Computers & Geosciences*, vol. 100, pp. 27–40, 2017.

[12] F. Li, X. M. Cui, and X. Y. Liu, "A semi-automatic algorithm of extracting urban road networks from airborne LiDAR point clouds," *Science of Surveying and Mapping*, vol. 40, pp. 88–92, 2015.

[13] A. Lamnii, M. Lamnii, and F. Oumellal, "Computation of Hermite interpolation in terms of B-spline basis using polar forms," *Mathematics and Computers in Simulation*, vol. 134, pp. 17–27, 2017.

[14] C. C. Wang, X. W. Wang, and X. C. Xu, "Study on the cylindrical surface fitting method," *Engineering of Surveying and Mapping*, vol. 3, p. 258, 2014.

[15] X. Zhao, C. Zhang, B. Yang, and P. Li, "Adaptive knot placement using a GMM-based continuous optimization algorithm in B-spline curve approximation," *CAD Computer Aided Design*, vol. 43, no. 6, pp. 598–604, 2011.

[16] D. Brujic, I. Ainsworth, and M. Ristic, "Fast and accurate NURBS fitting for reverse engineering," *International Journal of Advanced Manufacturing Technology*, vol. 54, no. 5-8, pp. 691–700, 2011.

[17] N. Chernov and H. Ma, "Least squares fitting of quadratic curves and surfaces," in *Computer Vision*, S. R. Yoshida, Ed., pp. 285–302, Nova Science Publishers, 2011.

[18] Y. Liu and W. Wang, "A revisit to least squares orthogonal distance fitting of parametric curves and surfaces, advances in geometric modeling and processing," in *Lecture Notes in Computer Science*, pp. 384–397, 2008.

[19] X. Cheng, Y. Chen, Z. Xing, Y. Li, and Y. Qin, "A novel online detection system for wheelset size in railway transportation," *Journal of Sensors*, vol. 2016, Article ID 9507213, 15 pages, 2016.

[20] H. Yang, X. Xu, and I. Neumann, "Optimal finite element model with response surface methodology for concrete structures based on Terrestrial Laser Scanning technology," *Composite Structures*, 2016.

[21] H. Yang, X. Xu, and I. Neumann, "Laser scanning-based updating of a finite-element model for structural health monitoring," *IEEE Sensors*, vol. 16, no. 7, pp. 2100–2104, 2016.

[22] H. Yang, X. Xu, and I. Neumann, "The benefit of 3D laser scanning technology in the generation and calibration of FEM models for health assessment of concrete structures," *Sensors (Switzerland)*, vol. 14, no. 11, pp. 21889–21904, 2014.

[23] H. Yang, M. Omidalizarandi, X. Xu, and I. Neumann, "Terrestrial laser scanning technology for deformation monitoring and surface modeling of arch structures," *Composite Structures*, vol. 169, pp. 173–179, 2017.

[24] L. Piegl and W. Tiller, *The NURBS Book*, Springer Science and Business Media, 2012.

[25] J. Bureick, H. Alkhatib, and I. Neumann, "Robust spatial approximation of laser scanner point clouds by means of free-form curve approaches in deformation analysis," *Journal of Applied Geodesy*, vol. 10, no. 1, pp. 27–35, 2016.

[26] L. Piegl, W. Tiller, and K. R. Koch, "Fitting Free-Form Surfaces to Laserscan Data by NURBS," in *Allgemeine Vermessungs-Nachrichten: AVN*, vol. 116, pp. 134–140, Allgemeine Vermessungs-Nachrichten, AVN, 2009.

[27] https://en.wikipedia.org/wiki/CloudCompare.

Bibliography

Al-Manasir, K. and Lichti, D. (2015). Self–calibration of a Lecia HDS7000 scanner. In *Processing in FIG Working Week*, Copenhagen, Denmark.

Alba, M., Fregonese, L., Prandi, F., Scaioni, M., and Valgoi, P. (2006). Structural monitoring of a large dam by terrestrial laser scanning. *The International Archives of the Photogrammetry, Remote Sensing and Spatial Information Sciencess*, 36(5):6.

Alkhatib, H. and Kutterer, H. (2013). Estimation of measurement uncertainty of kinematic TLS observation process by means of Monte-Carlo methods. *Journal of Applied Geodesy*, 7(2):125–134.

Alkhatib, H., Neumann, I., and Kutterer, H. (2009). Uncertainty modeling of random and systematic errors by means of Monte Carlo and fuzzy techniques. *Journal of Applied Geodesy*, 3(2):67–79.

Bae, K.-H. (2009). Evaluation of the convergence region of an automated registration method for 3D laser scanner point clouds. *Sensors*, 9:355–75.

Barnea, S. and Filin, S. (2013). Segmentation of terrestrial laser scanning data using geometry and image information. *ISPRS Journal of Photogrammetry and Remote Sensing*, 76:33–48.

Barrell, H. and Sears, J. (1939). The refraction and dispersion of air for the visible spectrum. *Philosophical Transactions of the Royal Society of London. Series A: Mathematical and Physical Sciences*, 238(786):1–64.

Besl, P. J. and McKay, N. D. (1992). Method for registration of 3D shapes. *Sensor Fusion IV: Control Paradigms and Data Structures*, 1611:586–607.

Bitelli, G., Dubbini, M., and Zanutta, A. (2004). Terrestrial laser scanning and digital photogrammetry techniques to monitor landslide bodies. *The International Archives of the Photogrammetry, Remote Sensing and Spatial Information Sciences*, 35(Part B5):246–251.

Blais, F. (2004). Review of 20 years of range sensor development. *Journal of electronic imaging*, 13(1):231–244.

Böhm, J. and Becker, S. (2007). Automatic marker-free registration of terrestrial laser scans using reflectance. In *Proceedings of the 8th Conference on Optical 3D Measurement Techniques*, pages 338–343, Zurich, Switzerland.

Borah, D. K. and Voelz, D. G. (2007). Estimation of laser beam pointing parameters in the presence of atmospheric turbulence. *Applied optics*, 46(23):6010–6018.

Borges, C. F. and Pastva, T. (2002). Total least squares fitting of Bézier and B-spline curves to ordered data. *Computer Aided Geometric Design*, 19(4):275–289.

Bureick, J., Alkhatib, H., and Neumann, I. (2016a). Robust spatial approximation of laser scanner point clouds by means of free-form curve approaches in deformation analysis. *Journal of Applied Geodesy*, 10(1):27–35.

Bureick, J., Neuner, H., Harmening, C., and Neumann, I. (2016b). Curve and surface approximation of 3D point clouds. *Allgemeine Vermessungs-Nachrichten (AVN)*, 123(11-12):315–327.

Burger, M., Wujanz, D., and Neitzel, F. (2018). Segmentierung von Punktwolken anhand von geometrischen und radiometrischen Informationen. pages 116–128, Oldenburger, German.

Burnham, K. P. and Anderson, D. R. (2004). *Model selection and multi-model inference: A Practical Information-Theoretic Approach.* Springer.

Camarda, M., Guarnieri, A., Milan, N., Vettore, A., et al. (2010). Health monitoring of complex structure using TLS and photogrammetry. *The International Archives of the Photogrammetry, Remote Sensing and Spatial Information Sciences*, 38:125–130.

Chen, D., Zhang, L., Mathiopoulos, P. T., and Huang, X. (2014). A methodology for automated segmentation and reconstruction of urban 3D buildings from ALS point clouds. *IEEE Journal of Selected Topics in Applied Earth Observations and Remote Sensing*, 7(10):4199–4217.

Chmelina, K., Jansa, J., Hesina, G., and Traxler, C. (2012). A 3D laser scanning system and scan data processing method for the monitoring of tunnel deformations. *Journal of Applied Geodesy*, 6(3-4):177–185.

Chow, J., Lichti, D., and Glennie, C. (2011). Point-based versus plane-based self-calibration of static terrestrial laser scanners. *The International Archives of the Photogrammetry, Remote Sensing and Spatial Information Sciences*, 38:121–126.

Cox, D. R. (1961). Tests of separate families of hypotheses. In *Proceedings of the Fourth Berkeley Symposium on Mathematical Statistics and Probability, Volume 1: Contributions to the Theory of Statistics*, pages 105–123, Berkeley, USA.

Delaloye, D. (2012). *Development of a new methodology for measuring deformation in tunnels and shafts with terrestrial laser scanning (LIDAR) using elliptical fitting algorithms.* Ph.D. thesis, Queen's University, Canada.

Dold, C. and Brenner, C. (2008). Analysis of score functions for the automatic registration of terrestrial laser scans. *The International Archives of the Photogrammetry, Remote Sensing and Spatial Information Sciences*, 37:417–422.

Douillard, B., Underwood, J., Kuntz, N., Vlaskine, V., Quadros, A., Morton, P., and Frenkel, A. (2011). On the segmentation of 3D LIDAR point clouds. In *IEEE International Conference on Robotics and Automation 2011*, pages 2798–2805, Shanghai, China.

Dupuis, J.and Holst, C. and Kuhlmann, H. (2016). Laser scanning based growth analysis of plants as a new challenge for deformation monitoring. *Journal of Applied Geodesy*, 10(1):37–44.

Dutescu, E. (2006). *Digital 3D documentation of cultural heritage sites based on terrestrial laser scanning.* Ph.D. thesis, Universität der Bundeswehr München.

Ehm, M.and Hesse, C. (2012). Entwicklung eines kinematischen laserscansystems für anwendungen im schiffbau. In *Konferenz Go-3D "Computergraphik für die Praxis"*, Rostock, Germany.

Eling, D. (2009). *Terrestrisches Laserscanning für die Bauwerksüberwachung.* Ph.D. thesis, Deutsche Geodätische Kommission bei der Bayerischen Akademie der Wissenschaften. Series C, No. 641.

Erdélyi, J., Kopáčik, A., Lipták, I., and Kyrinovič, P. (2017). Automation of point cloud processing to increase the deformation monitoring accuracy. *Applied Geomatics*, 9(2):105–113.

Fischler, M. A. and Bolles, R. C. (1981). Random sample consensus: a paradigm for model fitting with applications to image analysis and automated cartography. *Communications of the ACM*, 24(6):381–395.

Friedli, E., Presl, R., and Wieser, A. (2019). Influence of atmospheric refraction on terrestrial laser scanning at long range. In *4th Joint International Symposium on Deformation Monitoring (JISDM)*, Athens, Greece.

Ge, X. (2016). *Terrestrial Laser Scanning Technology from Calibration to Registration with Respect to Deformation Monitoring*. Ph.D. thesis, Technische Universität München.

Ge, X. and Wunderlich, T. (2016). Surface-based matching of 3D point clouds with variable coordinates in source and target system. *ISPRS journal of photogrammetry and remote sensing*, 111:1–12.

Gordon, B. (2008). *Zur Bestimmung von Messunsicherheiten terrestrischer Laserscanner*. Ph.D. thesis, Technische Universität Darmstadt.

Gordon, S. J. and Lichti, D. D. (2007). Modeling terrestrial laser scanner data for precise structural deformation measurement. *Journal of Surveying Engineering*, 133(2):72–80.

Grant, D. S. (2013). *Cloud to cloud registration for 3D point data*. Ph.D. thesis, Purdue University.

Gressin, A., Mallet, C., Demantké, J., and David, N. (2013). Towards 3D lidar point cloud registration improvement using optimal neighborhood knowledge. *ISPRS journal of photogrammetry and remote sensing*, 79:240–251.

Gruen, A. and Akca, D. (2005). Least squares 3D surface and curve matching. *ISPRS Journal of Photogrammetry and Remote Sensing*, 59(3):151–174.

Harmening, C. and Neuner, H. (2015). A constraint-based parameterization technique for B-spline surfaces. *Journal of Applied Geodesy*, 9(3):143–161.

Harmening, C. and Neuner, H. (2016). Choosing the optimal number of B-spline control points (Part 1: methodology and spproximation of curves). *Journal of Applied Geodesy*, 10(3):139–157.

Harmening, C. and Neuner, H. (2017). Choosing the optimal number of B-spline control points (Part 2: approximation of surfaces and applications). *Journal of Applied Geodesy*, 11(1):43–52.

Hejbudzka, K., Lindenbergh, R., Soudarissanane, S. S., and Humme, A. (2010). Influence of atmospheric conditions on the range distance and number of returned points in Leica ScanStation 2 point clouds. In *Proceedings ISPRS Commission V Mid-Term Symposium: Close Range Image Measurement Techniques*, Newcastle upon Tyne, UK.

Hennes, M. (2007). Konkurrierende Genauigkeitsmaße - Potential und Schwächen aus der Sicht des Anwenders. *Allgemeine Vermessungs-Nachrichten (AVN)*, (7):136–146.

Herrero-Huerta, M., Lindenbergh, R., Ponsioen, L., and van Damme, M. (2016). Morphological changes along a dike landside slope sampled by 4D high resolution terrestrial laser scanning. *The International Archives of the Photogrammetry, Remote Sensing and Spatial Information Sciences*, 41:227–232.

Hesse, C., Heer, R., Horst, S., and Neuner, H. (2006). A concept for monitoring wind energy turbines with geodetic techniques. In *Proceedings of 3rd IAG/12th FIG Symposium*, Baden, Austria.

Hesse, C., Heunecke, O., Speth, M., and Stelzer, I. (2000). Belastungsversuche an einem Schalentragwerk aus Ziegelsteinen. In *XIII. Intationaler Kurs für Ingenieurvermessung*, pages 340–345, Munich, German.

Heunecke, O., Kuhlmann, H., Welsch, W., Eichhorn, A., and Neuner, H. (2013). *Auswertung geodätischer Überwachungsmessungen, 2. Aufl. Ein Band der Reihe: Handbuch Ingenieurgeodäsie. H.* Wichmann.

Holst, C. and Kuhlmann, H. (2014). Aiming at self-calibration of terrestrial laser scanners using only one single object and one single scan. *Journal of applied geodesy*, 8(4):295–310.

Holst, C., Nothnagel, A., Blome, M., Becker, P., Eichborn, M., and Kuhlmann, H. (2015). Improved area-based deformation analysis of a radio telescopes main reflector based on terrestrial laser scanning. *Journal of Applied Geodesy*, 9(1):1–14.

Ingensand, H., Ryf, A., and Schulz, T. (2003). Performances and experiences in terrestrial laser-scanning. In *Proceedings of the 6th Conference on Optical 3D Measurement Techniques*, Zurich, Switzerland.

Ioannidis, C., Valan, A., Georgopoulos, A., and Tsiligiris, E. (2006). 3D model generation for deformation analysis using laser scanning data of a cooling tower. In *3rd IAG / 12th FIG Symposium*, Baden, Austria.

JCGM (2008). *Uncertainty of measurement-Part 3: Guide to the expression of uncertainty in measurement (GUM 1995 with minor corrections).*

Jian, L., Youchuan, W., and Xianjun, G. (2012). A new approach for subway tunnel deformation monitoring: high-resolution terrestrial laser scanning. *The International Archives of the Photogrammetry, Remote Sensing and Spatial Information Sciences*, 39:223–228.

Joeckel, R., Stober, M., and Huep, W. (2008). *Elektronische Entfernungsmessung und ihre Integration in aktuelle Positionierungsverfahren.* Wichmann.

Jurek, T., Kuhlmann, H., and Holst, C. (2017). Impact of spatial correlations on the surface estimation based on terrestrial laser scanning. *Journal of Applied Geodesy*, 11(3):143–155.

Kanade, T. (2012). *Three-Dimensional Machine Vision.* Springer.

Kang, Z., Li, J., Zhang, L., Zhao, Q., and Zlatanova, S. (2009). Automatic registration of terrestrial laser scanning point clouds using panoramic reflectance images. *Sensors*, 9(4):2621–2646.

Kargoll, B. (2012). *On the theory and application of model misspecification tests in geodesy.* Ph.D. thesis, Deutsche Geodätische Kommission bei der Bayerischen Akademie der Wissenschaften. Series C, No. 674.

Kauker, S., Holst, C., Schwieger, V., Kuhlmann, H., and Schön, S. (2016). Spatio-temporal correlations of terrestrial laser scanning. *Allgemeine Vermessungs-Nachrichten (AVN)*, 123:170–182.

Kauker, S. and Schwieger, V. (2017). A synthetic covariance matrix for monitoring by terrestrial laser scanning. *Journal of Applied Geodesy*, 11(2):77–87.

Kersten, T. P., Büyüksalİh, G., Baz, İ., and Jacobsen, K. (2009). Documentation of Istanbul historic peninsula by kinematic terrestrial laser scanning. *The Photogrammetric Record*, 24(126):122–138.

Koch, K.-R. (2008a). Determining uncertainties of correlated measurements by Monte Carlo simulations applied to laserscanning. *Journal of applied geodesy*, 2(3):139–147.

Koch, K.-R. (2008b). Evaluation of uncertainties in measurements by Monte Carlo simulations with an application for laserscanning. *Journal of Applied Geodesy*, 2(2):67–77.

Kopačik, A., Erdelyi, J., Liptak, I., and Kyrinovič, P. (2013). Deformation monitoring of bridge structures using TLS. In *2nd Joint International Symposium on Deformation Monitoring (JISDM)*, Nottingham, UK.

Lague, D., Brodu, N., and Leroux, J. (2013). Accurate 3D comparison of complex topography with terrestrial laser scanner: Application to the Rangitikei canyon (N-Z). *ISPRS Journal of Photogrammetry and Remote Sensing*, 82:10–26.

Lehmann, R. and Lösler, M. (2016). Multiple outlier detection: hypothesis tests versus model selection by information criteria. *Journal of Surveying Engineering*, 142(4):04016017.

Lewis, F., Butler, A., and Gilbert, L. (2011). A unified approach to model selection using the likelihood ratio test. *Methods in Ecology and Evolution*, 2(2):155–162.

Li, X., Li, Y., Xie, X., and Xu, L. (2018). Terrestrial laser scanner autonomous self-calibration with no prior knowledge of point-clouds. *IEEE Sensors Journal*, 18(22):9277–9285.

Lichtenstein, M. and Benning, W. (2009). Bestimmung räumlicher Transformationsparameter auf Grundlage von 3D Geraden und projektiver Geometrie. In *Photogrammetrie, Laserscanning, Optische 3D-Messtechnik, Beiträge der Oldenburger 3D-Tage 2009*, pages 67–73, Oldenburger, German.

Lichti, D. D. (2007). Error modelling, calibration and analysis of an am–cw terrestrial laser scanner system. *ISPRS Journal of Photogrammetry and Remote Sensing*, 61(5):307–324.

Lichti, D. D. (2010). Terrestrial laser scanner self-calibration: Correlation sources and their mitigation. *ISPRS Journal of Photogrammetry and Remote Sensing*, 65(1):93–102.

Lichti, D. D. and Gordon, S. J. (2004). Error propagation in directly georeferenced terrestrial laser scanner point clouds for cultural heritage recording. In *Proceedings of FIG Working Week*, Athens, Greece.

Lichti, D. D. and Harvey, B. (2002). The effects of reflecting surface material properties on time-of-flight laser scanner measurements. In *Symposium on Geospatial Theory, Processing and Applications*, Ottawa, Canada.

Lindenbergh, R. and Pfeifer, N. (2005). A statistical deformation analysis of two epochs of terrestrial laser data of a lock. In *Proceedings of the 7th Conference on Optical 3D Measurement Techniques*, Vienna, Austria.

Lindenbergh, R., Uchanski, L., Bucksch, A., and Van Gosliga, R. (2009). Structural monitoring of tunnels using terrestrial laser scanning. *Reports on geodesy*, 87:231–238.

Little, M. J. (2006). Slope monitoring strategy at PPRust open pit operation. In *International Symposium on Stability of Rock Slopes in Open Pit Mining and Civil Engineering*, pages 211–230, Johannesburg, South Africa.

Lõhmus, H., Ellmann, A., Märdla, S., and Idnurm, S. (2018). Terrestrial laser scanning for the monitoring of bridge load tests–two case studies. *Survey Review*, 50(360):270–284.

Ma, W. and Kruth, J.-P. (1995). Parameterization of randomly measured points for least squares fitting of B-spline curves and surfaces. *Computer-Aided Design*, 27(9):663–675.

Mauris, G., Lasserre, V., and Foulloy, L. (2001). A fuzzy approach for the expression of uncertainty in measurement. *Measurement*, 29(3):165–177.

Medić, T., Holst, C., and Kuhlmann, H. (2017). Towards system calibration of panoramic laser scanners from a single station. *Sensors*, 17(5):1145.

Monserrat, O. and Crosetto, M. (2008). Deformation measurement using terrestrial laser scanning data and least squares 3D surface matching. *ISPRS Journal of Photogrammetry and Remote Sensing*, 63(1):142–154.

Mukupa, W., Roberts, G. W., Hancock, C. M., and Al-Manasir, K. (2017). A review of the use of terrestrial laser scanning application for change detection and deformation monitoring of structures. *Survey Review*, 49(353):99–116.

Muralikrishnan, B., Wang, L., Rachakonda, P., and Sawyer, D. (2018). Terrestrial laser scanner geometric error model parameter correlations in the two-face, length-consistency, and network methods of self-calibration. *Precision Engineering*, 52:15–29.

Neitzel, F. (2007). Investigation of axes errors of terrestrial laser scanners. In *The 5th International Symposium Turkisch-German Joint Geodetic Days*, Berlin, Germany.

Neitzel, F., Ezhov, N., and Petrovic, S. (2019). Total least squares spline approximation. *Mathematics*, 7(5):462.

Neitzel, F. and Neumann, I. (2013). Scanning in Motion-Kinematisches TLS mittels mobiler Plattformen. In *Terrestrisches Laserscanning*, volume 72, pages 89–106, Fulda, Germany.

Neitzel, F., Niemeier, W., Weisbrich, S., and Lehmann, M. (2012). Investigation of low-cost accelerometer, terrestrial laser scanner and ground-based radar interferometer for vibration monitoring of bridges. In *Proceedings of the 6th European Workshop on Structural Health Monitoring*, pages 3–6, Dresden, Germany.

Neuner, H., Holst, C., and Kuhlmann, H. (2016). Overview on current modelling strategies of point clouds for deformation analysis. *Allgemeine Vermessungs-Nachrichten (AVN)*, 123:328–339.

Neuner, H., Schmitt, C., and Neumann, I. (2014). Zur Bestimmung der verkehrsseitig verursachten Dehnung an einem Brückentragwerk mittels terrestrischem Laserscanning. *Ingenieurvermessung'14. Beiträge zum 17th Internationalen Ingenieurvermessungskurs Zürich*, pages 231–243.

Niemeier, W. (2008). *Ausgleichungsrechnung: Statistische Auswertemethoden*. Walter de Gruyter.

Niemeyer, J., Rottensteiner, F., and Soergel, U. (2012). Conditional random fields for lidar point cloud classification in complex urban areas. *ISPRS Annals of the Photogrammetry, Remote Sensing and Spatial Information Sciences*, 3:263–268.

Nuttens, T., De Wulf, A., Bral, L., De Wit, B., Carlier, L., De Ryck, M., Stal, C., Constales, D., and De Backer, H. (2010). High resolution terrestrial laser scanning for tunnel deformation measurements. In *FIG Congress*, Sydney, Australia.

Nyland, L. S. (1998). Capturing dense environmental range information with a panning scanning laser rangefinder. Technical Report TR98-039.

Ogundare, J. O. (2015). *Precision surveying: the principles and geomatics practice*. John Wiley & Sons.

Ohlmann-Lauber, J. and Schäfer, T. (2011). Ansätze zur Ableitung von Deformationen aus TLS-Daten. In *DVW Seminal Terrestrisches Laserscanning-TLS 2011 mit TLS-Challenge*, Fulda, Germany.

Paffenholz, J.-A. (2012). *Direct geo-referencing of 3D point clouds with 3D positioning sensors*. Ph.D. thesis, Deutsche Geodätische Kommission bei der Bayerischen Akademie der Wissenschaften. Series C, No. 689.

Paffenholz, J.-A., Vennegeerts, H., and Kutterer, H. (2008). High frequency terrestrial laser scans for monitoring kinematic processes. In *Proceedings of the INGEO: 4th International Conference on Engineering Surveying*, Bratislava, Slovakia.

Pareja, T. F., Pablos, A. G., and y Oliva, J. d. V. (2013). Terrestrial laser scanner (TLS) equipment calibration. *Procedia Engineering*, 63:278–286.

Pelzer, H. (1971). *Zur Analyse geodätischer Deformations-messungen*. Ph.D. thesis, Deutsche Geodätische Kommission bei der Bayerischen Akademie der Wissenschaften. Series C, No. 164.

Pesci, A., Teza, G., and Boschi, E. (2015). Laser scanning-based detection of morphological changes of a historical building occurred during a seismic sequence: Method and Case study. *International Journal of Geomatics and Geosciences*, 5(3):427.

Piegl, L. and Tiller, W. (2012). *The NURBS Book*. Springer.

Rabbani, T., Van Den Heuvel, F., and Vosselmann, G. (2006). Segmentation of point clouds using smoothness constraint. *The International Archives of Photogrammetry, Remote sensing and Spatial Information Sciences*, 36(5):248–253.

Reshetyuk, Y. (2009). *Self-calibration and direct georeferencing in terrestrial laser scanning*. Ph.D. thesis, Royal Institute of Technology (KTH).

Reshetyuk, Y. (2010). A unified approach to self-calibration of terrestrial laser scanners. *ISPRS Journal of Photogrammetry and Remote Sensing*, 65(5):445–456.

Rietdorf, A. (2007). *Automatisierte Auswertung und Kalibrierung von scannenden Messsystemen mit tachymetrischem Messprinzip*. Ph.D. thesis, Deutsche Geodätische Kommission bei der Bayerischen Akademie der Wissenschaften. Series C, No. 582.

Rüeger, J. M. (1990). *Electronic Distance Measurement*. Springer.

Salo, P., Jokinen, O., and Kukko, A. (2008). On the calibration of the distance measuring component of a terrestrial laser scanner. In *Processing in the XXIth ISPRS Congress, Silk Road for Information from Imagery*, Beijing, China.

Schäfer, T. (2017). *Berührungslose und flächenhafte Deformationsmessungen an Betonoberflächen unter besonderer Berücksichtigung der Interaktion zwischen Laserstrahl und Oberfläche*. Ph.D. thesis, Deutsche Geodätische Kommission bei der Bayerischen Akademie der Wissenschaften. Series C, No. 805.

Schill, F., Sviridova, A., and Eichhorn, A. (2019). Deformation monitoring of noise barriers with profile laser scanning. In *4th Joint International Symposium on Deformation Monitoring (JISDM)*, Athens, Greece.

Schmitt, C., Neuner, H., and Kromoser, B. (2019). Geodetic surface based methods for structural analysis during construction phase. In *4th Joint International Symposium on Deformation Monitoring (JISDM)*, Athens, Greece.

Schneider, D. (2006). Terrestrial laser scanning for area based deformation analysis of towers and water damns. In *Proceedings of 3rd IAG/12th FIG Symposium*, Baden, Austria.

Schneider, D. and Schwalbe, E. (2008). Integrated processing of terrestrial laser scanner data and fisheye-camera image data. *The International Archives of the Photogrammetry, Remote Sensing and Spatial Information Science*, 37(Part B5):1037–1044.

Schuhmacher, S. and Böhm, J. (2005). Georeferencing of terrestrial laserscanner data for applications in architectural modeling. *The International Archives of the Photogrammetry, Remote Sensing and Spatial Information Sciences*, 36:209–220.

Schulz, T. (2008). *Calibration of a terrestrial laser scanner for engineering geodesy.* Ph.D. thesis, ETH Zurich.

Soudarissanane, S. S. (2016). *The geometry of terrestrial laser scanning: identification of errors, modeling and mitigation of scanning geometry.* Ph.D. thesis, Delft University of Technology.

Soudarissanane, S. S. and Lindenbergh, R. (2011). Optimizing terrestrial laser scanning measurement set-up. *International Archives of the Photogrammetry, Remote Sensing and Spatial Information Sciences*, 38:127–132.

Stephens, P. A., Buskirk, S. W., Hayward, G. D., and Del Rio, C. M. (2005). Information theory and hypothesis testing: a call for pluralism. *Journal of Applied Ecology*, 42(1):4–12.

Tapete, D., Casagli, N., Luzi, G., Fanti, R., Gigli, G., and Leva, D. (2013). Integrating radar and laser-based remote sensing techniques for monitoring structural deformation of archaeological monuments. *Journal of Archaeological Science*, 40(1):176–189.

Teunissen, P. J. G. (2000). *Testing theory.* Delft Academic Press.

Teunissen, P. J. G. and de Bakker, P. F. (2013). Single-receiver single-channel multi-frequency GNSS integrity: outliers, slips, and ionospheric disturbances. *Journal of Geodesy*, 87(2):161–177.

Teza, G., Galgaro, A., Zaltron, N., and Genevois, R. (2007). Terrestrial laser scanner to detect landslide displacement fields: a new approach. *International Journal of Remote Sensing*, 28(16):3425–3446.

Truong-Hong, L. and Lindenbergh, R. (2019). Measuring deformation of bridge structures using laser scanning data. In *4th Joint International Symposium on Deformation Monitoring (JISDM)*, Athens, Greece.

Tsakiri, M., Lichti, D., and Pfeifer, N. (2006). Terrestrial laser scanning for deformation monitoring. In *Proceedings of 3rd IAG/12th FIG Symposium*, Baden, Austria.

Van Gosliga, R., Lindenbergh, R., and Pfeifer, N. (2006). Deformation analysis of a bored tunnel by means of terrestrial laser scanning. *The International Archives of the Photogrammetry, Remote Sensing and Spatial Information*, 36(5):167–172.

Vezočnik, R., Ambrožič, T., Sterle, O., Bilban, G., Pfeifer, N., Stopar, B., et al. (2009). Use of terrestrial laser scanning technology for long term high precision deformation monitoring. *Sensors*, 9(12):9873–9895.

Vosselman, G. (1999). Building reconstruction using planar faces in very high density height data. *The International Archives of the Photogrammetry, Remote Sensing and Spatial Information Sciences*, 32:87–94.

Vosselman, G., Gorte, B. G., Sithole, G., and Rabbani, T. (2004). Recognising structure in laser scanner point clouds. *The International Archives of the Photogrammetry, Remote Sensing and Spatial Information Sciences*, 46(8):33–38.

Vosselman, G. and Maas, H.-G. (2010). *Airborne and Terrestrial Laser Scanning.* Whittle.

Vuong, Q. H. (1989). Likelihood ratio tests for model selection and non-nested hypotheses. *Econometrica: Journal of the Econometric Society*, 8:307–333.

Walsh, G. (2014). Telescope based calibration of a three dimensional optical scanner. Patent number: CA2745807 C.

Walton, G., Delaloye, D., and Diederichs, M. S. (2014). Development of an elliptical fitting algorithm to improve change detection capabilities with applications for deformation monitoring in circular tunnels and shafts. *Tunnelling and Underground Space Technology*, 43:336–349.

Wang, J. (2013a). Block-to-point fine registration in terrestrial laser scanning. *Remote Sensing*, 5(12):6921–6937.

Wang, J. (2013b). *Towards deformation monitoring with terrestrial laser scanning based on external calibration and feature matching methods.* Ph.D. thesis, Leibniz Universität Hannover.

Watanabe, T., Niwa, T., , and Masuda, H. (2016). Registration of point-clouds from terrestrial and portable laser scanners. *International Journal of Automation Technology*, 10(2):163–171.

Weichel, H. (1990). *Laser beam propagation in the atmosphere*, volume 3. SPIE.

Weinmann, M. and Jutzi, B. (2015). Geometric point quality assessment for the automated, markerless and robust registration of unordered TLS point clouds. *ISPRS Annals of the Photogrammetry, Remote Sensing and Spatial Information Sciences*, II-3/W5:89–96.

Welsch, W. and Heunecke, O. (2001). Models and terminology for the analysis of geodetic monitoring observations. In *The 10th FIG International Symposium on Deformation Measurements*, pages 390–412, Orange, California, USA.

Williams, D. A. (1970). Discrimination between regression models to determine the pattern of enzyme synthesis in synchronous cell cultures. *Biometrics*, 26(1):23–32.

Wujanz, D. (2016). *Terrestrial laser scanning for geodetic deformation monitoring.* Ph.D. thesis, Deutsche Geodätische Kommission bei der Bayerischen Akademie der Wissenschaften. Series C, No. 775.

Wujanz, D., Avian, M., Krueger, D., and Neitzel, F. (2014). Automatic registration of terrestrial laser scans for geological deformation monitoring. In *Beiträge der Vertical Geology Conference*, pages 29–33, Ausanne, Switzerland.

Wujanz, D., Burger, M., Mettenleiter, M., and Neitzel, F. (2017). An intensity-based stochastic model for terrestrial laser scanners. *ISPRS Journal of Photogrammetry and Remote Sensing*, 125:146–155.

Wujanz, D. and Neitzel, F. (2016). Model based viewpoint planning for terrestrial laser scanning from an economic perspective. *The International Archives of the Photogrammetry, Remote Sensing and Spatial Information Sciences*, 41:607–614.

Wujanz, D., Schaller, S., Gielsdorf, F., and Gründig, L. (2018). Plane-based registration of several thousand laser scans on standard hardware. *The International Archives of the Photogrammetry, Remote Sensing and Spatial Information Sciences*, 42(2):1207–1212.

Wunderlich, T., Niemeier, W., Wujanz, D., Holst, C., Neitzel, F., and Kuhlmann, H. (2016). Areal deformation analysis from TLS point clouds–the challenge. *Allgemeine Vermessungs-Nachrichten (AVN)*, 123(11–12):340–351.

Xie, X. and Lu, X. (2017). Development of a 3D modeling algorithm for tunnel deformation monitoring based on terrestrial laser scanning. *Underground Space*, 2(1):16–29.

Zámečníková, M., Neuner, H., Pegritz, S., and Sonnleitner, R. (2015). Investigation on the influence of the incidence angle on the reflectorless distance measurement of a terrestrial laser scanner. *Vermessung & Geoinformation*, 2+3/2015:208–218.

Zámečníková, M., Wieser, A., Woschitz, H., and Ressl, C. (2014). Influence of surface reflectivity on reflectorless electronic distance measurement and terrestrial laser scanning. *Journal of applied geodesy*, 8(4):311–326.

Zimmermann, F., Holst, C., Klingbeil, L., and Kuhlmann, H. (2018). Accurate georeferencing of tls point clouds with short GNSS observation durations even under challenging measurement conditions. *Journal of Applied Geodesy*, 12(4):289–301.

Zogg, H. and Ingensand, H. (2008). Terrestrial laser scanning for deformation monitoring–load tests on the felsenau viaduct (CH). *The International Archives of the Photogrammetry, Remote Sensing and Spatial Information Sciences*, 37:555–562.

Zoller+Fröhlich (2007). *Technical datasheet IMAGER 5006.* Zoller+Fröhlich GmbH.

Curriculum Vitae

Personal Information

Name:	Xin Zhao
Date of birth:	26.07.1986
Place of birth:	Taiyuan, Shanxi Province, P.R. China
Nationality:	Chinese

Education

09.2013 - 03.2014	Master student, Geodesy and Geoinformation Science, Institute of Geodesy and Geoinformation Technology, Technische Universität Berlin, Germany.
09.2010 - 06.2012	Survey engineering (Master), School of Environment Science and Spatial Informatics, China University of Mining Technology, Jiangsu, P.R. China.
09.2006 - 06.2010	Survey engineering (Bachelor), School of Environment Science and Spatial Informatics, China University of Mining Technology, Jiangsu, P.R. China.
09.2002 - 06.2005	Taiyuan Chengcheng Senior High School, Shanxi, P.R. China.

Working experience

09.2014 - now	PhD candidate, Geodetic Institute, Faculty of Civil Engineering and Geodetic Science, Gottfried Wilhelm Leibniz Universität Hannover, Germany.
07.2012 - 07.2013	Polytechnic Institute Taiyuan University of Technology (Lecturer), Shanxi, P.R. China.

Acknowledgment